DEVELOPMENT OF A PARALLEL GEOMECHANICS CODE BASED ON THE MESSAGE-PASSING-INTERFACE (MPI) APPROACH AND ITERATIVE COUPLING WITH A PARALLELIZED FLOW AND THERMAL SIMULATOR FOR THE ANALYSIS OF SYSTEM BEHAVIOR IN HYDRATE-BEARING GEOLOGIC MEDIA

A Dissertation

by

JIECHENG ZHANG

Submitted to the Graduate and Professional School of
Texas A&M University
in partial fulfillment of the requirements for the degree of

DOCTOR OF PHILOSOPHY

Chair of Committee,	George J. Moridis
Co-Chair of Committee,	Thomas A. Blasingame
Committee Members,	Jihoon Kim
	Theofanis Strouboulis
Head of Department,	Jeff Spath

August 2021

Major Subject: Petroleum Engineering

ABSTRACT

The Reservoir GeoMechanics Simulator (RGMS), a geomechanics simulator based on the finite element method and parallelized using the Message Passing Interface (MPI), is developed in this work to model the stresses and deformations in subsurface systems. RGMS can be used stand-alone, or coupled with flow and transport models. pT+H V1.5, a parallel MPI-based version of the serial T+H V1.5 code that describes mass and heat flow in hydrate-bearing porous media, is also developed. Using the fixed-stress split iterative scheme, RGMS is coupled with the pT+H V1.5 to investigate the geomechanical responses associated with gas production from hydrate accumulations. The code development and testing process involve evaluation of the parallelization and of the coupling method, as well as verification and validation of the results.

The parallel performance of the codes is tested on the Texas A&M University Ada Linux cluster using up to 512 processors, and on a Mac Pro computer with 12 processors. The investigated problems are:

Group 1: Geomechanical problems solved by RGMS in 2D Cartesian and cylindrical domains and a 3D problem, involving 4×10^6 and 3.375×10^6 elements, respectively;

Group 2: Realistic problems of gas production from hydrates using pT+H V1.5 in 2D and 3D systems with 2.45×10^5 and 3.6×10^6 elements, respectively;

Group 3: The problems in Group 2 solved with the coupled RGMS-pT+H V1.5 simulator, fully accounting for geomechanics.

Two domain partitioning options are investigated on the Ada Linux cluster, and the code parallel performance is monitored. Using 512 processors, the simulation speedups (a) of RGMS are 218.89, 188.13, and 284.70 in the Group 1 problems, (b) of pT+H V1.5 are 174.25 and 341.67 in the Group 2 cases, and (c) of the coupled simulators are 134.97 and 331.80 in the Group 3 cases.

The results produced in this work show (a) the necessity of using full geomechanics simulators in marine hydrate-related studies because of the associated pronounced geomechanical effects on production and displacements, (b) the importance of fine discretization, and (c) the effectiveness of the parallel simulators developed in this study, which can be the only realistic option in these complex simulations of large multidimensional domains.

DEDICATION

This dissertation is dedicated to my parents, Shimin Zhang and Xingmei Chen, and my wife, Dier Liu.

ACKNOWLEDGEMENTS

I would like to thank my committee chair, Dr. George J. Moridis, my committee co-chair, Dr. Thomas A. Blasingame, and my committee members, Dr. Jihoon Kim, Dr. Theofanis Strouboulis, for their guidance and support throughout the course of this research.

I would also like to thank my friends, colleagues, and the department faculty and staff for making my time at Texas A&M University a great experience.

Finally, I would like to thank my parents, Shimin Zhang and Xingmei Chen, and my wife, Dier Liu, for their love, support, patience, and encouragement.

CONTRIBUTORS AND FUNDING SOURCES

Contributors

This work was supervised by a dissertation committee consisting of Professor Dr. George J. Moridis [advisor], Dr. Thomas A. Blasingame [co- advisor], and Dr. Jihoon Kim of the Department of Petroleum Engineering, and Professor Dr. Theofanis Strouboulis of the Department of Aerospace Engineering.

The general parallel geomechanics simulator RGMS was developed based on the serial geomechanics simulator ROCMECH studying the problems in two- and three-dimensional Cartesian coordinate systems provided by Professor Dr. Jihoon Kim of the Department of Petroleum Engineering. The parallel flow and transport simulator for hydrate-bearing geologic media pT+H V1.5 was developed based on the serial flow and transport simulator for hydrate-bearing geologic media T+H V1.5 provided by Professor Dr. George J. Moridis of the Department of Petroleum Engineering.

All other work conducted for the thesis dissertation was completed by the student independently.

Funding Sources

Graduate study was supported by the Research Assistantship funded by a start-up research project under Dr. George J. Moridis from Texas A&M University.

NOMENCLATURE

$\Delta()$	Change
ΔH^0	Specific enthalpy of hydrate dissociation/formation [J·kg^{-1}]
∇	Del operator
A	Aqueous phase
C_R	Heat capacity of the dry rock [J·kg^{-1}·K^{-1}]
dA	Differential surface [m^2]
dV	Differential volume [m^3]
E	Young's modulus [Pa]
f_σ	Radiance emittance factor
G	Shear modulus [Pa] or gaseous phase
G_0	Shear modulus when the hydrate saturation is zero [Pa]
G_1	Shear modulus when the hydrate saturation is one [Pa]
H	Solid hydrate phase
h_β	Specific enthalpy of phase β [J·kg^{-1}]
I	Solid ice phase
i	Inhibitor component
k	Rock intrinsic permeability [m^2]
K_{dr}	Drained bulk modulus [Pa]
K_{dr0}	Drained modulus when the hydrate saturation is zero [Pa]
K_{dr1}	Drained modulus when the hydrate saturation is one [Pa]

K_s	Skeletal grain modulus [Pa]
k_h	Horizontal permeability [m^2]
k_r	Radial permeability [m^2]
$k_{r\beta}$	Relative permeability of phase β
k_z	Vertical permeability [m^2]
$\overline{k_\theta}$	Composite thermal conductivity of the medium/fluid ensemble [$W \cdot m^{-1} \cdot K^{-1}$]
$k_{\theta d}$	Formation thermal conductivity under desaturated conditions [$W \cdot m^{-1} \cdot K^{-1}$]
$k_{\theta w}$	Formation thermal conductivity under fully liquid-saturated conditions [$W \cdot m^{-1} \cdot K^{-1}$]
$k_{\theta I}$	Thermal conductivity of ice phase [$W \cdot m^{-1} \cdot K^{-1}$]
m	Methane component
M_W	Cumulative mass of produced water
M^θ	Heat accumulation term
M^κ	Mass accumulation of component κ [$kg \cdot m^{-3}$]
N	Shape function
P	Pressure [Pa]
P_A	Pressure of the aqueous phase [Pa]
P_{cGW}	Gas-water capillary pressure [Pa]
P_G	Pressure of the gaseous phase [Pa]
P_G^m	Methane vapor partial pressure in the gas phase [Pa]

P_G^w	Water vapor partial pressure in the gas phase [Pa]
P_t	Average mobile fluid pressure [Pa]
$P_{t,0}$	Initial equivalent pore pressure [Pa]
P_β	Pressure of phase β [Pa]
Q_A	Aqueous phase mass rate
Q_G	Gaseous phase mass rate
Q_{gA}	Volumetric rate of CH_4 well production from the aqueous phase
Q_{gG}	Volumetric rate of CH_4 well production from the gaseous phase
Q_{gT}	Volumetric rate of CH_4 well production from both the gaseous the aqueous phases
Q_R	Volumetric rate of CH_4 released from dissociation
Q_W	Water mass production rate
q_β	Production rate of phase β [$kg \cdot s^{-1}$]
q^κ	Source/sink term of component κ [$kg \cdot m^{-3} \cdot s^{-1}$]
r	Radial direction
R_{WG}	Instantaneous water-to-gas ratio
R_{WGT}	Cumulative water-to-gas ratio
S_β	Saturation of phase β
T	Temperature [K or °C]
t	Time [s]
U_β	Specific internal energy of phase β [$J \cdot kg^{-1}$]

V_F	Cumulative volume of CH_4 remaining in the deposit as free gas
V_{gA}	Cumulative volume of CH_4 produced at the well in the aqueous phase
V_{gG}	Cumulative volume of CH_4 produced at the well in the gaseous phase
V_{gT}	Cumulative volume of CH_4 produced at the well in both the gas and the aqueous phase
V_n	Volume of the subdomain [m^3]
V_R	Cumulative volume of CH_4 released from dissociation
w	Water component
x	Direction along the x-axis
X_{sA}	Mass fraction of salt in the produced aqueous phase
X_β^κ	Mass fraction of component κ in phase β
y	Direction along the y-axis
z	Direction along the z-axis
α	Biot's coefficient
α_P	Pore compressibility
β	Phase β
Γ_n	Surface of subdomain n [m^2]
γ	Shear strain or empirical permeability reduction factor
ε_v	Current volumetric strain
$\varepsilon_{v,0}$	Initial volumetric strain
θ	Circumferential direction
κ	Component κ

μ_A	Viscosity of the aqueous phase [Pa·s]
ν	Poisson's ratio
ρ_b	Bulk density [kg·m^{-3}]
ρ_f	Fluid density [kg·m^{-3}]
ρ_R	Rock density [kg·m^{-3}]
ρ_β	Density of phase β [kg·m^{-3}]
σ_0	Stefan-Boltzmann constant [5.6687×10^{-8} J·m^{-2}·K^{-4}]
σ_1'	Maximum principal effective stress
τ	Shear stress [Pa]
ϕ	Porosity
ϕ_0	Initial porosity
B	Deformation matrix
C	Elasticity tensor [Pa]
D	Elasticity matrix of moduli [Pa]
F	Force vector
$\mathbf{F}^\kappa$	Flux vector of component κ [kg·m^{-2}·s^{-1}]
g	Gravitational acceleration vector [m·s^{-2}]
I	Identity matrix
J	Jacobian matrix
K	Stiffness matrix
N	Shape function matrix

$\mathbf{n}$	Inward unit normal vector
$\mathbf{R}$	Residual vector
$\mathbf{t}$	External traction vector [Pa]
$\mathbf{u}$	Displacement vector [m]
$\tilde{\mathbf{u}}$	Nodal displacement vector [m]
$\mathbf{x}$	Unknown vector
$\boldsymbol{\varepsilon}$	Strain tensor
$\boldsymbol{\sigma}$	Total stress tensor [Pa]
$\boldsymbol{\sigma}'$	Effective stress tensor [Pa]

TABLE OF CONTENTS

Page

LIST OF FIGURES

Page

LIST OF TABLES

Page

1. INTRODUCTION AND RESEARCH OBJECTIVES

This chapter introduces geomechanics, hydrates, and the coupled flow, thermal, thermodynamic, chemical, and geomechanical processes involved in hydrate dissociation for gas production. It also introduces parallel computing, discusses the studies in the literature, and presents the research objectives.

1.1. Introduction

1.1.1. Geomechanics

Geomechanics plays an essential part in the response of the reservoir to oil production, water injection, and depletion (McPhee et al. 2015). In the recovery process of oil and gas, the pore pressure reduction increases the effective stress that compacts or consolidates the reservoir. These reservoir deformations affect the production performance as a result of the associated permeability and porosity changes, which can be significant in low-permeability and low-porosity unconventional reservoirs such as shale oil and shale gas systems (Zhao 2012).

A conventional reservoir simulator lacking a robust geomechanical component (*i.e.*, relying on a simplified approach that involves constant pore compressibility or empirical models to adjust porosity and permeability) can lead to erroneous results (almost certain when the fluid pressure changes are large). This is because the simplified methods it invokes can adjust the formation porosity and permeability as simple functions of pressure and temperature, but is unable to account for the effects of media deformations

and of the changes in the stress fields. This can only be accomplished by the use of a full geomechanical model that can accurately capture the mechanical behavior of the subsurface rocks, specifically (a) the deformation and (possible) failure of the reservoir media and the well assembly and (b) the effect of changes in the stresses, fluid pressures and temperatures on the associated flow properties (porosity and permeability) that control production, as well as (c) the interdependence of the system flow, thermal and geomechanical properties and conditions.

The finite element method (FEM) is a sophisticated numerical method that is widely used in the solution of problems of structural mechanics and has found significant applications in the solution of geomechanical problems. After discretizing the domain continuum into appropriate spatial subdivisions, the FEM forms finite elements with unknown nodal values and assembles equations of appropriate independent variables that are solved simultaneously to describe the status of the problem in space and time. Because accuracy is determined by both the number of elements and the order of the elements, the computational cost is very high in the solution of problems involving large domains, fine discretizations, and a high precision requirement. In such cases, a parallel geomechanics simulator based on the FEM is necessity, and possibly the only realistic option.

1.1.2. Hydrate

Gas hydrates are solid crystalline compounds in which the lattices of ice-like crystal structures are occupied by gas molecules. Hydrate formation or dissociation is described by the following general equation:

$$G+N_H H_2O=G\cdot N_H H_2O+\Delta H^0 \quad (1.1)$$

where G is the hydrate-forming gas, N_H is the hydration number, $G\cdot N_H H_2O$ is the hydrate, and ΔH^0 is the enthalpy of hydrate formation/dissociation (Moridis et al. 2019). The gas molecules in the hydrate crystals are called guests, and the lattice is called the host. CH_4-hydrates are the overwhelming majority of natural gas hydrates. Securing the trapped gas in the lattice (*i.e.*, hydrate stability) requires low-temperature and high-pressure conditions. In nature, such conditions are encountered in the vicinity of the permafrost and in deep oceanic environments. Although there is significant uncertainty regarding the occurrence and abundance of these natural hydrate accumulations, the scientific consensus is that the amount of CH_4 trapped in natural hydrate deposits is nothing short of vast, thus representing a potentially important energy resource if the associated CH_4 can be technically and economically recovered (Moridis et al. 2008, 2009).

1.1.3. Coupled Simulation

There are three main methods to induce dissociation in order to recover the hydrocarbon from hydrate deposits: (a) depressurization, (b) thermal stimulation, and (c) the use of inhibitors (Makogon 1997). All dissociation methods involve state and phase changes, and are often associated with significant geomechanical responses of the geologic system where the hydrates occur (Moridis et al. 2013).

Because of their interdependence, the coupling of the flow, thermal, and chemical processes with the associated geomechanical system response in numerical simulators becomes very important in the effort to accurately predict the fluid recovery and the

overall behavior of the hydrate-bearing geologic media under production. Some gas-hydrate reservoirs (especially those in marine settings) involve mechanically weak (soft) media (such as silts, clays, and muds) that exhibit significant deformation and displacement (mainly subsidence) during production. Such behavior may lead to substantial reductions in porosity and permeability, which in turn have a considerable impact on production and on the reservoir and well stability.

1.1.4. Parallel Computing

Most computational problems comprise two components: (a) the serial component, which is executed sequentially on a single processor and (b) the parallel component, in which multiple operations are executed simultaneously on different processors. The larger the second component in a problem, the better the parallel performance that can be achieved. Thus, achieving high parallel performance requires the minimization of the serial component.

The idea behind parallel computing is to break a problem into smaller problems that can be solved simultaneously and independently. The resulting individual problems need to be communicated at a certain point by parallel libraries, the most important of which are (a) the Message Passing Interface (MPI), designed for distributed memory systems and (b) OpenMP, designed for shared memory systems. Both libraries are available in programming languages C, C++, and FORTRAN. **Figure 1.1** shows that CPUs (or processors) can only access their assigned memory in the distributed memory system, requiring an interconnection network to share data. This parallel architecture is

implemented in large clusters and supercomputers, so that thousands of CPUs can be installed as long as they are connected by interconnection networks. **Figure 1.2** shows a shared memory system (used mainly small on multi-processor systems such as personal computers and workstations), in which all the CPUs access all the entire (same) memory.

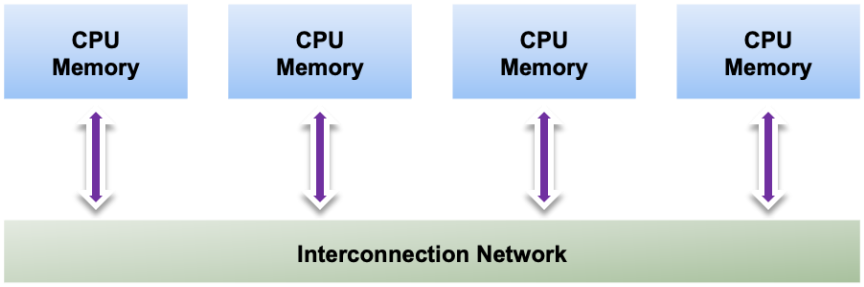

Figure 1.1 Illustration of distributed memory systems.

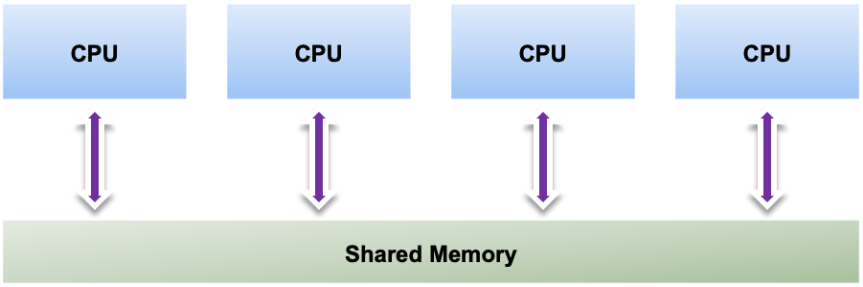

Figure 1.2 Illustration of shared memory systems.

Although MPI works with processes having individual resources and creates the multiprocessing environment, users often use processors instead of processes. In an MPI-based application/program, a process is typically assigned to a core for optimum performance, resulting in a number of processes (or processors) equal to the number of

the cores used for the task. MPI supports point-to-point and collective communications between processors. The common point-to-point communication involves sending data to a processor and receiving data from a processor, which is useful when exchanging boundary values. These operations can be accomplished via either blocking or non-blocking communications. A program will halt its operation until a blocking communication is completed. On the contrary, a non-blocking communication allows the program to perform computations even if the destination processor does not receive the sent data. The summation or maximum/minimum values among processors can be found by collective communications. OpenMP works with threads, which are the subset of processes, and creates a multithreading environment with shared resources. In other words, OpenMP can run multiple threads concurrently on a single process.

Compared to MPI, OpenMP is easier to implement and does not require substantial modifications of a program under parallelization. MPI is more flexible on parallelization but requires an extensive programming effort in addition to the original code modifications. MPI is applied in this study because of (a) the large-scale problems that are solved, involving millions of elements and (b) the large number of mass and heat balance equations per element. The size of the problems, the number of operations, and the very large memory requirement make their solution intractable for single-processor systems, making parallel solutions based on distributed memory systems the only practical (and possible) option.

1.2. Literature Review

Lei et al. (2015) developed a mechanical simulation module based on the FEM and the 3D extended Biot consolidation model and coupled it with the TOUGH2 family of codes (Pruess et al. 1999); the resulting serial simulator was TOUGH2Biot for thermal-hydrodynamic-mechanical (THM) simulations, in which the geomechanics simulation used 8-noded hexahedron elements. Although 3D prism elements can approximate the domain of 2D cylindrical problems (axisymmetric systems) by using wedge-shaped domains, the computational effort is still larger than for pure 2D simulations. Jin et al. (2018) integrated the mechanical module in TOUGH2Biot into T+H (Moridis et al. 2008) and developed a THM simulator hydrateBiot specific for gas hydrate production. However, parallelization was not introduced into the simulator to improve performance.

De La Fuente et al. (2019) used the FEM to develop a serial geomechanics simulator Hydrate-CASM. There were other powerful geomechanics simulators ROCMECH (Kim and Moridis 2013) and Millstone (Queiruga et al. 2019), but only serial versions were created. The commercial finite-difference simulator FLAC3D (Itasca Consulting Group 2002) can also be used to consider the reservoir deformation during production. However, its applicability was negatively affected by two serious shortcomings that stemmed from the inability to access the source code of the commercial FLAC3D simulator: (a) the need to exchange data between the flow simulator and the FLAC3D simulators through external files (*i.e.,* a process over 1,000 times slower than using shared memory), and (b) the reliance on serial or the very low-level standard parallelization of the FLAC3D simulations because the lack of access to the source code

precluded domain decomposition and MPI-based parallelization—and the consequent significant execution speed improvement—for the solution of large problems.

TOUGH+HYDRATE V1.5 (Moridis 2014; hereafter referred to as T+H) is a widely used simulator for the study of the system behavior in hydrate-bearing geologic media in settings that range from laboratory experiments to field studies, in which all the hydrate types are covered, *e.g.*, Class 1 (Moridis et al. 2007a, 2007b), Class 2 (Moridis and Reagan 2007b, 2011a, 2011b), Class 3 (Moridis and Reagan 2007a; Moridis et al. 2011b), and Class 4 (Moridis and Sloan 2007; Li et al. 2010; Moridis et al. 2011c). The T+H V1.5 code is the flow, thermal, and chemical simulator used in this study. Note that T+H V1.5 is a serial simulator.

Zhang et al. (2008) parallelized an earlier version of the T+H code by using the METIS (Karypis and Kumar 1999) partitioning software and the Aztec linear-equation solver (Tuminaro et al. 1999), but this earlier parallel code lacks the significant advances and enhancements of T+H V1.5. Guo et al. (2016) also applied METIS to partition the domain to reduce the load imbalance in the parallel reservoir simulation. Guo et al. (2017) conducted parallelization for the coupled non-isothermal fluid-heat flow and elastoplastic geomechanics by using MPI and OpenMP, tested the parallel performance with only up to 64 processors, and achieved the optimum overall speedup exceeding 14. Pan (2009) implemented MPI parallelization on the coupled geomechanics and compositional simulator based on the domain decomposition method and tested the parallel performance with up to 64 processors. Wang (2014) applied the generalized minimal residual method (GMRES) with the BoomerAMG preconditioner available in the hypre package (Falgout

and Yang 2002) and the geometric multigrid (GMG) solver from the UG4 software toolbox (Heppner et al. 2013) to solve the geomechanics linear equations and multilevel k-way mesh partitioning algorithm in METIS for parallel simulations of coupled flow and geomechanics in porous media.

1.3. Research Objectives

This study aims to address the limited capabilities of currently-available serial or parallel codes for the solution of large problems. The main objectives of this work are:

- To develop the Reservoir GeoMechanics Simulator (hereafter referred to as RGMS or RGM simulator), a new general, MPI-based parallel geomechanics simulator that closely follows the ROCMECH (Kim and Moridis 2013) approach and configuration for the solution of complex, large-scale problems. RGMS can be used as a stand-alone application or coupled with appropriate flow and transport simulators for the solution of both Cartesian (2D and 3D) and cylindrical coordinate (*i.e.*, single-well) systems. RGMS can describe the evolution of stresses, displacements, and of the resulting (a) reservoir deformation and (b) changes in the reservoir properties that are caused by the complex rock mechanics associated with the production operations.
- To parallelize the fully-implicit T+H V1.5 simulator describing the coupled flow, thermal, and chemical processes in hydrate-bearing geologic media; the resulting MPI-based parallel code is named pT+H V1.5 and can simulate complex, large-scale, CH_4-hydrate-related problems that are virtually intractable within any reasonable time

frame by the current serial version of the T+H V1.5 code even if computer memory is not a limitation.

- To seamlessly couple the RGMS and the pT+H V1.5 parallel codes, and use the coupled code for the solution of large-scale 2D and 3D problems that are either currently intractable by the serial codes or require inordinately long execution times (weeks to months) to completion.

2. PARALLEL GEOMECHANICS SIMULATION

This chapter presents detailed information on the RGMS code for the study of geomechanical problems, including the governing equations, the numerical method for their solution, the parallelization strategy, appropriate flow charts, and validations of the code (in terms of both the underlying numerical methods and of the implementation of the MPI-based parallelization) against solutions of standard geomechanical problems obtained from widely-used commercial simulators.

2.1. Governing Equations

The geomechanics problem is treated as a quasi-static problem, assuming that the fluid and the rock are in equilibrium all the time. The associated equation of conservation of momentum (Hughes 1987) is

$$\nabla \cdot \boldsymbol{\sigma} + \rho_b \mathbf{g} = \mathbf{0}, \tag{2.1}$$

where $\boldsymbol{\sigma}$ is the total stress tensor [Pa] and ρ_b is the bulk density [kg·m^{-3}].

The bulk density is calculated by

$$\rho_b = (1-\phi)\rho_R + \phi\rho_f, \tag{2.2}$$

where ϕ is the porosity, ρ_R is the rock density [kg·m^{-3}], and ρ_f is the fluid density [kg·m^{-3}]. For a multiphase flow system, the fluid density is the saturation weighted fluid density that is

$$\rho_f = \sum_{\beta} S_\beta \rho_\beta, \tag{2.3}$$

where S_β and ρ_β are the saturation and density of phase β [kg·m^{-3}], respectively,.

Based on the infinitesimal deformation assumption, the strain tensor is calculated as

$$\boldsymbol{\varepsilon} = \frac{1}{2}\left(\nabla \mathbf{u} + \nabla^{\mathrm{T}} \mathbf{u}\right), \tag{2.4}$$

where $\mathbf{u}$ is the displacement vector [m].

2.2. Constitutive Relationships

By convention, tensile stress is always taken to be positive in the following equations. Then, the constitutive relationship describing the stresses associated with the rock skeleton can be described as

$$\boldsymbol{\sigma} = \boldsymbol{\sigma}' - \alpha \mathbf{I} P_t = \mathbf{C} : \boldsymbol{\varepsilon} - \alpha \mathbf{I} P_t, \tag{2.5}$$

where $\boldsymbol{\sigma}'$ is the effective stress tensor [Pa], α is the Biot's coefficient (Biot 1941), which is defined as

$$\alpha = 1 - \frac{K_{dr}}{K_s}, \tag{2.6}$$

where K_{dr} is the drained bulk modulus [Pa] and K_s is the skeletal grain modulus [Pa], $\mathbf{I}$ is the identity matrix, $\mathbf{C}$ is the elasticity tensor [Pa], and P_t is the average mobile fluid pressure [Pa], which is computed as

$$P_t = \frac{\sum_\beta S_\beta P_\beta}{\sum_\beta S_\beta}, \tag{2.7}$$

where the phase β denotes only the mobile fluid phase.

In two-dimensional (2D) Cartesian problems involving plane strain conditions (based on the assumption of zero strain in the direction normal to the plane), the elasticity tensor is defined as

$$\mathbf{C} = \begin{bmatrix} K_{dr} + \frac{4}{3}G & K_{dr} - \frac{2}{3}G & 0 \\ K_{dr} - \frac{2}{3}G & K_{dr} + \frac{4}{3}G & 0 \\ 0 & 0 & G \end{bmatrix}, \tag{2.8}$$

where G is the shear modulus [Pa]. K_{dr} and G are described by the equations

$$K_{dr} = \frac{E}{3(1-2\nu)} \tag{2.9}$$

and

$$G = \frac{E}{2(1+\nu)}, \tag{2.10}$$

in which E is the Young's modulus and ν is the Poisson's ratio.

There is a particular 2D case that involves axisymmetric elements in cylindrical coordinate (r, z) systems. In this case, only displacements in these two directions are considered (*i.e.*, radial displacement and axial displacement). Since 2D cylindrical coordinate systems are commonly used in reservoir simulations involving single-well problems, it is vital to include such axisymmetric elements in geomechanical simulation for the coupled problem. When using axisymmetric elements, the elasticity tensor is

$$\mathbf{C} = \begin{bmatrix} K_{dr} + \frac{4}{3}G & K_{dr} - \frac{2}{3}G & K_{dr} - \frac{2}{3}G & 0 \\ K_{dr} - \frac{2}{3}G & K_{dr} + \frac{4}{3}G & K_{dr} - \frac{2}{3}G & 0 \\ K_{dr} - \frac{2}{3}G & K_{dr} - \frac{2}{3}G & K_{dr} + \frac{4}{3}G & 0 \\ 0 & 0 & 0 & G \end{bmatrix}, \tag{2.11}$$

For three-dimensional (3D) Cartesian problems, the elasticity tensor is defined as

$$\mathbf{C} = \begin{bmatrix} K_{dr} + \frac{4}{3}G & K_{dr} - \frac{2}{3}G & K_{dr} - \frac{2}{3}G & 0 & 0 & 0 \\ K_{dr} - \frac{2}{3}G & K_{dr} + \frac{4}{3}G & K_{dr} - \frac{2}{3}G & 0 & 0 & 0 \\ K_{dr} - \frac{2}{3}G & K_{dr} - \frac{2}{3}G & K_{dr} + \frac{4}{3}G & 0 & 0 & 0 \\ 0 & 0 & 0 & G & 0 & 0 \\ 0 & 0 & 0 & 0 & G & 0 \\ 0 & 0 & 0 & 0 & 0 & G \end{bmatrix}. \tag{2.12}$$

If a geomechanical simulation is coupled with a hydrate simulation, the hydrate phase can affect the mechanical properties because hydrates very often occur in unconsolidated media, providing the bulk of the mechanical strength of the latter. This is especially true when the hydrate saturation S_H is large, and there is an interdependence of flow and geomechanical properties and conditions as dissociation advances and S_H decreases. The dependence of the geomechanical properties on S_H has yet to be studied in depth, and is a subject of active research. Currently, the standard approach involves the following linear interpolation equations:

$$K_{dr} = K_{dr0}\left(1 - S_H\right) + K_{dr1}S_H \tag{2.13}$$

and

$$G = G_0\left(1 - S_H\right) + G_1 S_H\,, \tag{2.14}$$

where K_{dr0} and K_{dr1} are the drained moduli [Pa] when S_H = 0 and 1, respectively, and G_0 and G_1 are the drained moduli [Pa] when S_H = 0 and 1, respectively (Rutqvist and Moridis 2009).

2.3. Numerical Method

The geomechanics simulator RGMS uses the finite element method (FEM) for space discretization with standard linear elements. The weak form of Eq. (2.1) is derived based on virtual work theory as

$$\int_\Omega \delta\boldsymbol{\varepsilon} : \boldsymbol{\sigma}\mathrm{d}\Omega = \int_\Omega \delta\mathbf{u}\cdot\rho_b\mathbf{g}\mathrm{d}\Omega + \int_\Gamma \delta\mathbf{u}\cdot\mathbf{t}\mathrm{d}\Gamma\,, \tag{2.15}$$

where Ω is the matrix domain, Γ is the traction boundary, and **t** is the prescribed traction on Γ [Pa].

The FEM approximates the displacements **u** in the nodal displacement continuum of the discretized domain by the following equation

$$\mathbf{u} \approx \sum_a \mathbf{N}_a\tilde{\mathbf{u}}_a\,, \tag{2.16}$$

where $\mathbf{N}_a$ is the shape function that interpolates the solution based on the displacements $\tilde{\mathbf{u}}_a$ of node *a*. Obviously, $\mathbf{N}_a$ is defined as

$$\mathbf{N}_a = N_a\mathbf{I}\,, \tag{2.17}$$

in which the value of N_a is always 1 at node *a* but 0 at the other nodes.

After estimating the displacements, the stress and strain tensors can be computed. Because the stress tensor and the strain tensor are symmetric, they can be written in Voigt notation as simplified vectors by merging the symmetric off-diagonal parts.

For a 2D system, the displacements at node *a* are

$$\tilde{\mathbf{u}}_a = \begin{Bmatrix} \tilde{u}_a \\ \tilde{v}_a \end{Bmatrix}. \tag{2.18}$$

Considering a plane strain problem ($\varepsilon_y = 0$), the independent components of the strain $\boldsymbol{\varepsilon}$ (Zienkiewicz et al. 2005) are

$$\boldsymbol{\varepsilon} = \begin{Bmatrix} \varepsilon_x \\ \varepsilon_z \\ \gamma_{xz} \end{Bmatrix} = \begin{Bmatrix} \varepsilon_x \\ \varepsilon_z \\ 2\varepsilon_{xz} \end{Bmatrix} = \sum_a \begin{bmatrix} \frac{\partial N_a}{\partial x} & 0 \\ 0 & \frac{\partial N_a}{\partial z} \\ \frac{\partial N_a}{\partial z} & \frac{\partial N_a}{\partial x} \end{bmatrix} \begin{Bmatrix} \tilde{u}_a \\ \tilde{v}_a \end{Bmatrix} = \sum_a \mathbf{B}_a \tilde{\mathbf{u}}_a \,, \tag{2.19}$$

and the independent components of the stress $\boldsymbol{\sigma}$ are

$$\boldsymbol{\sigma} = \begin{Bmatrix} \sigma_x \\ \sigma_y \\ \sigma_z \\ \tau_{xz} \end{Bmatrix} = \begin{bmatrix} K_{dr} + \frac{4}{3}G & K_{dr} - \frac{2}{3}G & 0 \\ K_{dr} - \frac{2}{3}G & K_{dr} - \frac{2}{3}G & 0 \\ K_{dr} - \frac{2}{3}G & K_{dr} + \frac{4}{3}G & 0 \\ 0 & 0 & G \end{bmatrix} \begin{Bmatrix} \varepsilon_x \\ \varepsilon_z \\ \gamma_{xz} \end{Bmatrix}. \tag{2.20}$$

Note that σ_y is nonzero only if ν is nonzero because of the following equation

$$K_{dr} - \frac{2}{3}G = \frac{E\nu}{(1+\nu)(1-2\nu)}. \tag{2.21}$$

For axisymmetric elements in cylindrical coordinate systems, the independent components of strain $\boldsymbol{\varepsilon}$ are

$$\boldsymbol{\varepsilon} = \begin{Bmatrix} \varepsilon_r \\ \varepsilon_\theta \\ \varepsilon_z \\ \gamma_{rz} \end{Bmatrix} = \begin{Bmatrix} \varepsilon_r \\ \varepsilon_\theta \\ \varepsilon_z \\ 2\varepsilon_{rz} \end{Bmatrix} = \sum_a \begin{bmatrix} \frac{\partial N_a}{\partial r} & 0 \\ \frac{N_a}{r} & 0 \\ 0 & \frac{\partial N_a}{\partial z} \\ \frac{\partial N_a}{\partial z} & \frac{\partial N_a}{\partial r} \end{bmatrix} \begin{Bmatrix} \tilde{u}_a \\ \tilde{v}_a \end{Bmatrix} = \sum_a \mathbf{B}_a \tilde{\mathbf{u}}_a \,, \tag{2.22}$$

in which the radius is computed by

$$r = \sum_b N_b^{'} r_b \,, \tag{2.23}$$

and r_b are the locations of the nodal points that define the $N_b^{'}$ functions. The independent components of strain $\boldsymbol{\sigma}$ are

$$\boldsymbol{\sigma} = \begin{Bmatrix} \sigma_r \\ \sigma_\theta \\ \sigma_z \\ \tau_{rz} \end{Bmatrix} = \begin{bmatrix} K_{dr} + \frac{4}{3}G & K_{dr} - \frac{2}{3}G & K_{dr} - \frac{2}{3}G & 0 \\ K_{dr} - \frac{2}{3}G & K_{dr} + \frac{4}{3}G & K_{dr} - \frac{2}{3}G & 0 \\ K_{dr} - \frac{2}{3}G & K_{dr} - \frac{2}{3}G & K_{dr} + \frac{4}{3}G & 0 \\ 0 & 0 & 0 & G \end{bmatrix} \begin{Bmatrix} \varepsilon_r \\ \varepsilon_\theta \\ \varepsilon_z \\ \gamma_{rz} \end{Bmatrix} \tag{2.24}$$

For a 3D cartesian system, the displacements at node *a* are

$$\tilde{\mathbf{u}}_a = \begin{Bmatrix} \tilde{u}_a \\ \tilde{v}_a \\ \tilde{w}_a \end{Bmatrix}, \tag{2.25}$$

the independent components of strain $\boldsymbol{\varepsilon}$ are

$$\boldsymbol{\varepsilon} = \begin{Bmatrix} \varepsilon_x \\ \varepsilon_y \\ \varepsilon_z \\ \gamma_{yz} \\ \gamma_{xz} \\ \gamma_{xy} \end{Bmatrix} = \begin{Bmatrix} \varepsilon_x \\ \varepsilon_y \\ \varepsilon_z \\ 2\varepsilon_{yz} \\ 2\varepsilon_{xz} \\ 2\varepsilon_{xy} \end{Bmatrix} = \sum_a \begin{bmatrix} \frac{\partial N_a}{\partial x} & 0 & 0 \\ 0 & \frac{\partial N_a}{\partial y} & 0 \\ 0 & 0 & \frac{\partial N_a}{\partial z} \\ 0 & \frac{\partial N_a}{\partial z} & \frac{\partial N_a}{\partial y} \\ \frac{\partial N_a}{\partial z} & 0 & \frac{\partial N_a}{\partial x} \\ \frac{\partial N_a}{\partial y} & \frac{\partial N_a}{\partial x} & 0 \end{bmatrix} \begin{Bmatrix} \tilde{u}_a \\ \tilde{v}_a \\ \tilde{w}_a \end{Bmatrix} = \sum_a \mathbf{B}_a \tilde{\mathbf{u}}_a \,, \tag{2.26}$$

and the independent components of stress $\boldsymbol{\sigma}$ are

$$\boldsymbol{\sigma} = \begin{Bmatrix} \sigma_x \\ \sigma_y \\ \sigma_z \\ \tau_{yz} \\ \tau_{xz} \\ \tau_{xy} \end{Bmatrix} = \begin{bmatrix} K_{dr}+\frac{4}{3}G & K_{dr}-\frac{2}{3}G & K_{dr}-\frac{2}{3}G & 0 & 0 & 0 \\ K_{dr}-\frac{2}{3}G & K_{dr}+\frac{4}{3}G & K_{dr}-\frac{2}{3}G & 0 & 0 & 0 \\ K_{dr}-\frac{2}{3}G & K_{dr}-\frac{2}{3}G & K_{dr}+\frac{4}{3}G & 0 & 0 & 0 \\ 0 & 0 & 0 & G & 0 & 0 \\ 0 & 0 & 0 & 0 & G & 0 \\ 0 & 0 & 0 & 0 & 0 & G \end{bmatrix} \begin{Bmatrix} \varepsilon_x \\ \varepsilon_y \\ \varepsilon_z \\ \gamma_{yz} \\ \gamma_{xz} \\ \gamma_{xy} \end{Bmatrix} \tag{2.27}$$

Accounting for Eq. (2.5), the general matrix-vector form of Eq. (2.15) can be written as

$$\mathbf{K}\tilde{\mathbf{u}} = \mathbf{f} + \mathbf{Q}, \tag{2.28}$$

where the stiffness matrix **K**, coupling matrix **Q**, and external force vector **f** are

$$\mathbf{K} = \int_\Omega \mathbf{B}^{\mathrm{T}} \mathbf{D} \mathbf{B} \mathrm{d}\Omega, \tag{2.29}$$

$$\mathbf{Q} = \int_\Omega \alpha P_t \mathbf{B}^{\mathrm{T}} \mathbf{m} \mathrm{d}\Omega, \tag{2.30}$$

and

$$\mathbf{f} = \int_{\Gamma} \mathbf{N}^{\mathrm{T}} \mathbf{t} \mathrm{d}\Gamma + \int_{\Gamma} \mathbf{N}^{\mathrm{T}} \rho_b \mathbf{g} \mathrm{d}\Omega . \tag{2.31}$$

D in Eq. (2.29) is the elasticity matrix of moduli and **m** in Eq. (2.30) is a vector whose components are 1 in the normal direction to the element's surface but 0 otherwise.

Combing the two terms on the right-hand-side of Eq. (2.28) gives

$$\mathbf{K}\tilde{\mathbf{u}} = \mathbf{F} , \tag{2.32}$$

where **F** is the force vector.

To Assemble the stiffness matrix **K**, the stiffness matrix $\mathbf{K}^e$ for an element *e* consisting of *m* nodes is constructed first in the form

$$\mathbf{K}^e = \begin{bmatrix} \mathbf{K}_{11}^e & \mathbf{K}_{12}^e & \cdots & \mathbf{K}_{1m}^e \\ \mathbf{K}_{21}^e & \mathbf{K}_{22}^e & \cdots & \mathbf{K}_{2m}^e \\ \vdots & \vdots & \ddots & \vdots \\ \mathbf{K}_{m1}^e & \mathbf{K}_{m2}^e & \cdots & \mathbf{K}_{mm}^e \end{bmatrix} \tag{2.33}$$

in which $\mathbf{K}_{ab}^e$ accounts for the contributions of nodes *a* and *b* within element *e* and is a square submatrix with the size of $l \times l$, where *l* is the number of the degrees of freedom at each node.

Similarly, the force vector $\mathbf{F}^e$ is

$$\mathbf{F}^e = \begin{Bmatrix} \mathbf{F}_1^e \\ \mathbf{F}_2^e \\ \vdots \\ \mathbf{F}_m^e \end{Bmatrix} \tag{2.34}$$

in which $\mathbf{F}_a^e$ denotes the force at node *a* within element *e* and is a vector with the size of *l*. The displacement vector $\tilde{\mathbf{u}}^e$ is

$$\tilde{\mathbf{u}}^e = \begin{Bmatrix} \tilde{\mathbf{u}}_1^e \\ \tilde{\mathbf{u}}_2^e \\ \vdots \\ \tilde{\mathbf{u}}_m^e \end{Bmatrix} \tag{2.35}$$

in which $\tilde{\mathbf{u}}_a^e$ denotes the displacement at node *a* within element *e* and is a vector of size *l*. Because the nodal displacements are common, for simplicity the superscript *e* of $\mathbf{u}^e$ can be omitted.

Counting the components of all the elements contributing to node *a* yields

$$\left(\sum_e \mathbf{K}_{a1}^e\right)\tilde{\mathbf{u}}_1 + \left(\sum_e \mathbf{K}_{a2}^e\right)\tilde{\mathbf{u}}_2 + \cdots + \left(\sum_e \mathbf{K}_{am}^e\right)\tilde{\mathbf{u}}_m = \sum_e \mathbf{F}_a^e \,. \tag{2.36}$$

Repeating this process over all nodes assembles (a) the **K** matrix, in which $\mathbf{K}_{ab}$ is a square submatrix with the size of $l \times l$ associated with nodes *a* and *b*, and (b) the **F** vector, in which $\mathbf{F}_a$ is a vector with the size of *l* related to node *a*. The mathematical expressions for this assembly are

$$\mathbf{K}_{ab} = \sum_{e=1}^{m} \mathbf{K}_{ab}^e \tag{2.37}$$

and

$$\mathbf{F}_a = \sum_{e=1}^{m} \mathbf{F}_a^e \,. \tag{2.38}$$

In general, the stiffness matrix is

$$\mathbf{K} = \begin{bmatrix} K_{11} & K_{12} & \cdots & K_{1(n-1)} & K_{1n} \\ K_{21} & K_{22} & \cdots & K_{2(n-1)} & K_{2n} \\ \vdots & \vdots & \ddots & \vdots & \vdots \\ K_{(n-1)1} & K_{(n-1)2} & \cdots & K_{(n-1)(n-1)} & K_{(n-1)n} \\ K_{n1} & K_{n2} & \cdots & K_{n(n-1)} & K_{nn} \end{bmatrix}, \tag{2.39}$$

where n is the number of unknowns that reflects the total number of degrees of freedom of all nodes in the system, and the force vector is

$$\mathbf{F} = \begin{Bmatrix} F_1 \\ F_2 \\ \vdots \\ F_{n-1} \\ F_n \end{Bmatrix}. \tag{2.40}$$

The displacements are then obtained from

$$\tilde{\mathbf{u}} = \mathbf{K}^{-1}\mathbf{F}. \tag{2.41}$$

2.4. Parallelization

Solving the equations of the geomechanics problem is very time-consuming and needs a sufficiently large computer memory for large-scale studies. The problem is alleviated through parallelization, which involves the use of multiple processors and the introduction of a domain decomposition method that subdivides the entire domain into a number of subdomains. This process distributes (a) the computational workload of setting up and solving the matrix equations and (b) the corresponding memory requirement for data storage among the multiple processors of a multi-processor environment. The equations allocated to each processor are assembled and solved using a parallel solver

package based on the parallel operations provided by the Message Passing Interface (MPI) communication protocol that supports point-to-point and collective communications between processors, and which enables domain decomposition.

2.4.1. Domain Decomposition Method

The domain decomposition method involves partitioning either the elements or the nodes in a domain into many different groups, so that the associated workload can be subdivided and assigned to multiple processors. First, it needs to be determined whether the elements or nodes should be partitioned. Although the FEM divides the continuum into finite elements, the equations are assembled based on nodes (element vertices) to solve the nodal displacements. It is straightforward to partition the nodes in geomechanical simulations, and successful partitioning leads to computational efficiency because of the issue of workload balance that is discussed later in this section.

There are two schemes of domain decomposition: non-overlapped and overlapped. In the non-overlapped method, the various subdomains are in contact with each other only at interface boundaries, while in the overlapped method, the subdomains overlap (*i.e.*, some nodes belong to more than one subdomain and are thus handled by more than one processor). This study uses the overlapped method, in which the subdomains overlap by a single line/layer of nodes, called the “ghost” line/layer. Inclusion of the ghost lines/layers in subdomains of overlapped domain decomposition schemes is necessary to accurately account for the influence of displacements at neighboring nodes (and computed by

neighboring processors) along the perimeter/edges of the domain decomposition subdomain.

The degrees of freedom of the nodes on the ghost lines/layers are received from its neighboring processors utilizing MPI. In the MPI communication, each processor has a unique rank for identification purposes. For example, the rank can be used to identify the source processor and the destination processor when sending or receiving messages. Usually, the processor with the rank of 0 is the master processor.

Figure 2.1 illustrates a 2D domain decomposed into 9 subdomains, each one handled by a different processor. Each box in **Figure 2.1** represents a node and the associated number denotes the processor to which this node is assigned for the assembly of geomechanics equations. The subdomain enclosed by the red polygon defines the subdomain for the 5th processor and is representative of the non-overlapped method. **Figure 2.1** also includes two examples/stencils of overlapped domain decomposition methods: as well the elements assigned to the same processor in two types of overlapped method stencils: a star-type stencil and a box-type stencil, in which the nodes that the process are enclosed by the corresponding red polygons. As it is indicated by Eq. (2.36), the linear equation for a node involves the contribution from all its surrounding nodes in the FEM. Thus, **Figure 2.1** shows that there are 8 and 12 ghost nodes in addition to the 4 nodes in the subdomain assigned to the 5th processor in the star- and boxed-type stencils of the overlapped method, respectively.

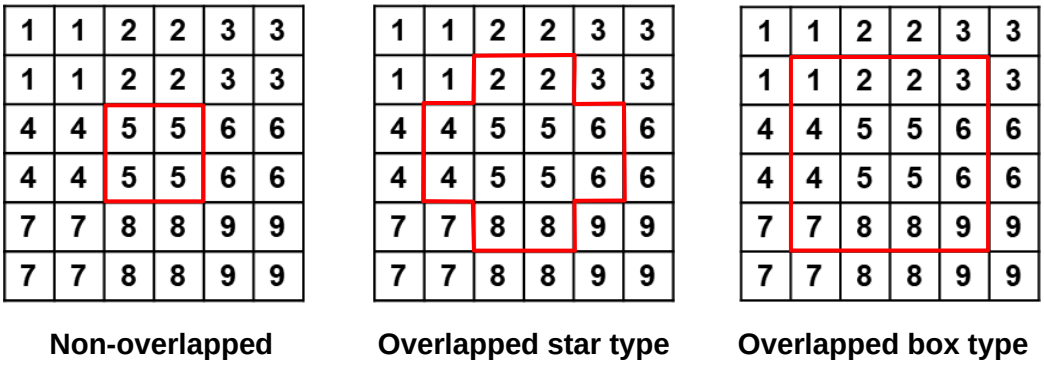

Figure 2.1 The subdomain for the fifth processor using the non-overlapped method, overlapped method in the star-type stencil, and overlapped method in the box-type stencil using 9 processors.

At particular points in the parallel simulation process, it may be necessary to ensure that all the processors complete their current tasks before proceeding further. If a processor has a significantly larger computational load, all other processors have to wait for it even after the completion of their computations. Thus, the performance of a parallel system is controlled and determined by the slowest processor. This makes it imperative that the workload be distributed among the processors as evenly as possible because the imbalance in the assignment of the workload can cause the parallel performance scalability to deteriorate. To minimize (and possibly alleviate) such imbalances, METIS (Karypis and Kumar 1999), a program for partitioning graphs and finite element meshes, is used to decompose the entire computational domain into non-overlapped subdomains (this is the only option for METIS), from which the overlapped subdomains can be derived. METIS can partition graphs or meshes using either the multilevel recursive bisection or the multilevel *k*-way partitioning paradigms, with the latter one providing more flexibility and

capabilities. In this work, the multilevel *k*-way partitioning is selected, and the selected objective option aims to minimize either the number of edge-cuts or the total communication volume.

METIS uses the data on the element-node array of the mesh (*i.e.*, elements and their vertices) as the input to create the connectivity list of the nodes for the partition. In RGMS, the master processor reads the mesh first, processes the data that yield the element-node array, and finally partitions the nodes using METIS.

The application of METIS does not lead to the inclusion of ghost elements, so the overlapped elements need to be added manually to the relevant subdomains. For each processor, the nodes for the geomechanical simulation are then reordered locally for the equation assembly. The nodes are classified into three sets: internal, border, and external. Internal nodes do not require any information outside of their processor in order to assemble the system of the associated equations, and thus do not create a need for processor-to-processor communication. Conversely, border and external nodes necessitate information from their neighboring processors for the assembly of their respective geomechanical equations. For border nodes, the processor sets up and solves the equations using information from both internal and external nodes. The external nodes are only reserved to store the information received from neighboring processors.

The system of equations is assembled locally on each processor, necessitating the local renumbering of all the node numbers. The internal nodes are numbered first, followed by the border nodes, and finally by the external nodes. An example is shown in **Figure 2.2**, in which each box can represent a node for the geomechanics simulation. The

number in the box is the node number before domain decomposition. **Table 2.1** lists the local numbers after renumbering using the box-type stencil of the overlapped method.

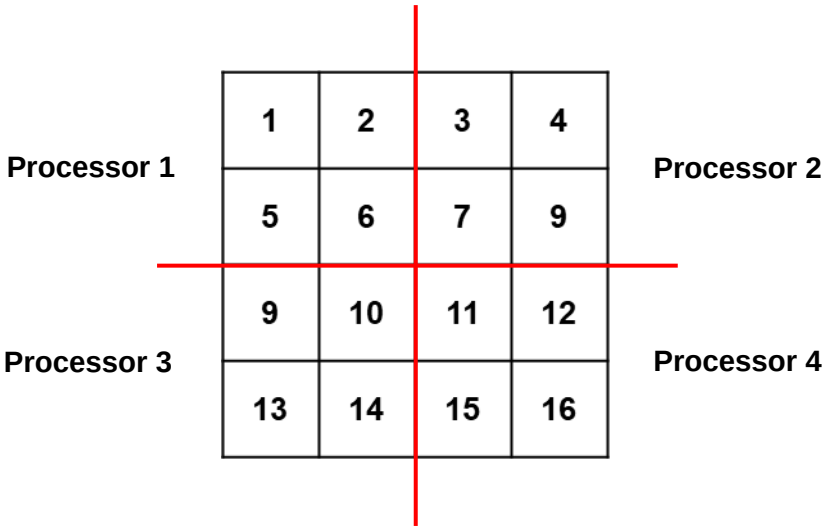

Figure 2.2 A domain partitioning of 16 elements or nodes using 4 processors.

This approach renumbers not only the node numbers, but also the degrees of freedom (more specifically, the displacements). The number of displacements at each node is equal to the number of dimensions in multi-dimensional geomechanics simulation, and their local numbers after renumbering are designated according to the node numbers. This numbering sequence reduces the processing time spent on sending and receiving information, and also makes it easier to assemble the global equations.

Table 2.1 Renumbering after the domain partitioning using the overlapped method in the box-type stencil for a domain shown in Figure 2.2.

		Internal	Border	External
Processor 1	Original number	1	2, 5, 6	3, 7, 9, 10, 11
	Local number	1	2, 3, 4	5, 6, 7, 8, 9
	Global number	1	2, 3, 4	6, 7, 10, 11, 14
Processor 2	Original number	4	3, 7, 9	2, 6, 10, 11, 12
	Local number	1	2, 3, 4	5, 6, 7, 8, 9
	Global number	5	6, 7, 8	2, 4, 11, 14, 15
Processor 3	Original number	13	9, 10, 14	5, 6, 7, 11, 15
	Local number	1	2, 3, 4	5, 6, 7, 8, 9
	Global number	9	10, 11, 12	3, 4, 7, 14, 16
Processor 4	Original number	16	11, 12, 15	6, 7, 9, 10, 14
	Local number	1	2, 3, 4	5, 6, 7, 8, 9
	Global number	13	14, 15, 16	4, 7, 8, 11, 12

After the processes and activities discussed above, the local stiffness matrix and force vector are constructed on each processor. Before moving to parallel iterative solvers, the local indices of these matrices and vectors need to be mapped to the global indices for the purpose of assembling the global matrices and vectors. The original numbers cannot be adopted because parallel iterative solvers require that the global matrix and vector be integrated on each processor after mapping. As a result, the global numbers are specified according to the processor rank. The global numbers for the external nodes are received from the neighboring processors, which have already established global numbers for internal and border nodes. The global numbers for the example of domain partitioning in

Figure 2.2 are listed in **Table 2.1**. Note that these global numbers reflect only node numbers, so the associated degrees of freedom need to be updated accordingly. After the local and global numbering is completed, the local matrices and vectors with the appropriate global indices are assembled and are ready to solve.

2.4.2. Parallel Solver

The matrix equations are solved using parallel iterative solvers executing on multiple processors. Each processor is assigned a part of the global matrix equation, as the very large memory requirements would render impractical (if not impossible) the storage of the global and local matrices and vectors on all processors. The iterative solvers converge toward the correct solution by computing a large number of dot products and matrix-vector products. Eq. (2.42) demonstrates the computational process of a dot product across multiple processors in a parallel environment.

$$\begin{Bmatrix} a_1 \\ a_2 \\ \vdots \\ a_n \end{Bmatrix} \cdot \begin{Bmatrix} b_1 \\ b_2 \\ \vdots \\ b_n \end{Bmatrix} = \sum_{i=1}^{n} a_i b_i \,, \tag{2.42}$$

in which the subscript number denotes the processor number and n is the total number of processors. In this case, a_1 is the partial vector owned by processor 1, a_2 is the partial vector owned by processor 2, and so forth. This arrangement/assignment also applies to vector **b** in Eq. (2.42), and to matrix **M** and vector **v** in Eq. (2.43). Thus, each processor computes the dot product of locally partial vectors, and then the partial dot products are

summed to provide the final result. Eq. (2.43) shows the process of matrix-vector multiplication across multiple processors.

$$\begin{bmatrix} \mathbf{M}_1 \\ \mathbf{M}_2 \\ \vdots \\ \mathbf{M}_n \end{bmatrix} \times \mathbf{v} = \begin{bmatrix} \mathbf{M}_1 \times \mathbf{v} \\ \mathbf{M}_2 \times \mathbf{v} \\ \vdots \\ \mathbf{M}_2 \times \mathbf{v} \end{bmatrix}, \tag{2.43}$$

where the vector **v** is

$$\mathbf{v} = \begin{Bmatrix} v_1 \\ v_2 \\ \vdots \\ v_n \end{Bmatrix}. \tag{2.44}$$

The result of a matrix-vector multiplication is a vector; a locally partial vector is stored on each processor, and the entire vector can be accessed between processors. Parallel iterative solvers only exchange partial sums and partial vectors between processors instead of storing all the data/information required for the computation of the solution. These communications in the multiprocessing environment are also based on the MPI protocol.

For optimum performance, the PETSc library (Balay et al. 2014) of parallel solvers is implemented in RGMS simulations. This package provides numerous MPI-based preconditioning and parallel solver options. Based on several scoping calculations, the generalized minimal residual method (GMRES) with a geometric algebraic multigrid (GAMG) preconditioner was chosen to provide the best performance in the geomechanics code and was used in all RGMS simulations.

2.5. Flow Chart

The flow chart of the parallel RGMS code, involving the domain decomposition methods and parallel iterative solver discussed earlier, is shown in **Figure 2.3**.

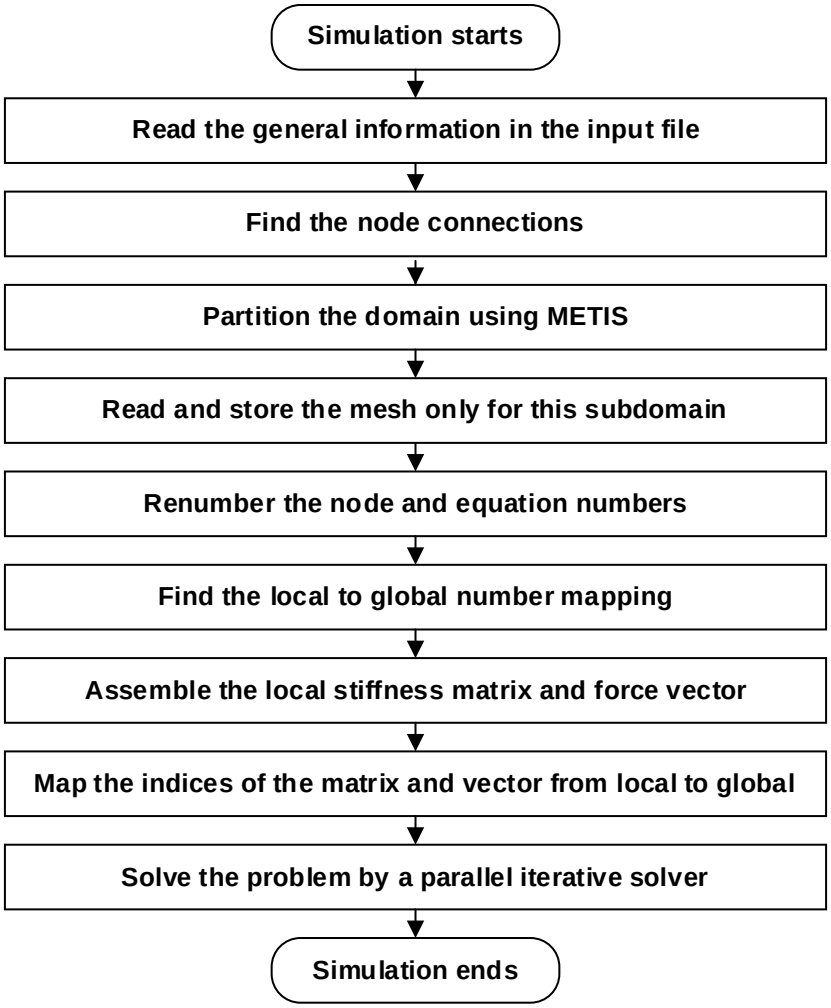

Figure 2.3 The flow chart of RGMS.

2.6. Validation

RGMS was validated by comparing its numerical results (the total displacement and the maximum principal effective stress) to those obtained from the Ansys Mechanical simulator (a commercial FEM-based software package) in the solution of 2D Cartesian, 2D cylindrical, and 3D Cartesian coordinate problems. The total displacement is the positive magnitude of the components of the displacement vector on the axes of the coordinate system of the investigated problem. The comparison of the maximum principal effective stresses was included to validate the stress computations for the prediction of possible material failure. Because a Cauchy stress tensor consists of normal and shear stresses, it is easier to compare the principal stresses (the eigenvalues of a Cauchy stress tensor that only has normal stresses) against material failure criteria. As the principal stresses are computed through complex processes, the analytical solution is limited, resulting in only the numerical result from the ANSYS Mechanical simulator used for validation. The RGMS results were obtained using (a) a single processor and (b) four processors in order to confirm the parallelization process by the coincidence of the two solutions. The parameters used in all the validation cases are summarized in **Table 2.2**.

Table 2.2 Parameters of the validation problems for RGMS.

Young's modulus	2.0×10^8 Pa
Poisson's ratio	0.3
Biot's coefficient	1
Initial pressure	1.0×10^7 Pa

Table 2.2 Continued

Bulk density	2.6×10^3 kg/m^{-3}
Gravitational acceleration	9.81 m/s^{-2}
Traction 1 (T_1)	2.0×10^7 Pa
Traction 2 (T_2)	1.0×10^7 Pa

2.6.1. Two-Dimensional Problems

The side lengths (x, z) and (r, z) of the domains of the 2D validation problems were all equal to 200 m (as shown in **Figure 2.4**), and were discretized into 200 subdivisions of uniform size (4-noded rectangular elements) in both directions by MeshGenerator V1.0 developed in this study based on MeshMaker V1.5 (Moridis 2016). The left, right, and bottom boundaries were supported by the rollers (*i.e.*, ensuring that the normal displacements be 0), and traction was applied to the top boundary.

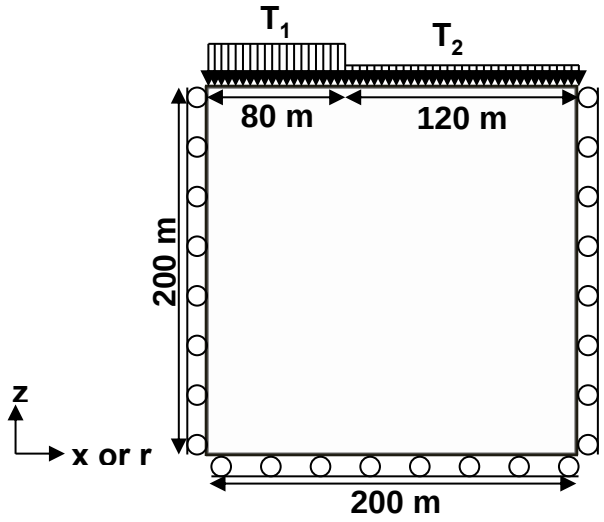

Figure 2.4 The geometry of the 2D Cartesian and cylindrical validation problems.

2.6.1.1. Cartesian Coordinate System

The total displacement at z = 0 m and the maximum principal effective stress at z = -20.5 m in this 2D Cartesian problem are shown in **Figures 2.5** and **2.6**, respectively. The numerical results from RGMS using 1 and 4 processors practically coincide with those from the Ansys Mechanical package, providing evidence of the validity of the equation assembly, the matrix solving process, and the implementation of parallelization in the RGMS simulator for 2D Cartesian problems.

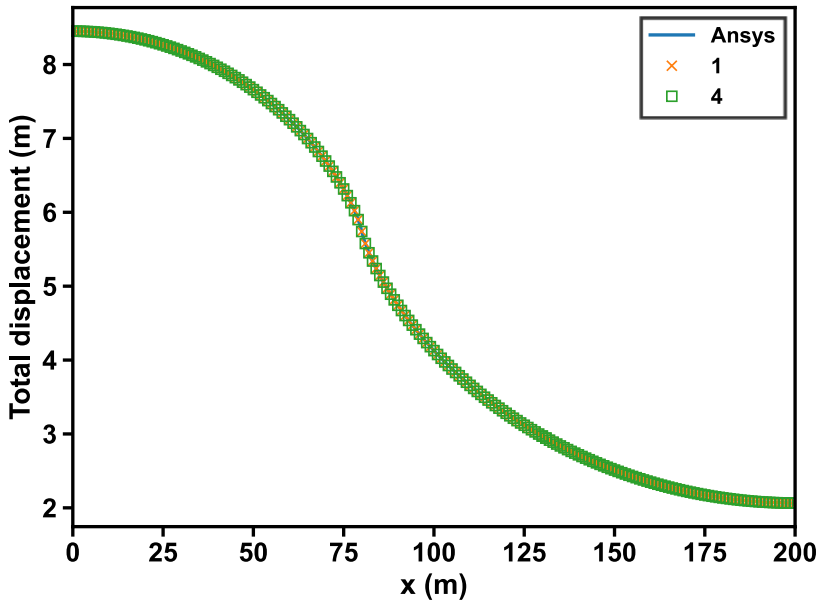

Figure 2.5 Total displacements at the top boundary obtained from the Ansys Mechanical and RGMS solutions (using 1 and 4 processors) of the 2D Cartesian problem of Figure 2.4.

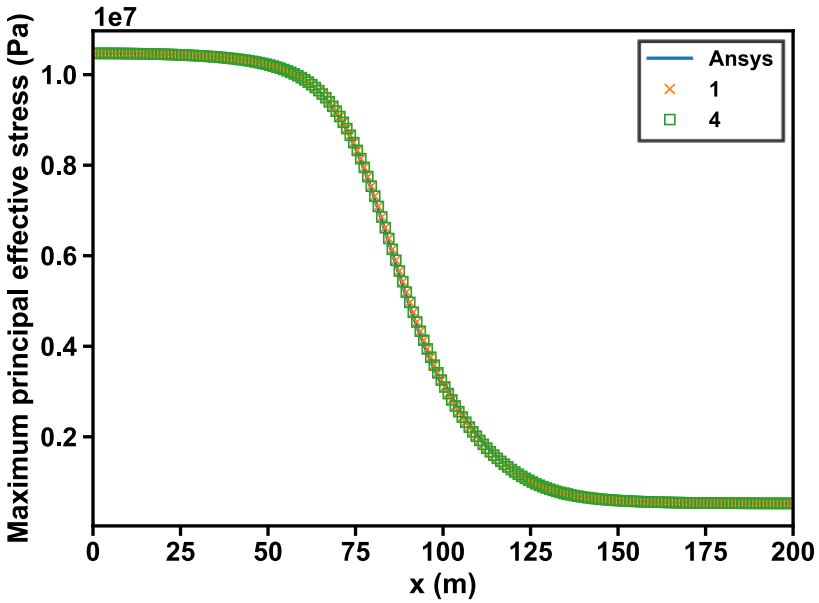

Figure 2.6 The maximum principal effective stress at *z* = -20.5 m obtained from the Ansys Mechanical and RGMS solutions (using 1 and 4 processors) of the 2D Cartesian problem of Figure 2.4.

2.6.1.2. Cylindrical Coordinate System

For the 2D cylindrical validation problem of **Figure 2.4**, **Figure 2.7** shows the total displacement at the top boundary, and **Figure 2.8** shows the maximum principal effective stress at *z* = -20.5 m. The RGMS solutions using different numbers of processors capture all the displacement and stress changes, and both the serial and the parallel simulation results are virtually identical with those obtained from the Ansys Mechanical simulator.

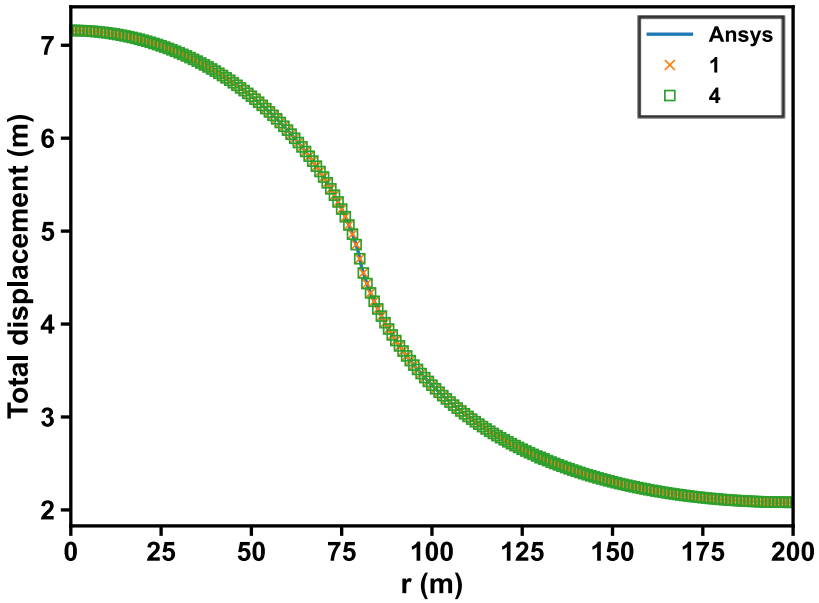

Figure 2.7 Total displacements at the top boundary obtained from the Ansys Mechanical and RGMS solutions (using 1 and 4 processors) of the 2D cylindrical problem of Figure 2.4.

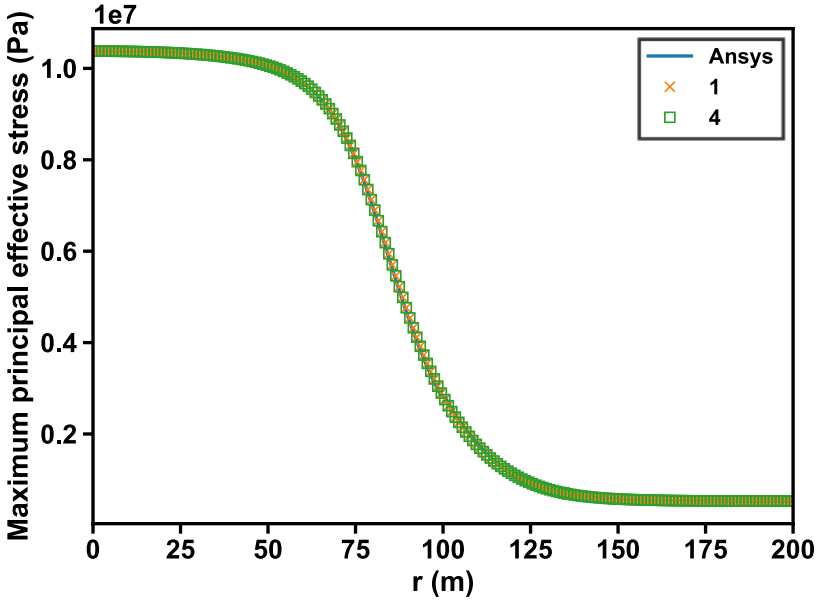

Figure 2.8 The maximum principal effective stress at *z* = -20.5 m obtained from the Ansys Mechanical and RGMS solutions (using 1 and 4 processors) of the 2D cylindrical problem of Figure 2.4.

2.6.2. Three-Dimensional Cartesian Coordinate Problem

The domain for this validation was a box with the dimensions indicated in **Figure 2.9**. The dimensions of the domain were subdivided into 30 equally-sized elements (8-noded hexahedron elements) in the *x*-, *y*-, and *z*-directions by MeshGenerator V1.0, resulting in a total of 27,000 uniform elements. The rollers supported all the system boundaries except the top one, where traction was applied.

The total displacements along the line defined by (y, z) = (0 m, 0 m) are plotted in **Figure 2.10**, which includes the Ansys Mechanical results and the RGMS solutions from the serial (single-processor) and parallel (4-processor) simulations. The three sets of results coincide, all showing a continuous decrease in displacements along the *x*-direction. The same near-perfect agreement of the three solutions of the maximum principal effective stress along x at (y, z) = (0.25 m, -2.25 m) in **Figure 2.11** provides further evidence of the validity and reliability of the physics and mathematics in RGMS, and of the implementation of its parallelization.

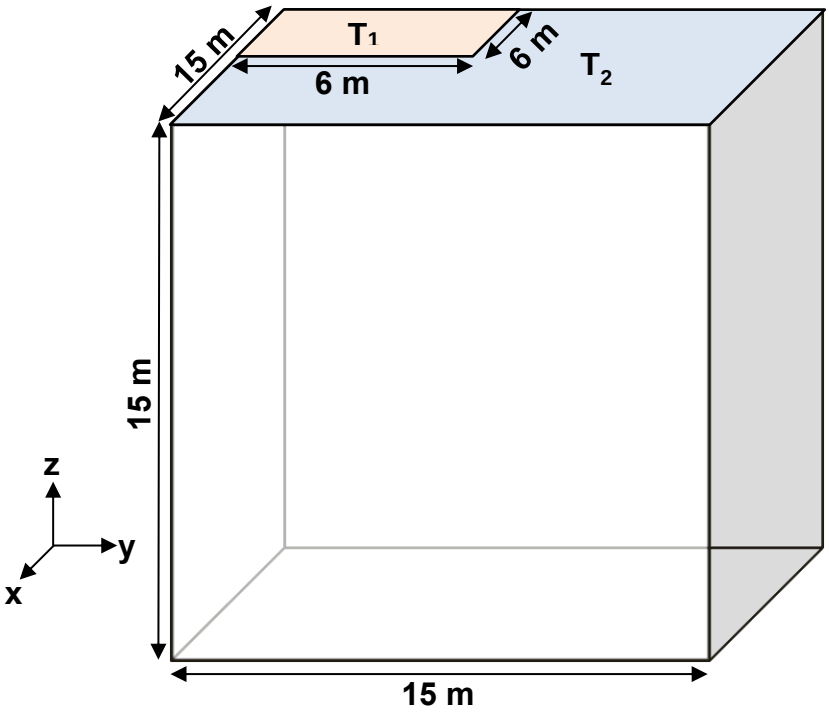

Figure 2.9. Geometry of the 3D Cartesian validation problem.

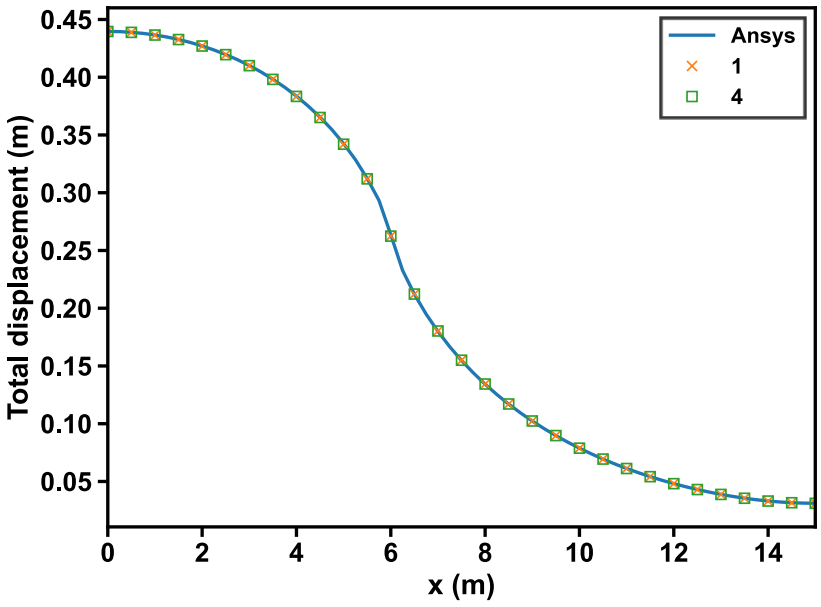

Figure 2.10 Total displacements along the *x*-coordinate at (*y*, *z*) = (0 m, 0 m) obtained from the Ansys Mechanical and the RGMS simulations (using 1 and 4 processors) of the 3D Cartesian problem of Figure 2.9.

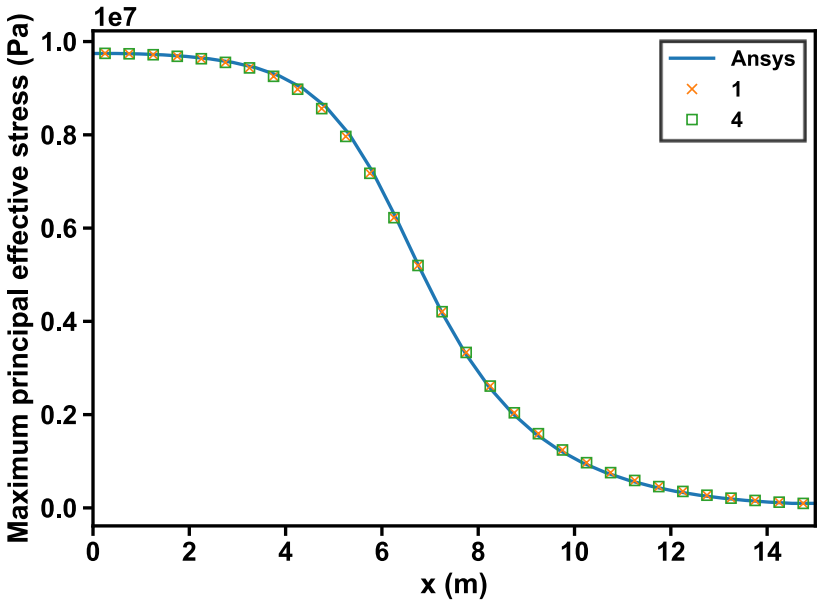

Figure 2.11 The maximum principal effective stress along the *x*-coordinate at (*y*, *z*) = (0.25 m, -2.25 m) obtained from the Ansys Mechanical and the RGMS simulations (using 1 and 4 processors) of the 3D Cartesian problem of Figure 2.9.

3. PARALLEL FLUID AND THERMAL SIMULATION

This chapter presents detailed information on the pT+H V1.5 simulator describing the system behavior (involving coupled flow, thermal, thermodynamic and chemical processes) in hydrate-bearing geologic media, including the governing equations, the porosity-permeability relationship, a simplified geomechanical model, the underlying numerical method, the MPI-based parallelization method, a flow chart, and validation of the implementation of parallelization.

3.1. Governing Equations for Fluid and Thermal Flow

Following Moridis and Pruess (2014), the mass and energy balance equation associated with the accumulation and flow/transport through a control volume in a porous medium is given by

$$\frac{d}{dt}\int_{V_n} M^\kappa \mathrm{d}V = \int_{\Gamma_n} \mathbf{F}^\kappa \cdot \mathbf{n}\mathrm{d}A + \int_{V_n} q^\kappa \mathrm{d}V\,, \tag{3.1}$$

where V_n is the volume of subdomain n with differential $\mathrm{d}V$ [m^3], M^κ is the mass accumulation of component κ [$kg \cdot m^{-3}$], Γ_n is the surface area of subdomain n with differential $\mathrm{d}A$ [m^2], $\mathbf{F}^\kappa$ is the flux vector of component κ [$kg \cdot m^{-2} \cdot s^{-1}$], $\mathbf{n}$ is the inward unit normal vector, q^κ is the source/sink term of component κ [$kg \cdot m^{-3} \cdot s^{-1}$], and t is the time [s].

3.1.1. Mass Accumulation Terms

The mass accumulation M^κ for each component κ in Eq. (3.1) are given by

$$M^\kappa = \sum_{\beta=A,G,I,H} \phi S_\beta \rho_\beta X_\beta^\kappa, \ \kappa = w,m,i\,, \tag{3.2}$$

where ϕ is the porosity, S_β is the saturation of phase β, ρ_β is the density of phase β [kg·m^{-3}], X_β^κ is the mass fraction of component κ in phase β, *A* is the aqueous phase, *G* is the gaseous phase, *I* is the solid ice phase, *H* is the solid hydrate phase, and *w*, *m* and *i* denote the H_2O, CH_4 and inhibitor mass components, respectively.

3.1.2. Heat Accumulation Terms

The heat accumulation term M^θ includes contributions from the rock matrix and from all the phases, and is given by the equation

$$M^\theta = (1-\phi)\rho_R C_R T + \sum_{\beta=A,G,I,H} \phi S_\beta \rho_\beta U_\beta + Q_{diss}\,, \tag{3.3}$$

where

$$Q_{diss} = \begin{cases} \Delta\left(\phi\rho_H S_H \Delta H^0\right) & \text{for equilibrium dissociation} \\ Q_H \Delta H^0 & \text{for kinetic dissociation} \end{cases}, \tag{3.4}$$

ρ_R is the rock density [kg·m^{-3}], C_R is the heat capacity of the dry rock [J·kg^{-1}·K^{-1}], *T* is the temperature [K], U_β is the specific internal energy of phase β [J·kg^{-1}], $\Delta()$ denotes the change of the quantity within the parentheses during a given timestep, and ΔH^0 is the specific enthalpy of hydrate dissociation/formation [J·kg^{-1}].

3.1.3. Mass Flux Terms

The mass flux terms of H_2O, CH_4, and inhibitor include contributions from the aqueous and gaseous phases and are given by

$$\mathbf{F}^{\kappa} = \sum_{\beta=A,G} \mathbf{F}_{\beta}^{\kappa}, \ \kappa = w, m, i \,. \tag{3.5}$$

The mass flux term $\mathbf{F}_A$ is described by Darcy's law as

$$\mathbf{F}_A = -k \frac{k_{rA}\rho_A}{\mu_A}\left(\nabla P_A - \rho_A \mathbf{g}\right), \tag{3.6}$$

where k is the rock intrinsic permeability [m^2], k_{rA} is the relative permeability of the aqueous phase, μ_A is the viscosity of the aqueous phase [Pa·s], P_A is the pressure of the aqueous phase [Pa], and $\mathbf{g}$ is the gravitational acceleration vector [$m \cdot s^{-2}$].

The pressure of the aqueous phase P_A is calculated by

$$P_A = P_G + P_{cGW} \tag{3.7}$$

$$P_G = P_G^m + P_G^w \,, \tag{3.8}$$

where P_G is the pressure of the gaseous phase [Pa], P_{cGW} is the gas-water capillary pressure [Pa], P_G^m and P_G^w are the CH_4 and H_2O vapor partial pressures in the gas phase [Pa], respectively.

3.1.4. Heat Flux Term

The heat flux term $\mathbf{F}^{\theta}$ is computed by

$$\mathbf{F}^{\theta} = -\overline{k_{\theta}} \nabla T + f_{\sigma} \sigma_0 \nabla T^4 + \sum_{\beta=A,G} h_{\beta} \mathbf{F}_{\beta} \,, \tag{3.9}$$

where $\overline{k_\theta}$ is the composite thermal conductivity of the medium/fluid composite system [W·m^{-1}·K^{-1}], h_β is the specific enthalpy of phase β [J·kg^{-1}], f_σ is the radiance emittance factor, σ_0 is the Stefan-Boltzmann constant [5.6687×10^{-8} J·m^{-2}·K^{-4}].

3.1.5. Source and Sink Terms

For sources (production), the mass production rate of component κ is given by

$$q^\kappa = \sum_{\beta=A,G} X_\beta^\kappa q_\beta, \ \kappa = w, m, \tag{3.10}$$

where q_β is the production rate of phase β [kg·s^{-1}]. For sinks (injection), the mass injection rate q^κ of the component κ is known/specified.

3.2. Porosity-Permeability Relationship

The permeability is updated using the general expression of Rutqvist and Tsang (2003) as

$$\frac{k}{k_0} = \exp\left[\gamma\left(\frac{\phi}{\phi_0} - 1\right)\right], \tag{3.11}$$

where γ is an empirical permeability reduction factor that ranges between 5 (for soft unconsolidated media) and 29 (for lithified, highly consolidated media) and 0 denotes an initial or reference state.

3.3. Simplified Geomechanical Model

The simplified geomechanical model can be a constant pore compressibility α_P depending on pressure and temperature, resulting in the porosity change as

$$\phi = \phi_0 \exp\left[\alpha_P \left(P - P_0\right) + \alpha_T \left(T - T_0\right)\right] \tag{3.12}$$

where the subscript 0 denotes a reference state, α_P is the pore compressibility [Pa^{-1}], and α_T is the thermal expansivity of the porous medium [K^{-1}].

In the hydrate simulation, a constant pore compressibility α_P (commonly used in conventional reservoir simulators) is not adequate to describe porosity changes because of cementing solid phases (ice and/or hydrate) affecting the stiffness of media. The effect of cementing solid phases on the pore compressibility is predicted by an empirical model (Moridis and Pruess 2014) that is:

$$\alpha_P = \exp\left\{\ln \alpha_{PL} + \left(\ln \alpha_{PU} - \ln \alpha_{PL}\right)\left[1 - B_x\left(2.25, 2.25, S_S^*\right)\right]\right\}, \tag{3.13}$$

where

$$S_S^* = \frac{S_S - S_{S_{\min}} + \delta}{S_{S_{\max}} - S_{S_{\min}} + 2\delta}, \tag{3.14}$$

in which α_{PL} is the lower limit of the medium compressibility considering the full stiffening effect caused by the presence of cementing solid phases, α_{PU} is the upper limit of the medium compressibility not considering the presence of cementing solid phases, B_x is the incomplete beta function, $S_{S_{\min}}$ is the lowest S_S at which $\alpha_P = \alpha_{PU}$, $S_{S_{\max}}$ is the largest S_S at which $\alpha_P = \alpha_{PL}$, and δ is a smoothing factor.

3.4. Numerical Method

The non-isothermal flow and transport simulator T+H discretizes the continuum in space using the integral finite difference method (IFDM) (Edwards 1972; Narasimhan and Witherspoon 1976; Narasimhan et al. 1978), uses a single-point backward approximation of the time derivatives, and provides a fully implicit solution based on the Newton-Raphson (NR) iteration and the solution of the Jacobian. To simulate multi-phase multi-component flow, there are several primary variables that need to be solved in each element of the discretized domain. The total number of unknowns is the product of the number of active elements and the number of primary variables for each element.

3.4.1. Space Discretization

T+H uses the IFDM (Edwards 1972; Narasimhan and Witherspoon 1976; Narasimhan et al. 1978) to discretize the continuum in space. Using IFDM, the integral of the mass accumulation of a component is replaced by the simple algebraic expression

$$\int_{V_n} M dV = V_n M_n , \tag{3.15}$$

where M is a volume-normalized extensive quantity, and M_n is the average value of M over V_m. The IFDM concepts allow the approximation of the surface integral in Eq. (3.1) by the discrete sum of the fluxes over the surface segments A_{nm} according to

$$\int_{\Gamma_n} \mathbf{F}^{\kappa} \cdot \mathbf{n} d\Gamma = \sum_m A_{nm} F_{nm} , \tag{3.16}$$

where F_{nm} is the average value of the inward-pointing normal component of **F** over the surface segment A_{nm} between volume elements V_n and V_m. The discretization approach used in the IFDM and the definition of the geometric data are shown in **Figure 3.1**.

The discretized flux can be written in terms of averages of the parameters in elements V_m and V_m. The Darcy term in Eq. (3.6) becomes

$$F_{\beta,nm} = -k_{nm}\left[\frac{k_{r\beta}\rho_\beta}{\mu_\beta}\right]_{nm}\left[\frac{P_{\beta,n}-P_{\beta,m}}{D_{nm}} - \rho_{\beta,nm}g_{nm}\right], \tag{3.17}$$

where the subscript *nm* indicates a suitable averaging at the interface between the elements *n* and *m* (*e.g.*, interpolation, harmonic weighting, or upstream weighting). $D_{nm} = D_n + D_m$ is the distance between the nodal points *n* and *m* shown in **Figure 3.1**, and g_{nm} is the component of the gravitational acceleration in the direction from the nodal point *m* to *n*.

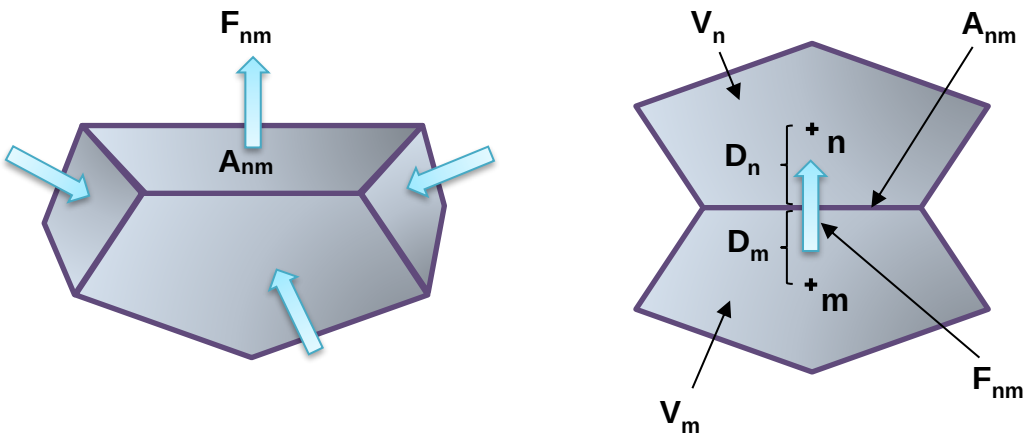

Figure 3.1 Space discretization and geometry parameters in the integral finite difference method.

Substituting Eqs. (3.15) and (3.16) into Eq. (3.1) yields

$$\frac{dM_n^\kappa}{dt} = \frac{1}{V_n}\sum_m A_{nm}F_{nm}^\kappa + q_n^\kappa, \tag{3.18}$$

which results in a set of first-order ordinary differential equations valid in each element.

3.4.2. Time Discretization

For the time discretization, T+H V1.5 employs a fully implicit scheme, in which the thermodynamic parameters are evaluated at the current/new time level, $t^{k+1} = t^k + \Delta t$, and the unknowns are implicitly defined in the resulting equations (Peaceman 1977). Because flow/thermal (FT) simulations solve strongly nonlinear problems involving multiphase flow and phase changes, the fully implicit scheme in T+H V1.5 evaluates the flux and sink and source terms on the right-hand side of Eq. (3.18) at the new time level t^{k+1}, thus ensuring numerical stability. The resulting equation is

$$R_n^{\kappa,k+1} = M_n^{\kappa,k+1} - M_n^{\kappa,k} - \frac{\Delta t}{V_n}\left(\sum_m A_{nm}F_{nm}^{\kappa,k+1} + V_n q_n^{\kappa,k+1}\right) = 0 \tag{3.19}$$

where $R_n^{\kappa,k+1}$ is the residual. In a problem involving N_κ components and N_E elements, the total number of simultaneous equations to be solved (and the associated number of unknowns) is $N_E \times N_\kappa$.

3.4.3. The Newton-Raphson Method

The $N_E \times N_\kappa$ unknowns are the independent primary variables x that define the state of the flow system at the new time level t^{k+1}. Expanding the residual $R_n^{\kappa,k+1}$ in Eq. (3.19) at the iteration step $(p+1)$ in a Taylor series in terms of the iteration step p yields

$$R_n^{\kappa,k+1}\left(x_{i,p+1}\right) = R_n^{\kappa,k+1}\left(x_{i,p}\right) + \sum_i \left.\frac{\partial R_n^{\kappa,k+1}}{\partial x_i}\right|_p \left(x_{i,p+1} - x_{i,p}\right) + \cdots = 0\,. \tag{3.20}$$

Considering only the first order term of the series results in the equation

$$-\sum_i \left.\frac{\partial R_n^{\kappa,k+1}}{\partial x_i}\right|_p \left(x_{i,p+1} - x_{i,p}\right) = R_n^{\kappa,k+1}\left(x_{i,p}\right), \tag{3.21}$$

the left-hand side of which is the Jacobian and the right-hand side is the residual vector. The derivatives in the Jacobian matrix of Eq. (3.21) are computed by numerical differentiation. Eq. (3.21) can be written in the matrix-vector form as

$$-\mathbf{J}_p^{k+1}\left(\mathbf{x}_{p+1}^{k+1} - \mathbf{x}_p^{k+1}\right) = \mathbf{R}_p^{k+1} \tag{3.22}$$

in which the expanded form of the Jacobian matrix is

$$\mathbf{J} = \begin{bmatrix} \frac{\partial R_1}{\partial x_1} & \frac{\partial R_1}{\partial x_2} & \cdots & \frac{\partial R_1}{\partial x_{n-1}} & \frac{\partial R_1}{\partial x_n} \\ \frac{\partial R_2}{\partial x_1} & \frac{\partial R_2}{\partial x_2} & \cdots & \frac{\partial R_2}{\partial x_{n-1}} & \frac{\partial R_2}{\partial x_n} \\ \vdots & \vdots & \ddots & \vdots & \vdots \\ \frac{\partial R_{n-1}}{\partial x_1} & \frac{\partial R_{n-1}}{\partial x_2} & \cdots & \frac{\partial R_{n-1}}{\partial x_{n-1}} & \frac{\partial R_{n-1}}{\partial x_n} \\ \frac{\partial R_n}{\partial x_1} & \frac{\partial R_n}{\partial x_2} & \cdots & \frac{\partial R_n}{\partial x_{n-1}} & \frac{\partial R_n}{\partial x_n} \end{bmatrix}, \tag{3.23}$$

the vector of the unknowns is

$$\mathbf{x} = \begin{bmatrix} x_1 \\ x_2 \\ \vdots \\ x_{n-1} \\ x_n \end{bmatrix}, \tag{3.24}$$

and the vector of the residuals is

$$\mathbf{R} = \begin{bmatrix} R_1 \\ R_2 \\ \vdots \\ R_{n-1} \\ R_n \end{bmatrix}. \tag{3.25}$$

The solution is updated at every iteration of the Newton-Raphson method as

$$\mathbf{x}_{p+1}^{k+1} = \mathbf{x}_{p}^{k+1} + \left(\mathbf{J}_{p}^{k+1}\right)^{-1} \mathbf{R}_{p}^{k+1}. \tag{3.26}$$

The Newton-Rapson iteration continues until it meets the following conditions:

$$\left| \frac{R_{n,p+1}^{\kappa,k+1}}{M_{n,p+1}^{\kappa,k+1}} \right| \leq \varepsilon_1 \tag{3.27}$$

where ε_1 (usually 10^{-5}) is the relative tolerance defined in the input file.

3.5. Parallelization

The development of the pT+H V1.5 in this study involved appropriate modification of the pre-existing serial T+H V1.5 simulator (Moridis and Pruess, 2014; Moridis, 2014) to ensure maximum (and effective) MPI-based parallelization. The equilibrium reaction of hydrate dissociation/formation results in up to 4 mass and heat

balance equations in each element into which the domain is subdivided; the kinetic reaction results in up to 5 equations per element.

The problem size (as quantified by the order of the Jacobian matrix to be solved) increases dramatically in systems with large, multi-dimensional domain in which fine discretization is required to accurately describe the strongly non-linear processes associated with hydrate association and the related sharp fronts. In the pT+H V1.5 code, a domain decomposition method (see discussion in Section 2.4.1) is necessary in order to distribute the workload among the various processors and run the simulation in parallel. The domain decomposition scheme in pT+H uses overlapped subdomains and the corresponding ghost elements to appropriately evaluate the flux terms in the governing equations at neighboring processors. Note that these ghost elements are different from those for the geomechanical problems because of the different numerical methods employed by the two simulators. The pT+H simulator only needs the elements with which a given element is connected in order to predict the associated flux terms, so the overlapped method involves 8 ghost elements arranged in the star-type stencil depicted in the example of **Figure 2.1**, in which each box represents an element in the discretized domain of the pT+H problem, and the associated number is the assigned processor rank needed to renumber the FT equation numbers later.

Before partitioning the mesh by METIS, the master processor reads the mesh file to construct the connectivity information required during the partitioning process. The partitioned results from METIS do not consider ghost elements, and these need to be added manually to each processor-assigned subdomain.

Recalling Section 2.4.1, the node numbers need to be renumbered in each subdomain for optimal performance in geomechanics simulations. In FT simulations, the pT+H code processes the element numbers in the same manner and numbers them in the following order: internal, border, and external elements. **Table 3.1** shows the original, local, and global element numbers for the discretized domain shown in **Figure 2.2** using the star-type stencil of the overlapped method. Because each element involves multiple equations, the primary variables are also renumbered according to their element numbers. The local Jacobian matrix and residual vector are assembled using the new local numbers, the corresponding global indices are mapped accordingly, and the associated equations are prepared for the solution by the parallel solver.

Table 3.1 Renumbering after the domain partitioning using the overlapped method in the star-type stencil for a domain shown in Figure 2.2.

		Internal	**Border**	**External**
Processor 1	Original number	1	2, 5, 6	3, 7, 9, 10
	Local number	1	2, 3, 4	5, 6, 7, 8
	Global number	1	2, 3, 4	6, 7, 10, 11
Processor 2	Original number	4	3, 7, 9	2, 6, 11, 12
	Local number	1	2, 3, 4	5, 6, 7, 8
	Global number	5	6, 7, 8	2, 4, 14, 15
Processor 3	Original number	13	9, 10, 14	5, 6, 11, 15
	Local number	1	2, 3, 4	5, 6, 7, 8
	Global number	9	10, 11, 12	3, 4, 14, 16
Processor 4	Original number	16	11, 12, 15	7, 9, 10, 14
	Local number	1	2, 3, 4	5, 6, 7, 8
	Global number	13	14, 15, 16	7, 8, 11, 12

The Jacobian matrix in the pT+H simulations of hydrate reactions (formation or dissociation) is non-symmetric and ill-conditioned because of the strong non-linearities imposed by the coupled processes and the need for upstream weighting (without which mathematically correct but non-physical solutions are often obtained in multi-phase problems). Conversely, the matrix associated with the geomechanical response of a hydrate-bearing system undergoing pressure- and/or temperature-induced changes is positive definite. Different solver configurations are expected for these two matrix equation systems. Thus, the Jacobian matrix equation obtained from the hydrate simulation using pT+H V1.5 is solved using the generalized minimal residual method (GMRES) with a block Jacobi preconditioner (BJACOBI) that are available in the PETSc package (Balay et al. 2014).

The parallelization of the pT+H simulation must ensure that the results are monitored correctly in addition to partitioning domain and PETSc implementation. The T+H V1.5 code can monitor the evolution of (a) the pore volume-averaged properties and conditions in user-defined subdomains, (b) the flow through user-defined interfaces, (c) the flow through user-defined groups of sources and sinks, and (d) the gas hydrate mass and its formation/dissociation reaction in the entire domain. The domain is not partitioned and distributed to multiple processors in the serial simulation, so monitoring these results does not pose any difficulties; however, this activity requires significant effort in the development of the MPI-based environment of pT+H V1.5. The subdomains, interfaces, and sources/sinks defined by users are unlikely to be constrained to a single processor when multiple processors are involved, necessitating extensive MPI communications to

determine the elements and components of a monitored subdomain when these are assigned to different processors. Both point-to-point and collective communications are applied during this process.

3.6. Flow Chart

Figure 3.2 presents the flow chart of pT+H V1.5.

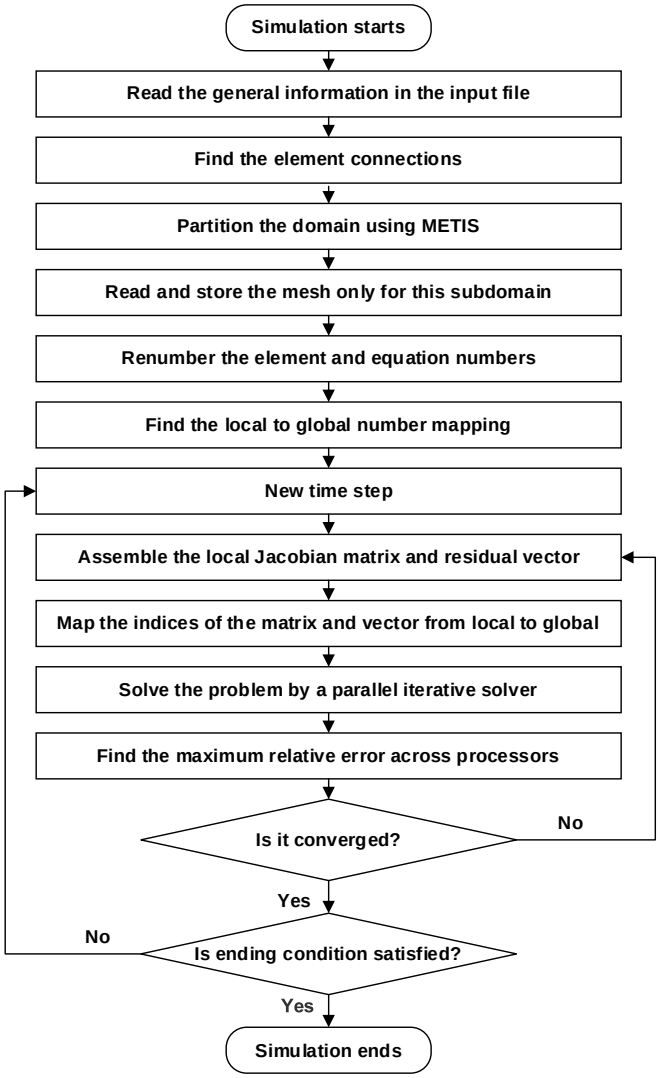

Figure 3.2 The flow chart of pT+H V1.5.

3.7. Parallelization Validation

The validation process was based on comparisons of the pT+H V1.5 results for various numbers of processors to the corresponding solutions obtained from the serial T+H V1.5 version. The problem in the validation study involved different production scenarios from a 2D cylindrical domain (*i.e.*, a single-well problem) and explored different porosity-permeability dependency options.

3.7.1. Problem Description

Two production scenarios were investigated: reservoir fluids produced at (a) a constant bottomhole pressure P_{bh} = 3 MPa and (b) a constant mass flow rate Q_m = 18.955 kg·s^{-1}. Both Cases S1 and S1P involved production at the constant P_{bh} and accounted for the porosity-permeability relationship of Eq. (3.11), differing only the empirical permeability reduction factor γ, which was zero in Case S1 and nonzero in Case S1P. Cases S2 and S2P involved production at the constant Q_m, and differed only the treatment of γ, which was the same as in Cases S1 and S1P, respectively.

3.7.1.1. System Description and Geometry

Reagan et al. (2019) firstly studied this 2D cylindrical problem depicting a real-life oceanic hydrate accumulation, in which the geologic model and the associated computational domain involved three major layers: the overburden layer (OB), the hydrate accumulation/production target, comprising hydrate-bearing layers and hydrate-free interlayer units, and the underburden layer (UB). More specifically, the production target

consisted of three layers of hydrate-bearing sandy sediments (H1, H2, and H3), two hydrate-free interlayers of soft oceanic muds (M1 and M2), and an aquifer layer (A1). For brevity, HBL stands for the hydrate-bearing layer, ML stands for the mud layer, and AL stands for the aquifer layer. The simple sketch of the geologic model of this deposit in **Figure 3.3** shows the system geometry and the thickness of all relevant layers/units. The overburden and underburden were accurate representations of the geometry of this real-life system, and were sufficiently large to provide the necessary heat and water exchange with the reservoir. The top and bottom boundaries were represented in the simulation domain by very thin layers with time-invariant conditions and properties.

	Δz (m)
Sea	2200.00
Overburden (OB)	214.90
Hydrate Deposit	53.60
Underburden (UB)	33.15

Hydrate Deposit	Δz (m)
Hydrate (H1)	10.60
Mud (M1)	0.30
Hydrate (H2)	15.25
Mud (M2)	27.05
Hydrate (H3)	15.50
Aquifer (A1)	4.90

Figure 3.3 The geological model with layered geometries of the 2D cylindrical problem.

3.7.1.2. Well Description

Reservoir fluids were produced through a vertical well perforated from the top of the H1 layer to the bottom of the H3 layer. The well was located at the center of the cylindrical domain that extends to an outer boundary at r_{max} = 2000 m, where conditions and properties were constant (time-invariant) at their initial level. The right boundary was located at a sufficiently large distance to mimic an infinite-acting boundary behavior within the time frame of the simulations.

The flow in the wellbore was approximated by a Darcy flow through a pseudo-porous medium representing the interior (annulus/tubing) of the well, in an approach validated in earlier studies (Moridis and Reagan 2007a). This pseudo-medium had a ϕ = 1, a very high vertical permeability ($k_z = 5\times10^{-9}$ m^2), a capillary pressure of zero, and phase relative permeabilities that were linear functions of the phase saturations in the wellbore. The well had a very small irreducible gas saturation, set at 0.005, to allow the emergence of a free gas phase in the well.

3.7.1.3. Domain Discretization

For reliable/accurate predictions, the 2D domain was finely discretized into 342 subdivisions in the radial direction and 354 subdivisions in the vertical direction, resulting in a total of 121,068 elements (gridblocks). Along the radial direction, the Δr subdivisions were increased logarithmically from the well radius r_w = 0.05 m to r_{max}. The vertical discretization was also very fine, with $0.15 \leq \Delta z \leq 0.4$ m in the reservoir, but with larger

Δz's in the hydrate-free overburden and underburden because of the diffusive behavior of pressure at these locations.

Assuming that hydrate dissociation/formation can be accurately described by an equilibrium reaction, the presence of salt in this oceanic system led to (a) a system involving 3 mass components (H_2O, CH_4, and NaCl) and heat and, consequently, (b) 4 equations per element, resulting in about 480,000 simultaneous equations and unknowns.

3.7.1.4. System Properties

The hydraulic and thermal properties for this 2D problem are summarized in **Table 3.2**. The parameters used for the simplified geomechanical model are shown in **Table 3.3**.

Table 3.2 Properties of the hydrate deposit in Cases S1, S1P, S2, and S2P.

Initial pressure at top boundary (P_T)	23.0 MPa
Pressure distribution	Hydrostatic
Initial temperature at top boundary (T_T)	4.35 °C
Initial temperature at bottom boundary (T_B)	38.335 °C
Gas composition	100% CH_4
Initial saturations of HBLs H1 and H2	S_H = 0.47
Initial saturation of HBL H3	S_H = 0.73
Intrinsic permeabilities of HBLs	$k_r = 1.0 \times 10^{-12}$ m^2; $k_z = 0.01k_r$
Porosity ϕ of HBLs	0.37

Table 3.2 Continued.

Intrinsic permeabilities of MLs	$k_r = 1.0 \times 10^{-14}$ m^2; $k_z = 0.1k_r$
Porosity ϕ of MLs	0.37
Intrinsic permeabilities of ALs	$k_r = 1.0 \times 10^{-14}$ m^2; $k_z = 0.1k_r$
Porosity ϕ of ALs	0.37
Intrinsic permeabilities of OB	$k_r = 5.0 \times 10^{-19}$ m^2; $k_z = 0.2k_r$
Porosity ϕ of OB	0.44
Intrinsic permeabilities of UB	$k_r = 5.0 \times 10^{-19}$ m^2; $k_z = 0.2k_r$
Porosity ϕ of UB	0.43
Dry thermal conductivity (all layers)	$k_{\theta d} = 0.50$ W·m^{-1}·K^{-1}
Wet thermal conductivity (all layers)	$k_{\theta w} = 1.16$ W·m^{-1}·K^{-1}
Specific heat C_R (all layers)	1000 J kg^{-1} K^{-1}
Grain density ρ_R (all layers)	2650 kg^{-1} m^{-3}
Composite thermal conductivity model	$\overline{k_\theta} = k_{\theta d} + \left(\sqrt{S_A} + \sqrt{S_H}\right)\left(k_{\theta w} - k_{\theta d}\right) + \phi S_I k_{\theta I}$
Relative permeability model	$k_{rA} = \max\left\{0, \min\left\{\left[\frac{S_A - S_{irA}}{1 - S_{irA}}\right]^n, 1\right\}\right\}$; $k_{rG} = \max\left\{0, \min\left\{\left[\frac{S_G - S_{irG}}{1 - S_{irA}}\right]^{n_G}, 1\right\}\right\}$; $k_{rH} = 0$
S_{irA}, S_{irG}, n, n_G of HBLs	0.15; 0.01; 4.30; 3.20
S_{irA}, S_{irG}, n, n_G of MLs	0.55; 0.03; 3.50; 2.50
S_{irA}, S_{irG}, n, n_G of AL	0.55; 0.03; 3.50; 2.50

Table 3.2 Continued.

S_{irA}, S_{irG}, n, n_G **of OB**	0.65; 0.05; 5.50; 4.50
S_{irA}, S_{irG}, n, n_G **of UB**	0.65; 0.05; 5.50; 4.50
Capillary pressure model	$P_{cap} = -P_0\left[\left(S^*\right)^{-\frac{1}{\lambda}} - 1\right]^{1-\lambda}$ $S^* = \frac{S_A - S_{irA}}{S_{mxA} - S_{irA}}$
λ, P_0, S_{irA}, S_{mxA} **of HBLs**	0.45; 1×10^4 Pa; 0.14; 1.0
λ, P_0, S_{irA}, S_{mxA} **of MLs**	0.45; 1×10^5 Pa; 0.54; 1.0
λ, P_0, S_{irA}, S_{mxA} **of AL**	0.45; 1×10^5 Pa; 0.54; 1.0
λ, P_0, S_{irA}, S_{mxA} **of OB**	0.45; 5×10^5 Pa; 0.64; 1.0
λ, P_0, S_{irA}, S_{mxA} **of UB**	0.45; 5×10^5 Pa; 0.64; 1.0
Empirical permeability reduction factor γ	8.0 (HBLs); 6.0 (MLs, AL, OB, UB)

Table 3.3 Geomechanical parameters using the simplified geomechanical model of the hydrate deposit in the 2D cylindrical problem.

α_{PL}	2.0×10^{-9} Pa^{-1}
$S_{S_{\max}}$	0.40
α_{PU}	1.0×10^{-8} Pa^{-1}
$S_{S_{\min}}$	0.15
δ	0.015

3.7.1.5. Initial Conditions

The initial conditions in the reservoir were determined by the initialization process described by Moridis and Reagan (2007b). To obtain the initial temperature distribution, the temperatures at the top and bottom boundaries were set to the values listed in **Table 3.2**. To obtain the initial pressure distribution in the reservoir profile, the pressure at the top boundary was set to the value listed in **Table 3.2** and the bottom boundary was made impermeable. After defining these boundary conditions, an initialization simulation was conducted using a single column of the domain until thermal, hydrostatic, and chemical equilibria (*i.e.*, steady-state conditions) were reached. The pressure and temperature profiles resulting from the initial equilibration simulations were applied to the entire domain and used as the initial conditions for the subsequent production simulations.

A gridblock above the uppermost well gridblock was used as the internal boundary for the constant-pressure production, or the element where the constant mass flow rate of fluid production was assigned. Note that the well was treated as a pseudo-porous medium mentioned in Section 3.7.1.4, so the well gridblocks were included in the computational domain and the conditions therein were continuously monitored.

3.7.2. Validation Results

All the cases were simulated by both the serial T+H V1.5 and the parallel pT+H V1.5 codes in order to compare their simulation results: the production rates and cumulative production of the gaseous and aqueous phases in all cases. The pT+H simulations of Cases S1, S2, S1P, and S2P used 64 processors in the parallel environment.

The production period in all cases lasted 540 days, *i.e.*, a time frame sufficiently long to allow even small computational error caused by the parallelization to be amplified by the end of production.

In Case S1, the production rate and cumulative production of the gaseous phase are presented in **Figure 3.4**, and those of the aqueous phase are in **Figure 3.5**. The serial and parallel results are identical in this long-term production test. The same near-perfect agreement is observed in **Figures 3.6** and **3.7** related to Case S1P, **Figures 3.8** and **3.9** related to Case S2, and **Figures 3.10** and **3.11** related to Case S2P. The coincidence of the serial T+H V1.5 and the parallel pT+H V1.5 results in the solution of these large and complex problems provided strong evidence of the validity of the parallel code.

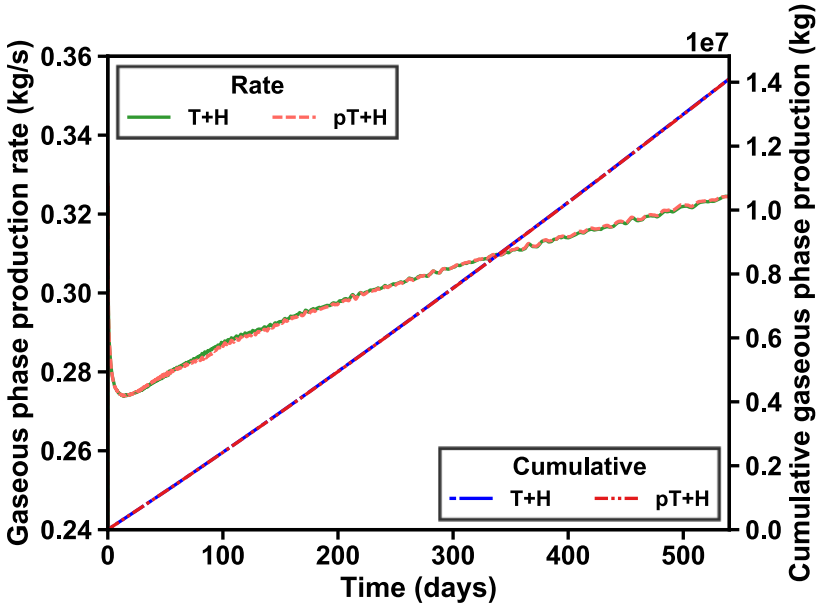

Figure 3.4 The parallelization validation on the production rate and cumulative production of the gaseous phase in Case S1.

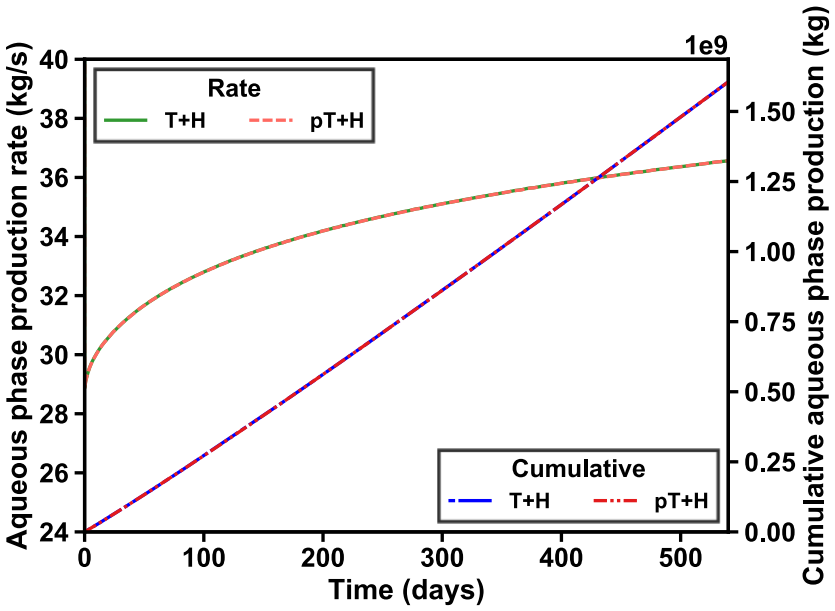

Figure 3.5 The parallelization validation on the production rate and cumulative production of the aqueous phase in Case S1.

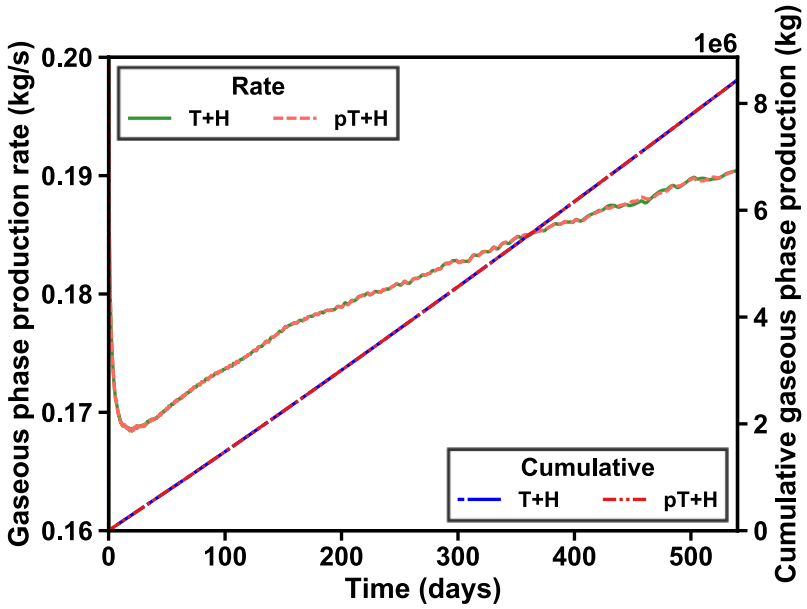

Figure 3.6 The parallelization validation on the production rate and cumulative production of the gaseous phase in Case S1P.

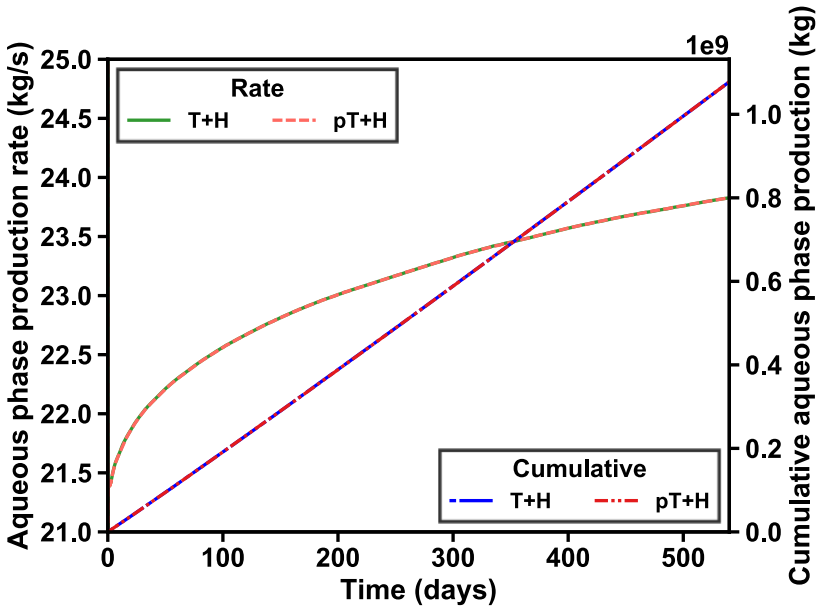

Figure 3.7 The parallelization validation on the production rate and cumulative production of the aqueous phase in Case S1P.

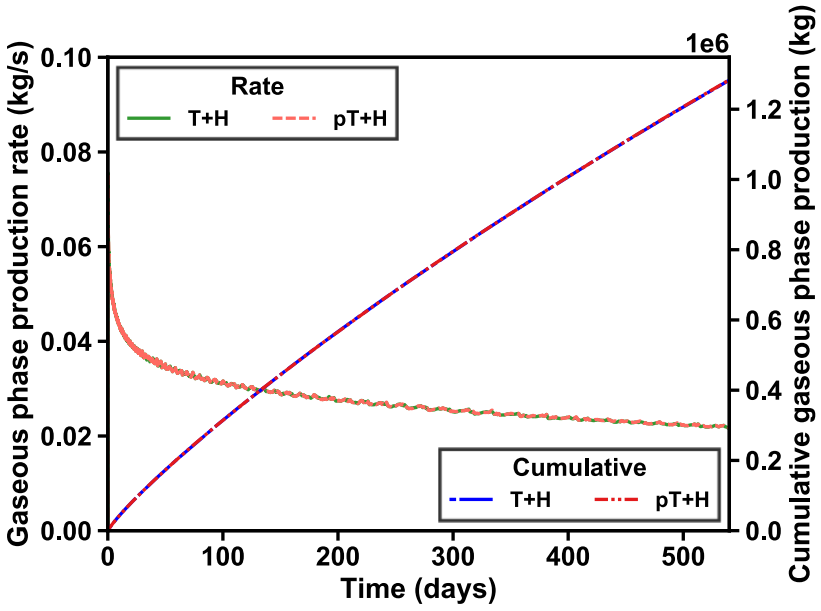

Figure 3.8 The parallelization validation on the production rate and cumulative production of the gaseous phase in Case S2.

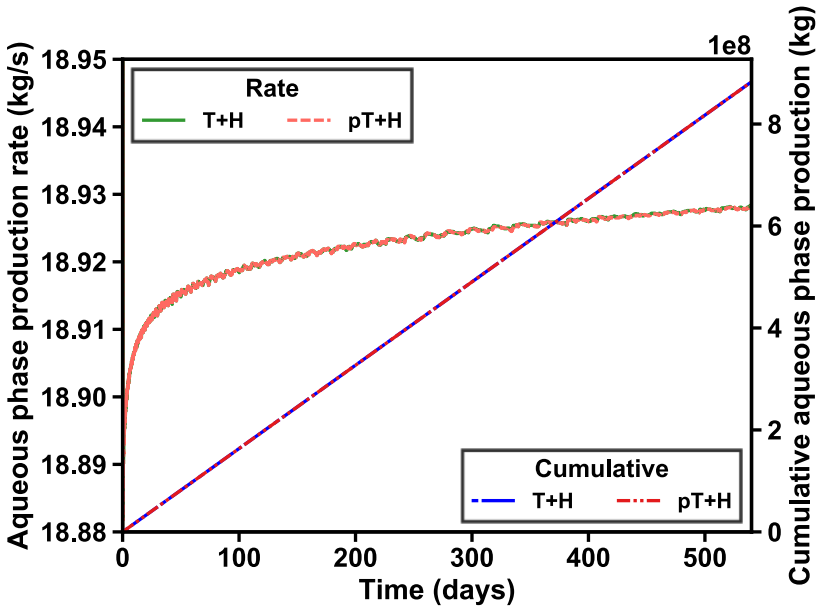

Figure 3.9 The parallelization validation on the production rate and cumulative production of the aqueous phase in Case S2.

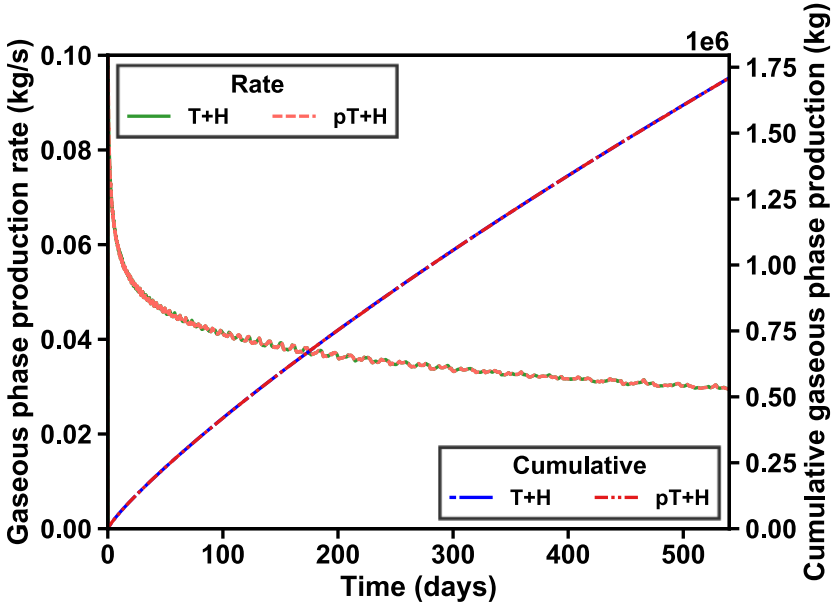

Figure 3.10 The parallelization validation on the production rate and cumulative production of the gaseous phase in Case S2P.

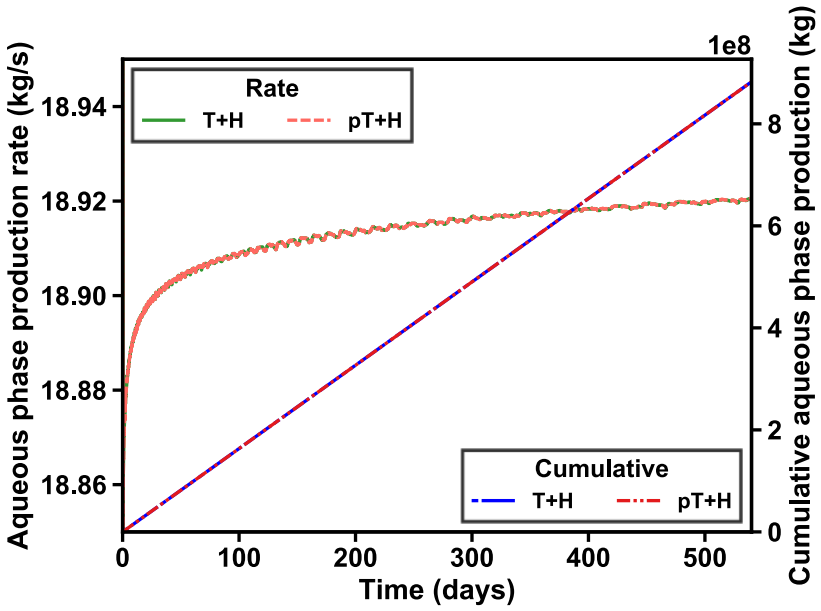

Figure 3.11 The parallelization validation on the production rate and cumulative production of the aqueous phase in Case S2P.

4. PARALLEL COUPLED FLUID FLOW/GEOMECHANICS SIMULATION

This chapter presents detailed information on the coupling pT+H V1.5 and RGMS codes, including details on the coupling method, on the respective parallelization approaches, flow charts, and examples involving problems of hydrate dissociation-related coupled processes computed in a parallel simulation environment.

4.1. Coupling Method

The coupling of the flow, thermal, chemical, and geomechanical processes describes the interdependence of the associated properties and involves the updating of (a) pressure, temperature, and flow properties (porosity and permeability) in response to geomechanical changes and of (b) stresses, strains, and displacements in response to changes in the fluid pressure, temperature, and flow properties. The porosity mentioned in the previous sections is the reservoir porosity, which is the ratio of the pore volume in the deformed system to the total volume in the original (non-deformed) configuration. In addition to the reservoir porosity, the true porosity is defined as the ratio of the pore volume to the total volume when both are in the deformed configuration. The relation between the reservoir porosity and the true porosity is

$$\phi = \phi^{*}(1+\varepsilon_{v}), \tag{4.1}$$

where ϕ^{*} is the true porosity and ε_{v} is the volumetric strain.

In a deformed porous medium, the true porosity variation is computed by (Geertsma 1957)

$$\delta\phi^* = \phi^*\left[\frac{1}{\phi^*}\left(\frac{1}{K_{dr}}-\frac{1}{K_s}\right)-\frac{1}{K_{dr}}\right]\left(\delta\sigma_v+\delta P_t\right)=\left(\frac{1}{\phi^*}\frac{\alpha}{K_{dr}}-\frac{1}{K_{dr}}\right)\left(\delta\sigma_v+\delta P_t\right), \quad (4.2)$$

where σ_v is the total mean stress.

There are two major methods to account for the above porosity change: the fully coupled method and the sequentially coupled method. The sequential method includes the following options: fixed-strain split, fixed-stress split, drained split, and undrained split. Under conditions of isothermal single-phase flow of a slightly compressible fluid in isotropic geological media, (a) the undrained and fixed-stress splits are unconditionally stable, and (b) the fixed-stress split is more accurate than the undrained split (Kim et al. 2011a, 2011b). When the geomechanics simulation is coupled with the hydrate simulations, the Young's modulus is a function of the hydrate saturation S_H, and the associated non-linearity adversely affects the accuracy and efficiency of the sequentially coupled method.

Compared to the sequentially coupled method, the fully coupled method requires unifying the two simulations, assembling the flow, thermal, and geomechanical equations in a single matrix, and solving all equations simultaneously. The equations associated with the mass and heat balance are already ill-conditioned; the equations of the fully-coupled system become much more ill-conditioned because the entries of the stiffness matrix that originate from the geomechanics simulation are usually very large in magnitude, thus significantly increasing the condition number of the fully coupled matrix and making its solution much more difficult. Additionally, the solution of the augmented fully-coupled matrix is more time-consuming than the solution of the two separate matrices in the

sequential approach even when the conditioning of the matrix is unaffected. Therefore, the fixed-stress split with an iterative scheme is implemented in the coupled RGMS and pT+H V1.5 codes in order to maximize the execution speed while maintaining as high a level of accuracy of the numerical solution as that of the fully-coupled method.

The fixed-stress split iterative scheme is an iterative coupling method that solves the flow problem and the geomechanics problems sequentially at each time step, but it only proceeds to the next time step when the coupled solution converges within a predetermined tolerance. The FT simulation is conducted first by freezing the total mean stress $\left(\delta\sigma_v = 0\right)$, so the true porosity variation computed from the FT simulation becomes

$$\delta\phi^* = \frac{\alpha - \phi^*}{K_{dr}}\delta P_t. \tag{4.3}$$

Because the flow problem is non-linear and it is solved using the NR iteration method and the Jacobian, the true porosity change can be written as

$$\phi^{*k} = \phi^{*k-1} + \frac{\alpha - \phi^{*k-1}}{K_{dr}}\delta P_t^{k-1}, \tag{4.4}$$

where k is the NR iteration count. Combining Eq. (4.1) and Eq. (4.4) yields

$$\phi^k = \phi^{k-1} + \frac{\alpha\left(1+\varepsilon_v\right) - \phi^{k-1}}{K_{dr}}\delta P_t^{k-1}. \tag{4.5}$$

The above equation shows that the reservoir porosity is a function of (a) the pore pressure and (b) the volumetric strain. Of those, the first is computed from the FT simulation, and the second is estimated from the geomechanical simulation.

Following the update in the porosity, the equations in the geomechanical simulation are assembled using the equivalent pore pressure that has been updated from the results of the FT simulation. The total mean stress can be written in terms of the volumetric strain (Biot 1941) as

$$\delta\sigma_v = K_{dr}\delta\varepsilon_v - \alpha\delta P_t, \tag{4.6}$$

and substitution in Eq. (4.2) leads to

$$\delta\phi^* = \left(\alpha - \phi^*\right)\delta\varepsilon_v + \frac{\left(\alpha - \phi^*\right)\left(1-\alpha\right)}{K_{dr}}\delta P_t. \tag{4.7}$$

Following Coussy (2004), the terms $\left(\alpha - \phi^*\right)$ and $\frac{\left(\alpha - \phi^*\right)\left(1-\alpha\right)}{K_{dr}}$ can be treated as constants when linear poroelasticity is assumed. Although the drained bulk modulus varies with S_H, the iterative scheme ensures that the solutions converge rapidly toward the fully coupled solutions. Thus, the true porosity can be found by integrating Eq. (4.7), leading to

$$\phi^* - \phi_0^* = \left(\alpha - \phi_0^*\right)\left(\varepsilon_v - \varepsilon_{v0}\right) + \frac{\left(\alpha - \phi_0^*\right)\left(1-\alpha\right)}{K_{dr}}\left(P_t - P_{t0}\right), \tag{4.8}$$

where ϕ_0^* is the initial true porosity, ε_{v0} is the initial volumetric strain, and P_{t0} is the initial equivalent pore pressure.

Combining Eq. (4.1) and Eq. (4.8) results in

$$\phi^n = \phi_0^* + \alpha\left(\varepsilon_v - \varepsilon_{v0}\right) + \frac{\left(\alpha - \phi_0^*\right)\left(1-\alpha\right)}{K_{dr}}\left(P_t - P_{t0}\right) + O\left(\varepsilon_v^2\right). \tag{4.9}$$

Accepting as valid the assumption of infinitesimal deformation (Dana et al. 2018), Eq. (4.9) can be approximated as

$$\phi^n = \phi_0^* + \alpha\left(\varepsilon_v - \varepsilon_{v0}\right) + \frac{\left(\alpha - \phi_0^*\right)\left(1-\alpha\right)}{K_{dr}}\left(P_t - P_{t0}\right). \tag{4.10}$$

If $\varepsilon_{v0} = 0$, the initial true porosity and the initial reservoir porosity are the same, so Eq. (4.10) can be further reduced to

$$\phi^n = \phi_0 + \alpha\varepsilon_v + \frac{\left(\alpha - \phi_0\right)\left(1-\alpha\right)}{K_{dr}}\left(P_t - P_{t0}\right) \tag{4.11}$$

The flow chart of the coupled simulation is shown in **Figure 4.1**. The coupling convergence criterion is that the maximum value of $\frac{\phi^n - \phi^k}{\phi^n}$ be smaller than a given tolerance that is provided as an input. Additionally, the maximum numbers of the fixed-stress iteration and of the NR iteration are also provided as inputs to control the time step, which is reduced if either of these two maximum numbers is reached. To speed up the coupled simulation, the time step can be increased when meeting some criteria (*e.g.*, for a specific time step, the convergence of the fixed-stress is attained in 4 or fewer iterations, and convergence of the NR solution of the FT equation is attained within 5 iterations).

When RGMS is coupled with pT+H in order to investigate the geomechanical response to hydrate dissociation and/or formation, the bulk density in Eq. (2.2) is expanded to

$$\rho_b = \phi \sum_{\beta=A,G,I,H} S_\beta \rho_\beta + \left(1-\phi\right)\rho_s, \tag{4.12}$$

and the average mobile fluid pressure in Eq. (2.7) is written as

$$P_t = \frac{\sum_{\beta=A,G} S_\beta P_\beta}{\sum_{\beta=A,G} S_\beta} \tag{4.13}$$

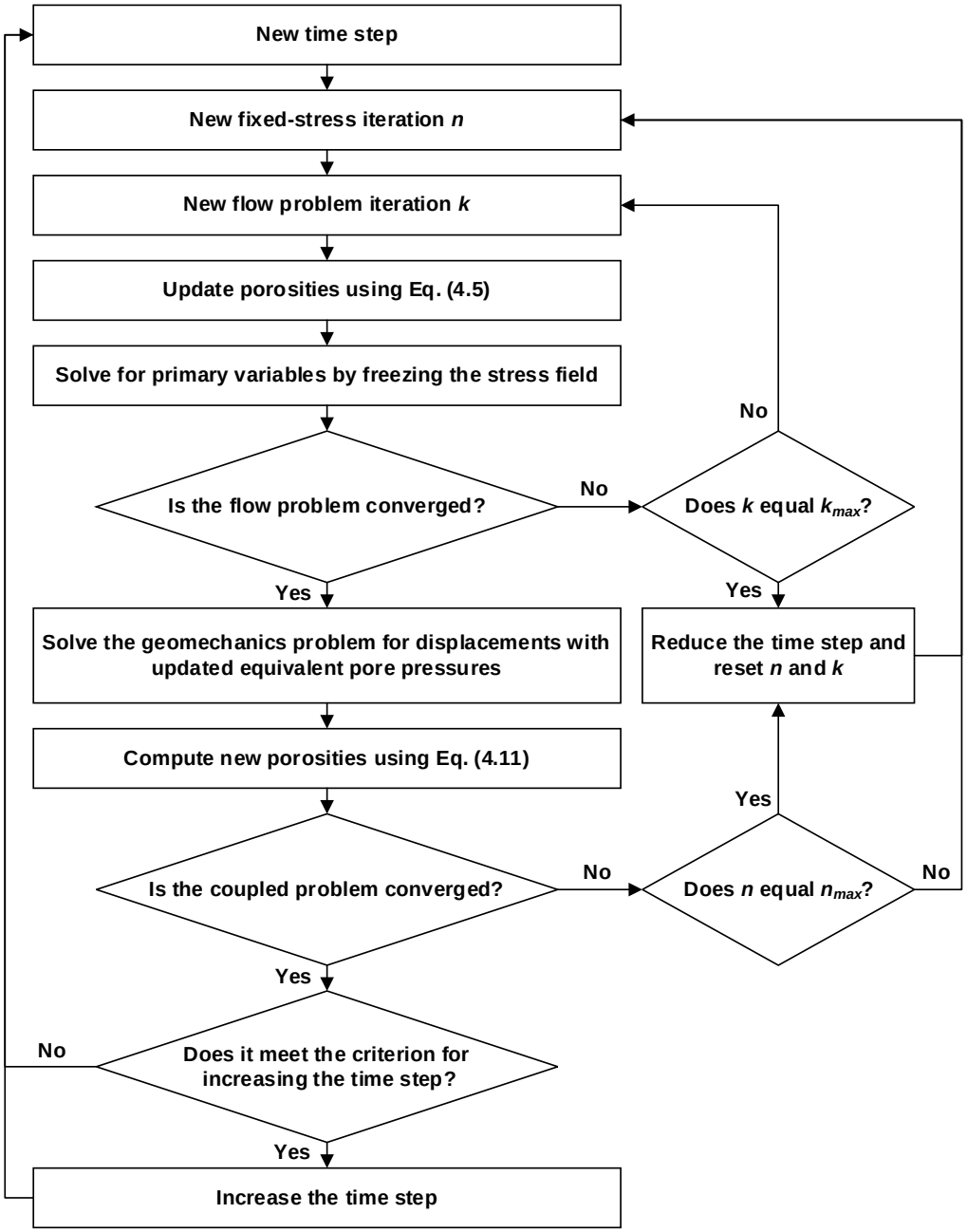

Figure 4.1 The flow chart of the coupled simulation based on the fixed-stress split iterative scheme.

4.2. Parallelization

The computational domains are the same in both the pT+H and the RGMS simulators, and the two simulators use the exact same discretization. This may increase the pT+H computational load because the domain for the hydrate simulations needs to be expanded by including significant parts of the overburden and underburden that do not contribute to hydrate, but which is necessary in the geomechanical computations. However, this is not necessarily a significant problem because the discretizations in the expended domain (overburden and underburden) can be coarse in the absence of hydrate and, additionally, this approach eliminates the need to interpolate between different grids used for the pT+H flow simulation and the RGMS geomechanical simulation, a process that is cumbersome, time-consuming and can lead to errors. However, unique treatments are necessary for parallelizing the two constituent codes of the coupled simulator because different numerical methods are used in the geomechanics and FT simulations.

The partitioned domain resulting from the application of METIS cannot be assigned directly to a processor without some additional manipulation that is needed for the coupled simulation. The FT simulator assembles the equations based on elements, but the geomechanics simulator assembles the equations based on nodes. If METIS is used to partition the elements and the nodes separately, it is possible that the partitioned element subdomains may not coincide with partitioned node subdomains, leading to situations of nodes being handled by a different processor that of the element with which they are associated. This can lead to additional communications between processors and performance deterioration if the nodes are assigned to processors handling distant

elements. To maintain the one-to-one coupling scheme that eliminates the need for interpolation, the partition of the domain is based on the elements involved in the FT problem, and is the same for the geomechanics problem. That is, the same group of elements is assigned to the same processor for both simulations, *i.e.*, the partitioned subdomains are the same for both simulations.

In addition to the partition of elements, it is necessary to partition the nodes in the geomechanics simulation. METIS partitioning assigns a processor rank to every element, and the processor only processes the elements that have its own processor rank. An element involves 4 nodes in 2D problems and 8 nodes in 3D problems, which means that a node can belong to several elements. To eliminate possible conflicts, this node is assigned to the highest processor rank of the elements with which the node is associated. Following this rule, all the nodes can be partitioned without ruining the one-to-one coupling scheme.

4.3. Flow Chart

The flow chart of the coupled pT+H V1.5 and RGM simulator is presented in **Figure 4.2**.

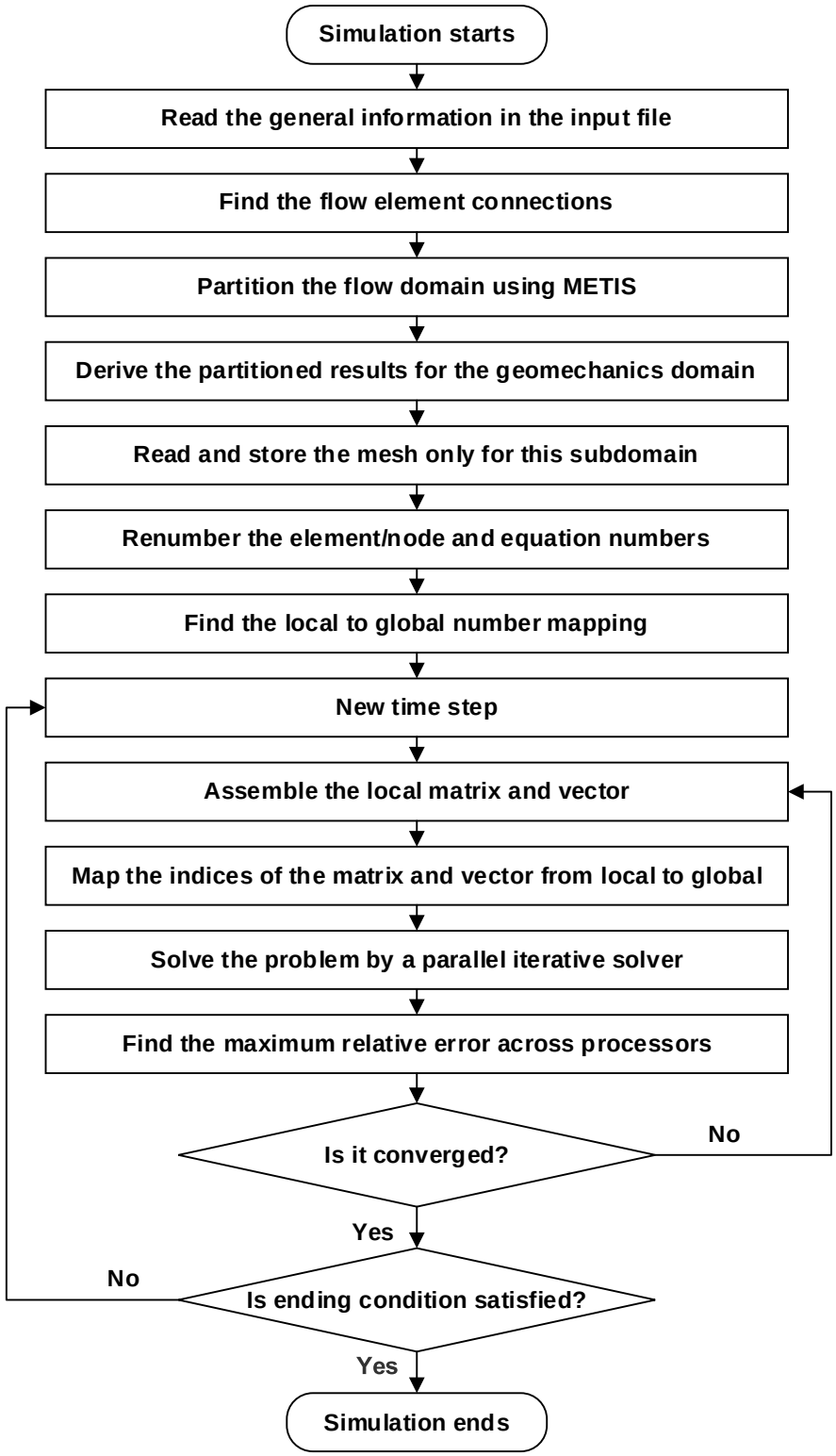

Figure 4.2 The flow chart of the coupled pT+H V1.5 and RGM simulator.

4.4. Coupling Validation

The coupling method used in the coupled pT+H V1.5 and RGMS codes was validated through comparison to the analytical solutions of the Terzaghi problem (Terzaghi and Peck 1948) and McNamee-Gibson problem (McNamee and Gibson 1960a, 1960b) in serial simulations.

4.4.1.1. The Terzaghi Problem

This problem, often referred to as the Terzaghi problem, is a classical poroelastic problem of consolidation in response to draining of the pore fluid. The fluid pressure is expected to increase immediately after traction is applied to the top boundary when the rollers support the left, right, and bottom boundaries (thus preventing normal displacements at these locations). The parameters used for this problem are summarized in **Table 4.1**, and the discretized computational domain, comprising 18 uniform elements, is shown in **Figure 4.3**. The analytical solution and the numerical prediction from the coupled simulator at an observation point located at (x, z) = (0.5 m, -17.5 m) are compared in **Figure 4.4**, which shows an excellent agreement of the two estimates of the relative pore pressure and provides additional evidence in support of the validation of both the constituent codes and of the underlying fixed-stress split iterative scheme in the coupled simulator.

Table 4.1 Parameters of the Terzaghi validation problem.

Width (*W*)	1 m
Height (*H*)	18 m

Table 4.1 Continued.

Mesh number	1 ×18
Porosity	0.25
Permeability	50 mD
Young's modulus	450 MPa
Poisson's ratio	0
Biot's coefficient	1
Fluid compressibility	4×10^{-10} Pa^{-1}
Fluid viscosity	1×10^{-3} Pa·s
Traction (*T*)	13.25 Mpa
Initial pressure (P_i)	10 Mpa
Consolidation coefficient (*c*)	0.0213 $m^2 \cdot s^{-1}$

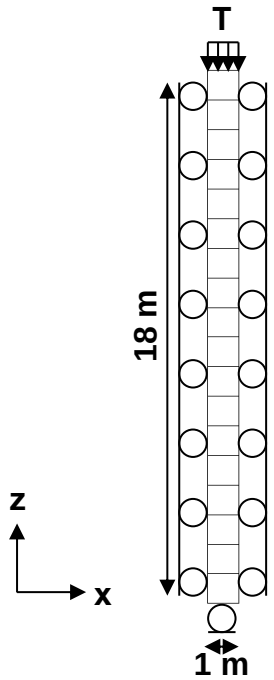

Figure 4.3 The computational domain and boundary conditions for the Terzaghi problem.

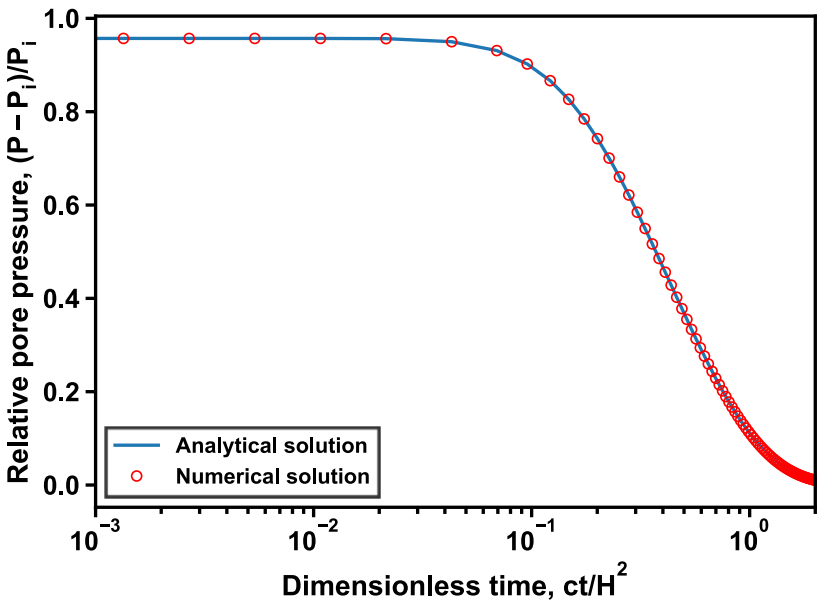

Figure 4.4 Evolution of the relative pore pressure vs. dimensionless time at the observation point for the Terzaghi problem.

4.4.1.2. The McNamee-Gibson Problem

This problem involves constant loads applied to the top boundary of a poroelastic medium, while the normal displacements are fixed at the left, right, and bottom boundaries. The fluid pressure is expected to increase instantaneously with the loading of the medium. The parameters used for this problem are listed in **Table 4.2**. The discretized computational domain is shown in **Figure 4.5**, in which traction is applied to the top, and the left, right, and bottom boundaries that are supported by the rollers and eliminate displacements there. The lengths of subdivisions increase along the positive x-direction and negative z-direction: (a) $0.0001 \leq \Delta x \leq 16$ m and (b) $0.0001 \leq \Delta x \leq 16$ m. The numerical results at the centroid of the fifth element on the left boundary located at (x, z)

= (0.00005 m, -3.5 m) are compared to the analytical solution in **Figure 4.6**, which shows the evolution of the relative pore pressure over the dimensionless time at that observation point. The excellent agreement of the two solutions, as well as the capture of the Mandel-Cryer effect, further validates the coupled simulator.

Table 4.2 Parameters of the McNamee-Gibson validation problem.

Model dimension	110 ×110 m
Mesh number	21 ×21
Porosity	0.25
Permeability	50 mD
Young's modulus	450 MPa
Poisson's ratio	0
Biot's coefficient	1
Fluid compressibility	4×10^{-10} Pa^{-1}
Fluid viscosity	1×10^{-3} Pa·s
Traction 1 (T_1), applied range (a_1)	20 MPa, 0 – 4 m
Traction 2 (T_2), applied range (a_2)	10 MPa, 4 – 110 m
Initial pressure (P_i)	10 MPa
Consolidation coefficient (c)	0.0213 $m^2 \cdot s^{-1}$

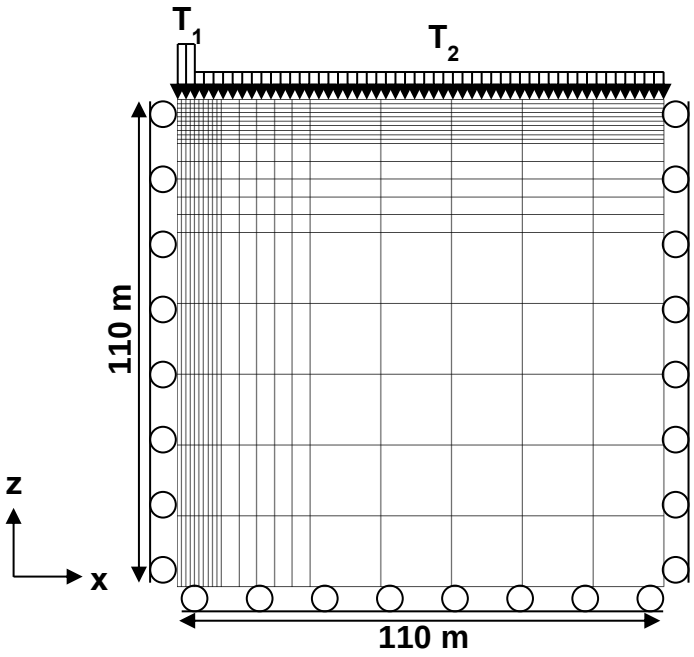

Figure 4.5 The computational domain and boundary conditions for the McNamee-Gibson problem.

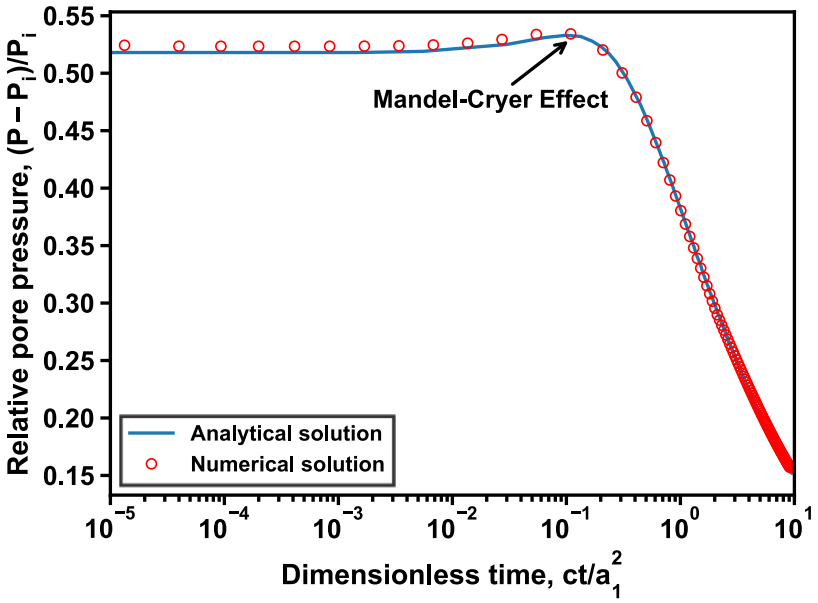

Figure 4.6 Evolution of the relative pore pressure vs. dimensionless time at the observation point for the McNamee-Gibson problem.

4.5. Parallelization Validation

This section describes work that was undertaken to validate the MPI-based parallelization in the coupled pT+H V1.5 and RGM simulator by comparing the estimates, obtained from a single and multiple processors, of the phase production rate and of the corresponding cumulative production mass in the analogous Cases S1G, S1PG, S2G, and S2PG, which involve the same systems and conditions in Cases S1, S1P, S2, and S2P but involve the full geomechanical model RGMS.

4.5.1. Problem Description

4.5.1.1. Flow-Related Description and Parameters

The flow-related problem description and parameters are in Section 3.7.1.

4.5.1.2. Geomechanics-Related Description and Properties

In the geomechanics simulation, the left, right, and bottom boundaries are supported by rollers so the displacements in the normal direction to these boundaries are fixed to zero. When coupling the flow and the geomechanics simulations, the initial effective stress field is forced to be zero, so that the initial total stress field can be determined without modifications of the initial conditions generated from the T+H simulation. Consequently, there was no need to apply normal traction to the top boundary of the domain. The geomechanical properties of the various geologic layers are listed in **Table 4.3**, and are obtained from Reagan et al. (2019). A total of about 720,000

simultaneous equations are solved in this problem: about 480,000 FT equations and about 240,000 geomechanics equations.

Table 4.3 Geomechanical properties of the hydrate deposit in Cases S1G, S1PG, S2G, and S2PG.

Young's modulus in H1, H2, H3	E = 500 MPa at S_H = 0; E = 1990 MPa at S_H = 1
Young's modulus in OB, UB, M1, M2, A1	E = 1096 MPa
Poisson's ratio in H1, H2, H3	ν = 0.4
Poisson's ratio in OB, UB, M1, M2, A1	ν = 0.3
Biot's coefficient	α = 0.99

4.5.2. Validation Results

All the cases were simulated by the coupled pT+H V1.5 and RGMS codes using a single processor in the serial simulations, and multiple processors in the parallel simulations. In the parallel simulations, Cases S1G and S2G were simulated using 16 processors, and Cases S1PG and S2PG were simulated using 128 processors. The duration of the production tests was set at 60 days, *i.e.*, a time that is deemed sufficiently long to enlarge/accentuate possible small errors introduced by the parallelization.

The production rates and cumulative production (a) of the gaseous phase in Cases S1G, S1PG, S2G, and S2GP are shown in **Figures 4.7**, **4.9**, **4.11**, and **4.13**, respectively, and (b) of the aqueous phase in Cases S1G, S1PG, S2G, and S2GP are presented in **Figures 4.8**, **4.10**, **4.12**, and **4.14**, respectively. The virtual coincidence of the serial and

parallel results during this 60-day production test provides additional confirmation of the validity of the MPI-based parallelization of the coupled pT+H V1.5 and RGMS codes.

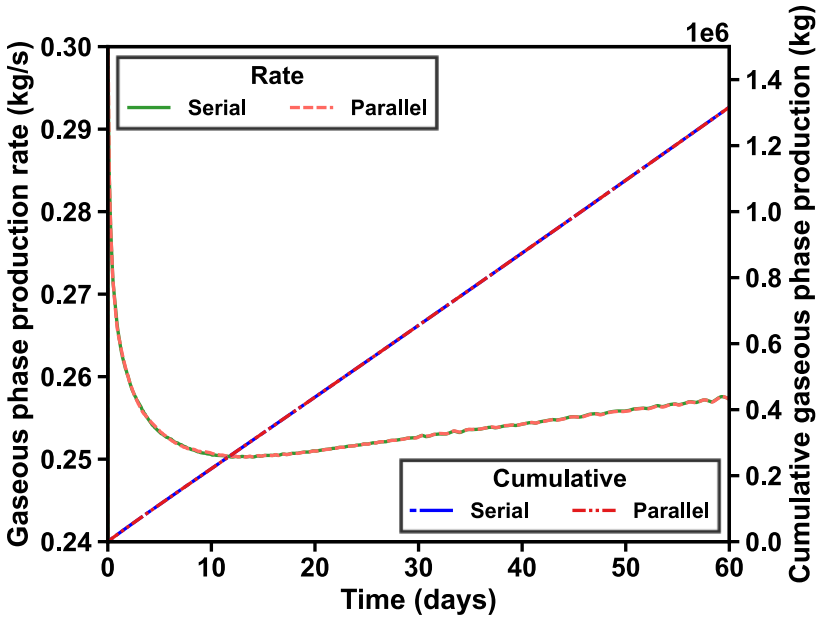

Figure 4.7 The parallelization validation on the production rate and cumulative production of the gaseous phase in Case S1G.

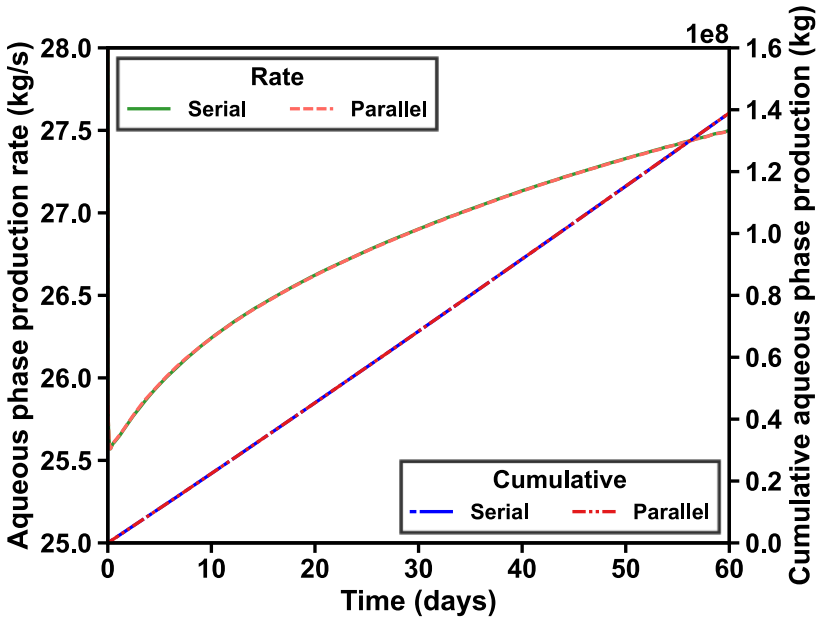

Figure 4.8 The parallelization validation on the production rate and cumulative production of the aqueous phase in Case S1G.

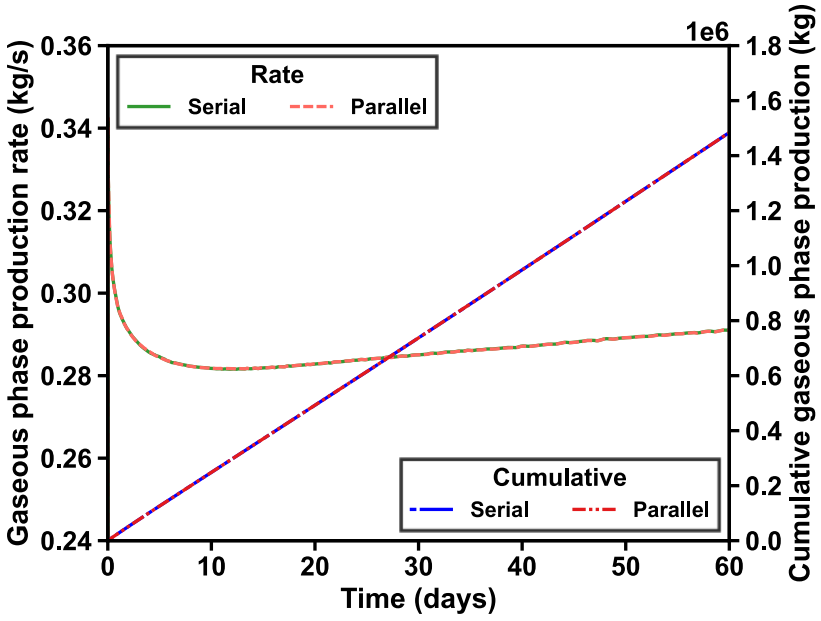

Figure 4.9 The parallelization validation on the production rate and cumulative production of the gaseous phase in Case S1PG.

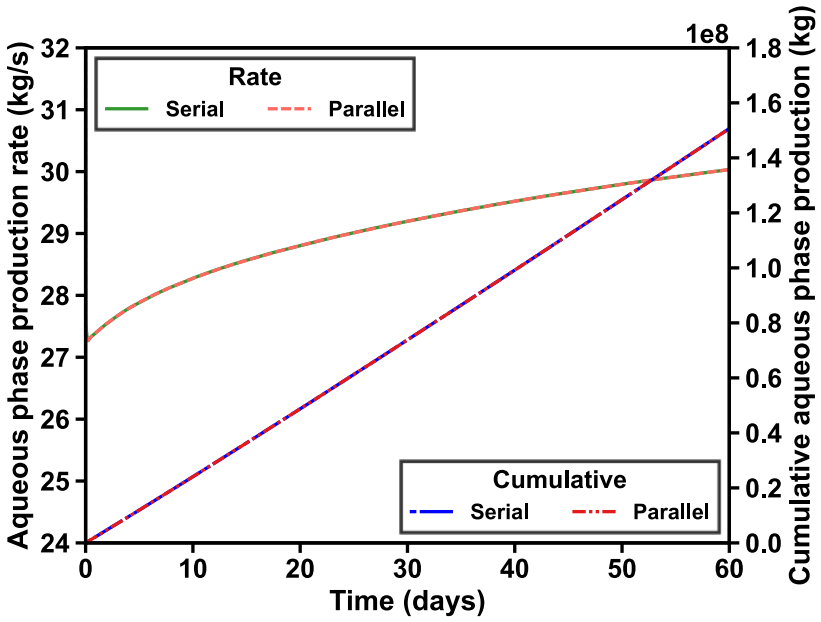

Figure 4.10 The parallelization validation on the production rate and cumulative production of the aqueous phase in Case S1PG.

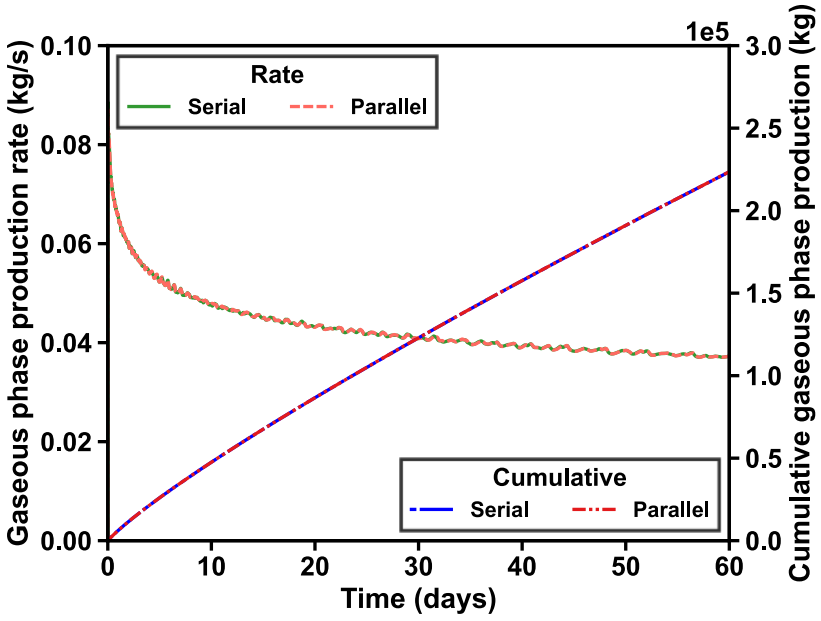

Figure 4.11 The parallelization validation on the production rate and cumulative production of the gaseous phase in Case S2G.

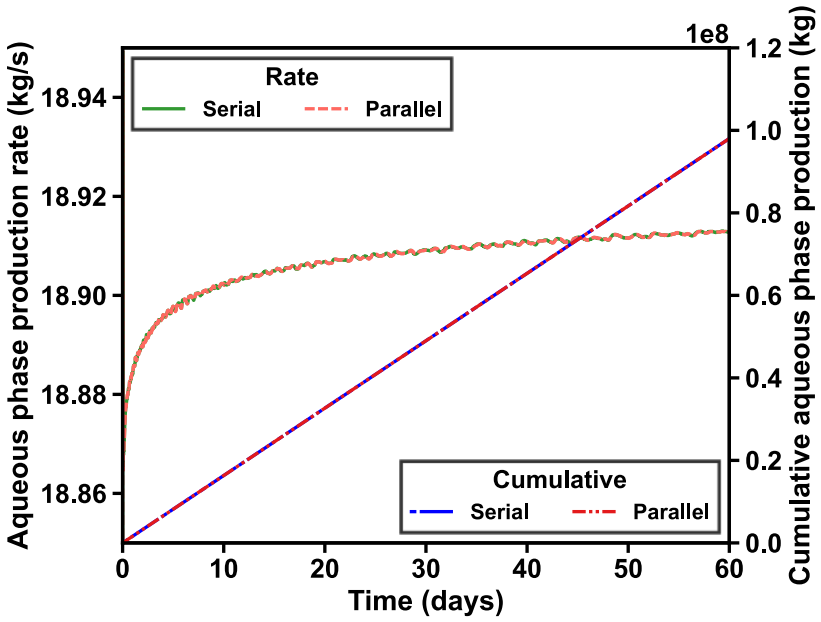

Figure 4.12 The parallelization validation on the production rate and cumulative production of the aqueous phase in Case S2G.

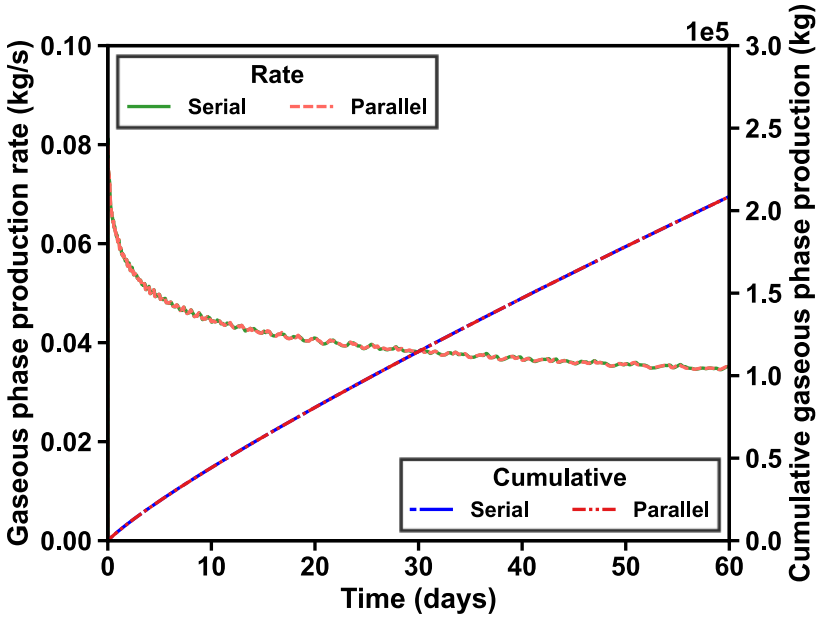

Figure 4.13 The parallelization validation on the production rate and cumulative production of the gaseous phase in Case S2PG.

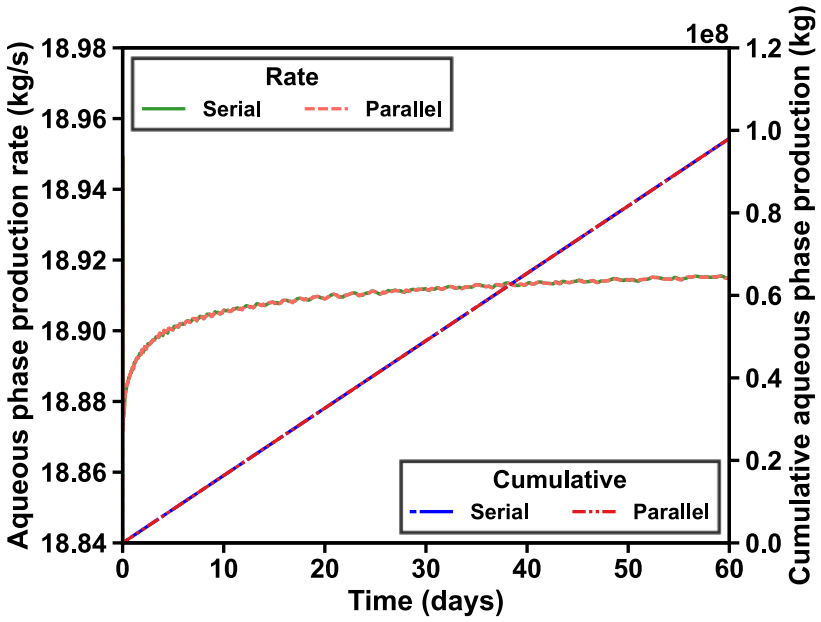

Figure 4.14 The parallelization validation on the production rate and cumulative production of the aqueous phase in Case S2PG.

5. PARALLEL PERFORMANCE

The parallel performance of RGMS, pT+H V1.5, and the coupled pT+H V1.5 and RGM simulator was tested on two platforms: (a) the Mac Pro had an Intel Xeon E5-2697 v2 2.7 GHz processor with 12 cores and 64 GB 1,866 MHz memory, and (b) the Texas A&M University Ada Linux cluster equipped with 856 compute nodes in various configurations using FDR-10 InfiniBand as the interconnect; each computer node used for the simulations in this study comprised 2 Intel Xeon E5-2670 v2 2.5 GHz processors with 10 cores per processor and 64 GB 1,866 MHz memory. Although the processor in the Mac Pro (shared memory system) runs faster than that in the Ada Linux cluster (distributed memory system), the latter has much more processors available for parallel computing. As multiple processors are installed in the Ada Linux cluster, data is transmitted between processors via the interconnect. In addition to different architectures, different compilers and MPI libraries were used as shown in **Table 5.1**.

Table 5.1 Compilers and MPI libraries used on the Ada Linux cluster and Mac Pro.

Programming Language	**Mac Pro**	**Ada Linux Cluster**
FORTRAN	GCC 10.2.0	Intel Fortran Compiler 19.0.5.281
C/ C++	Clang 12.0.0	Intel C++ Compiler 19.0.5.281
MPI	OpenMPI 4.0.5	Intel(R) MPI Library, Version 2018 Update 5

A detailed wall-clock time profile is generated for performance comparisons, including the elapsed time spent on (a) reading the input files t_{inp}, (b) partitioning the domain t_{par}, (c) the simulation cycle computations t_{sim}, (d) estimating the coefficients of the equations t_{equ}, (e) the solution of the matrix equations t_{sol}, (f) updating the unknowns of external elements/nodes t_{upd}, and (g) preparing the output results t_{out}. Thus, the total elapsed time (total simulation time) t_{tot} is

$$t_{tot} = t_{inp} + t_{par} + t_{sim} + t_{out}\,, \tag{5.1}$$

in which

$$t_{sim} = t_{equ} + t_{sol} + t_{upd}\,. \tag{5.2}$$

Usually, t_{upd} is negligible compared to all the other elapsed times.

The speedup associated with parallel codes is a metric used to evaluate the performance of parallel codes, and is defined as

$$s = \frac{t_s}{t_p}\,, \tag{5.3}$$

where t_s is the elapsed time in the serial simulation and t_p is the elapsed time in the parallel simulation. The greater the speedup, the better the parallel performance. Correspondingly, 7 types of speedups can be computed: s_{inp}, s_{par}, s_{sim}, s_{equ}, s_{sol}, s_{upd}, and t_{out}. If the problem is so massive that a single processor cannot solve it, the serial elapsed time is approximated by the product of the smallest number of working processors and its elapsed time.

To evaluate the effects of different partitioning methods in METIS, the parallel performance tests are divided into two groups: (a) a first group with case names ending in "C," denoting a partitioning objective of minimization of the number of edge-cuts (MEC),

and (b) a second group with case names ending with "V," in which the partitioning objective was to minimize the total communication volume (MCV). Note that the speedups of both groups are computed based on the same serial elapsed times because METIS is not involved in the serial simulation. For larger problems that cannot be simulated in serial mode, the serial elapsed time is inferred from the parallel result obtained for the minimum possible number of processors. Additionally, the faster result from two groups (reflecting the two partitioning objectives) is used for computing the estimated elapsed time in the serial simulation.

5.1. Parallel Performance of RGMS

The RGMS tests were limited to a single simulation cycle without continuously updating flow properties either from a flow simulator or the input files. The time for reading files and for writing result outputs can be significant in geomechanics-only simulations. The parallelization mainly improves the performance of the simulation processes, so only t_{sim} including t_{eqn} and t_{sol} are evaluated in RGMS runs. When RGMS is coupled with a flow simulator, the number of simulation cycles is sufficiently large to make t_{sim} dominate.

5.1.1. Problem Description

The validation problems in Section 2.6 were used for testing the parallel performance of RGMS. The initial discretization discussed in that section was substantially refined in order to create relatively large problems. Using uniformly-sized

subdivisions, the number of elements in each direction in the 2D problems (Cartesian and cylindrical) was increased to 2,000, and to 150 in the 3D problem. This resulted in 4,000,000 elements in the 2D problems (Cases G1 and G2 of the 2D Cartesian and cylindrical problems, respectively), and in 3,375,000 elements in the 3D Cartesian problem (Case G3). All the boundary conditions of the validation problems were preserved.

5.1.2. Results

The elapsed times and speedups of Cases G1, G2, and G3 running on the Ada Linux cluster and on the Mac Pro with different numbers of processors N_p are reported.

5.1.2.1. Ada Linux Cluster

Cases G1C, G1V, G2C, G2V, G3C, and G3V were tested on the Ada Linux cluster using N_p = 1, 2, 4, 8, 16, 32, 64, 128, 256, and 512. As shown in **Figure 5.1**, t_{eqn} in Cases G1C and G1V decreases faster than t_{sol} with an increasing number of processors, so the latter takes a larger and larger portion of t_{sim}. Interestingly, the simulation cycle time in Case G1V becomes larger than that in Case G1C using 512 processors. **Figure 5.2** proves the scalability of the equation assembly in both cases, and shows that s_{sol} has a noticeable difference with the partitioning objective in METIS when $N_p \geq 64$, in which case the MEC option is better than MCV when N_p = 512. The detailed simulation cycle times and speedups in Cases G2C and G2V are summarized in **Figures 5.3** and **5.4**, exhibiting the same trends identified in Cases G1C and G1V.

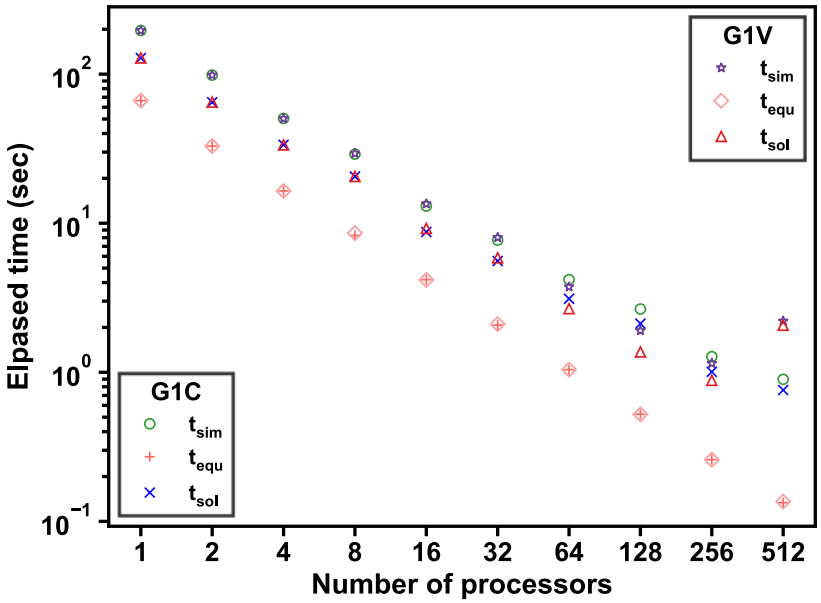

Figure 5.1 The elapsed times of the detailed simulation cycle (setting up equations and matrix solving) in Cases G1C and G1V on the Ada Linux cluster.

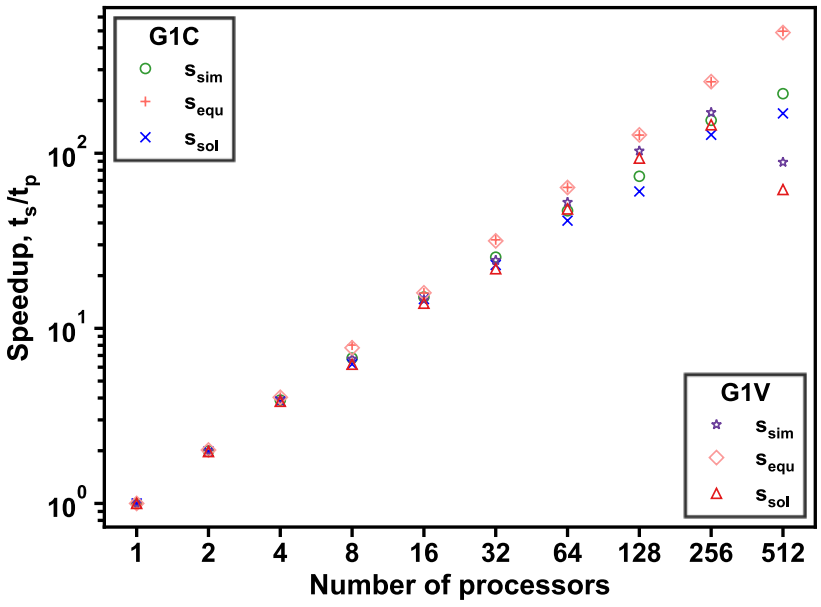

Figure 5.2 The speedups of the detailed simulation cycle (setting up equations and matrix solving) in Cases G1C and G1V on the Ada Linux cluster.

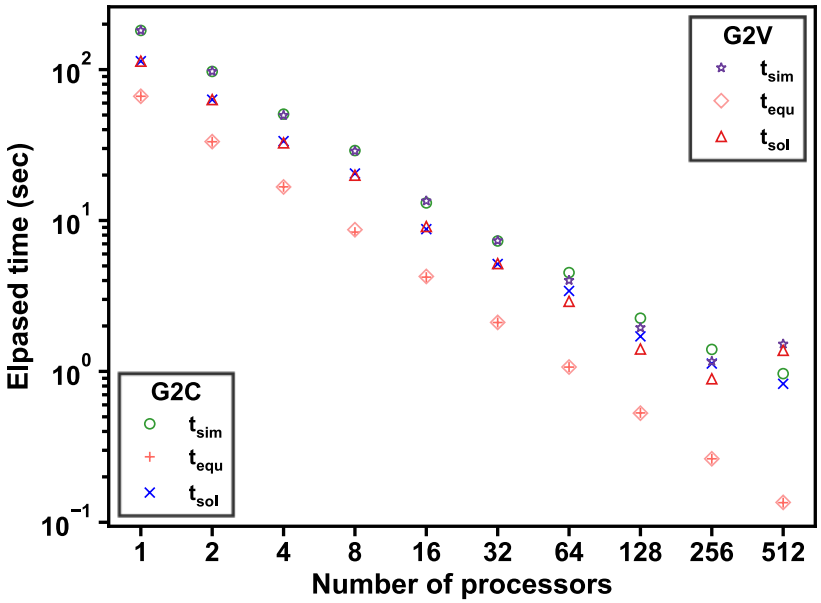

Figure 5.3 The elapsed times of the detailed simulation cycle (setting up equations and matrix solving) in Cases G2C and G2V on the Ada Linux cluster.

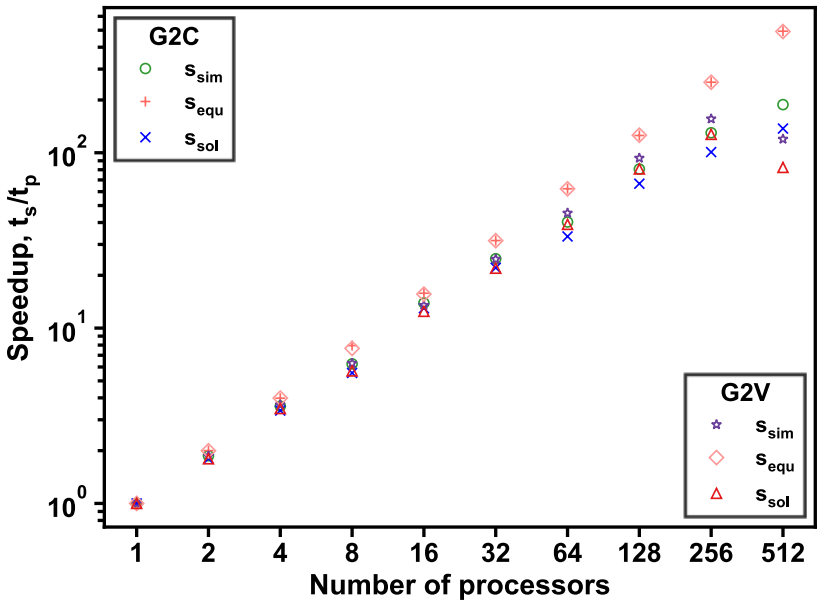

Figure 5.4 The speedups of the detailed simulation cycle (setting up equations and matrix solving) in Cases G2C and G2V on the Ada Linux cluster.

Figure 5.5 compares the simulation cycle time (setting up equations and matrix solving) in the 3D problems of Cases G3C and G3V. t_{sim} is 1,355.89 seconds in the serial simulation; it is reduced to 5.02 seconds in Case G3C and 7.53 seconds in Case G3V when using 512 processors, in which t_{sol} is 1.89 seconds in Case G3C and 5.39 seconds in Case G3V. **Figure 5.6** shows that s_{equ} is very significant and matches the conclusions drawn in the 2D studies. s_{sim} increases significantly when using a large number of processors, and reaches 284.70 in Case G3C and 189.83 in Case G3V when 512 processors are involved, which indicates the MEC option should be used in Case G3 to obtain the optimal s_{sim}.

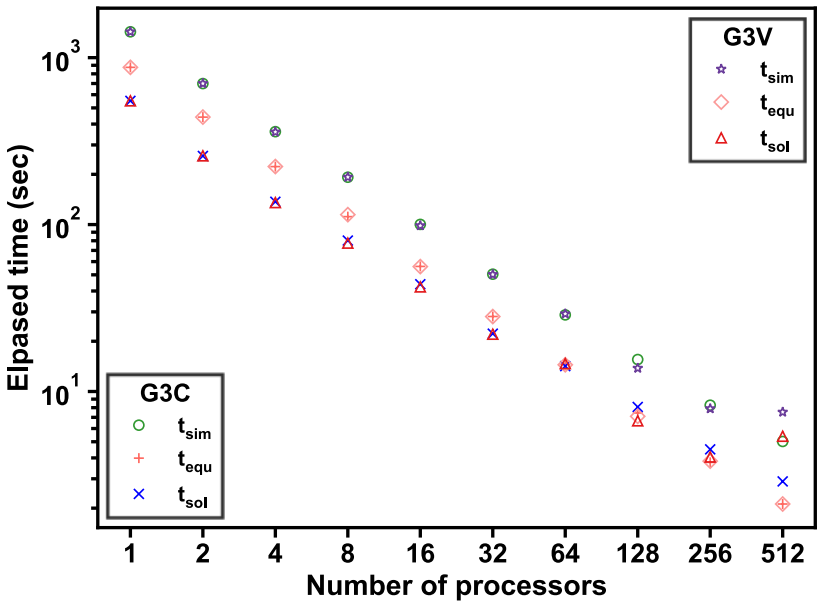

Figure 5.5 The elapsed times of the detailed simulation cycle (setting up equations and matrix solving) in Cases G3C and G3V on the Ada Linux cluster.

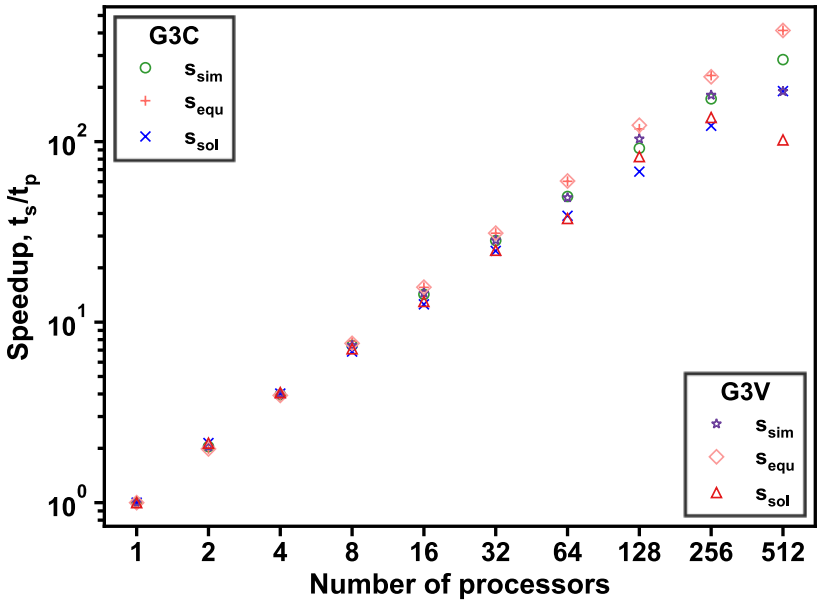

Figure 5.6 The speedups of the detailed simulation cycle (setting up equations and matrix solving) in Cases G3C and G3V on the Ada Linux cluster.

5.1.2.2. Mac Pro

Because the tests on the Ada Linux cluster showed that the partitioning objectives in METIS affect the parallel performance mainly when hundreds of processors are used, it is unnecessary to study their influences on the parallel performance on a Mac Pro with 12 processors. Only Cases G1C, G2C, and G3C were tested on the Mac Pro using N_p = 1, 2, 4, 6, 8, 10, and 12. **Figures 5.7** and **5.8** show the detailed calculation times and corresponding speedups in Case G1C with different numbers of processors. t_{sim} decreases monotonically as the number of processors increases, and t_{sol} is less than t_{eqn} when using no more than 4 processors. As for the speedups, the equation assembly is always more

sensitive to the number of processors than the solving process. When N_p = 12, s_{sim} is 6.19, s_{eqn} is 9.26, and s_{sol} is 4.08.

The detailed simulation cycle times and speedups in Case G2C are presented in **Figures 5.9** and **5.10**. When up to 4 processors are used, the performance is similar to that discussed in Case G1C, with t_{eqn} exceeding t_{sol}. Generally, an improvement in performance is observed when the number of processors increases, although this is not consistent in the case of matrix solving, which shows anomalous and contrary behavior when N_p increases from 6 to 8 and from 10 to 12. This is attributed to the different memory management and processor communication methods between the Ada cluster the Mac Pro desktop system. The maximum s_{sim} is 6.09, which is practically the same as the speedup in Case G1C.

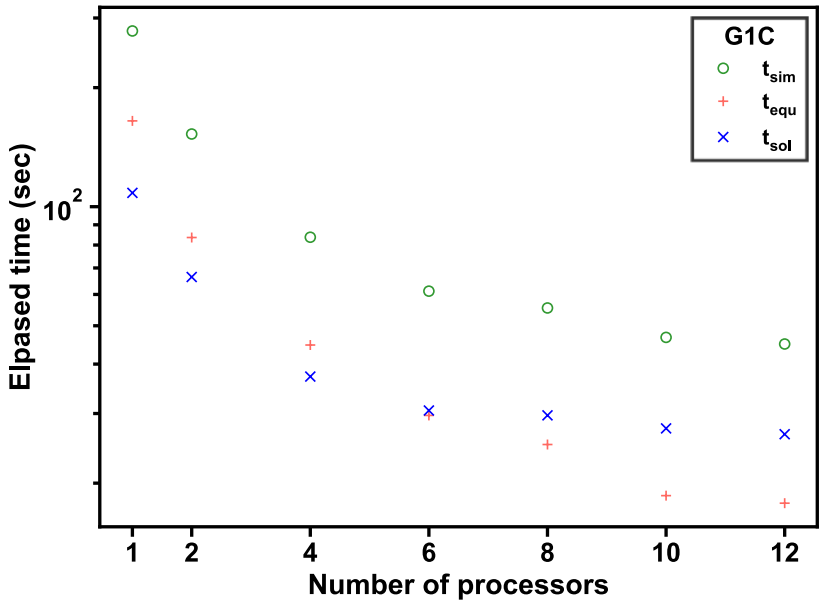

Figure 5.7 The elapsed times of the detailed simulation cycle (setting up equations and matrix solving) in Case G1C on the Mac Pro.

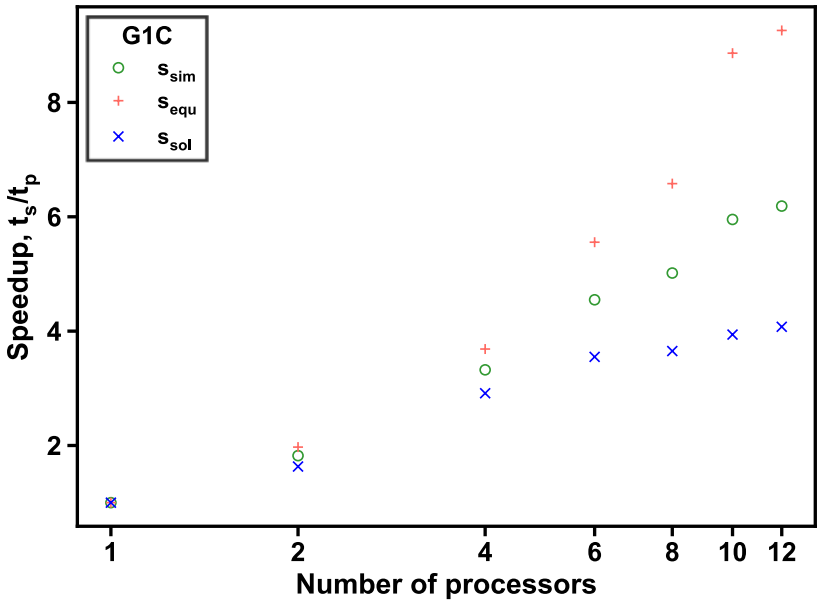

Figure 5.8 The speedups of the detailed simulation cycle (setting up equations and matrix solving) in Case G1C on the Mac Pro.

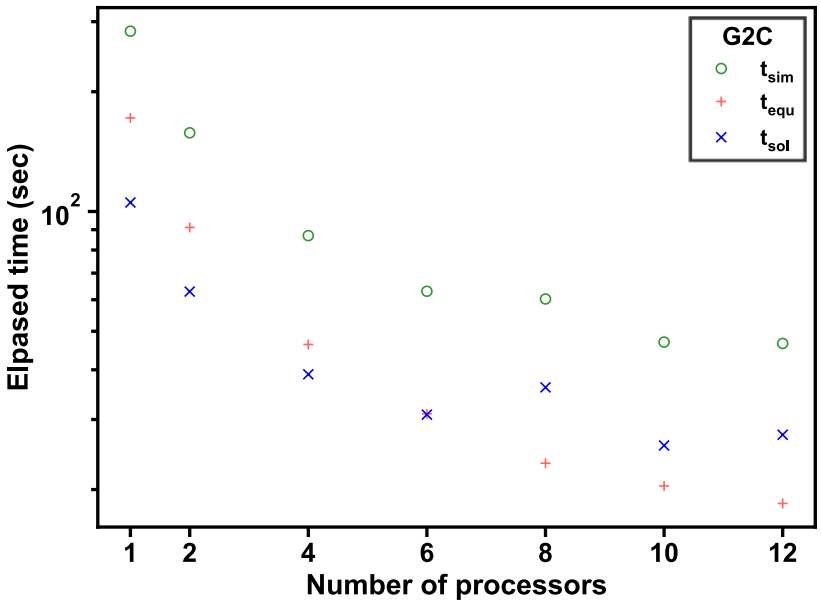

Figure 5.9 The elapsed times of the detailed simulation cycle (setting up equations and matrix solving) in Case G2C on the Mac Pro.

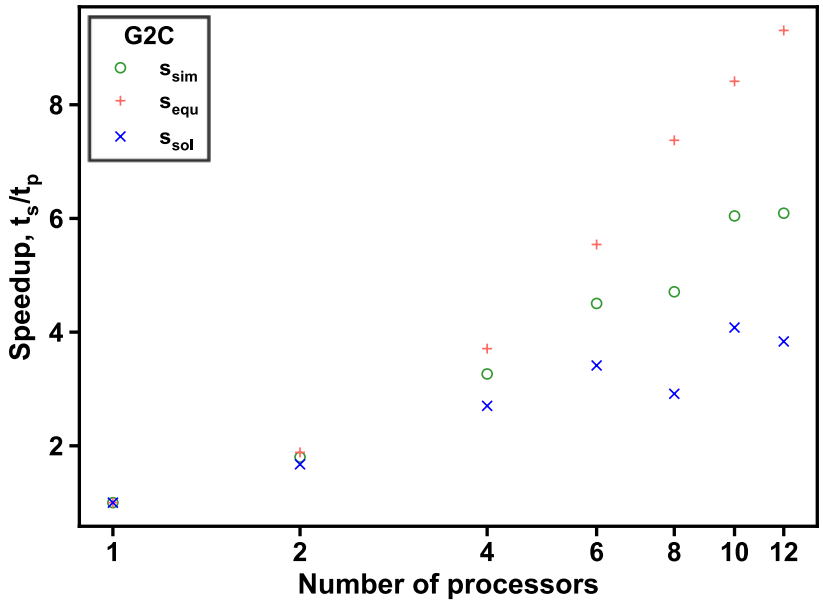

Figure 5.10 The speedups of the detailed simulation cycle (setting up equations and matrix solving) in Case G2C on the Mac Pro.

Figure 5.11 provides the detailed information on the calculation time in the 3D simulation of Case G3C on the Mac Pro. Unlike the 2D results, setting up the equations is consistently the most time-consuming part of the simulation. Compared to the matrix solving process, assembly of the equations can concentrate in the processor and requires less communication between processors, resulting in the higher speedups in **Figure 5.12**. Using 12 processors, the speedups of calculation, setting up equations, and matrix solving are 7.19, 9.11, and 4.56, respectively. Again, as in all Mac Pro cases discussed up to now, t_{sim} decreases monotonically with an increasing number of processors. This was to be expected, given the indications provided by the parallelization performance on the Ada cluster from tests with a much larger number of processors.

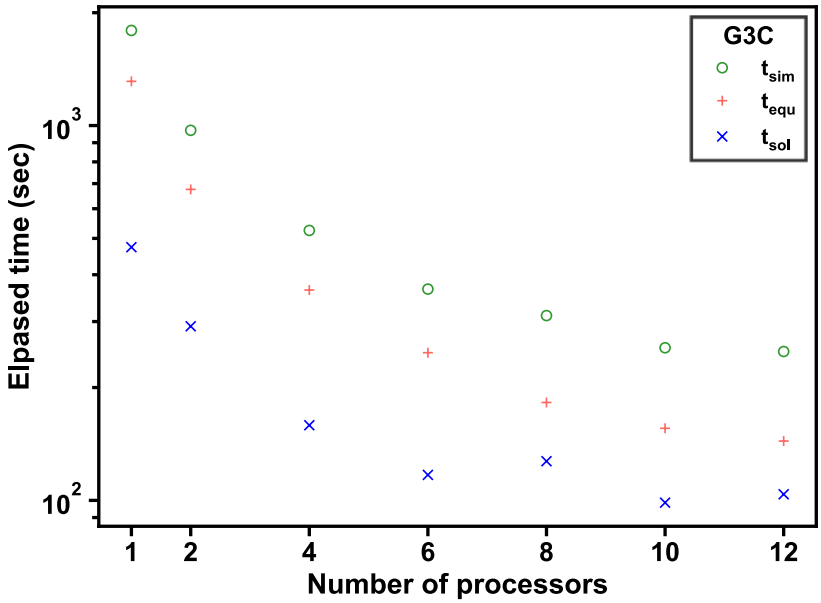

Figure 5.11 The elapsed times of the detailed simulation cycle (setting up equations and matrix solving) in Case G3C on the Mac Pro.

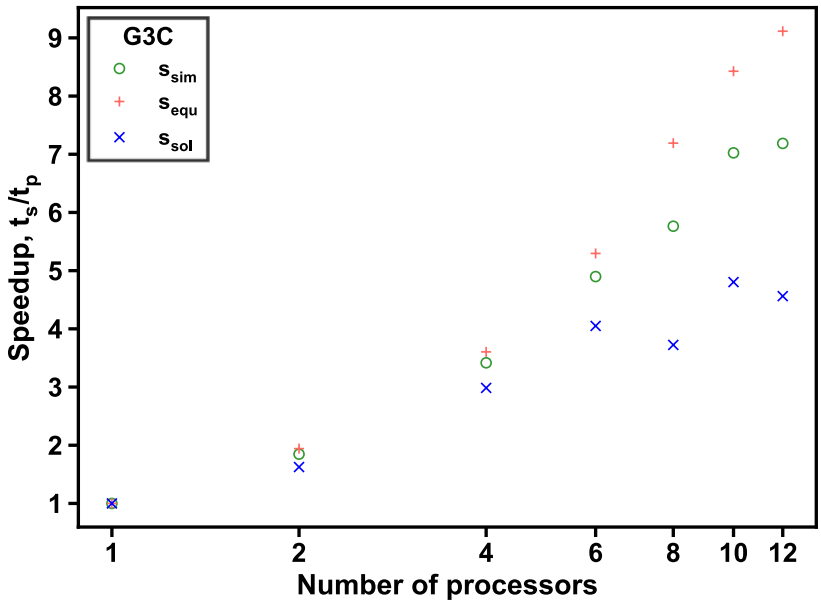

Figure 5.12 The speedups of the detailed simulation cycle (setting up equations and matrix solving) in Case G3C on the Mac Pro.

5.1.3. Summary

The parallel performance of RGMS is satisfactory on the Ada Linux cluster and the Mac Pro. The parallel performance is unaffected by the METIS partitioning objectives when using 64 or fewer processors, but minimization of the number of edge cuts in METIS leads to (a) a consistently better performance for more than 64 processors and (b) the performance continues to improve as the number of processors increases. Note that the elements in the above tests are uniform in size; it is possible that different conclusions can be derived with non-uniform-sized elements, and this issue needs to be further studied.

5.2. Parallel Performance of pT+H V1.5

The parallel performance of pT+H V1.5 was evaluated in the solution of two large-scale problems: (a) Case U1, which was based on the study of a 2D cylindrical (single-well) system in a hydrate deposit at the UBGH2-6 site in the Ulleung basin but involving a finer mesh than that used in the original study of the problem (Moridis et al. 2013), and (b) a 3D Cartesian problem of gas production from an offshore hydrate deposit in the Krishna-Godawari Basin of India that involved over 3.6 million elements (Boswell et al. 2019; Moridis et al. 2019). Both cases were simulated on the Ada Linux cluster using up to 512 processors and on the Mac Pro using up to 12 processors. The same nomenclature and naming conventions that were introduced in the earlier studies applies here.

The abbreviations stated for the geologic system in Section 3.7.1.1 are used in the problem descriptions of Cases U1 and T1. In these simulations, hydrate dissociation/formation was described as an equilibrium reaction, in line with the findings

of Kowalski and Moridis (2007), resulting in 4 equations (3 mass components and heat) per element. In addition, both cases used the pseudo-porous medium mentioned in Section 3.7.1.2 to approximate the flow in the wellbore. The initialization processes for both cases were the same as discussed in Section 3.7.1.5.

5.2.1. Description of the Two-Dimensional Cylindrical Problem in Case U1

5.2.1.1. System Description and Geometry

The geologic model and the associated computational domain in Case U1 comprised three major units (OB, the hydrate deposit unit, and UB). The hydrate deposit unit consisted of five layers of hydrate-bearing sandy sediments and four hydrate-free interlayers of soft oceanic muds. **Figure 5.13** shows the thickness of each layer.

	Δz (m)
Sea	2157.00
Overburden (OB)	140.00
Hydrate Deposit	12.67
Underburden (UB)	347.43

Hydrate Deposit	Δz (m)
Hydrate (H1)	1.01
Mud (M1)	4.38
Hydrate (H2)	1.15
Mud (M2)	2.23
Hydrate (H3)	0.37
Mud (M3)	0.45
Hydrate (H4)	0.74
Mud (M4)	1.52
Hydrate (H5)	0.82

Figure 5.13 The geological model with layered geometries of Case U1.

5.2.1.2. Well Description

The vertical production well at the center of the cylindrical domain of this problem was perforated from the top of the H1 layer to the bottom of the H5 layer. The well was produced at a constant bottomhole pressure of P_{bh} = 9 MPa, which was attained by lowering the pressure at the well from its initial/discovery level at a rate of 0.5 MPa/hr.

5.2.1.3. Domain Discretization

The 2D domain was finely discretized into 752 subdivisions in the radial direction and 322 subdivisions in the vertical direction, resulting in a total of 242,144 elements. The Δr subdivisions were very fine along the radial direction (0.10 m for $r_w < r \leq 15$ m, 0.20 m for 15 m $\leq r \leq 30$ m), increased logarithmically from r = 30 m to r_{max} = 600 m. The Δz subdivisions were between 0.05 and 0.1 m within the hydrate deposit, and larger (but not exceeding 0.5 m) in the hydrate-free (and more forgiving) OB and UB. **Figure 5.14** presents the mesh used in Case U1 and **Figure 5.15** presents the mesh in the hydrate accumulation near the wellbore. The treatment of the hydrate dissociation/formation as an equilibrium reaction involved 4 equations per element, resulting on a total of about 960,000 simultaneous equations.

5.2.1.4. System Properties

Table 5.2 presents the hydraulic and thermal properties in Case U1. **Table 5.3** shows the parameters used for the simplified geomechanical model.

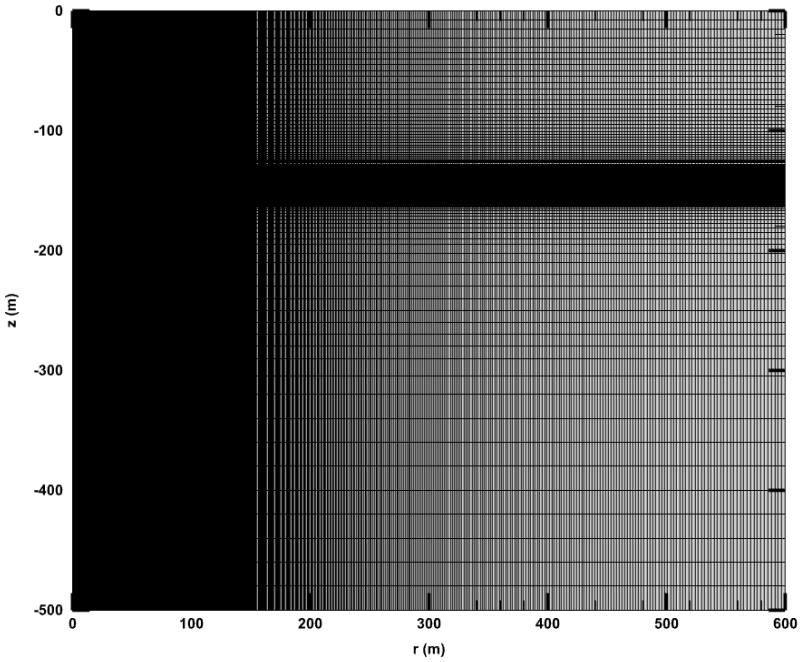

Figure 5.14 Mesh used in the problem of Case U1.

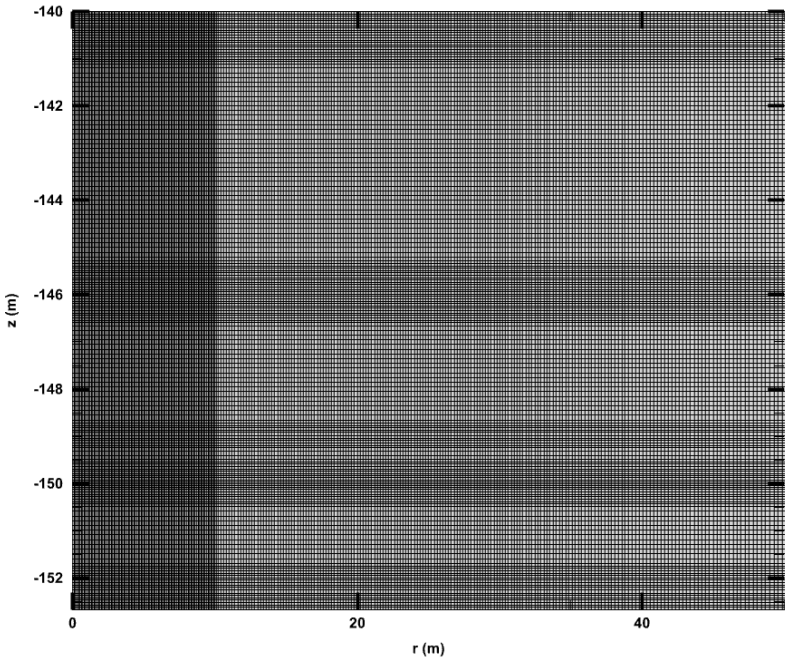

Figure 5.15 Mesh in the hydrate accumulation near the well used in the problem of Case U1.

Table 5.2 Properties of the hydrate deposit in Case U1.

Initial pressure at top boundary (P_T)	22.261 MPa
Pressure distribution	Hydrostatic
Initial temperature at top boundary (T_T)	0.482 °C
Initial temperature at bottom boundary (T_B)	60.0 °C
Gas composition	100% CH_4
Initial saturations of HBLs	$S_H = 0.65$
Intrinsic permeabilities of HBLs	$k_r = 1.78 \times 10^{-13}$ m^2; $k_z = k_r$
Porosity ϕ of HBLs	0.45
Intrinsic permeabilities of MLs	$k_r = 2.0 \times 10^{-16}$ m^2; $k_z = k_r$
Porosity ϕ of MLs	0.67
Intrinsic permeabilities of OB	$k_r = 2.0 \times 10^{-16}$ m^2; $k_z = k_r$
Porosity ϕ of OB	0.65
Intrinsic permeabilities of UB	$k_r = 2.0 \times 10^{-16}$ m^2; $k_z = k_r$
Porosity ϕ of UB	0.50
Dry thermal conductivity (all layers)	$k_{\theta d} = 1$ W·m^{-1}·K^{-1}
Wet thermal conductivity of HBLs	$k_{\theta w} = 1.45$ W·m^{-1}·K^{-1}
Wet thermal conductivity of MLs, OB, UB	$k_{\theta w} = 1.00$ W·m^{-1}·K^{-1}
Specific heat C_R (all layers)	800 J kg^{-1}·K^{-1}
Grain density ρ_R of HBLs	2650 kg·m^{-3}
Grain density ρ_R of MLs	2630 kg·m^{-3}
Grain density ρ_R of OB	2620 kg·m^{-3}

Table 5.2 Continued.

Grain density ρ_R of UB	2660 kg·m^{-3}
Composite thermal conductivity model	$\overline{k_\theta} = k_{\theta d} + \left(\sqrt{S_A} + \sqrt{S_H}\right)\left(k_{\theta w} - k_{\theta d}\right) + \phi S_I k_{\theta I}$
Relative permeability model	$k_{rA} = \max\left\{0, \min\left\{\left[\frac{S_A - S_{irA}}{1 - S_{irA}}\right]^n, 1\right\}\right\};$ $k_{rG} = \max\left\{0, \min\left\{\left[\frac{S_G - S_{irG}}{1 - S_{irA}}\right]^{n_G}, 1\right\}\right\};$ $k_{rH} = 0$
S_{irA}, S_{irG}, n, n_G of HBLs	0.25; 0.01; 3.50; 2.50
S_{irA}, S_{irG}, n, n_G of MLs, OB, UB	0.55; 0.05; 5.00; 3.00
Capillary pressure model	$P_{cap} = -P_0\left[\left(S^*\right)^{-\frac{1}{\lambda}} - 1\right]^{1-\lambda}$ $S^* = \frac{S_A - S_{irA}}{S_{mxA} - S_{irA}}$
λ, P_0, S_{irA}, S_{mxA} of HBLs	0.45; 10^4 Pa; 0.19; 1.0
λ, P_0, S_{irA}, S_{mxA} of MLs, OB, UB	0.15; 10^5 Pa; 0.49; 1.0
Empirical permeability reduction factor γ (all layers)	5.0

Table 5.3 Geomechanical parameters using the simplified geomechanical model of the hydrate deposit in Case U1.

α_{PL}	2.0×10^{-9} Pa^{-1}
$S_{S_{max}}$	0.40
α_{PU}	1.0×10^{-8} Pa^{-1}

Table 5.3 Continued.

$S_{S_{\min}}$	0.15
δ	0.015

5.2.2. Case U1: Results and Discussion

The simulations were run for a total of 100 time steps, and all the simulations covered the same length of the production period. The elapsed times of the entire simulation and of the various components/activities in the simulation were recorded and the corresponding speedups were calculated.

5.2.2.1. Ada Linux Cluster

Cases U1C and U1V were tested on the Ada Linux cluster using N_p = 1, 2, 4, 8, 16, 32, 64, 128, 256, and 512. The elapsed times of the total simulation and simulation cycles in Cases U1C and U1V are shown in **Figure 5.16**. The elapsed time expended on the simulation cycles t_{sim} (see Eqs. [5.1] and [5.2]) always comprises the majority of the total execution time t_{tot} regardless of the partitioning option in METIS. Some oscillations about the clear trends notwithstanding, t_{sim} in both Cases U1C and U1V are very similar. Additionally, t_{tot} in Case U1C appears to decrease in a more consistent manner and at a relatively stable rate compared to that in Case U1V. A significant observation from **Figure 5.16** is that t_{tot} appears to be a monotonic function of the number of processors, decreasing at a consistently steep rate with an increasing N_p. **Figure 5.17** compares the elapsed time

spent on setting up equations t_{equ} and matrix solving t_{sol} in Cases U1C and U1V, and shows that the partitioning option mainly influences the matrix-solving time t_{sol}.

The total and simulation cycling speedups (s_{tot} and s_{sim}, respectively) are presented in **Figure 5.18**, and the computed speedups of setting up equations and matrix solving (s_{equ} and s_{sol}, respectively) are shown in **Figure 5.19**. When 512 processors are used, s_{tot} are 162.81 in Case U1C and 174.25 in Case U1V, *i.e.*, the option of MCV in METIS appears to confer a modest speed advantage in parallel simulations; s_{sim} are 204.72 in Case U1C and 218.59 in Case U1V; s_{equ} are 490.08 in Case U1C and 602.46 in Case U1V, indicating that the associated operations are highly parallelizable; and the speedups of matrix solving are 191.30 in Case U1C and 202.99 in Case U1V. Because of the proximity in the values of t_{tot} and t_{sim} (t_{sim} being by far the dominant component of t_{tot}), the total speedups approach the simulation cycling speedups. The general conclusion from these results is the consistent and monotonic improvement in the parallel performance (as quantified by the reduction in the execution times and the increase in the speedups) as N_p increases.

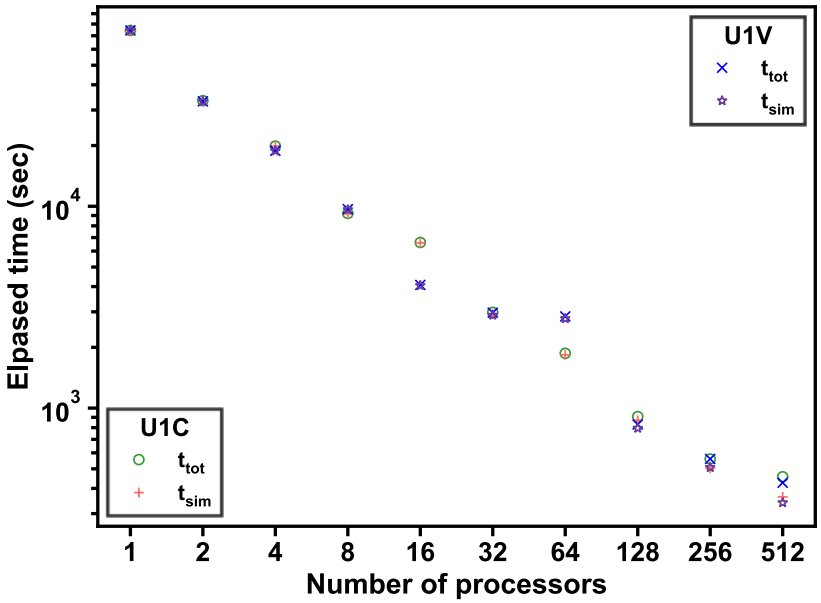

Figure 5.16 The elapsed times of the total simulation and simulation cycles in Cases U1C and U1V on the Ada Linux cluster.

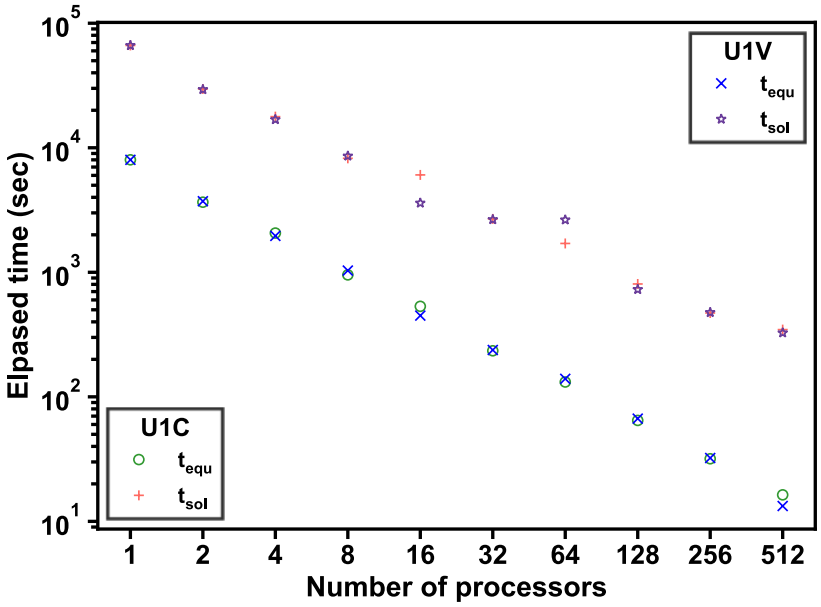

Figure 5.17 The elapsed times of setting up equations and matrix solving in Cases U1C and U1V on the Ada Linux cluster.

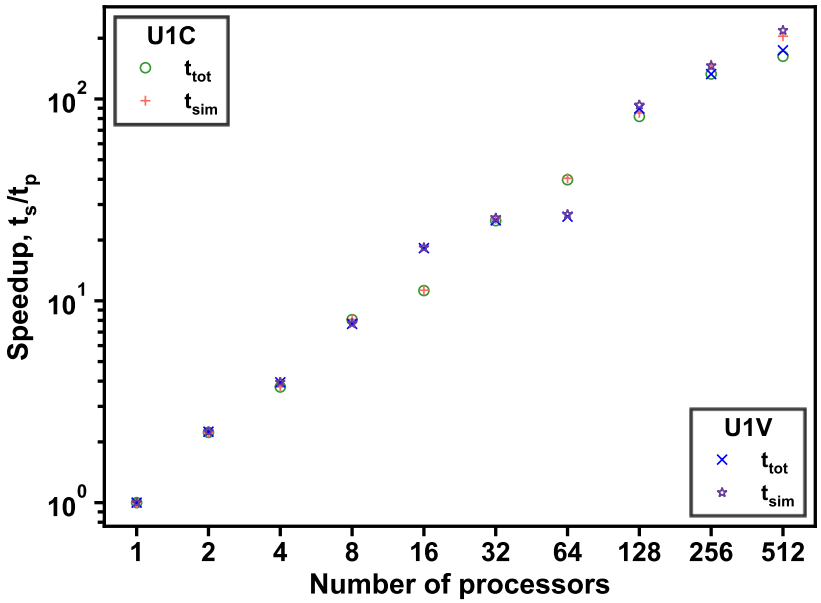

Figure 5.18 The speedups of the total simulation and simulation cycles in Cases U1C and U1V on the Ada Linux cluster.

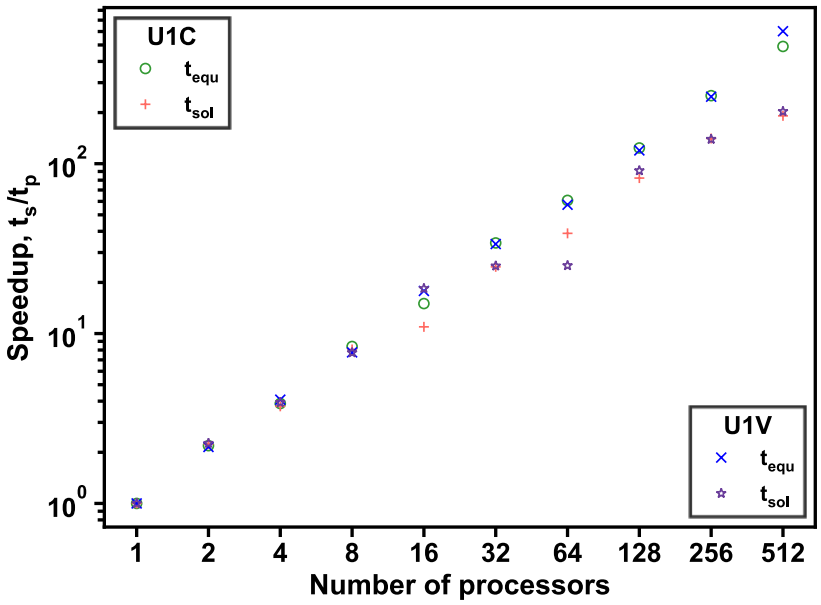

Figure 5.19 The speedups of setting up equations and matrix solving in Cases U1C and U1V on the Ada Linux cluster.

5.2.2.2. Mac Pro

For the reason discussed in Section 5.1.2.2, the testing of the parallel performance of the pT+H V1.5 on a Mac Pro was limited to Case U1C, and involved N_p = 1, 2, 4, 6, 8, 10, and 12. **Figure 5.20** shows that t_{tot} and t_{sim} decrease consistently with an increasing N_p to a maximum of 8; the trend is interrupted for $N_p > 8$, and the worst performance occurs when N_p =10. This is further demonstrated in **Figure 5.21**, which shows deterioration of the parallel performance, as quantified by the time t_{sol} expended in the solution of the matrix equation for $N_p > 6$. This is attributed to the memory management and processor communications in the shared memory system of the Mac Pro, in addition to the nature of matrix solving that is not amenable to easy parallelization (already observed in the Ada simulations); conversely, setting up the equations is an eminently parallelizable operation, and this reflected in the continuous decline of t_{equ} with an increasing N_p in **Figure 5.21**. Of particular interest is the observation that t_{sol} is always dominant in the Ada Linux cluster simulations, but not on the Mac Pro when N_p is low. In addition to potential reasons that have already been discussed, different compilers and MPI libraries used in these two systems can be the potential reason leading to the above results. As expected from the results in **Figure 5.20**, the total and simulation cycling speedups in **Figure 5.22** reach peaks when N_p = 8, and the speedup of matrix solving in **Figure 5.23** peaks for N_p = 6 (as **Figure 5.21** suggests). These results indicate that the excellent parallel performance of setting up the equations can help improve the overall parallel performance even when the speedup of the matrix solving process no longer increases.

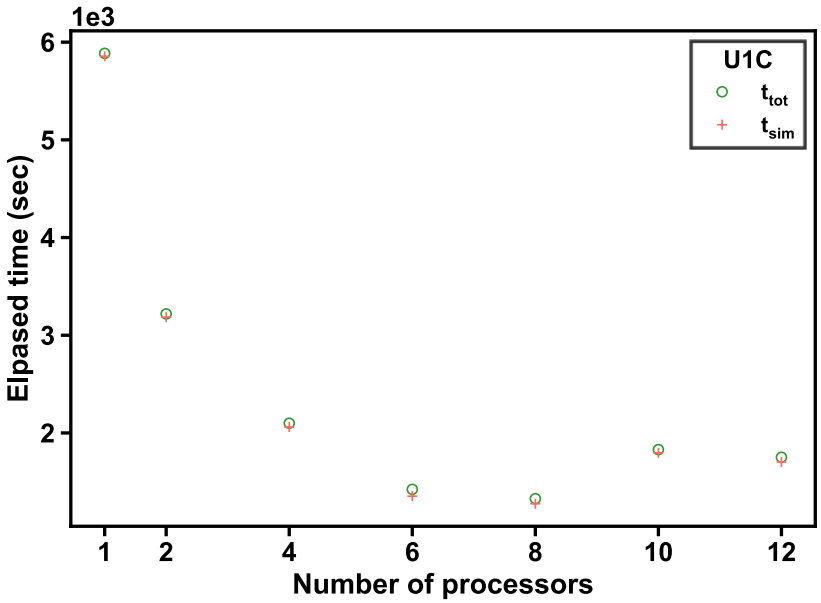

Figure 5.20 The elapsed times of the total simulation and simulation cycles in Case U1C on the Mac Pro.

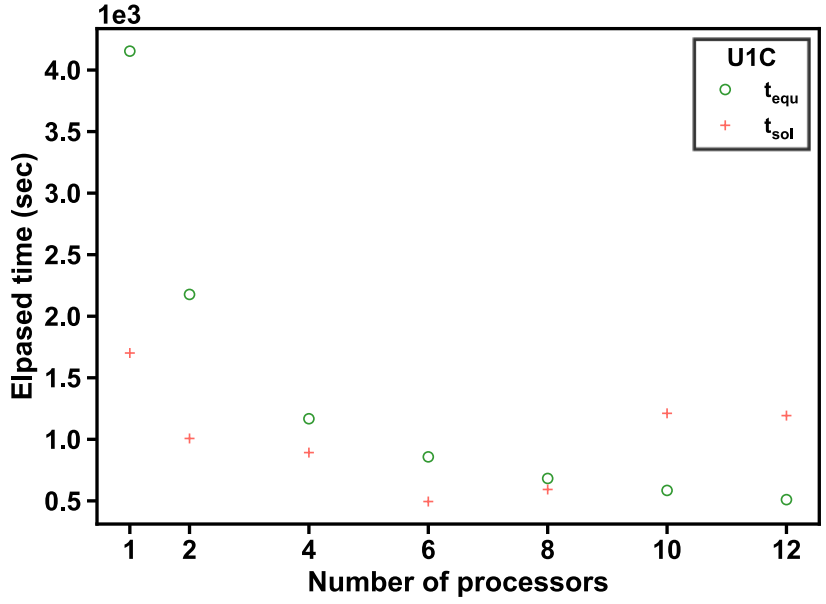

Figure 5.21 The elapsed times of setting up equations and matrix solving in Case U1C on the Mac Pro.

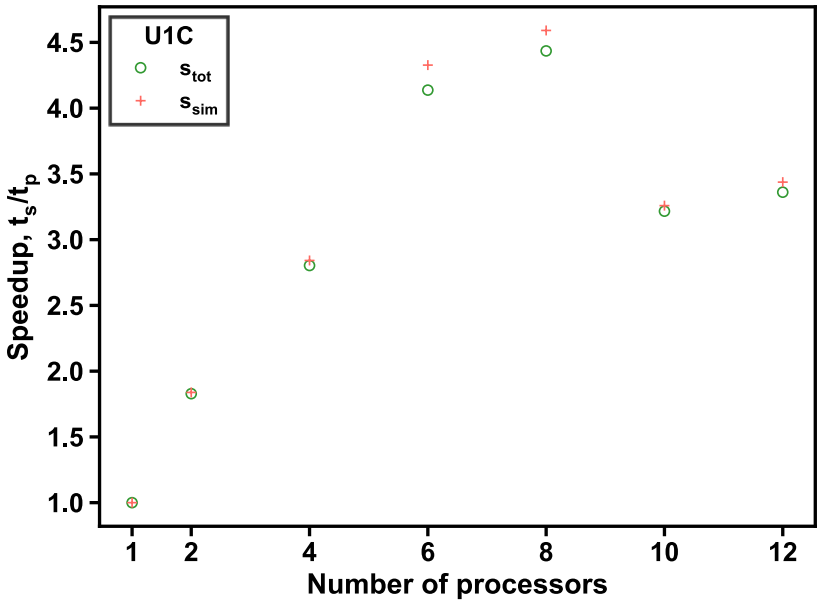

Figure 5.22 The speedups of the total simulation and simulation cycles in Case U1C on the Mac Pro.

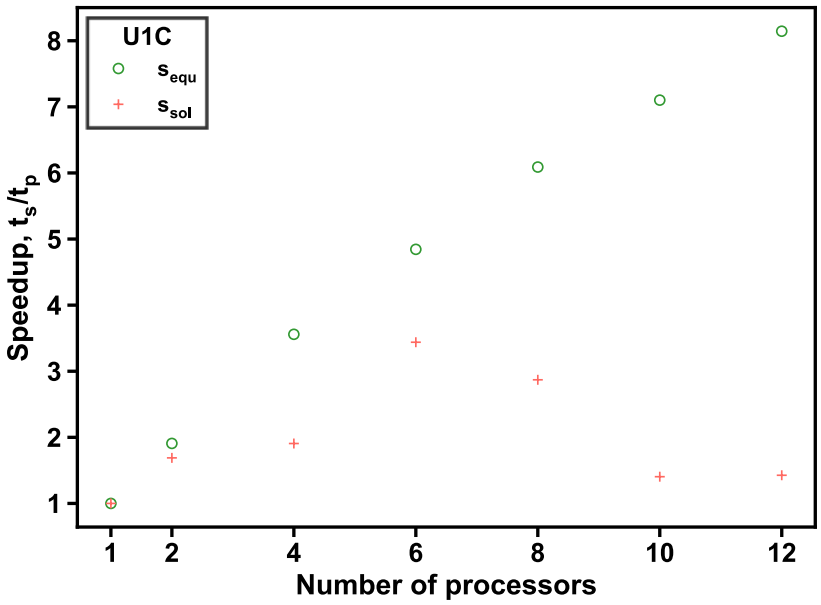

Figure 5.23 The speedups of setting up equations and matrix solving in Case U1C on the Mac Pro.

5.2.3. Description of the Three-Dimensional Cartesian Problem in Case T1

5.2.3.1. System Description and Geometry

The 3D domain in the T1 study comprises the 3 major units (OB, the hydrate accumulation, and UB) shown in the geologic model of **Figure 5.24**, which also shows the unit thicknesses and provides a detailed description of the layering within the hydrate accumulation. Thus, the hydrate accumulation is composed of 25 layers of hydrate-bearing sandy sediments, 14 hydrate-free interlayers of soft oceanic muds, and 10 hydrate-free (sandy) aquifer layers. The overall dimensions of this study were 425 m in the *x*-direction, 200 m in the *y*-direction, and 600 m in the *z*-direction. The same nomenclature and name convention discussed in earlier sections apply here.

	Δz (m)
Overburden (OB)	214.91
Hydrate Deposit	53.60
Underburden (UB)	331.5

Hydrate Deposit	Δz (m)
Hydrate (H1)	1.80
Aquifer (A1)	0.80
Hydrate (H2)	1.30
Aquifer (A2)	0.50
Hydrate (H3)	1.10
Aquifer (A3)	0.20
Hydrate (H4)	0.80
Aquifer (A4)	0.60
Hydrate (H5)	3.30
Mud (M1)	0.50
Hydrate (H6)	1.30
Mud (M2)	0.40
Hydrate (H7)	0.30
Mud (M3)	0.20
Hydrate (H8)	0.40
Mud (M4)	0.20
Hydrate (H9)	0.50
Mud (M5)	0.20
Hydrate (H10)	1.30
Aquifer (A5)	1.10
Hydrate (H11)	0.80
Aquifer (A6)	0.30
Hydrate (H12)	1.10
Aquifer (A7)	0.40
Hydrate (H13)	0.70
Aquifer (A8)	1.30
Hydrate (H14)	2.60
Mud (M9)	1.20
Hydrate (H15)	1.30
Aquifer (A10)	6.90
Hydrate (H16)	1.70
Mud (M6)	0.60
Hydrate (H17)	2.30
Mud (M7)	0.40
Hydrate (H18)	0.50
Mud (M8)	0.40
Hydrate (H19)	0.50
Mud (M9)	0.40
Hydrate (H20)	1.20
Mud (M10)	0.40
Hydrate (H21)	1.40
Mud (M11)	0.60
Hydrate (H22)	1.50
Mud (M12)	2.00
Hydrate (H23)	0.80
Mud (M13)	0.40
Hydrate (H24)	1.20
Mud (M14)	1.40
Hydrate (H25)	2.50

Figure 5.24 The geological model with layered geometries of Case T1.

Moridis et al. (2019) first investigated the gas production potential of this hydrate accumulation during (a) a long-term production test involving a single vertical well in a cylindrical 2D domain and (b) a long-term full production (basin-wide) system involving a large number of vertical wells. Case T1 differs from the earlier Moridis et al. (2019) study in that

(a) it investigates the gas production potential of this hydrate deposit using a vertical two-well system, of which one is used for fluid production and the second for warm water injection, in an effort to augment the depressurization-induced dissociation at the production well by thermal dissociation at the injection well, further enhanced by the presence of salt (a known inhibitor) in the injected water, and

(b) the two-well configuration in Case T1 necessitates the use of a 3D Cartesian system that describes half the domain involved in the production study because of symmetry about the vertical plane passing by the center axes of the two vertical wells.

5.2.3.2. Well Description

The two vertical wells were perforated from the top to the bottom of the reservoir: (a) the first well (production well) produced reservoir fluids at a constant bottomhole pressure P_{bh} = 3 MPa located at (x, y) = (200 m, 0.025 m), and (b) the second well (injection well) injected 60 °C pure H_2O at a constant mass flow rate $Q_{w,inj}$ = 1.93 kg·s^{-1} and NaCl (the inhibitor) at a constant mass flow rate $Q_{i,inj}$ = 0.07 kg·s^{-1} located at (x, y) = (225 m, 0.025 m), with the combination of the two injectates representing ocean water with a typical salinity of 3.5%.

5.2.3.3. Domain Discretization

The 3D domain in this study was finely discretized into 224 subdivisions in the *x*-direction, 70 subdivisions in the *y*-direction, and 231 subdivisions in the *z*-direction, leading to a total of 3,622,080 elements. **Figure 5.25** shows the discretized domain and the higher resolutions at the locations of expected intense/active processes: the two wells and the hydrate-accumulations. The lengths of subdivisions in all directions in the vicinity of the two wellbores were very small: (a) $0.1 \leq \Delta x \leq 0.25$ m, (b) $0.1 \leq \Delta y \leq 0.25$ m, and (c) $0.15 \leq \Delta z \leq 0.45$ m. This discretization, and the assumption of equilibrium dissociation in the presence of salt, resulted in about 14,480,000 simultaneous equations.

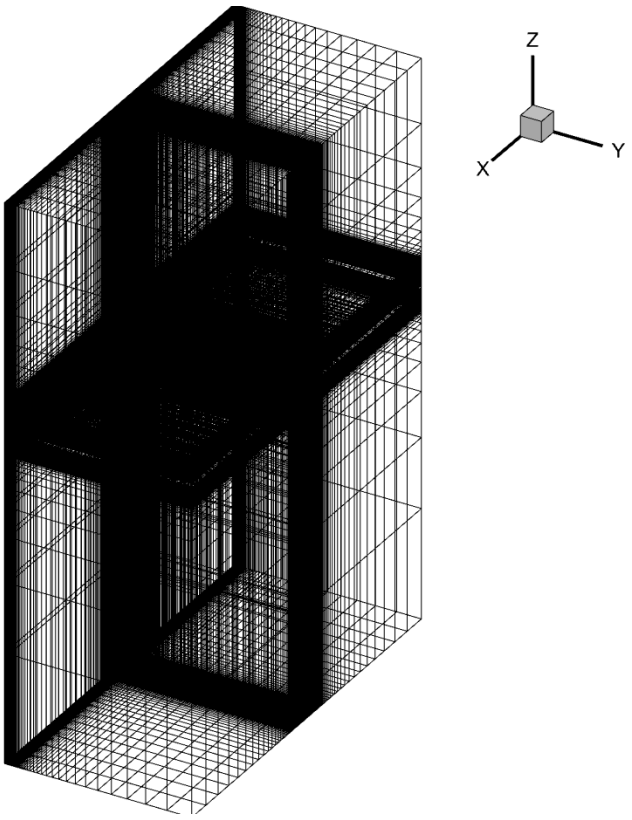

Figure 5.25 Mesh used in the problem of Case T1.

5.2.3.4. System Properties

Table 5.4 summarizes the hydraulic and thermal properties in Case T1. **Table 5.5** presents the parameters used for the simplified geomechanical model.

Table 5.4 Properties of the hydrate deposit in Case T1.

Initial pressure at top boundary (P_T)	25.45 MPa
Pressure distribution	Hydrostatic
Initial temperature at top boundary (T_T)	3.46 °C
Initial temperature at bottom boundary (T_B)	38.42 °C
Gas composition	100% CH_4
Initial saturations of HBLs	$S_H = 0.75$
Intrinsic permeabilities of HBLs	$k_h = 1.0 \times 10^{-11}$ m^2; $k_z = k_h$
Porosity ϕ of HBLs	0.45
Intrinsic permeabilities of MLs	$k_h = 1.0 \times 10^{-17}$ m^2; $k_z = k_h$
Porosity ϕ of MLs	0.45
Intrinsic permeabilities of ALs	$k_h = 1.0 \times 10^{-11}$ m^2; $k_z = k_h$
Porosity ϕ of ALs	0.45
Intrinsic permeabilities of OB	$k_h = 1.0 \times 10^{-17}$ m^2; $k_z = k_h$
Porosity ϕ of OB	0.44
Intrinsic permeabilities of UB	$k_h = 1.0 \times 10^{-17}$ m^2; $k_z = k_h$
Porosity ϕ of UB	0.45
Dry thermal conductivity (all layers)	$k_{\theta d} = 0.3$ W·m^{-1}·K^{-1}

Table 5.4 Continued.

Wet thermal conductivity (all layers)	$k_{\theta w}$ = 1.76 W·m^{-1}·K^{-1}
Specific heat C_R (all layers)	1000 J kg^{-1}·K^{-1}
Grain density ρ_R	2700 – 2750 kg·m^{-3}
Composite thermal conductivity model	$\overline{k_\theta} = k_{\theta d} + \left(\sqrt{S_A} + \sqrt{S_H}\right)\left(k_{\theta w} - k_{\theta d}\right) + \phi S_I k_{\theta I}$
Relative permeability model	$k_{rA} = \max\left\{0, \min\left\{\left[\frac{S_A - S_{irA}}{1 - S_{irA}}\right]^n, 1\right\}\right\}$; $k_{rG} = \max\left\{0, \min\left\{\left[\frac{S_G - S_{irG}}{1 - S_{irA}}\right]^{n_G}, 1\right\}\right\}$; $k_{rH} = 0$
***S_{irA}*, *S_{irG}*, *n*, *n_G* of HBLs**	0.10; 0.01; 3.855; 3.855
***S_{irA}*, *S_{irG}*, *n*, *n_G* of MLs**	0.90; 0.03; 3.500; 2.500
***S_{irA}*, *S_{irG}*, *n*, *n_G* of ALs**	0.10; 0.03; 3.855; 3.855
***S_{irA}*, *S_{irG}*, *n*, *n_G* of OB**	0.90; 0.05; 3.500; 2.500
***S_{irA}*, *S_{irG}*, *n*, *n_G* of UB**	0.90; 0.05; 5.500; 4.500
Capillary pressure model	$P_{cap} = -P_0\left[\left(S^*\right)^{-\frac{1}{\lambda}} - 1\right]^{1-\lambda}$; $S^* = \frac{S_A - S_{irA}}{S_{mxA} - S_{irA}}$
***λ*, *P_0*, *S_{irA}*, *S_{mxA}* of HBLs**	0.45; 1 × 10^4 Pa;0.099; 1.000
***λ*, *P_0*, *S_{irA}*, *S_{mxA}* of MLs**	0.45; 1 × 10^5 Pa;0.899; 1.000
***λ*, *P_0*, *S_{irA}*, *S_{mxA}* of ALs**	0.45; 1 × 10^5 Pa;0.099; 1.000
***λ*, *P_0*, *S_{irA}*, *S_{mxA}* of OB**	0.45; 5 × 10^5 Pa;0.899; 1.000

Table 5.4 Continued.

λ, P_0, S_{irA}, S_{mxA} **of UB**	0.45; 5×10^5 Pa;0.899; 1.000
Empirical permeability reduction factor γ	8.0 (HBLs); 6.0 (MLs, ALs, OB, UB)

Table 5.5 Geomechanical parameters using the simplified geomechanical model of the hydrate deposit in Case T1.

α_{PL}	5.0×10^{-9} Pa^{-1}
$S_{S_{\max}}$	0.40
α_{PU}	1.0×10^{-8} Pa^{-1}
$S_{S_{\min}}$	0.15
δ	0.015

5.2.4. Case T1: Results and Discussion

The parallel performance in the solution of Case T1 was tested in simulations limited to 50 timesteps that all covered the same production period. The associated t_{tot} and t_{sim} (which include t_{equ} and t_{sol}, see Eqs. [5.1] and [5.2]) were recorded, and the related speedups were computed and compared. The size of the problem in Case T1 was too large to be solved in a serial simulation, so the serial elapsed time could not be recorded and had to be estimated by other means: it was based on results from simulation conducted with the smallest possible number of processors, namely 16 on the Ada Linux cluster and 2 on the Mac Pro. Thus, the serial elapsed times were estimated as $16t_{p,16}$ on the Ada Linux cluster and $2t_{p,2}$ on the Mac Pro, where $t_{p,j}$ were the recorded times of parallel execution

with $N_p = j$. Tests with the two different METIS partitioning options were simulated on the Ada Linux cluster, and the shortest $t_{p,16}$ of the two (corresponding to Case T1C) was used to approximate the serial elapsed times.

5.2.4.1. Ada Linux Cluster

Cases T1C and T1V were tested on the Ada Linux cluster using N_p = 16, 32, 64, 128, 256, and 512. When N_p = 128, the t_{tot} and t_{sim} times corresponding to Case T1V in **Figure 5.26** are obviously smaller than those in Case T1C because its major two constituents (*i.e.*, t_{equ} and t_{sol}, see Eqs. [5.1] and [5.2]) that are shown in **Figure 5.27** are accordingly smaller. When N_p = 512, t_{sol} in Case T1C is almost half of that in Case T1V. These results, and those from the variants in Case U1, indicate that the MEC option in the METIS domain decomposition process appears to be the best option in most cases. As can be seen in **Figure 5.28**, (a) the maximum total speedups in Cases T1C and T1V are 341.67 and 229.93, respectively, and (b) the maximum speedups of simulation cycles in Case T1C and T1V are 601.96 and 347.39, respectively. In **Figure 5.29**, the maximum speedup of setting up equations in Cases T1C and T1V are 538.37 and 468.43, respectively, and the maximum speedups of matrix solving in Cases T1C and T1V are 632.72 and 315.34, respectively.

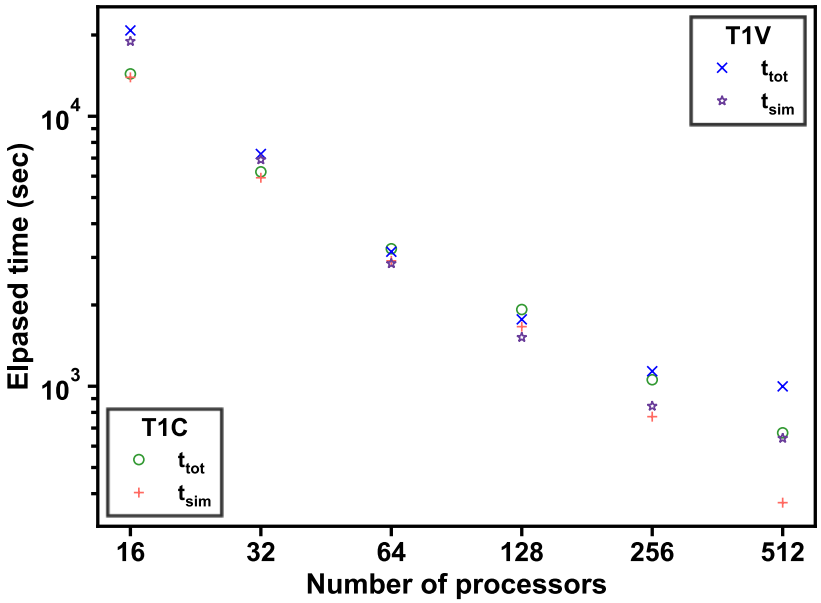

Figure 5.26 The elapsed times of the total simulation and simulation cycles in Cases T1C and T1V on the Ada Linux cluster.

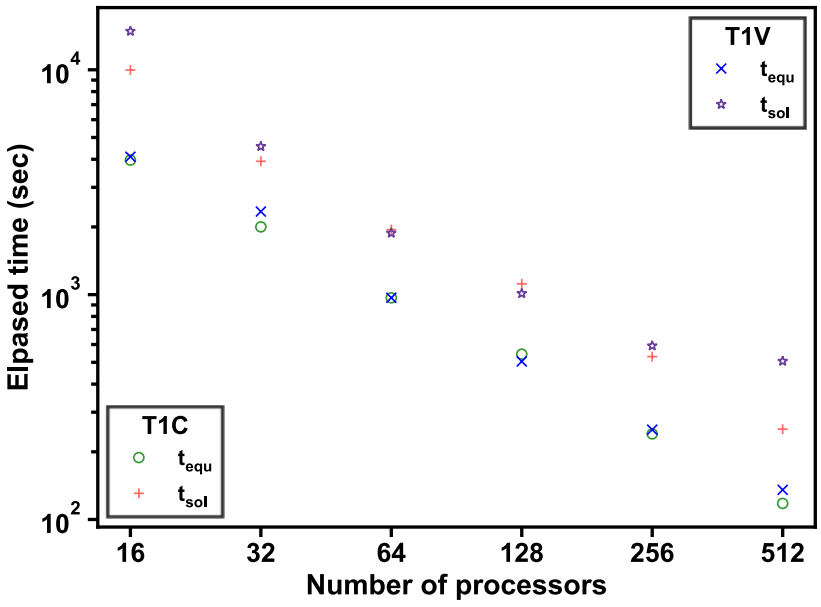

Figure 5.27 The elapsed times of setting up equations and matrix solving in Cases T1C and T1V on the Ada Linux cluster.

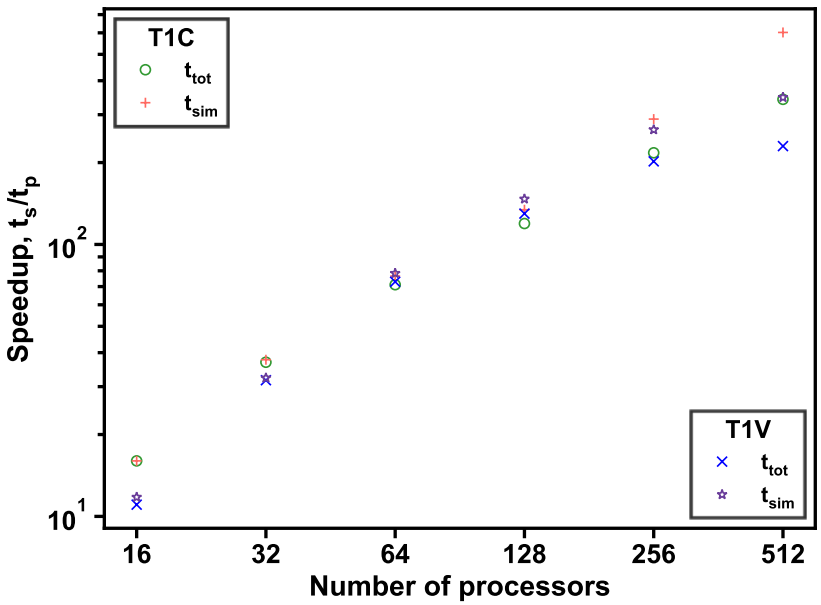

Figure 5.28 The speedups of the total simulation and simulation cycles in Cases T1C and T1V on the Ada Linux cluster.

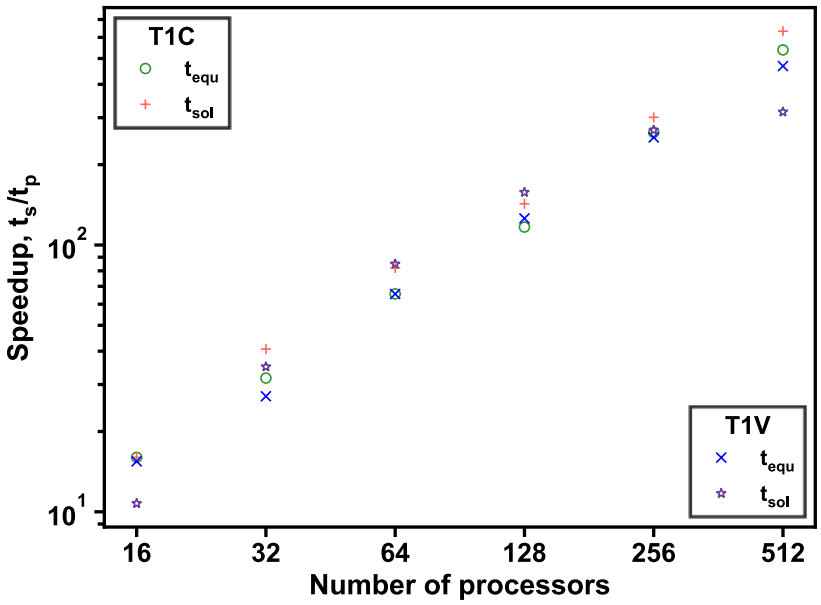

Figure 5.29 The speedups of setting up equations and matrix solving in Cases T1C and T1V on the Ada Linux cluster.

5.2.4.2. Mac Pro

Only Case T1C was tested on the Mac Pro using N_p = 2, 4, 6, 8, 10, and 12. **Figure 5.30** shows that there is a distinctly downward trend of the t_{tot} and t_{sim} times with an increasing N_p, but there is an anomaly for N_p = 8 that is attributed to the particularities of the memory and communication handling in the shared memory system of the Mac Pro. In **Figure 5.31**, t_{sol} exhibits optimal performance (indicated by its lowest value) for N_p = 6, which is consistent with the observations in Case U1 (see **Figure 5.21**). This means that the best overall parallel performance that is observed for N_p = 12 (see **Figure 5.30**), *i.e.*, past that for the dominant t_{sol} that peaks at N_p = 6, is made possible because of the continuing improvement in t_{equ}, which continues to decline monotonically with an increasing N_p because it is more amenable to parallelization. Accordingly, the speedups of the total simulation and simulation cycles in **Figure 5.32** increase with an increasing N_p, but (a) there is still a performance anomaly for N_p = 8 (associated with the worst parallel performance observed in **Figure 5.30**), and (b) the improvement in performance with an increasing N_p is much more modest for N_p > 8. The maximum total speedup observed for N_p = 12 is 4.21. **Figure 5.33** shows that the speedup of the equation set-up operations improves steadily with an increasing N_p.

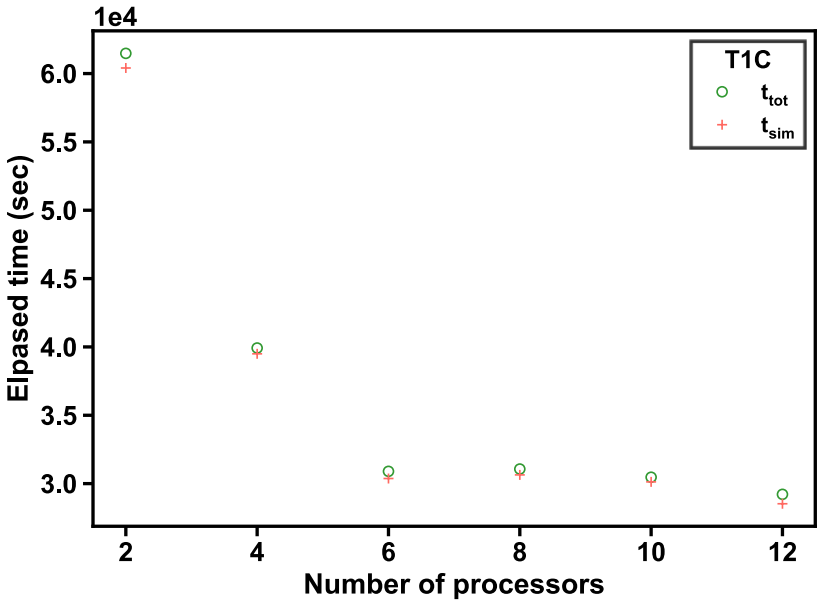

Figure 5.30 The elapsed times of the total simulation and simulation cycles in Case T1V on the Mac Pro.

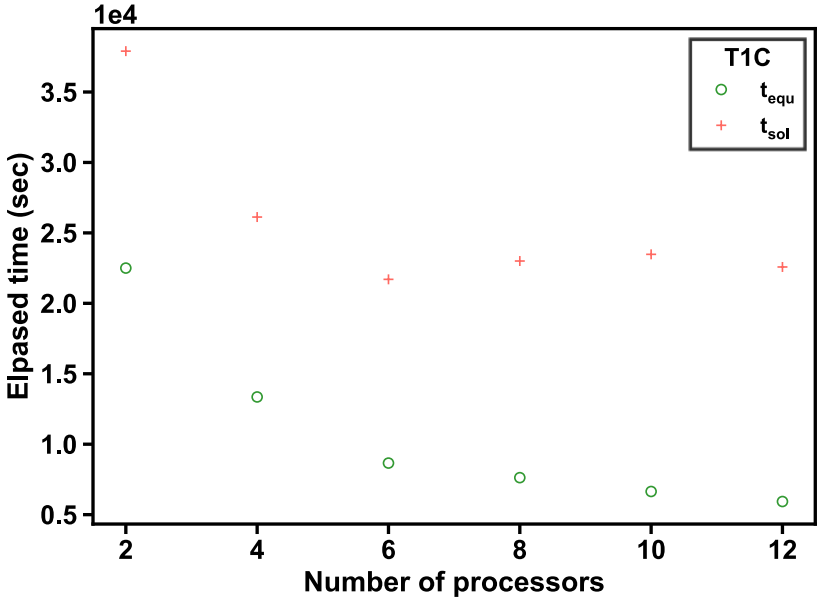

Figure 5.31 The elapsed times of setting up equations and matrix solving in Case T1V on the Mac Pro.

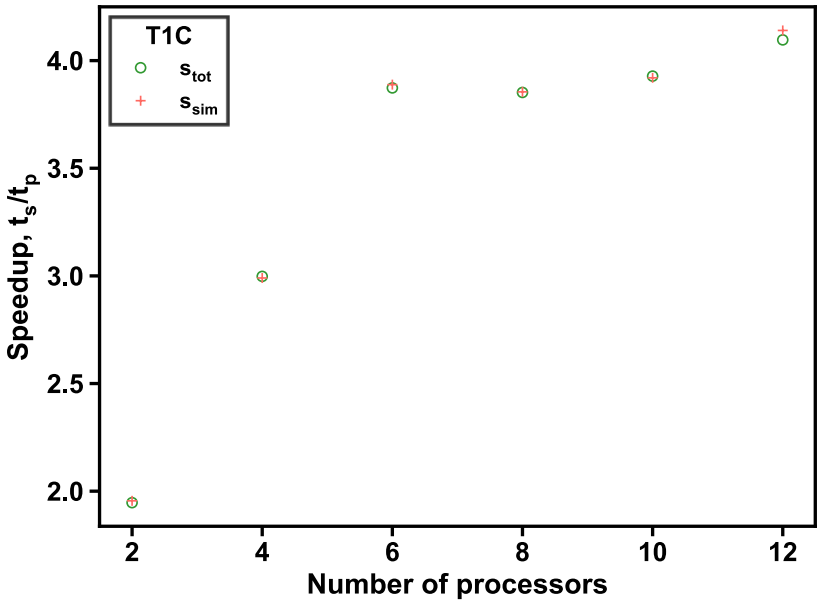

Figure 5.32 The speedups of the total simulation and simulation cycles in Case T1V on the Mac Pro.

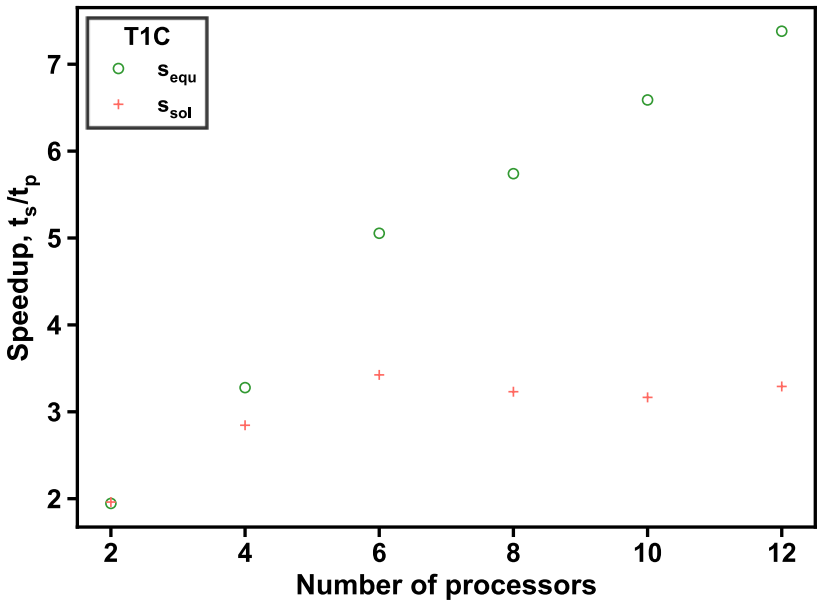

Figure 5.33 The speedups of setting up equations and matrix solving in Case T1V on the Mac Pro.

5.2.5. Summary

The parallel performance tests of the pT+H V1.5 simulator indicate that maximum total speedups on the Ada Linux cluster are obtained for N_p = 512. The maximum speedup of 174.24 in the 2D Case U1 is recorded when the METIS option of MCV is invoked; the maximum speedup of 341.67 in the 3D Case T1 is recorded when the METIS option of MEC is invoked and indicates a much improved parallel performance than in the 2D Case U1. On the Mac Pro, the maximum total speedups are (a) 4.44 in Case U1 with N_p = 8 and (b) 4.21 in Case T1 with N_p = 12, respectively. On current evidence, the partitioning option of choice appears to be MEC, which always results in reliably consistent parallel performance even when it does not lead to optimal (fastest) execution. There appears to be no *a-priori* information on what can lead to the anomalous parallel behavior on the Mac Pro for a certain N_p, and, consequently, no way (other than trial and error) to effectively prevent the deterioration of the parallel performance by selecting the appropriate N_p. However, it is generally safe to assume that (a) a consistent improvement in the parallel performance is expected on a Mac Pro for an increasing $N_p \leq 6$ and (b) the parallel performance is generally inconsistent for $N_p > 6$.

5.3. Parallel Performance of the Coupled pT+H V1.5 and RGM Simulator

The parallel performance of the coupled pT+H V1.5 and RGMS codes was evaluated by Cases U1G and T1G, which differ from Cases U1 and T1 in that their consideration of the full geomechanical model implemented in RGMS.

5.3.1. Description of the Two-Dimensional Cylindrical Problem in Case U1G

5.3.1.1. Flow-Related Description and Parameters

The description and parameters of the flow-related aspects of the problem are stated in Section 5.2.1.

5.3.1.2. Geomechanics-Related Description and Properties

This initialization method to obtain the initial total stress field and boundary conditions in this problem were the same with those described in Section 4.5.1.2. The geomechanical properties of the various geologic layers are summarized in **Table 5.6**. Solution of this 2D cylindrical problem required solving (a) about 480,000 geomechanics equations, in addition to (b) 960,000 FT simultaneous equations, for a total of about 1,440,000 equations.

5.3.2. Case U1G: Results and Discussion

For consistent comparisons, the coupled simulations were run for a total of 100 time steps on both the Ada Linux cluster and Mac Pro, covering the same production period in all the investigated cases. The standard nomenclature and naming conventions discussed earlier are applies here.

Table 5.6 Geomechanical properties of the hydrate deposit in Case U1G.

Young's modulus of HBLs	E = 40 MPa at S_H = 0; E = 1.4 GPa at S_H = 1
Young's modulus of MLs	E = 18 MPa

Table 5.6 Continued.

Young's modulus of OB	E = 14 MPa
Young's modulus of UB	E = 20 MPa
Poisson's ratio of HBLs	v = 0.25
Poisson's ratio of MLs	v = 0.35
Poisson's ratio of OB	v = 0.35
Poisson's ratio of UB	v = 0.35
Biot's coefficient	α = 0.99

5.3.2.1. Ada Linux Cluster

Cases U1GC and U1GV were tested on the Ada Linux cluster using N_p = 1, 2, 4, 8, 16, 32, 64, 128, 256, and 512.

Figures 5.34, **5.35**, **5.36**, and **5.37** show the elapsed times t_{tot}, t_{sim}, t_{equ}, and t_{sol} in Cases U1GC and U1GV. In **Figure 5.34**, the t_{tot} of the coupled simulation decreases monotonically with an increasing N_p in Case U1GV, and the same behavior is observed in Case U1GC except for N_p = 512. Increasing N_p from 128 to 512 does not lead to a decrease of the RGMS-associated t_{tot} in Case U1GC (actually, quite the opposite: t_{tot} increases for N_p > 128); conversely, the RGMS-associated t_{tot} in Case U1GV continues to decrease consistently for an increasing N_p, and this holds true for the entire range of N_p values investigated in this study. This being the case, the communication-volume minimizing option of METIS appears to be the better domain decomposition choice for more predictable, consistent, and scalable parallel performance of the coupled codes.

The t_{sim} results in **Figure 5.35** are consistent with the observations in **Figure 5.34** for reasons already discussed. The t_{equ} results in Cases U1GC and U1GV in **Figure 5.36** show that (a) the parallel performance of the equation set-up operation is practically insensitive to the METIS partitioning option, (b) t_{equ} decreases consistently and monotonically with an increasing N_p for reasons already discussed, and (c) the t_{equ} associated with RGMS component of the coupled code is much lower than that related to the pT+H component (as expected, given the smaller number of the geomechanical equations). On the other hand, the computationally-intensive matrix solving operations (which constitute a major fraction of the overall operations) result in the t_{sol} behavior shown in **Figure 5.37**, and its pattern is replicated in the t_{tot} and t_{sim} behavior in **Figures 5.34** and **5.35** that t_{sol} constitutes a large (if not dominant) part of them (See Eqs. [5.1] and [5.2]).

Figures 5.38, **5.39**, **5.40**, and **5.41** compare the speedups s_{tot}, s_{sim}, s_{equ}, and s_{sol} in Cases U1GC and U1GV. **Figure 5.38** provides the most direct evidence of the importance of the METIS partitioning option on the parallel performance, which is shown to have a very significant impact on the performance of the RGMS component of the coupled simulation. The parallel performance in Case U1GC appears to be better than that in Case U1GC for $N_p \leq 128$ in all the components of the coupled simulation, *i.e.*, the pT+H V1.5 simulation, the RGMS computations, and their coupling. However, the s_{tot} (and its constituents) associated with Case U1GC deteriorates rapidly for $N_p > 128$, and its decline is largely (if not exclusively) associated with an unsatisfactory parallel performance of RGMS when the option of MEC is invoked. Thus, MCV invoked in Case U1GV leads to

better parallel performance for $N_p > 128$; when $N_p = 512$, the maximum s_{tot} levels are attained in Case U1GV, and are 134.97, 142.60, and 109.07 for the coupled simulation, the pT+H operations, and the RGMS computations, respectively. As shown in **Figure 5.39**, the maximum s_{sim} of the coupled simulation, pT+H, and RGMS are 182.01, 193.01, and 145.20, respectively, and they are observed in Case U1GV when $N_p = 512$. These speedups can be even higher if the times expended on reading input files and printing results are excluded from the total. As has already been observed in all previous cases, the s_{equ} in **Figure 5.40** is nearly proportional to N_p because these computations are particularly well-suited to parallelization. This is clearly demonstrated not only by the consistent and monotonic increase in the s_{equ} components that is evident in **Figure 5.40**, but also by the coincidence of the s_{equ} for the RGMS and pT+H computations, and by the s_{equ} magnitudes: for $N_p = 512$ processors, the s_{equ} in best-performing Case U1GV are 529.49, 544.01, and 434.36 in the couped simulation, the pT+H simulation, and the RGMS computations, respectively. Unfortunately, the equation set-up does not constitute a significant component of the overall computational load (and consequently does not significantly influence s_{tot}), the latter being dominated by matrix solving operations. The results in **Figure 5.37** lead to the s_{sol} shown in **Figure 5.41**, in which the difference between the performance of Cases U1GC and U1GV is considerable and mirrors the patterns of the s_{tot} and s_{sim}, being the dominant contributor to both of them. The s_{sol} in Case U1GC appears superior to those in Case U1GV for $N_p \leq 128$, but deteriorates rapidly when $N_p > 128$ and leads to the behavior shown in **Figures 5.38** and **5.39** because matrix solving is probably the most computationally intensive part of all components of the coupled simulation. The

s_{sol} in Case U1GV are consistently higher when N_p > 128, and for N_p = 512, they reach their highest levels at 142.68, 147.66, and 127.00 in the coupled simulation, the pT+H computations, and the RGMS calculations, respectively.

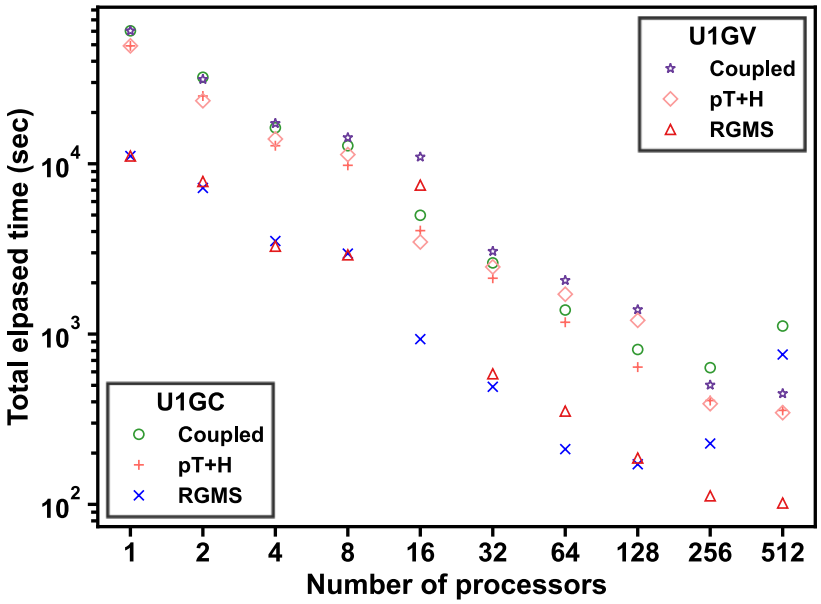

Figure 5.34 The total elapsed times in Cases U1GC and U1GV on the Ada Linux cluster.

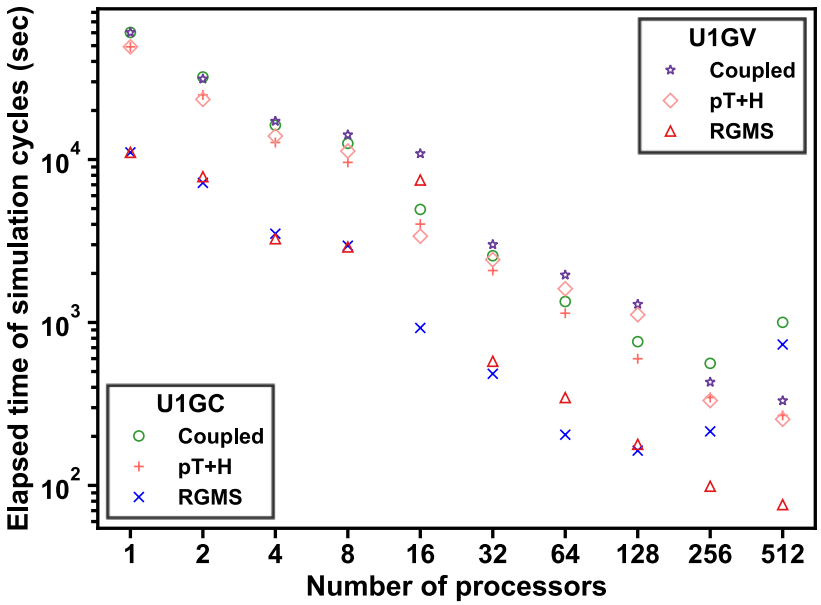

Figure 5.35 The elapsed times of simulation cycles in Cases U1GC and U1GV on the Ada Linux cluster.

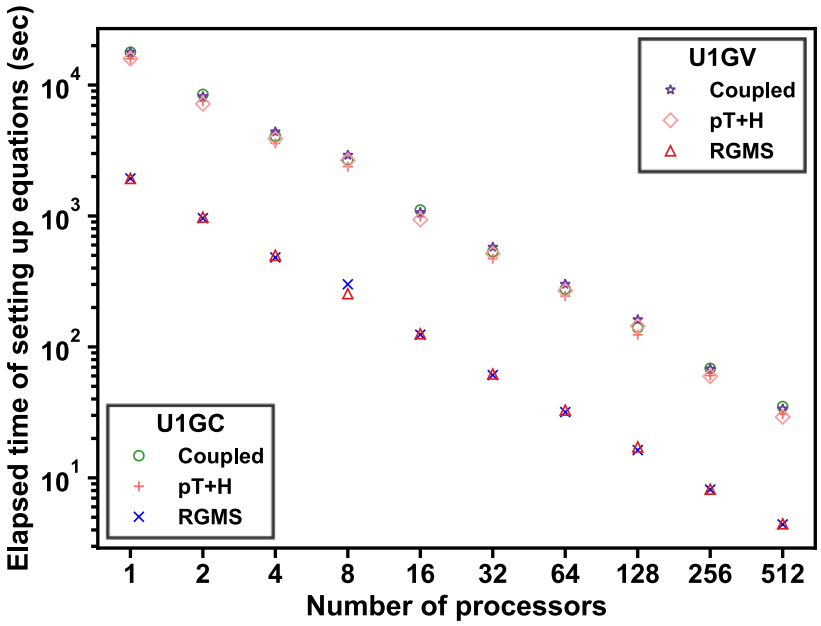

Figure 5.36 The elapsed times of setting up equations in Cases U1GC and U1GV on the Ada Linux cluster.

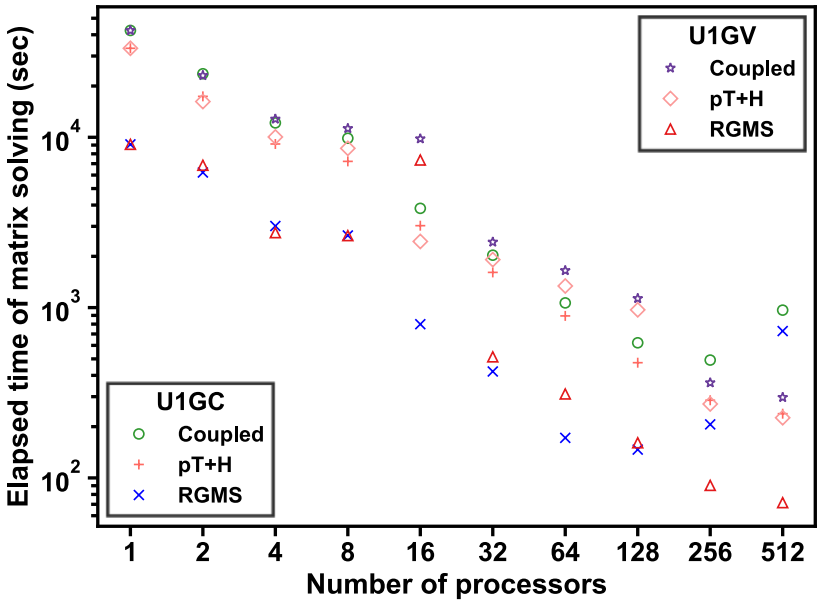

Figure 5.37 The elapsed times of matrix solving in Cases U1GC and U1GV on the Ada Linux cluster.

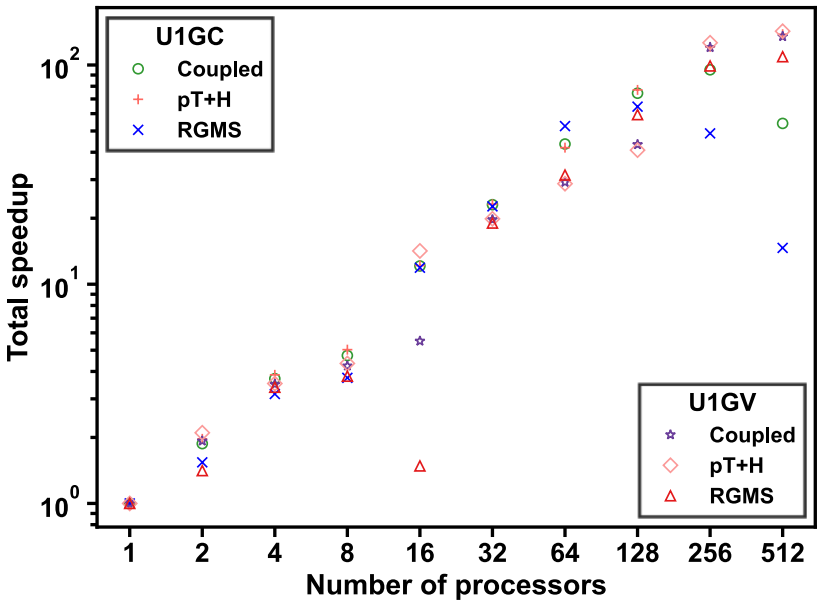

Figure 5.38 The total speedups in Cases U1GC and U1GV on the Ada Linux cluster.

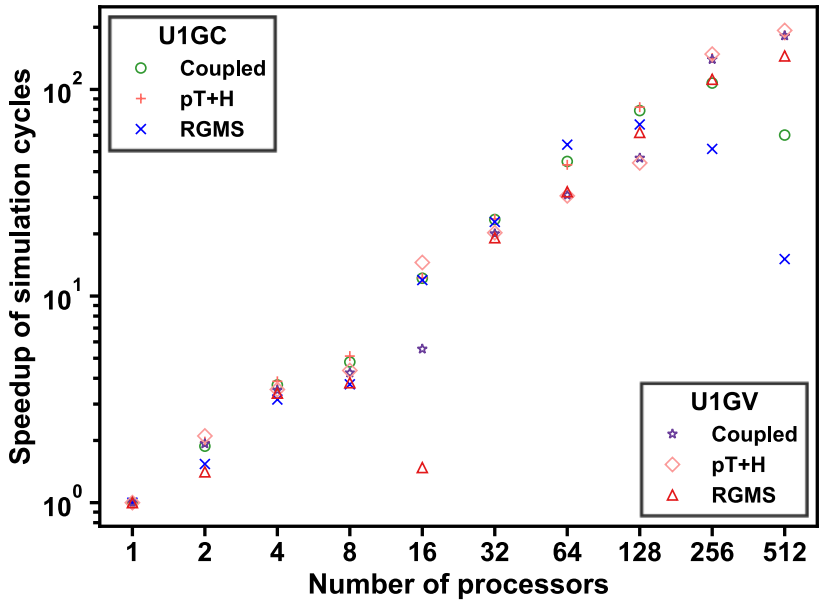

Figure 5.39 The speedups of simulation cycles in Cases U1GC and U1GV on the Ada Linux cluster.

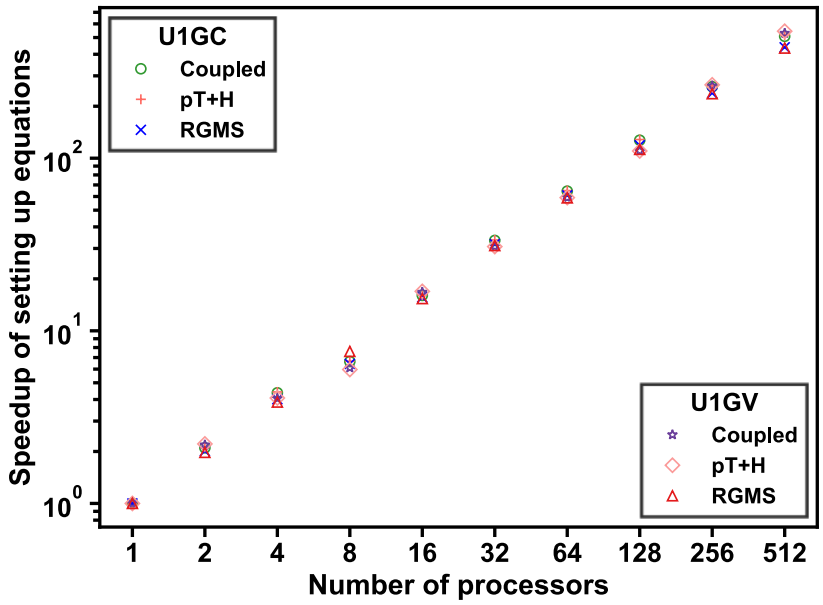

Figure 5.40 The speedups of setting up equations in Cases U1GC and U1GV on the Ada Linux cluster.

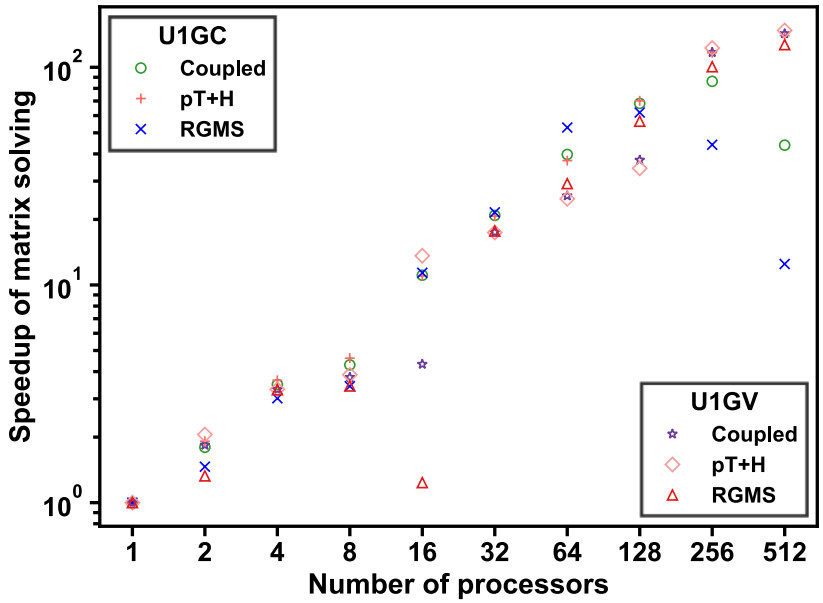

Figure 5.41 The speedups of matrix solving in Cases U1GC and U1GV on the Ada Linux cluster.

5.3.2.2. Mac Pro

For reasons discussed earlier, only Case U1GC was tested on the Mac Pro using N_p = 1, 2, 4, 6, 8, 10, and 12.

Figures 5.42, **5.43**, **5.44**, and **5.45** present the elapsed times t_{tot}, t_{sim}, t_{eq}, and t_{sol} in Case U1GC. **Figure 5.42** shows a complicated t_{tot} pattern but with a general declining trend, interrupted by strongly anomalous behavior for N_p = 4 and less so for N_p = 10. The reason for this behavior is unknown, and is ascribed to the peculiarities of the memory management and processor communication in the architecture of the Mac Pro processors. The RGMS parallel computations appear to be the reason for the deterioration in performance when N_p = 4. The parallel performance of the pT+H V1.5 code appears to

initially improve with an increasing N_p, but seems insensitive to N_p and stagnates for $N_p >$ 4. Thus, the worst parallel performance of the coupled simulation occurs for $N_p = 4$, for which t_{tot} is almost the same as that for $N_p = 1$; the best t_{tot} performance occurs when $N_p =$ 12. Unfortunately, there appears to be no way to determine the N_p that can cause such problematic parallel performance of the coupled code on a Mac Pro prior to the initiation of a simulation; testing the simulator performance for a limited number of timesteps in initial scoping/exploratory simulations appears to be the only possible strategy to identify both problematic and optimal N_p values. The t_{sim} pattern and magnitude in **Figure 5.43** are almost identical to those of t_{tot} in **Figure 5.42**, as was expected because t_{sim} represents the overwhelmingly dominant part of t_{tot}. Because of the scalability and ease of parallelization of the equation set-up process, t_{equ} in **Figure 5.44** decreases continuously with an increasing N_p, following the same t_{equ} pattern identified in all previous cases. Additionally, the t_{equ} associated with the RGMS parallel computations is much lower than that for the pT+H calculations because of the fewer geomechanical equations. For reasons already explained (and related to its oversized presence in t_{tot} and t_{sim}), the t_{sol} pattern and its relationship to N_p in **Figure 5.45** are practically the same as those of t_{tot} and t_{sim} observed in **Figures 5.42** and **5.43**.

Figures 5.46, **5.47**, **5.48**, and **5.49** present the speedups s_{tot}, s_{sim}, s_{equ} and s_{sol}, respectively, in Case U1GC. The s_{tot}, s_{sim}, and s_{sol} relationships to N_p in **Figure 5.46** and the practically identical **Figures 5.47** and **5.48** (for reasons already discussed) are direct consequences of the t_{tot}, t_{sim}, and t_{sol} behavior (from which they are derived) in **Figures 5.42**, **5.43**, and **5.45**. Thus, s_{tot}, $s_{sim,}$ and s_{sol} generally increase with N_p, but (a) they all

exhibit the same very anomalous parallel behavior associated with the RGMS component of the coupled code for N_p = 4 and the less pronounced one for N_p = 10, and (b) their parallel performance associated with the pT+H component is characterized by stagnation and shows no improvement for N_p > 4, and (c) the highest s_{tot}, $s_{sim,}$ and s_{sol} generally are attained for N_p = 12. Thus, for N_p = 12, the overall s_{tot} values of the coupled simulation, pT+H, and RGMS are 4.10, 3.88, and 5.03, respectively; the corresponding s_{sim} values are very similar, which are 4.14, 3.93, and 5.04, as are the associated s_{sol} values. Because of the scalability of the equation set-up operations (already discussed), the s_{equ} of the coupled simulation, RGMS, and pT+H in **Figure 5.48** increase continuously with an increasing N_p, they practically coincide for $N_p \leq 4$; the parallel RGMS computations exhibit a higher s_{equ} for N_p > 4. Although the s_{equ} values here are higher than the s_{tot}, $s_{sim,}$ and s_{sol} ones, they do not affect them significantly because equation set-up is not a computationally intensive component of the coupled computations.

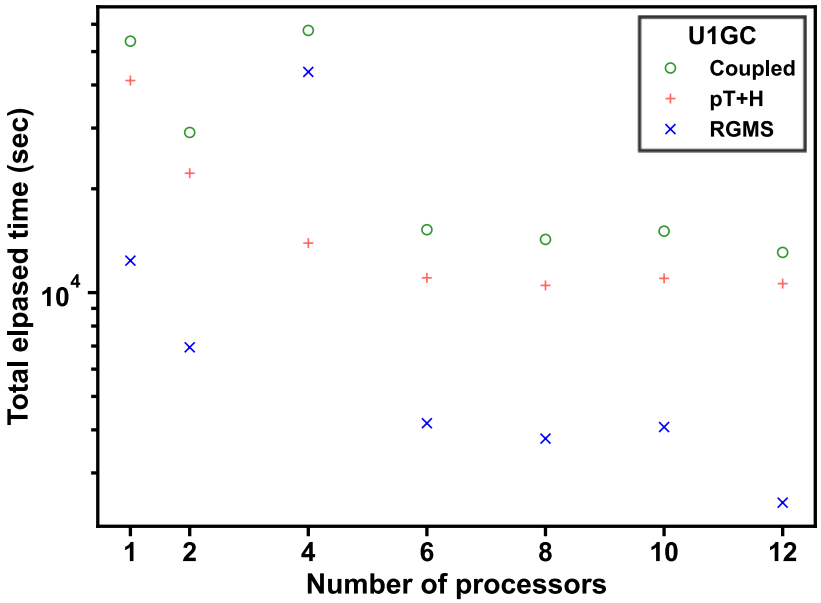

Figure 5.42 The total elapsed times in Case U1GC on the Mac Pro.

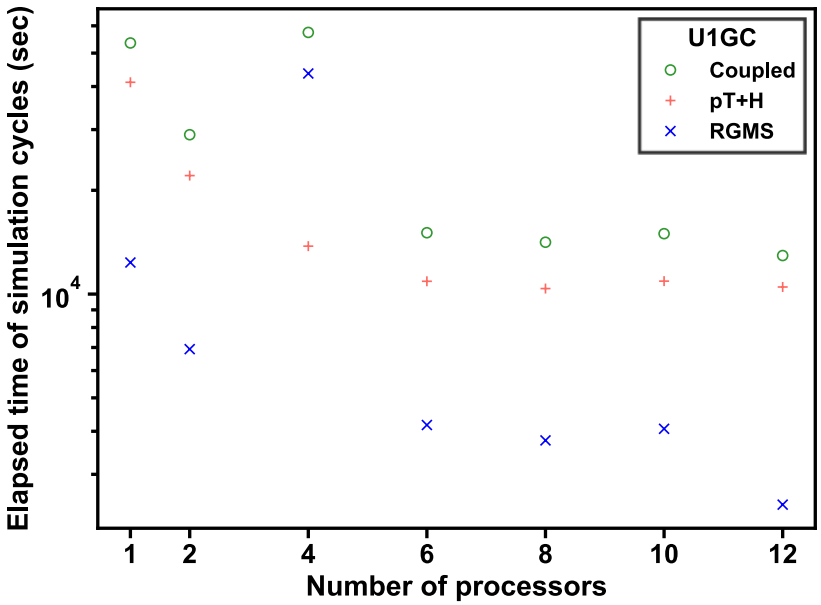

Figure 5.43 The elapsed times of simulation cycles in Case U1GC on the Mac Pro.

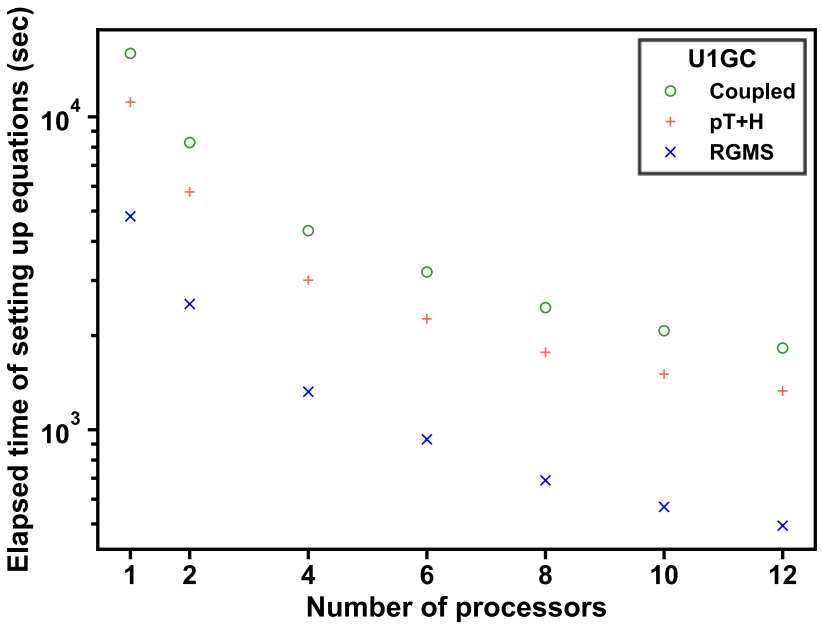

Figure 5.44 The elapsed times of setting up equations in Case U1GC on the Mac Pro.

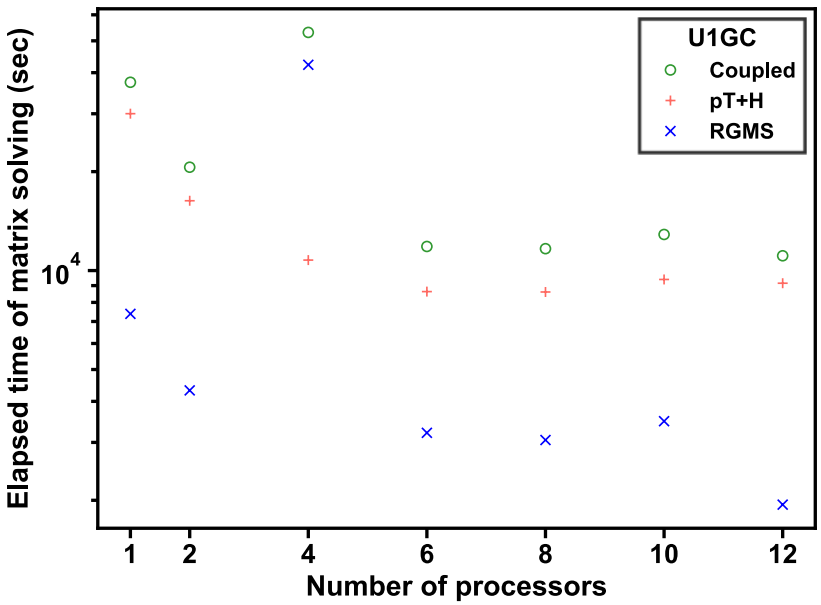

Figure 5.45 The elapsed times of matrix solving in Case U1GC on the Mac Pro.

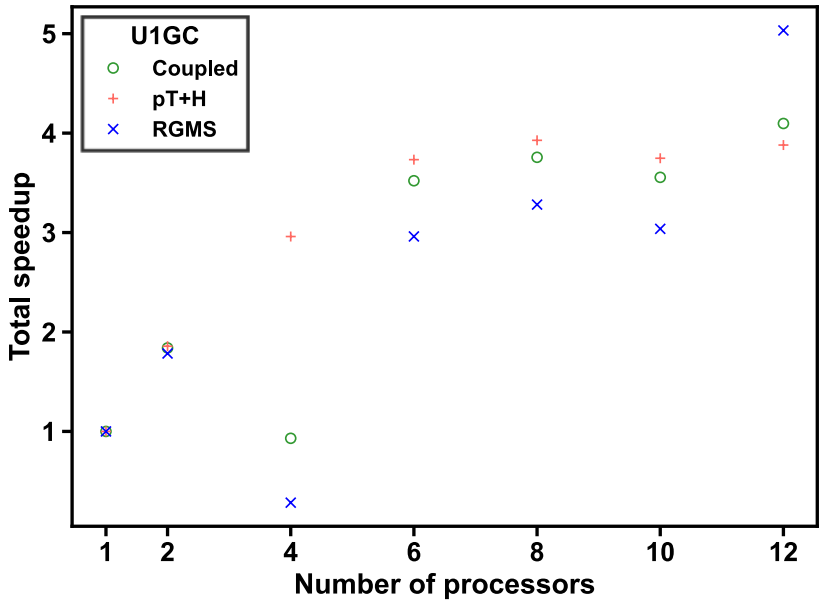

Figure 5.46 The total speedups in Case U1GC on the Mac Pro.

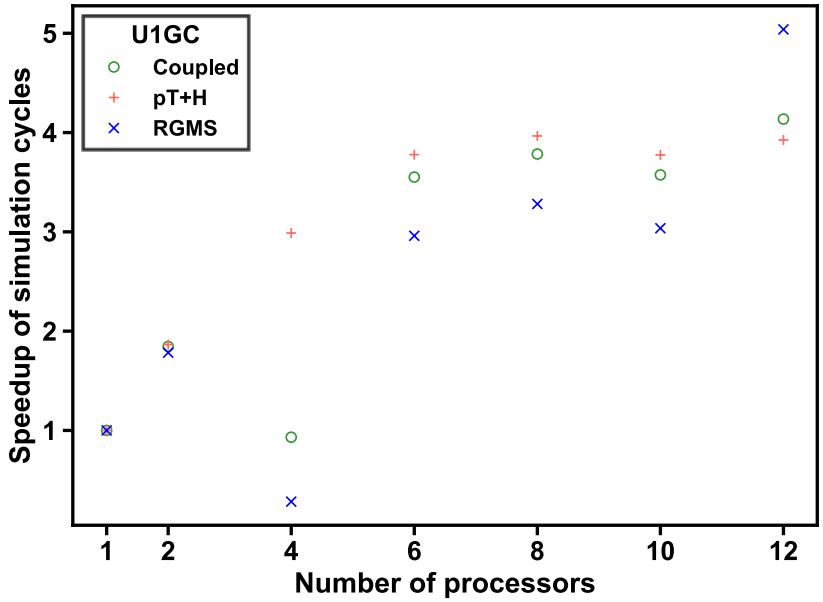

Figure 5.47 The speedups of simulation cycles in Case U1GC on the Mac Pro.

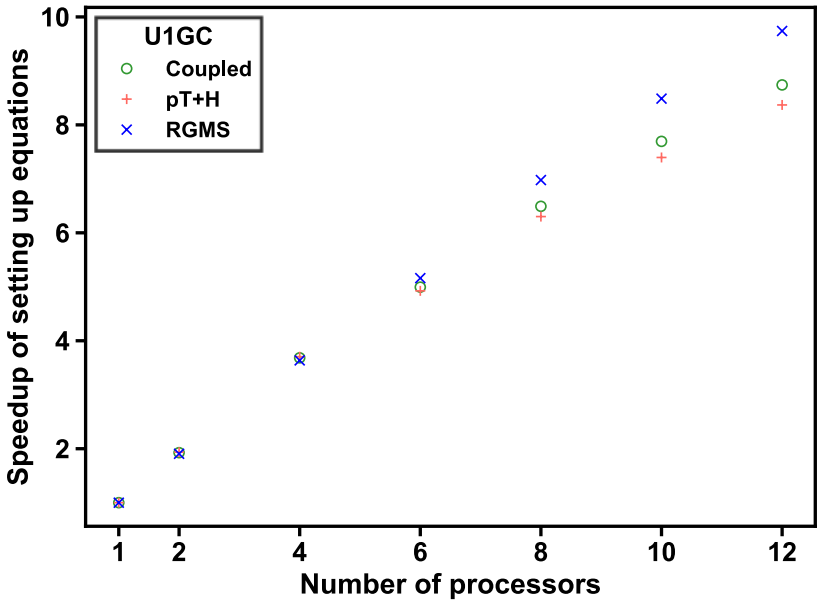

Figure 5.48 The speedups of setting up equations in Case U1GC on the Mac Pro.

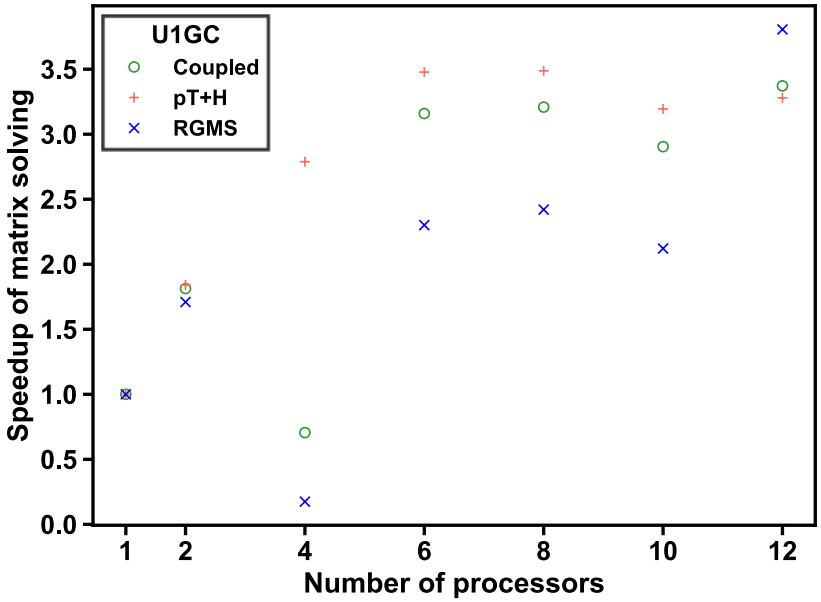

Figure 5.49 The speedups of matrix solving in Case U1GC on the Mac Pro.

5.3.3. Description of the Three-Dimensional Cartesian Problem in Case T1G

5.3.3.1. Flow-Related Description and Parameters

The flow-related problem description and parameters are discussed in Section 5.2.3.

5.3.3.2. Geomechanics-Related Description and Properties

All the boundaries except the top boundary are supported by rollers, thus preventing displacements at these locations. The initialization method used to determine the initial total stress field is as described in Section 4.5.1.2. **Table 5.7** presents the geomechanical properties used in this study, taken from Reagan et al. (2019). In the geomechanics simulation, displacements are obtained in three directions (= the number of coordinates) at each node, resulting in about 11,120,000 equations covering the entire domain. Adding the 14,480,000 equations in the FT simulation, the coupled simulator has to solve a total of about 25,600,000 equations.

Table 5.7 Geomechanical properties of the hydrate deposit in Case T1G.

Young's modulus in HBLs	E = 500 MPa at S_H = 0; E = 1990 MPa at S_H = 1
Young's modulus in OB, UB, MLs, ALs	E = 1096 MPa
Poisson's ratio in HBLs	ν = 0.4
Poisson's ratio in OB, UB, MLs, ALs	ν = 0.3
Biot's coefficient	α = 0.99

5.3.4. Case T1G: Results and Discussion

These 3D simulations were run for (a) 50 timesteps on the Ada Linux cluster and (b) 25 timesteps on the Mac Pro. Because it was not possible to solve this problem using the serial version of the simulators and record the elapsed time, the latter was estimated by following the approach described in Section 5.2.4 that was based on the timing information obtained from runs involving the minimum number of processors used for the solution of this problem: namely, 32 processors on the Ada Linux cluster, and 2 processors on the Mac Pro. The nomenclature and naming conventions introduced earlier apply also to this case.

5.3.4.1. Ada Linux Cluster

Cases T1GC and T1GV were simulated for a total of 50 time steps (covering the same production period) on the Ada Linux cluster using N_p = 32, 64, 128, 256, 512.

Figures 5.50, **5.51**, **5.52**, and **5.53** show the elapsed times t_{tot}, t_{sim}, t_{equ}, and t_{sol} in Cases T1GC and T1GV.

In **Figure 5.50**, the t_{tot} of the coupled simulation decreases monotonically with an increasing N_p in Case T1GV; the t_{tot} behavior in Case T1GC is far less consistent, exhibiting anomalous behavior for N_p = 128 (when its performance is worse than that for N_p = 32) and for N_p = 512 processors. This is caused by deterioration in the RGMS-associated t_{tot} performance in Case T1GC at these N_p levels for reasons that are not obvious. Conversely, the RGMS-associated t_{tot} in Case T1GV continues to decrease consistently for an increasing N_p, and this holds true for the entire range of N_p values

investigated in this study. Based on these results, the obvious conclusion is that the MCV option of METIS is the desirable choice for domain decomposition because it delivers a more consistent, predictable, and scalable parallel performance of the coupled simulators.

The t_{sim} and t_{sol} results in **Figures 5.51** and **5.53** follow the same patterns and have similar values because of the reasons discussed in detail previously (*e.g.*, see Section 5.3.2.1). As in Cases U1GC and U1GV, the t_{equ} results in Cases T1GC and T1GV in **Figure 5.52** show that (a) the parallel performance of the equation set-up operation is practically insensitive to the METIS partitioning option in the RGMS computations and slightly so in the pT+H computations, (b) t_{equ} decreases consistently and monotonically with an increasing N_p for reasons already discussed, (c) the t_{equ} associated with RGMS component of the coupled code is not very different from that related to the pT+H component (not unexpected, given the similarity of the numbers of the FT and geomechanical equations), and (d) the t_{equ} for the coupled simulations are similar in both METIS partitioning option.

Figures 5.54, **5.55**, **5.56**, and **5.57** compare the speedups s_{tot}, s_{sim}, s_{equ}, and s_{sol} in Cases T1GC and T1GV, respectively. **Figure 5.54** provides the most direct evidence of the importance of the METIS partitioning option on the parallel performance, which is shown to have a very significant impact on the performance of the RGMS component of the coupled simulation (even more so than in Cases U1GC and U1GV). Given the unpredictability of the MEC option of the METIS-based domain decomposition in Case T1GC, the MCV option invoked in Case T1GV leads to consistently better, more predictable, and more scalable parallel performance for any N_p level; when N_p = 512, the

maximum s_{tot} level attained in Case T1GV is 331.80 for the coupled simulation, significantly larger than the 208.26 attained in the best performance of Case T1GC for N_p = 256. The corresponding s_{sim} numbers in **Figure 5.55** are 235.14 in Case T1GC with N_p = 256 and 422.40 in Case T1GV with N_p = 512, and these numbers are expected to tend toward the s_{tot} ones as the number of time steps increases.

As has already been observed in all previous cases, the s_{equ} in **Figure 5.56** is nearly proportional to N_p because these computations are particularly well-suited to parallelization. This is clearly demonstrated not only by the consistent and monotonic increase in the s_{equ} components that is evident in **Figure 5.56**, but also by the proximity of the s_{equ} for the RGMS and pT+H computations, and by the s_{equ} magnitudes. Unfortunately, the equation set-up does not constitute a significant component of the overall computational load—the latter being dominated by matrix solving operations—and cannot materially affect the s_{tot} in Case T1GC. The results in **Figure 5.53** lead to the s_{sol} shown in **Figure 5.57**, in which the difference between the performance of Cases T1GC and T1GV is considerable and follows closely the patterns of s_{tot} and s_{sim} in **Figures 5.54** and **5.55**, being the dominant contributor to both of them. The s_{sol} in Case T1GV is consistently higher than that in Case T1GV, confirming the superiority of the MCV option of METIS as the most desirable domain decomposition method for optimal (reliable, predictable, consistent, and scalable) parallel performance of the coupled RGMS and pT+H V1.5 codes.

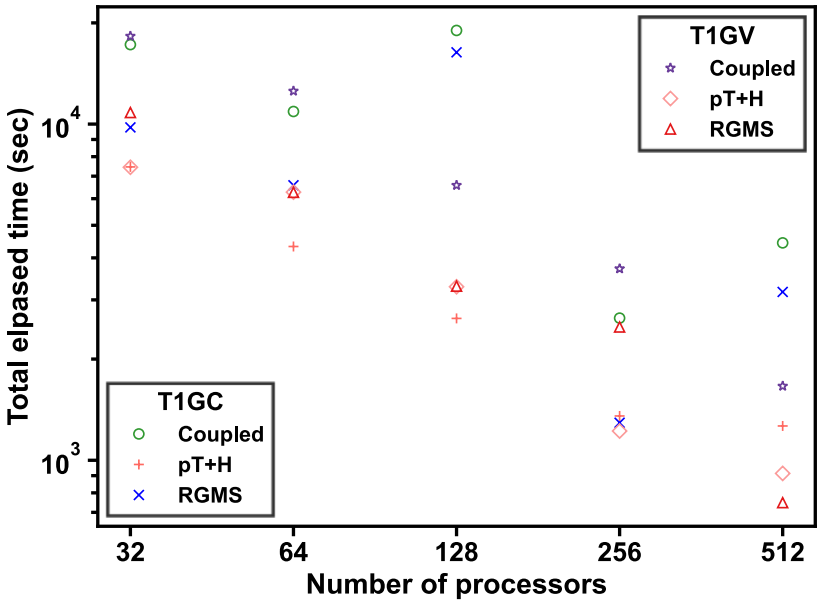

Figure 5.50 The total elapsed times in Cases T1GC and T1GV on the Ada Linux cluster.

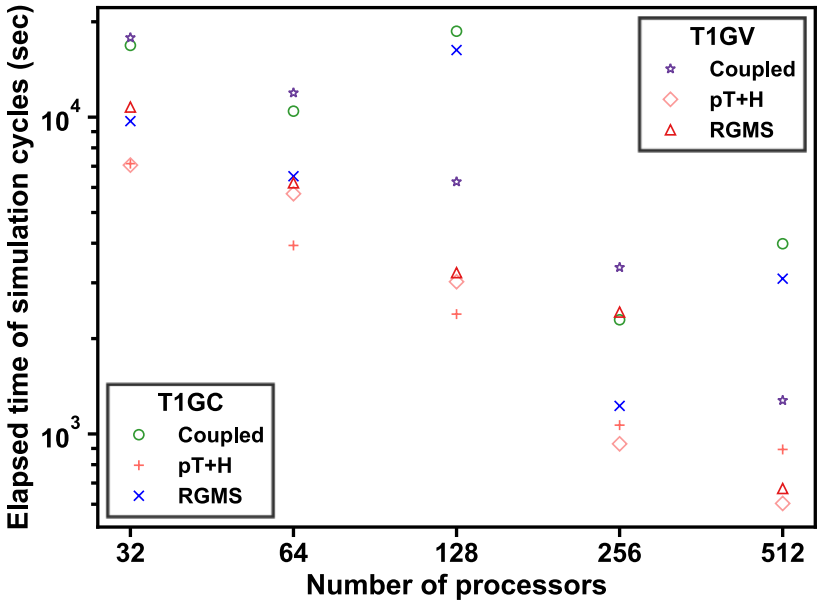

Figure 5.51 The elapsed times of simulation cycles in Cases T1GC and T1GV on the Ada Linux cluster.

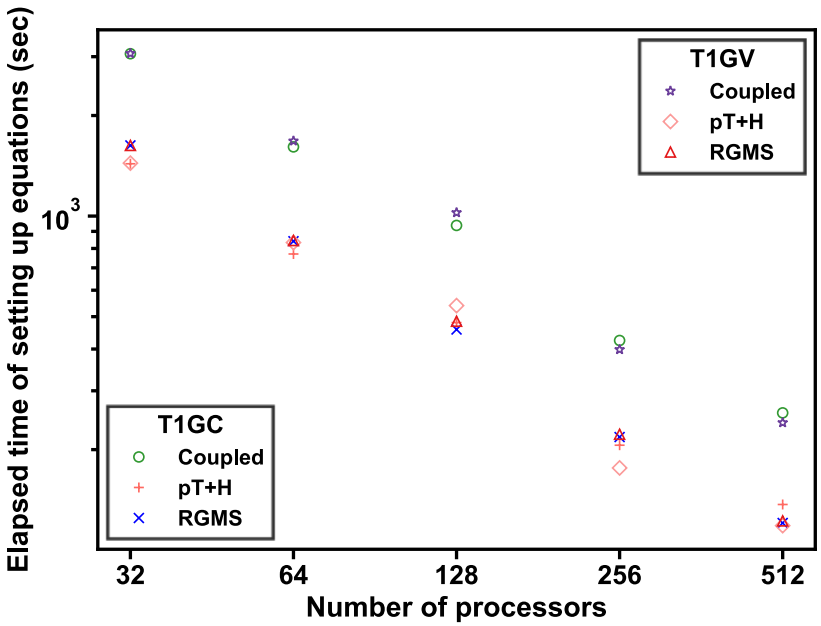

Figure 5.52 The elapsed times of setting up equations in Cases T1GC and T1GV on the Ada Linux cluster.

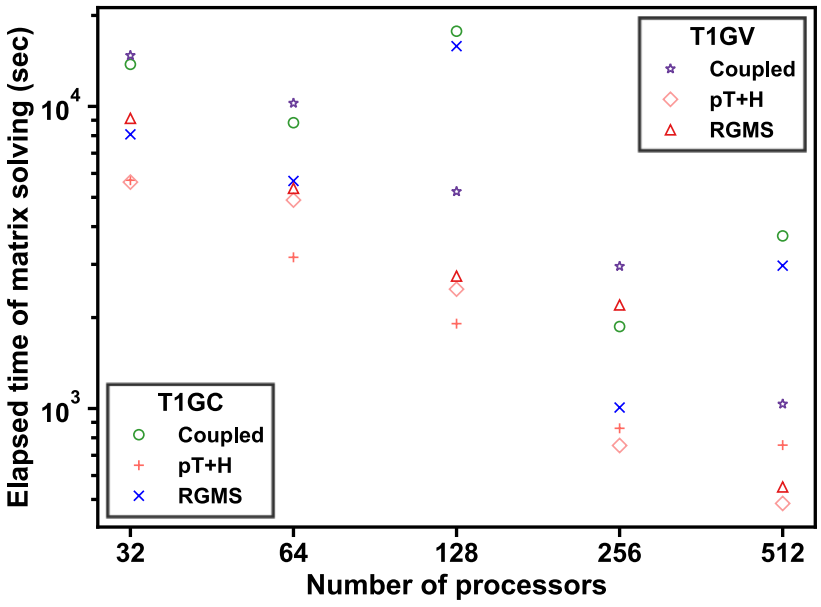

Figure 5.53 The elapsed times of matrix solving in Cases T1GC and T1GV on the Ada Linux cluster.

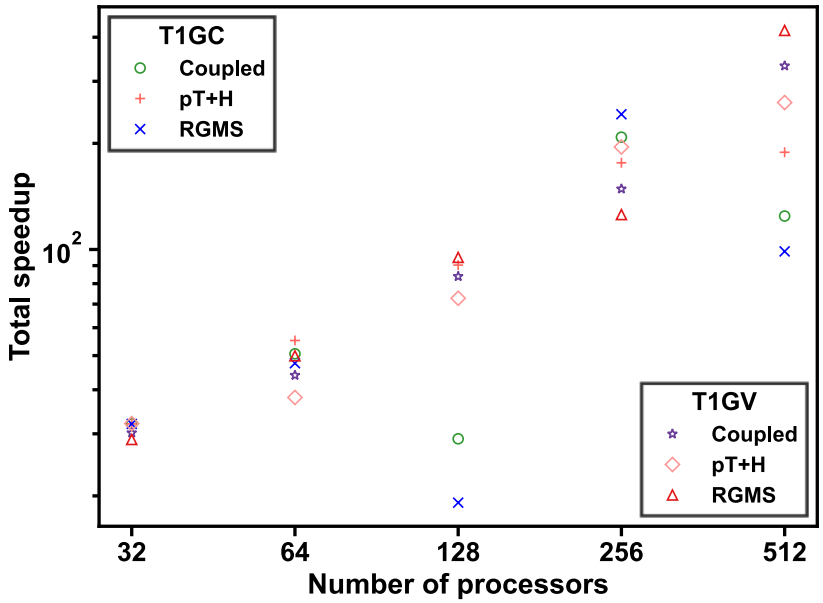

Figure 5.54 The total speedups in Cases T1GC and T1GV on the Ada Linux cluster.

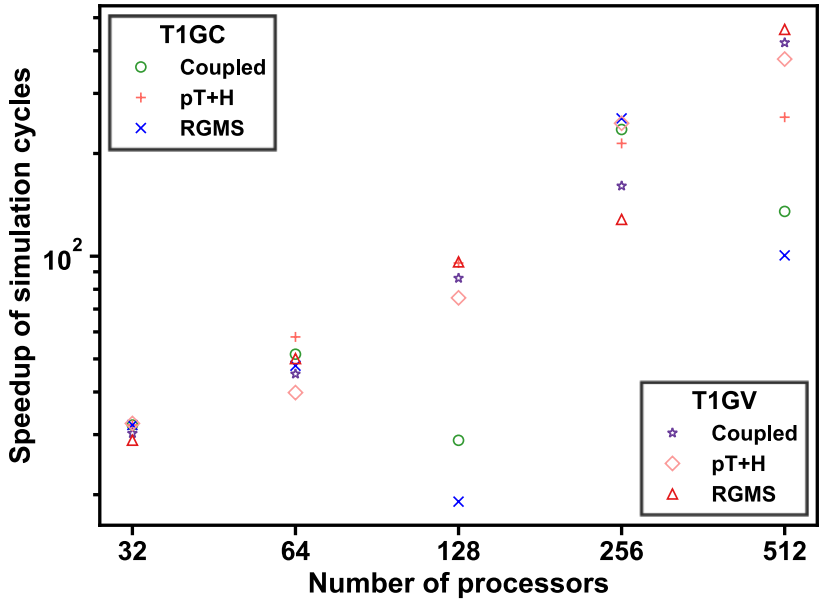

Figure 5.55 The speedups of simulation cycles in Cases T1GC and T1GV on the Ada Linux cluster.

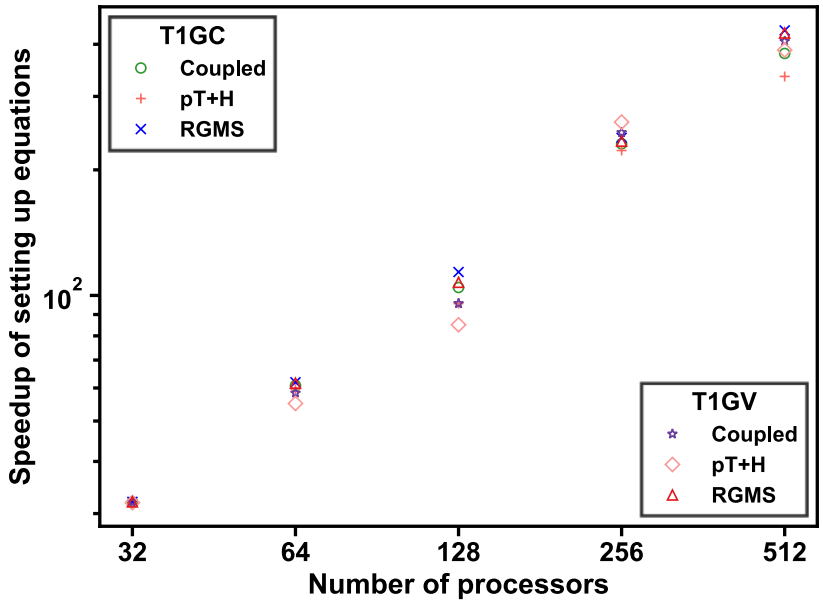

Figure 5.56 The speedups of setting up equations in Cases T1GC and T1GV on the Ada Linux cluster.

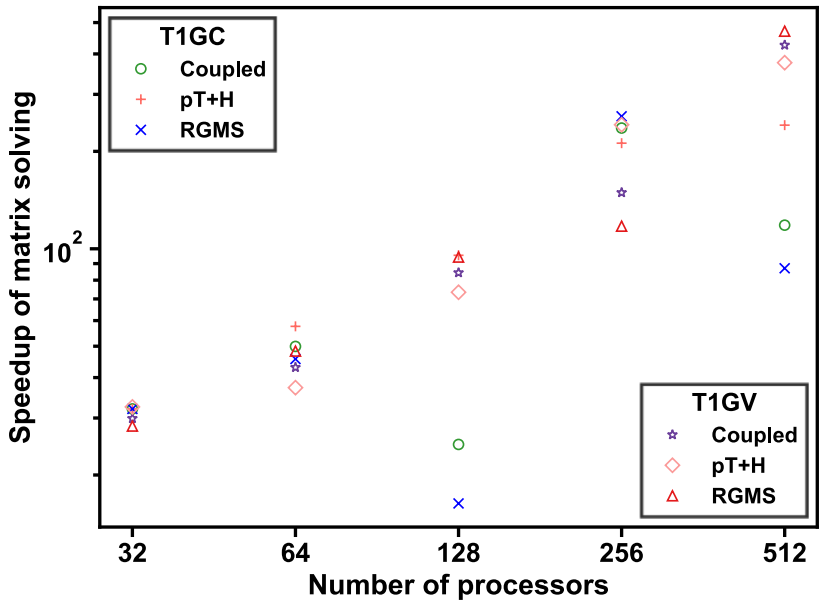

Figure 5.57 The speedups of matrix solving in Cases T1GC and T1GV on the Ada Linux cluster.

5.3.4.2. Mac Pro

Case T1GC was tested on Mac Pro with 2, 4, 6, 8, 10, 12 processors.

Figures 5.58, **5.59**, **5.60**, and **5.61** present the elapsed times t_{tot}, t_{sim}, t_{equ}, and t_{sol}, respectively, in Case T1GC. **Figure 5.58** shows a complicated t_{tot} pattern but with a declining trend for $N_p \leq 6$, but an unpredictable and deteriorating parallel performance for $N_p > 6$ that is worse than that for $N_p = 2$. The unsatisfactory performance for $N_p > 6$ applies to both the RGMS and the pT+H computations. As in Case U1GC on the Mac Pro, the reason for this behavior is unknown, and is attributed to the memory management and processor communication in the architecture of the Mac Pro processors. Thus, the best parallel performance of the coupled simulation occurs when $N_p = 6$. Because of the inability to determine *a-priori* the N_p that can cause an unsatisfactory parallel performance of the coupled code on a Mac Pro, testing the simulator performance for a limited number of timesteps in initial scoping/exploratory simulations in order to determine optimal N_p values is highly recommended. The t_{sim} pattern and magnitude in **Figure 5.59** are almost identical to those of t_{tot} in **Figure 5.58**, as was expected because t_{sim} represents the overwhelmingly dominant part of t_{tot}.

This is the first case in which the general scalability and ease of parallelization of the equation set-up process fail to yield a t_{equ} in **Figure 5.60** that decreases continuously with an increasing N_p for the entire range of processors available in the Mac Pro: t_{equ} exhibit anomalous behavior when $N_p = 8$ and 12 in the pT+H calculations. Because the matrix solving portion requires the most computational effort, the t_{sol} pattern and its

relationship to N_p in **Figure 5.61** are practically the same as those of t_{tot} and t_{sim} observed in **Figures 5.58** and **5.59**.

Figures 5.62, **5.63**, **5.64**, and **5.65** present the speedups s_{tot}, s_{sim}, s_{equ}, and s_{sol}, respectively, in Case T1GC. **Figures 5.62** and **5.63** show that the maximum attainable s_{tot} and s_{sim} is 3.93 and occurs when N_p = 6. Comparing the s_{equ} components in **Figure 5.64** leads to the conclusion that the RGMS and the pT+H contributions are about the same until N_p = 6, beyond which no pattern is evident. In **Figure 5.65**, s_{sol} follows the same pattern as, and very similar values to, those of s_{tot} and s_{sim} in **Figures 5.62** and **5.63** for previously explained reasons.

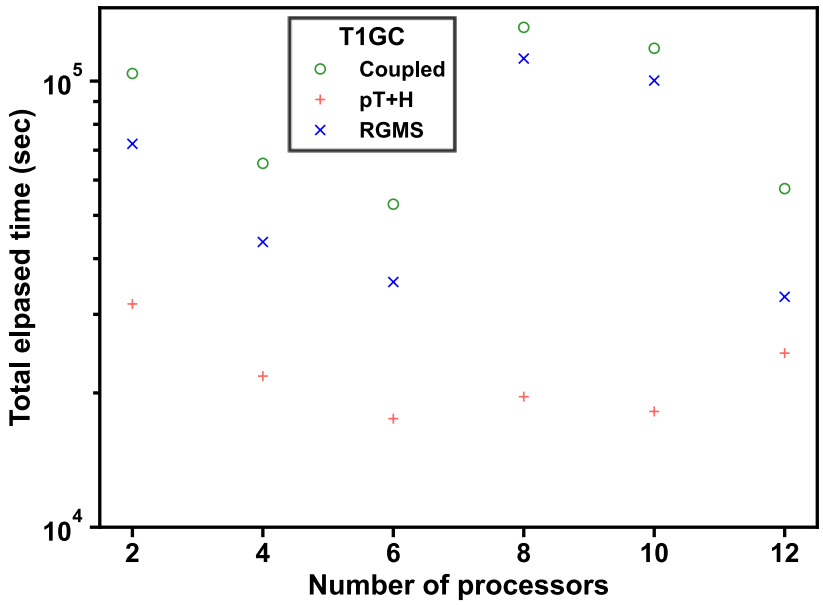

Figure 5.58 The total elapsed times in Case T1GC on the Mac Pro.

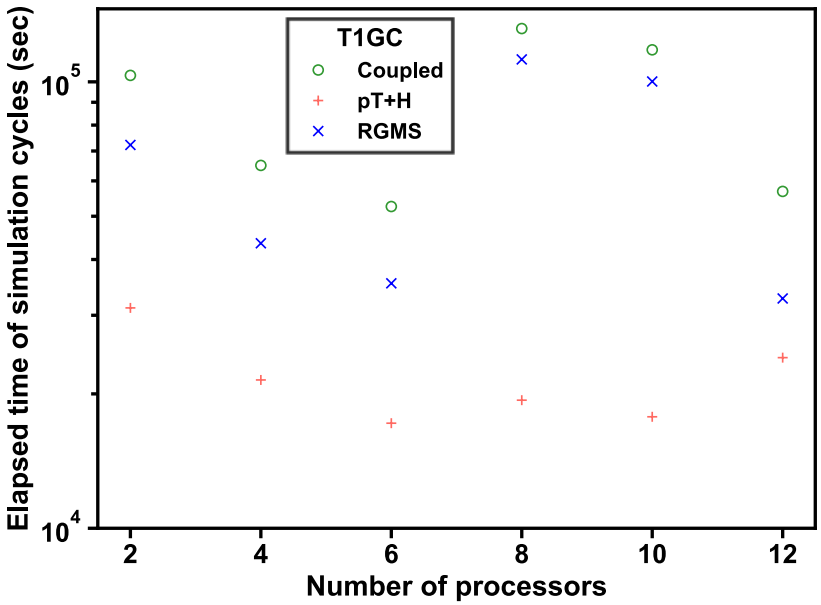

Figure 5.59 The elapsed times of simulation cycles in Case T1GC on the Mac Pro.

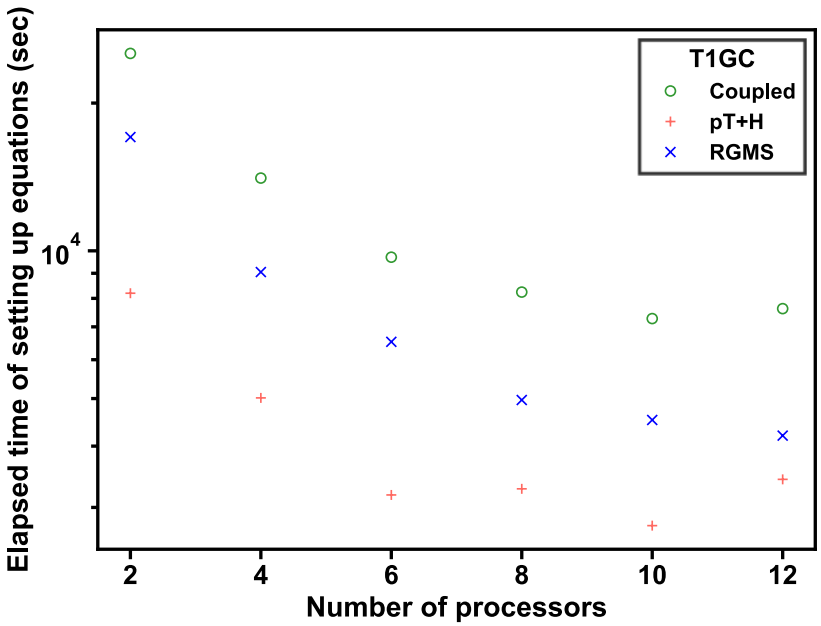

Figure 5.60 The elapsed times of setting up equations in Case T1GC on the Mac Pro.

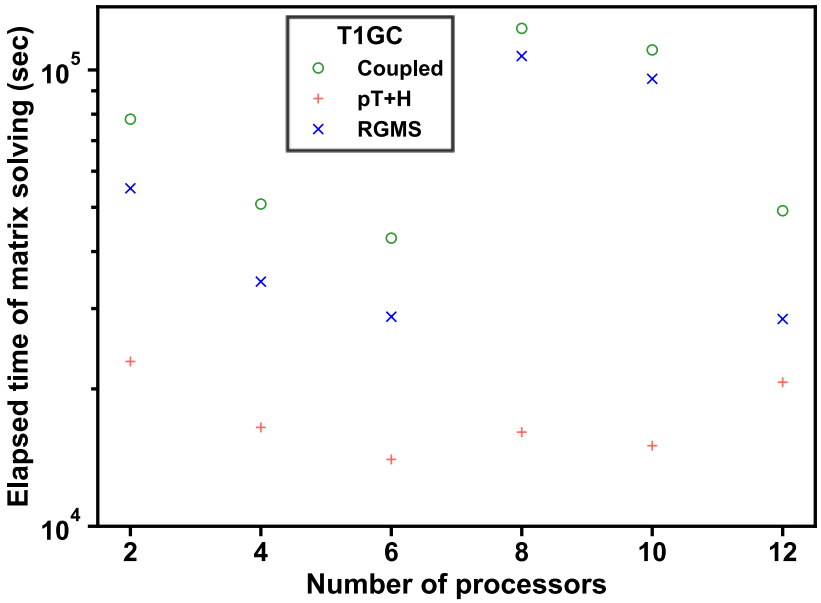

Figure 5.61 The elapsed times of matrix solving in Case T1GC on the Mac Pro.

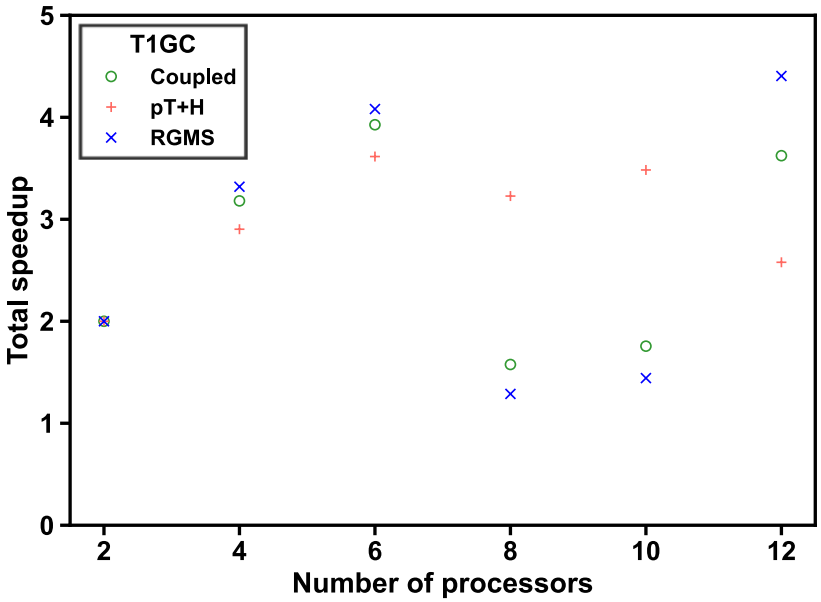

Figure 5.62 The total speedups in Case T1GC on the Mac Pro.

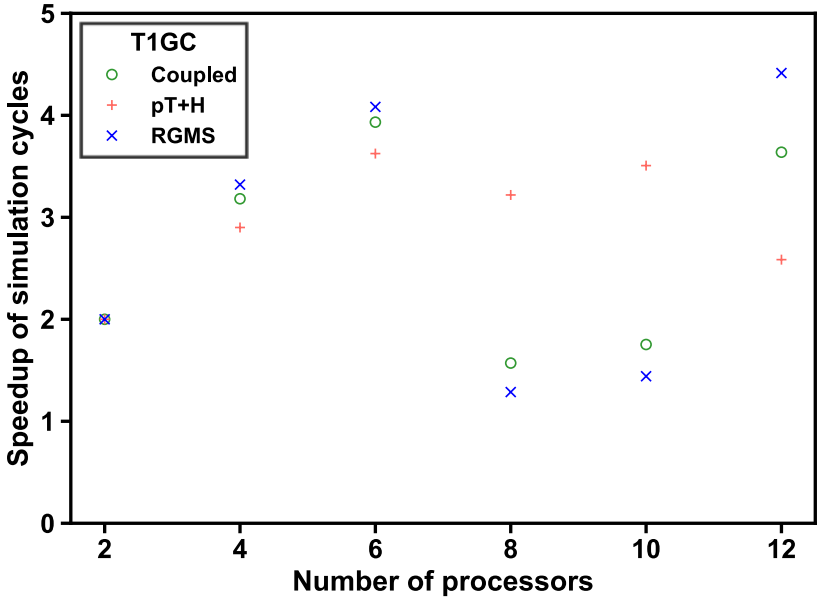

Figure 5.63 The speedups of simulation cycles in Case T1GC on the Mac Pro.

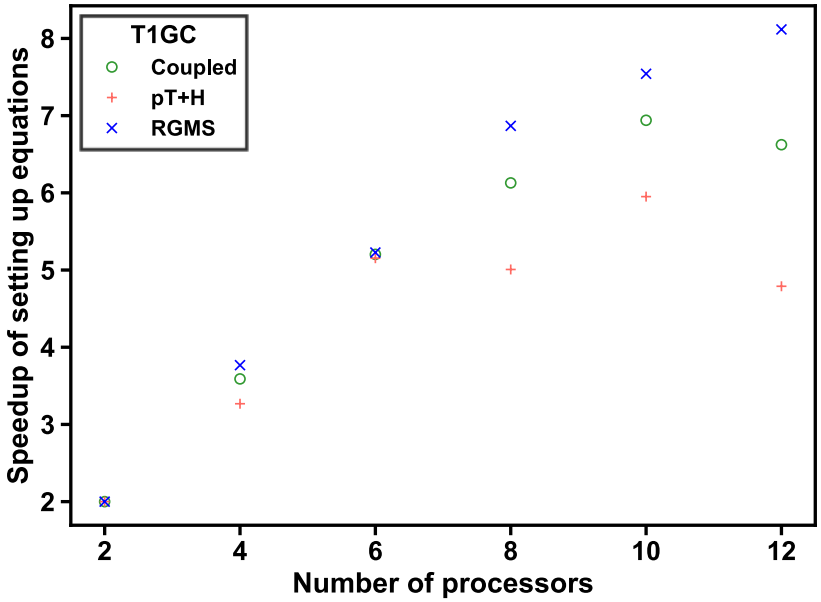

Figure 5.64 The speedups of setting up equations in Case T1GC on the Mac Pro.

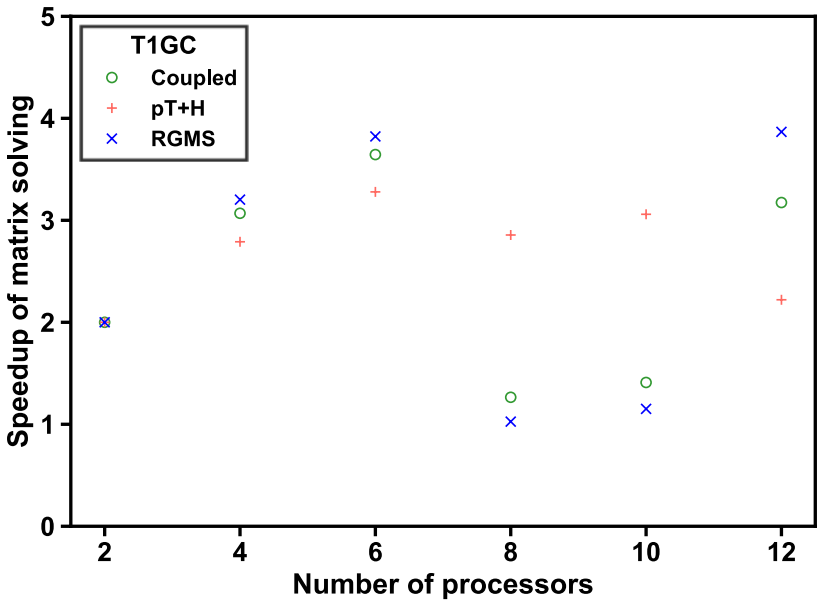

Figure 5.65 The speedups of matrix solving in Case T1GC on the Mac Pro.

5.3.5. Summary

For the coupled pT+H V1.5 and RGM simulations, the execution time associated with the pT+H computations is longer than that related to the RGMS calculations in Case U1G, but this is reversed in Case T1G. On the Ada Linux cluster, the maximum overall speedups in Cases U1G and T1G are 134.97 and 331.80, respectively, when N_p = 512 and the METIS partitions the domain based on the option of MCV. On the Mac Pro, the maximum overall speedups in Cases U1G and T1G are 4.10 when N_p = 12 and 3.93 when N_p = 6, respectively. Based on the results of the parallel performance study, to achieve the maximum total speedup, the METIS-based domain partitioning needs to be based on the MCV option, and optimal results are obtained for N_p = 256 and 512 in Case U1G, and 128 and 512 in Case T1G.

6. CASE STUDIES OF TWO- AND THREE-DIMENSIONAL PROBLEMS

These realistic problems (involving 2D cylindrical and 3D Cartesian domains) are simulated by two methods: (a) using only the pT+H V1.5 simulator with its simplified geomechanical model of hydrate-dependent pore compressibility (Moridis 2014), and (b) the coupled pT+H V1.5 and RGM simulator that involves a full geomechanical model.

6.1. The Two-Dimensional Cylindrical Cases U1 and U1G

These two cases are mainly used to analyze the impact of considering a full geomechanical model in the solution of these 2D cylindrical problems when soft hydrate-free mud interlayers are interlaced with hydrate-bearing sandy media within the hydrate deposit.

6.1.1. Problem Description

Complete problem descriptions of Cases U1 and U1G are provided in Sections 5.2.1 and 5.3.1, respectively.

6.1.2. Results

In the analysis of the system behavior, the following flow-related conditions and parameters were monitored: the spatial distributions of pressure (P), temperature (T), gas saturation (S_G), and hydrate saturation (S_H); the mass rates of the gaseous and aqueous phases production (Q_G and Q_A, respectively); the cumulative masses of the produced

gaseous and aqueous phases (M_G and M_A, respectively); the volumetric rates of CH_4 released from dissociation, the CH_4 production in the gaseous phase, the CH_4 production in the aqueous phase, and total CH_4 production in both the gaseous and aqueous phases (Q_R, Q_{gG}, Q_{gA}, and Q_{gT}, respectively); the cumulative volumes of CH_4 released from dissociation, produced at the well in the gaseous phase, produced at the well in the aqueous phase, produced at the well in both the gaseous and aqueous phases, and remaining in the deposit as free gas (V_R, V_{gG}, V_{gA}, V_{gT}, and V_F, respectively); the water mass production rate at the well (Q_W) and cumulative mass of produced water (M_W); the instantaneous and cumulative water-to-gas ratio ($R_{WG} = Q_W/Q_{gT}$ and $R_{WGT} = M_W/V_{gT}$, respectively); the mass fraction X_{sA} of salt in the produced aqueous phase; and the water flows across key boundaries and interfaces. The following geomechanics-related conditions and parameters were also monitored: the spatial distributions of displacements (u), of the maximum principal effective stress (σ_1'), of the volumetric strain (ε_v); and the vertical displacements at key locations. Note that compressive stress and strain are positive in the following results.

6.1.2.1. Gas Production and Water Production in Cases U1 and U1G

Figure 6.1 shows the evolution of Q_G and Q_A from the single vertical well at the center of the cylindrical reservoir in Cases U1 and U1G. Both Q_G and Q_A in Case U1 increase monotonically, but those in Case U1G fluctuate at the beginning of production and stabilize later. Because the reservoir is under compression, Q_G and Q_A in Case U1G

are lower than those in Case U1, leading to the correspondingly lower M_G and M_A shown in **Figure 6.2**.

Figure 6.3 shows the evolution of Q_R, Q_{gG}, Q_{gA}, and Q_{gT} in Cases U1 and U1G. Critical conclusions from this figure are that: (a) all the rates listed above increase monotonically in Case U1 and are larger than those in Case U1G; (b) Q_{gG} is the main contributor to Q_{gT} in both Cases U1 and U1G; and (c) Q_{gT} is higher than Q_R in Cases U1 and U1G, indicating a significant contribution of exsolution-originating gas to the gas production, in addition to hydrate dissociation. The cumulative volumes V_R, V_{gG}, V_{gA}, V_{gT}, and V_F over the testing period that are shown in **Figure 6.4** are consistent with the results shown in **Figure 6.3**. The relatively low V_F in Cases U1 and U1G indicates a limited volume of gas accumulating in the reservoir.

Figures 6.5 and **6.6** present the evolution of Q_W and M_W produced from the single vertical well in Cases U1 and U1G. Because water is by far the dominant component of the aqueous phase, the trends of Q_W and M_W in **Figures 6.5** and **6.6** are similar to those of Q_A and M_A in **Figures 6.1** and **6.2**, respectively.

Figure 6.7 compares the evolution of R_{WG} and R_{WGT} in Cases U1 and U1G. Because of continuing (and advancing) depressurization-induced dissociation and the associated increasing gas production at the well, R_{WG} and R_{WGT} decrease rapidly at the beginning of production. After t = 5 days of production, R_{WG} in Case U1 remains stable, but increases in Case U1G, thereby indicating continuous water inflows through the boundaries.

Figure 6.8 shows the evolution of X_{sA} in the production stream at the well in Cases U1 and U1G. A lower X_{sA} is caused by the dilution effect of the fresh water released from dissociation; an elevated X_{sA} can be the result of hydrate formation and/or the inflow of saline water from the boundary. Consequently, the initial X_{sA} decline in Cases U1 and U1G indicates fast hydrate dissociation, and the subsequent (slow) upward trends indicate saline water inflows from the boundary (and possibly localized secondary hydrate formation). Note that the results in **Figure 6.8** indicate the larger difference between water inflows and hydrate dissociation in Case U1G than in Case U1.

Figures 6.9 and **6.10** show the evolution of water inflows through key boundaries in Cases U1 and U1G, respectively. Water inflows from the ocean floor and from the bottom of the domain are zero in Cases U1 and U1G during the time covered by the simulation, which means that the size of the domain is sufficiently large enough to prevent the pressure disturbance caused by the production at the well from reaching these boundaries. Because of the larger amounts of water produced at the well in Case U1, water inflows from the boundaries into the reservoir are higher in this case than in Case U1G. Water inflows through the top boundary of the hydrate accumulation are always larger than the inflow through the bottom in Case U1; this is also observed initially in Case U1G, but the relative magnitude of the inflows is reversed after about 19 days of production.

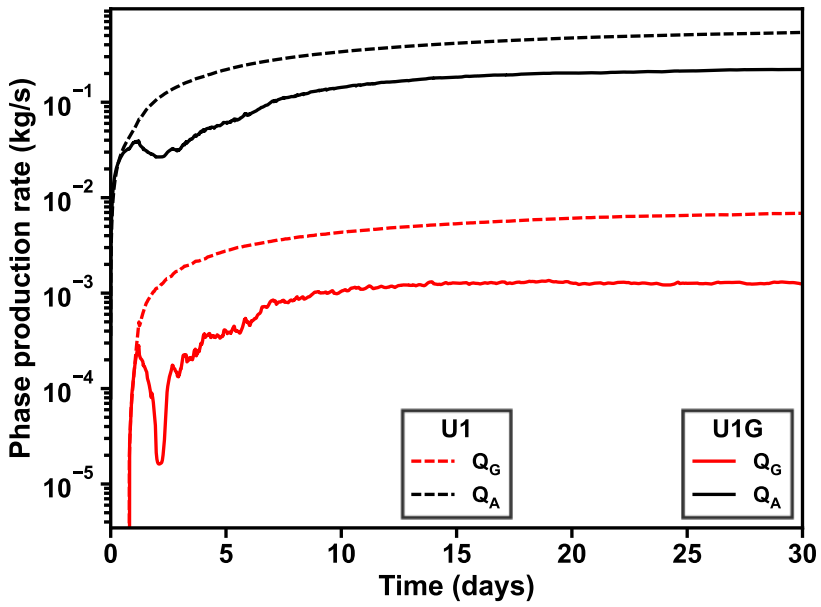

Figure 6.1 Evolution of Q_G and Q_A in Cases U1 and U1G.

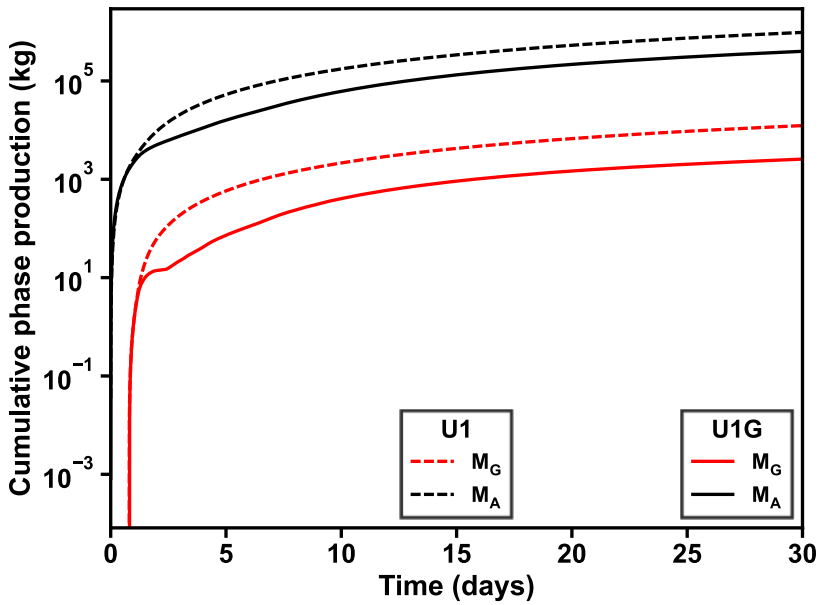

Figure 6.2 Evolution of M_G and M_A in Cases U1 and U1G.

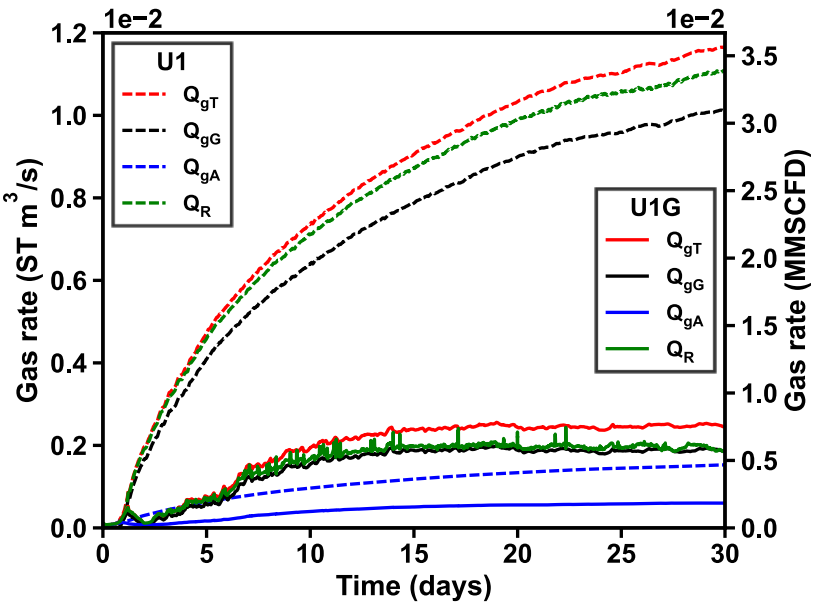

Figure 6.3 Evolution of Q_R, Q_{gG}, Q_{gA}, and Q_{gT} in Cases U1 and U1G.

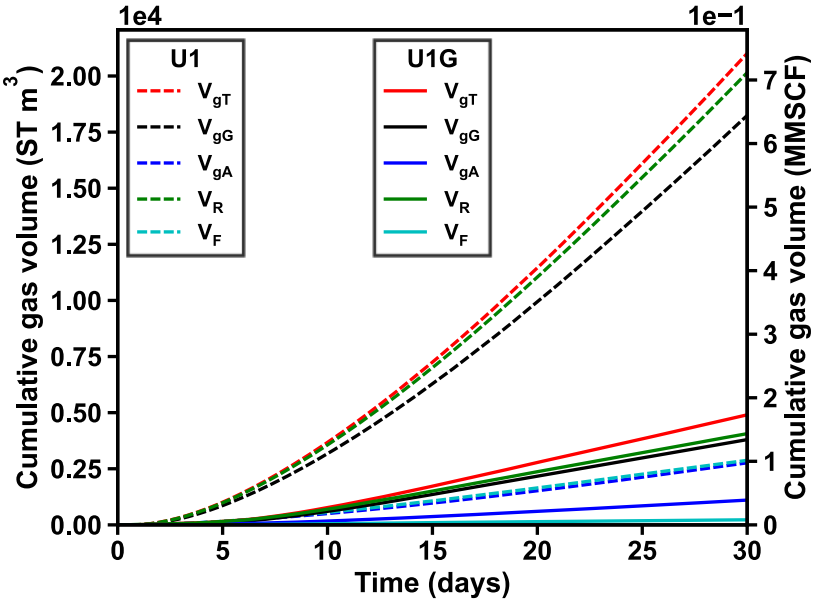

Figure 6.4 Evolution of V_R, V_{gG}, V_{gA}, V_{gT}, and V_F in Cases U1 and U1G.

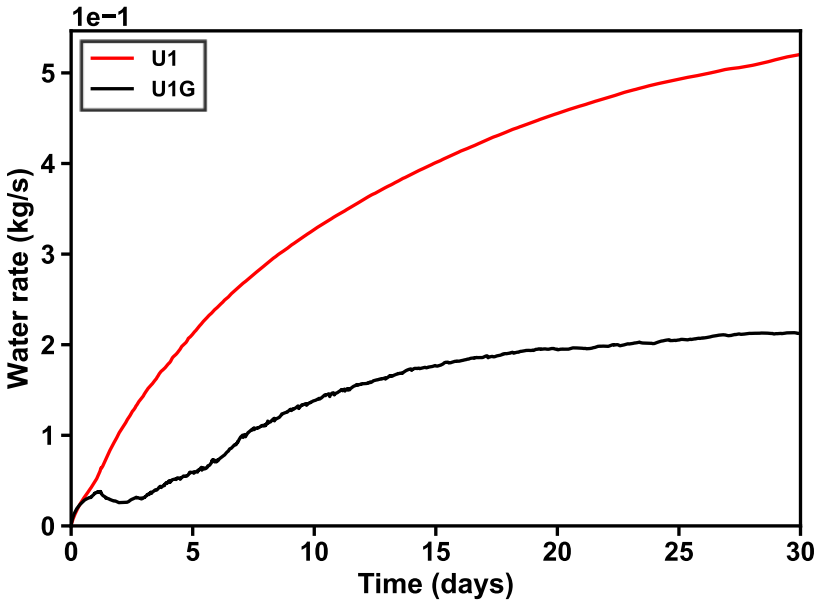

Figure 6.5 Evolution of Q_W in Cases U1 and U1G.

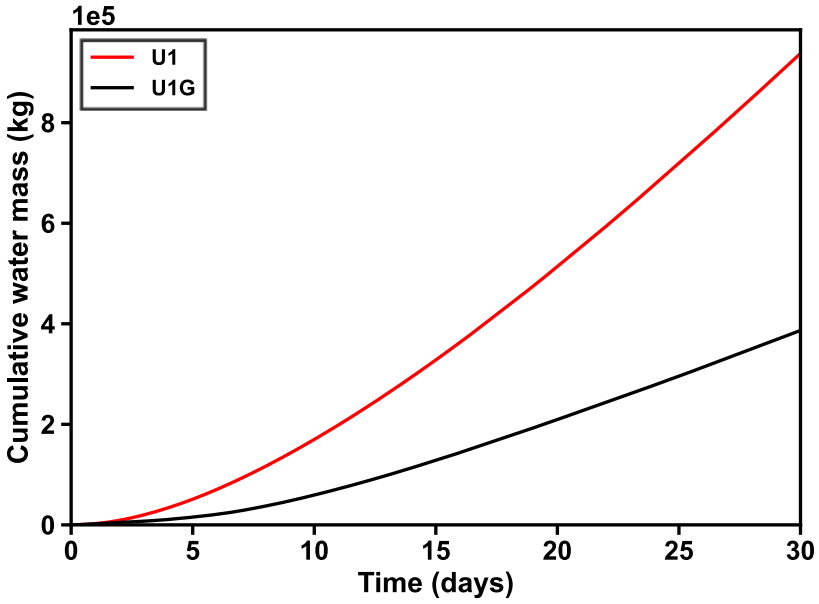

Figure 6.6 Evolution of M_W in Cases U1 and U1G.

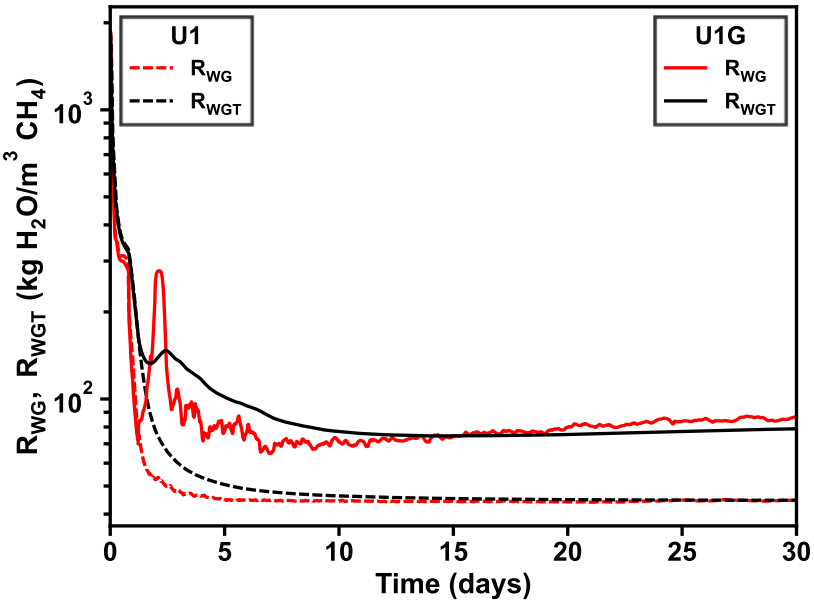

Figure 6.7 Evolution of R_{WG} and R_{WGT} in Cases U1 and U1G.

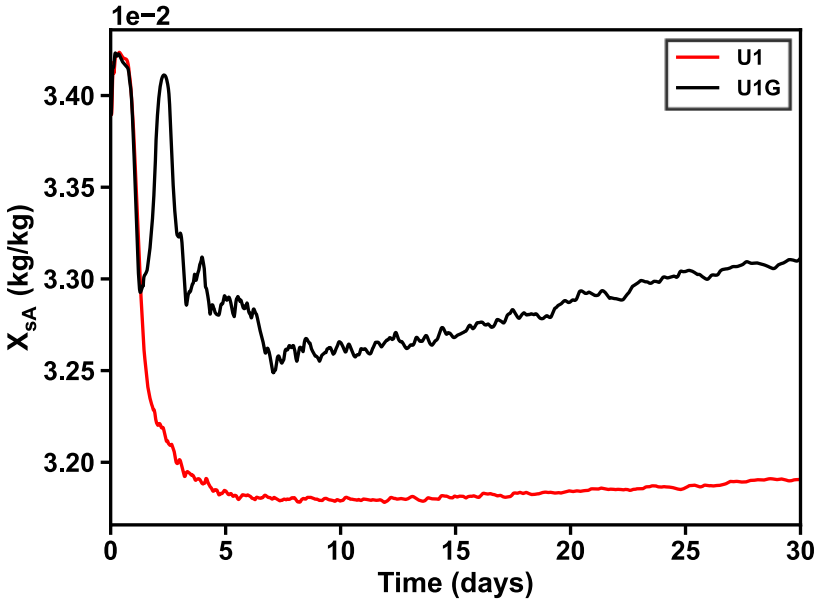

Figure 6.8 Evolution of X_{sA} in Cases U1 and U1G.

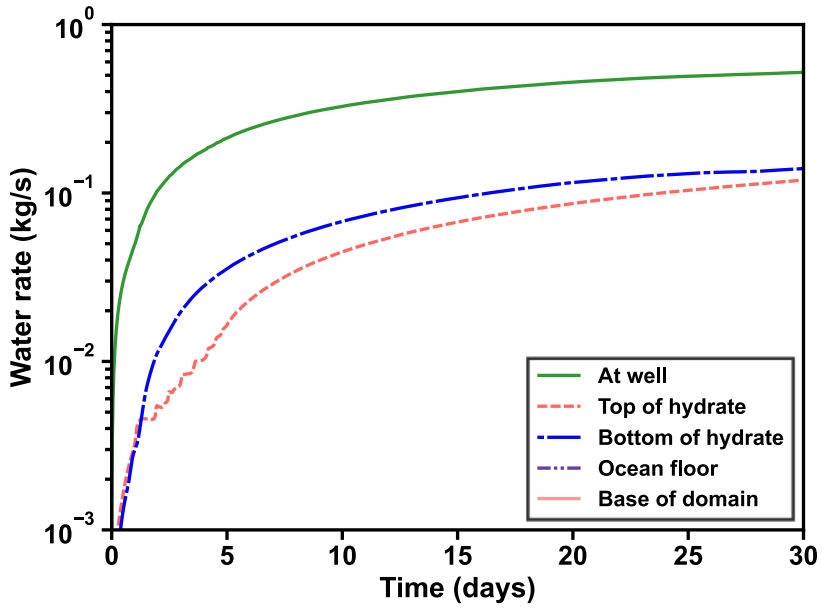

Figure 6.9 Evolution of water flows across key boundaries and interfaces, compared to Q_W in Case U1.

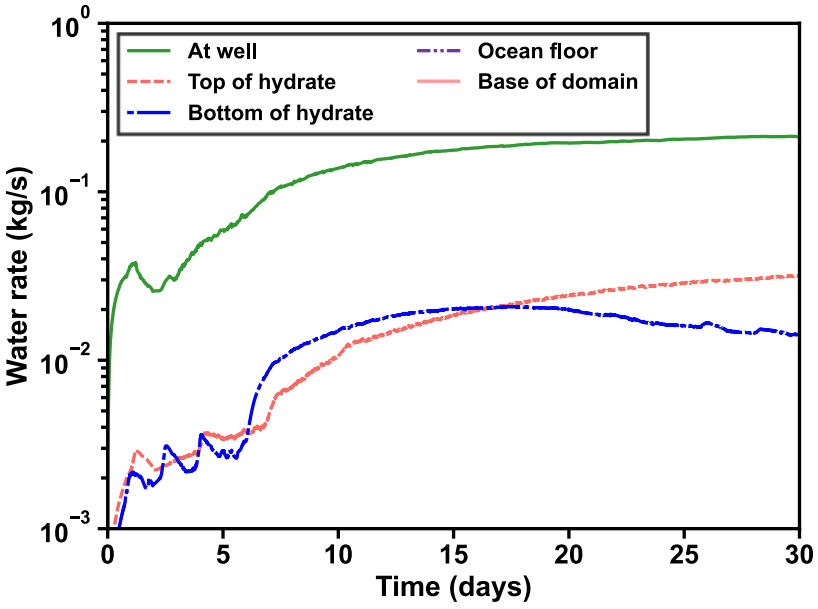

Figure 6.10 Evolution of water flows across key boundaries and interfaces, compared to Q_W in Case U1G.

6.1.2.2. Spatial Distributions of P, T, S_H, and S_G in Cases U1 and U1G

The spatial evolution of P, T, S_H, and S_G in Case U1 (with the simplified geomechanical model) are shown in **Figures 6.11**, **6.12**, **6.13**, and **6.14**, respectively. In **Figure 6.11**, the front of the pressure drop propagates outward from the well along the radial direction over time. The largest pressure drop is observed close to the vertical well where hydrate dissociation occurs in the HBLs. As can be seen in **Figure 6.12**, the low-temperature area indicates hydrate dissociation and is caused by the endothermic nature of the hydrate dissociation process. **Figure 6.13** shows that S_H decreasing near the well, with hydrate dissociation concentrating mainly near the upper and boundaries of each HBL. What is striking about the H5 layer is that a wormhole grows in the middle section. High S_G occurrence in **Figure 6.14** is observed where S_H is low in the HBLs because of active dissociation at these locations. The highest S_G is observed near the top of the H4 layer.

The spatial evolution of P, T, S_H, and S_G in Case U1G (with the full geomechanical model) are shown in **Figures 6.15**, **6.16**, **6.17**, and **6.18**, respectively. The pressure drop front in Case U1G (shown in **Figure 6.15**) does not advance very far into the formation and, compared to the pressure profile in Case U1, it exhibits a heterogeneous/uneven vertical distribution within each HBL that is attributed to geomechanically induced changes in the porosity and permeability of these layers and the mud interlayers. In the MLs, the media are so soft that the decreased porosity causes a lower effective permeability and the smaller pressure drop. **Figure 6.16** shows a low-temperature area (indicative of active hydrate dissociation) that is less extensive in Case U1G than in Case

U1. In **Figure 6.17**, the spatial distribution of S_H in Case U1G shows that the hydrate dissociates in the lower section of the H1 and H2 layers, and no wormhole growth in the H5 layer, which is different from the dissociation pattern in Case U1. The spatial distribution of S_G shown in **Figure 6.18** confirms the observation from **Figure 6.17** that active hydrate dissociation mainly occurs in the lower section of the H1 and H2 layers in the full-geomechanics Case U1G.

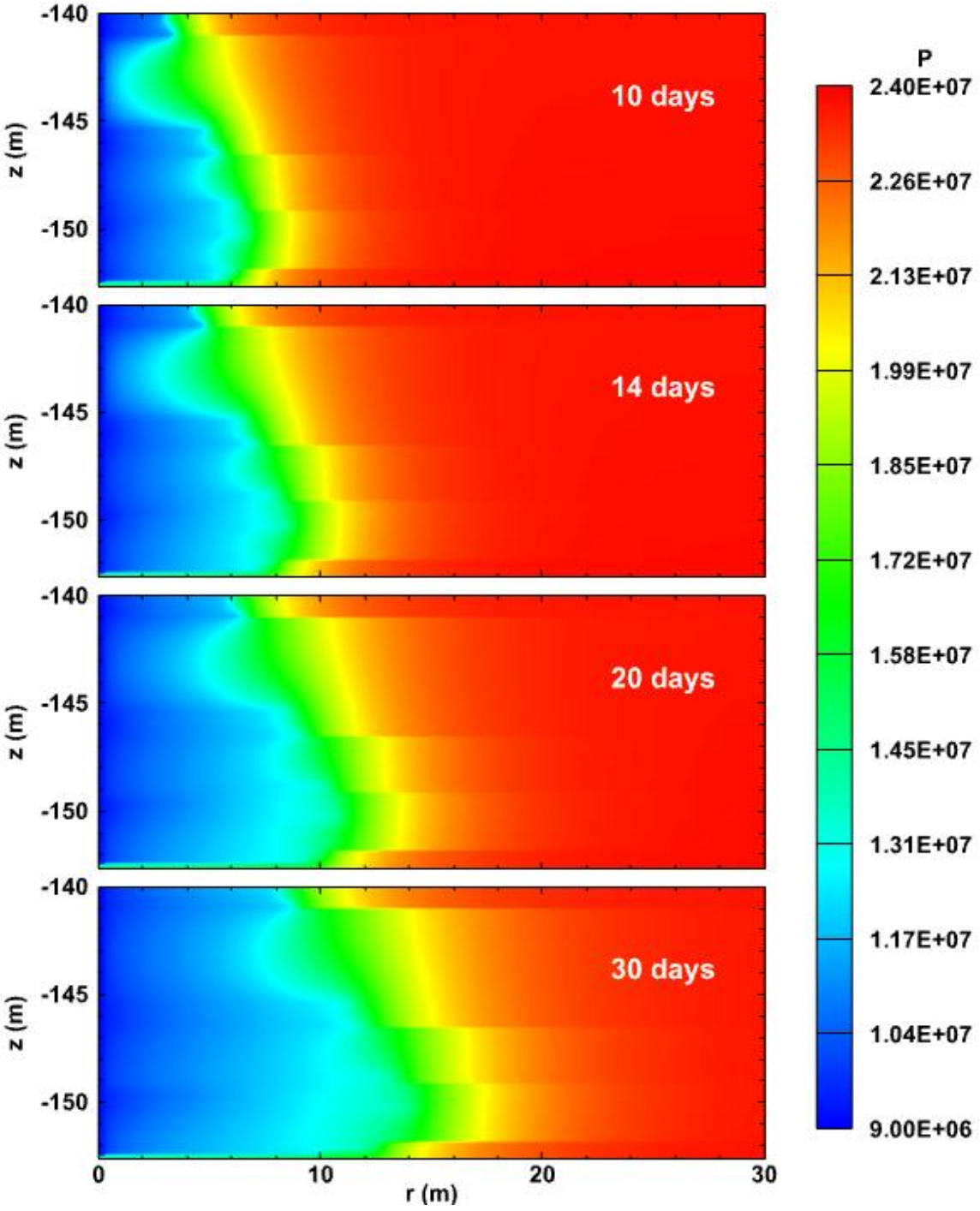

Figure 6.11 Evolution of the spatial distribution of pressure (Pa) in the reservoir of Case U1.

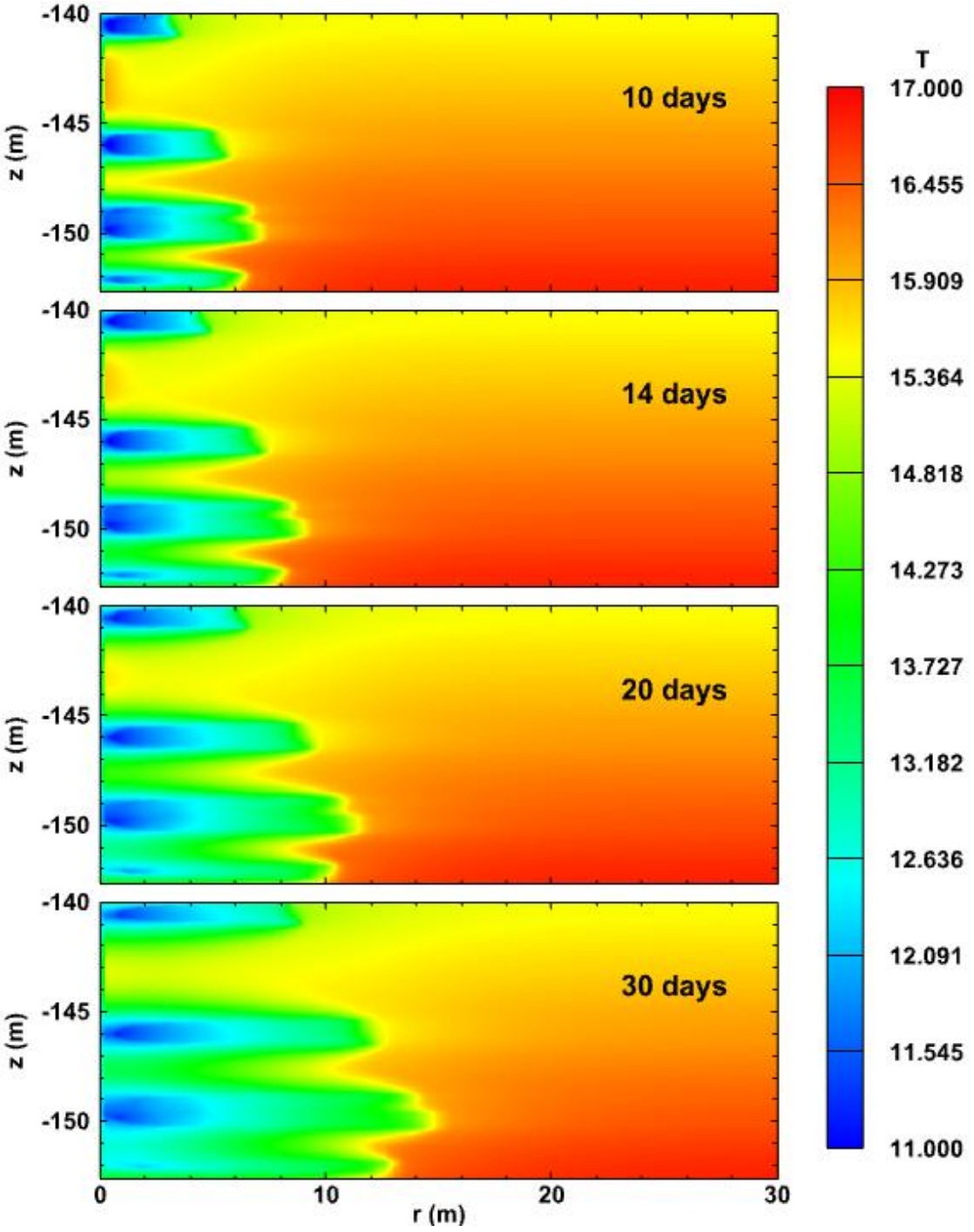

Figure 6.12 Evolution of the spatial distribution of temperature (°C) in the reservoir of Case U1.

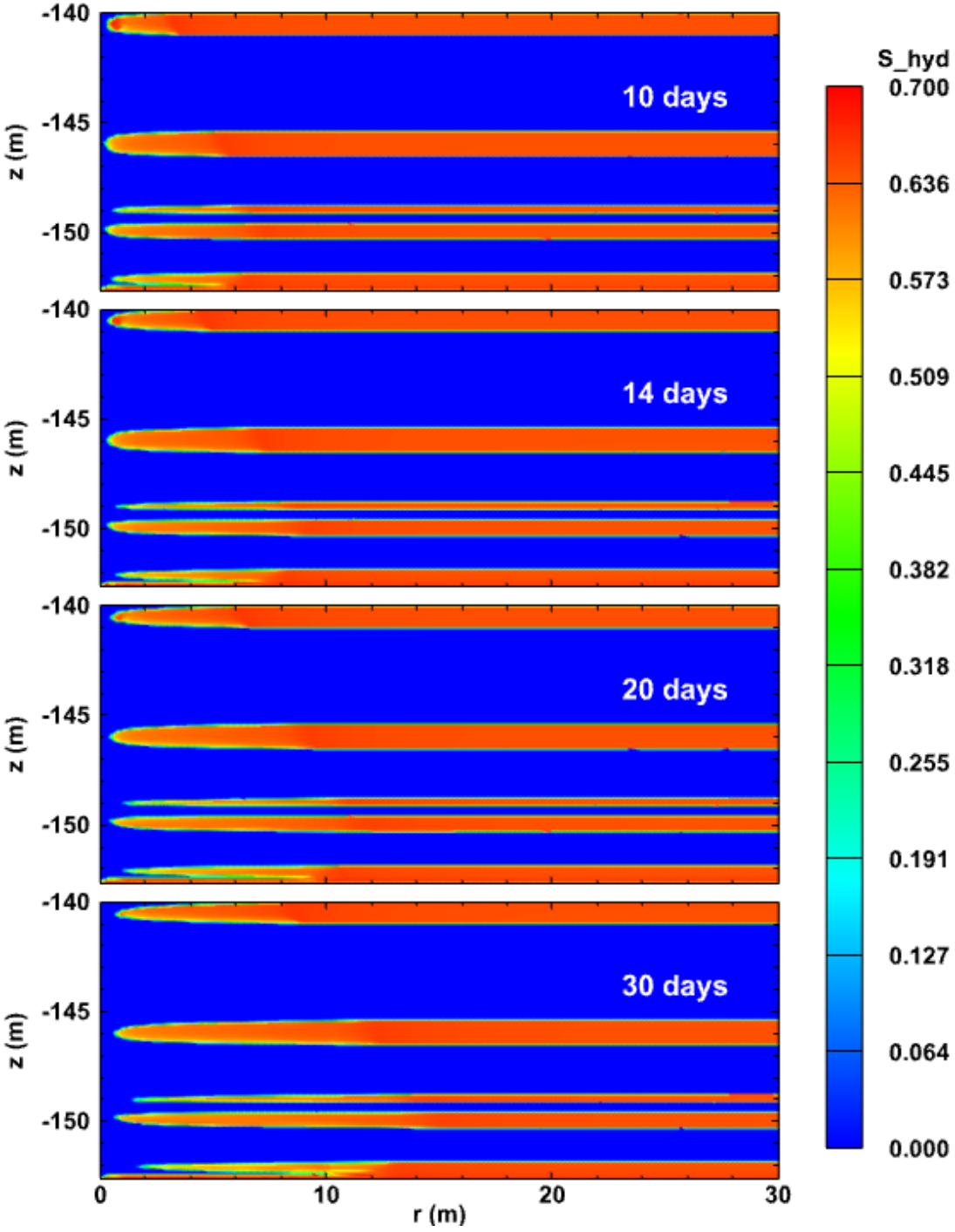

Figure 6.13 Evolution of the spatial distribution of hydrate saturation in the reservoir of Case U1.

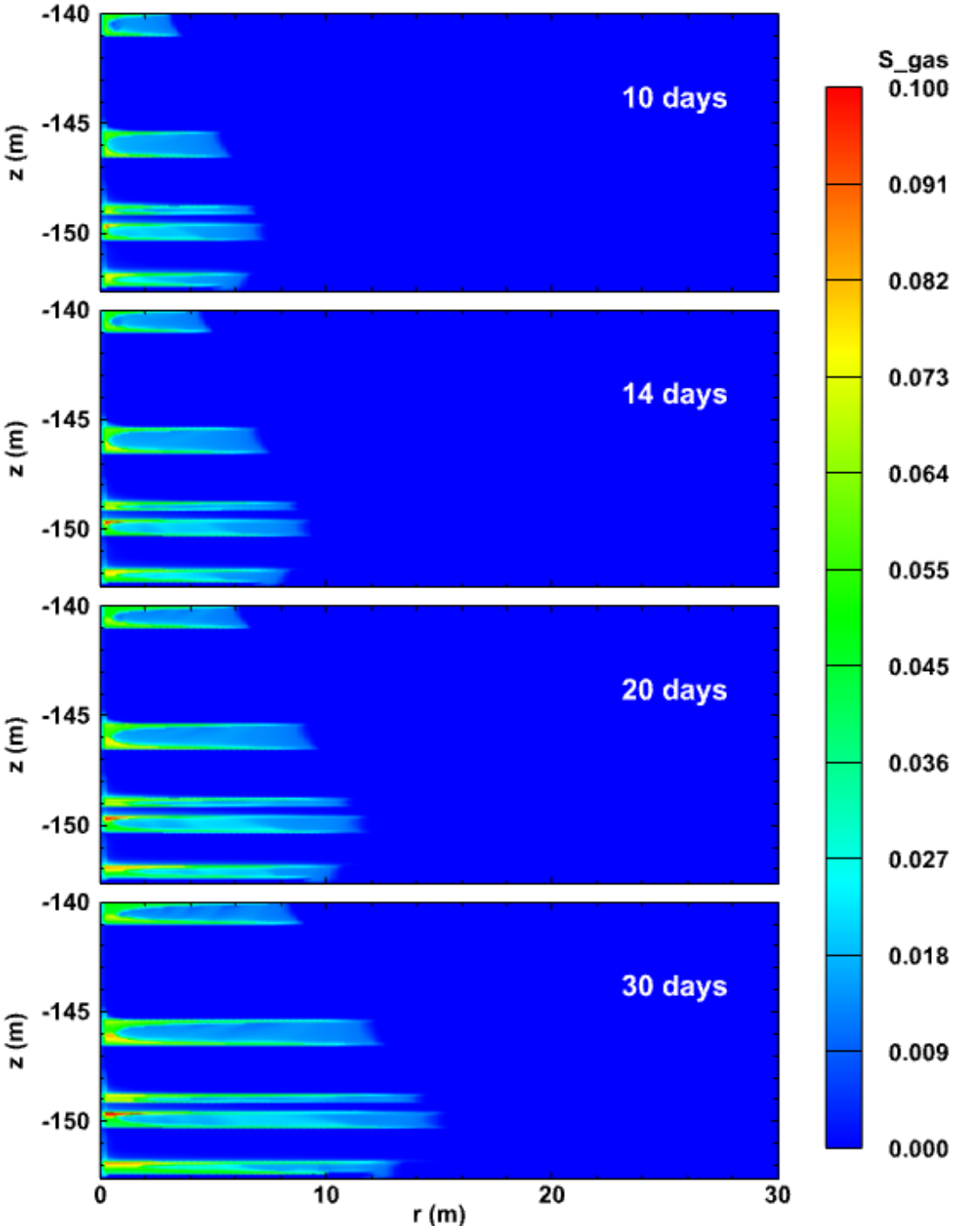

Figure 6.14 Evolution of the spatial distribution of gas saturation in the reservoir of Case U1.

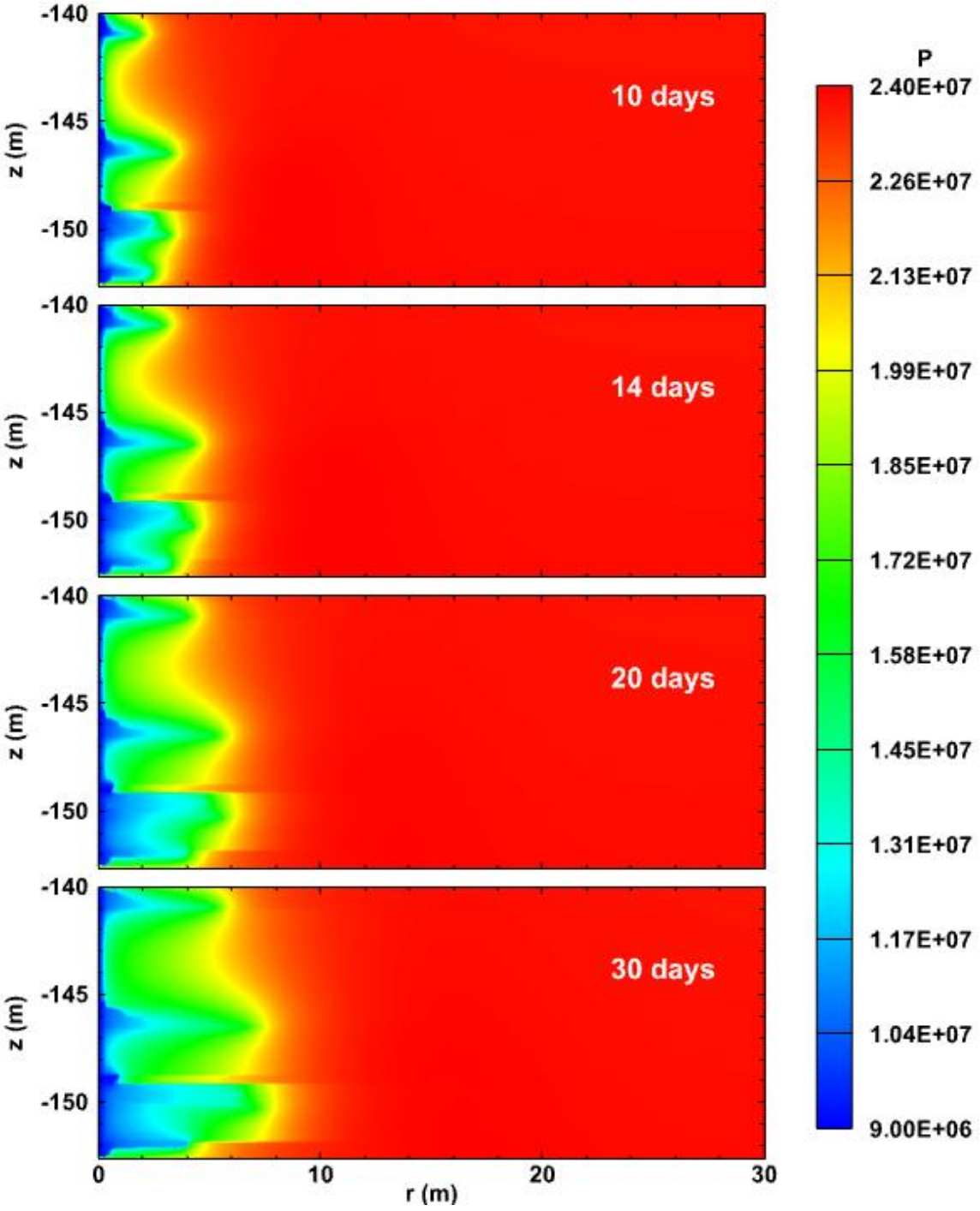

Figure 6.15 Evolution of the spatial distribution of pressure (Pa) in the reservoir of Case U1G.

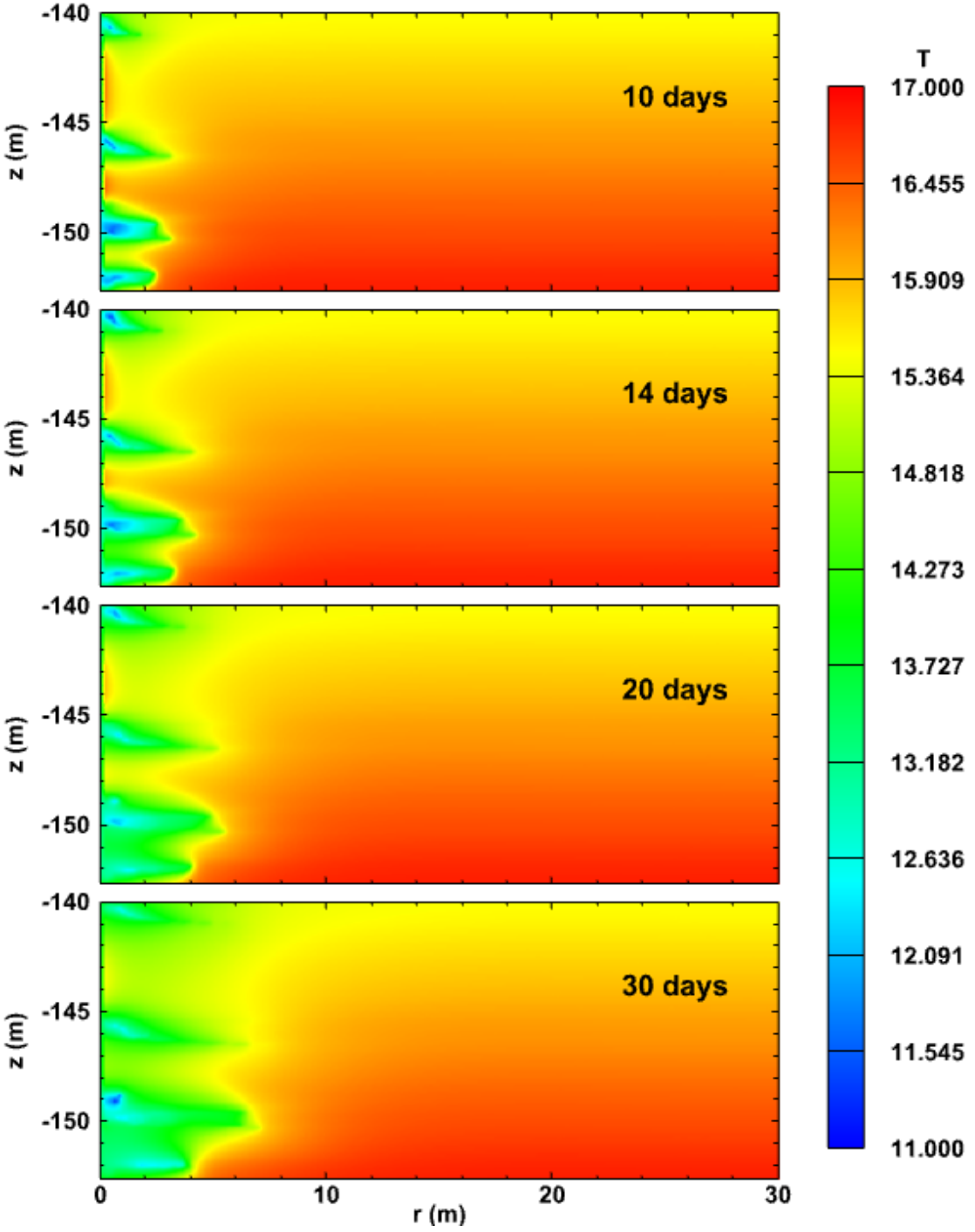

Figure 6.16 Evolution of the spatial distribution of temperature (°C) in the reservoir of Case U1G.

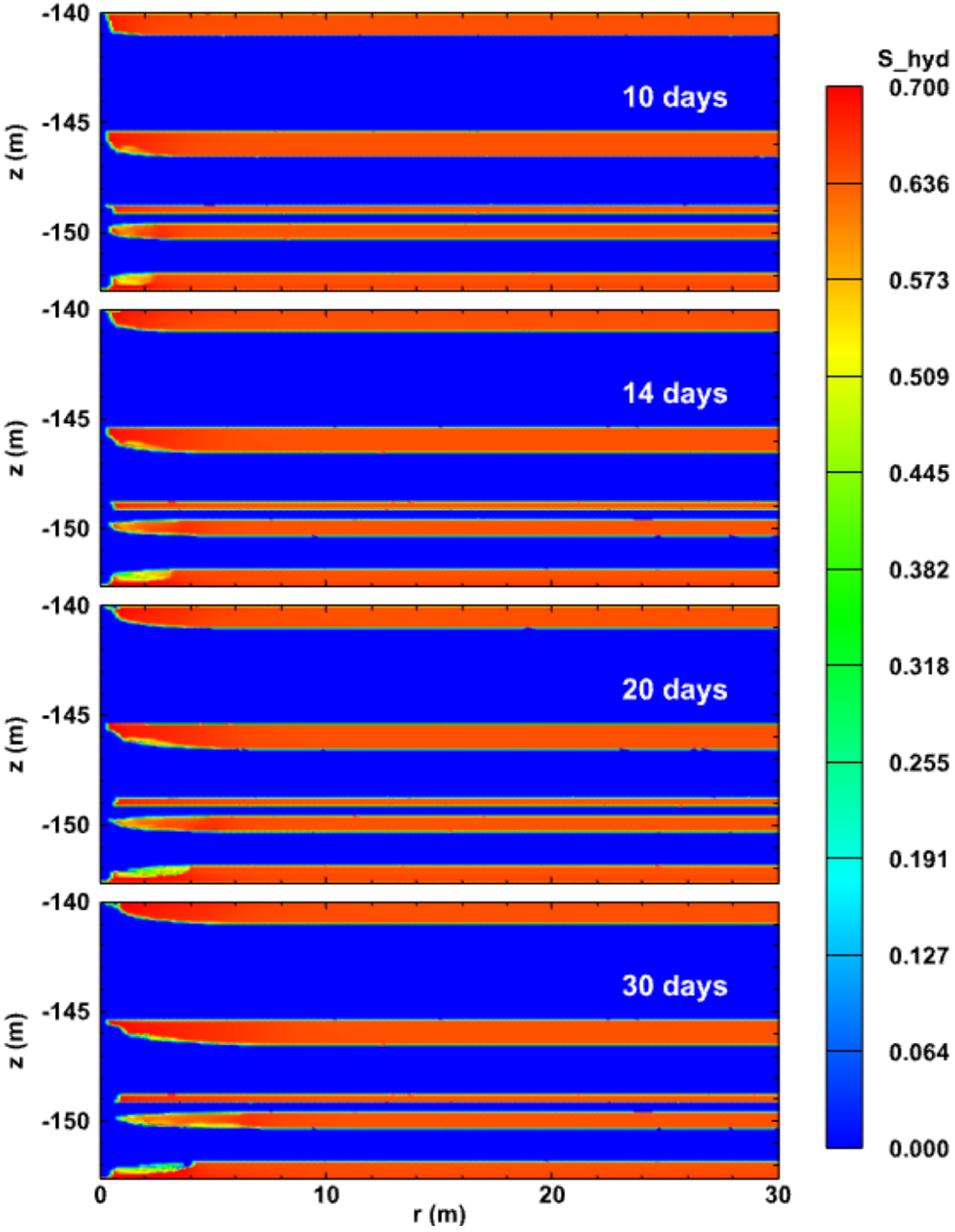

Figure 6.17 Evolution of the spatial distribution of hydrate saturation in the reservoir of Case U1G.

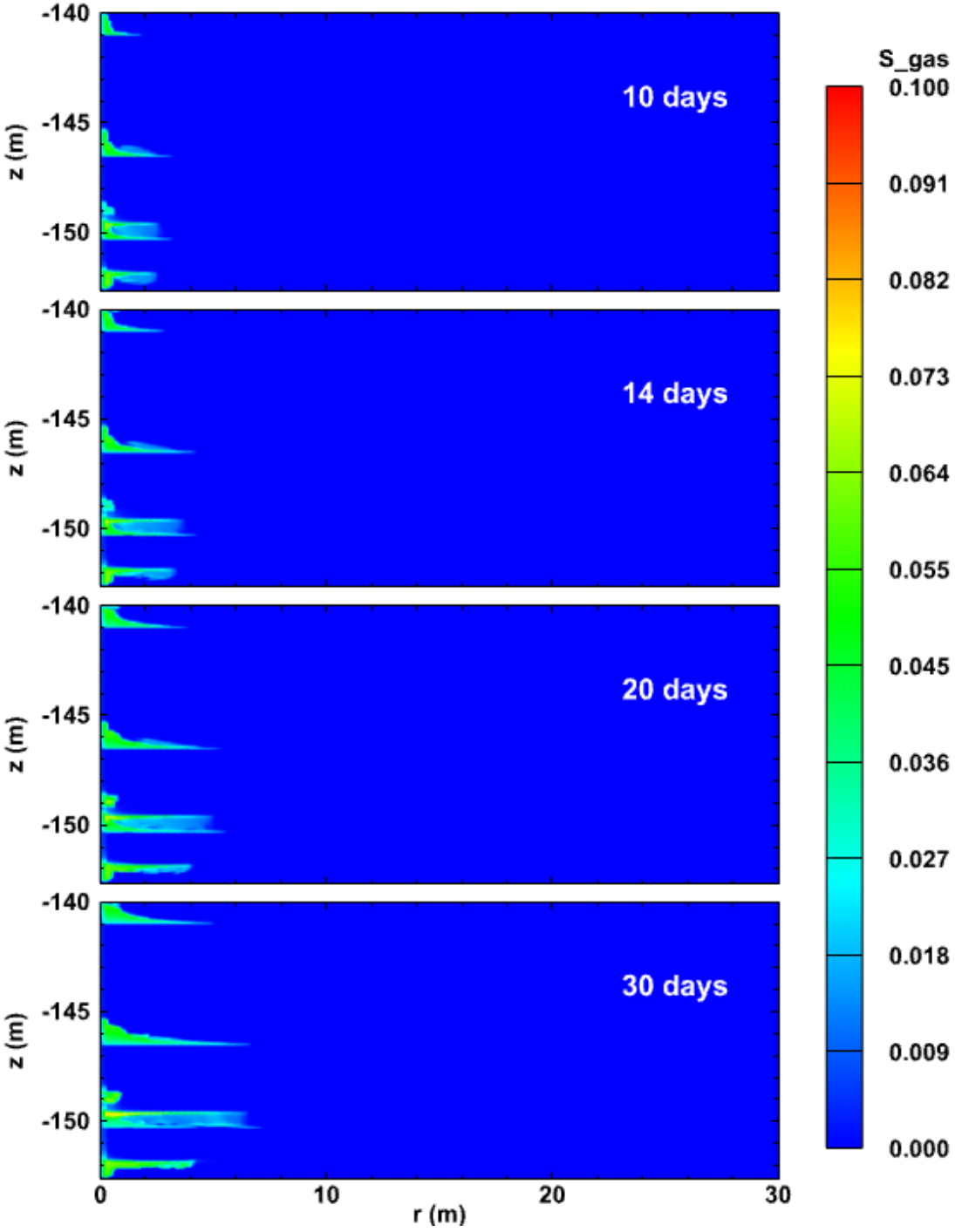

Figure 6.18 Evolution of the spatial distribution of gas saturation in the reservoir of Case U1G.

6.1.2.3. Evolution of Displacement in Case U1G

Figure 6.19 shows the evolution of the vertical displacements u_z at the wellbore (r = 0 m) and at (a) the top of the reservoir (z = -140 m) and (b) the bottom of the reservoir (z = -152.67 m). The largest subsidence occurs at (r, z) = (0 m, -140 m) and reaches 0.78 m at t = 30 days because of the pore pressure continues to drop in the reservoir, which causes compaction of the formation near the wellbore. Because of this reason, the bottom of the reservoir at the wellbore is uplifted by 0.78 m at t = 30 days. The displacement difference is 1.56 m, which is more than 10% of the reservoir thickness. A higher bottomhole location should be considered if such large displacements and reservoir compaction near the well are to be avoided.

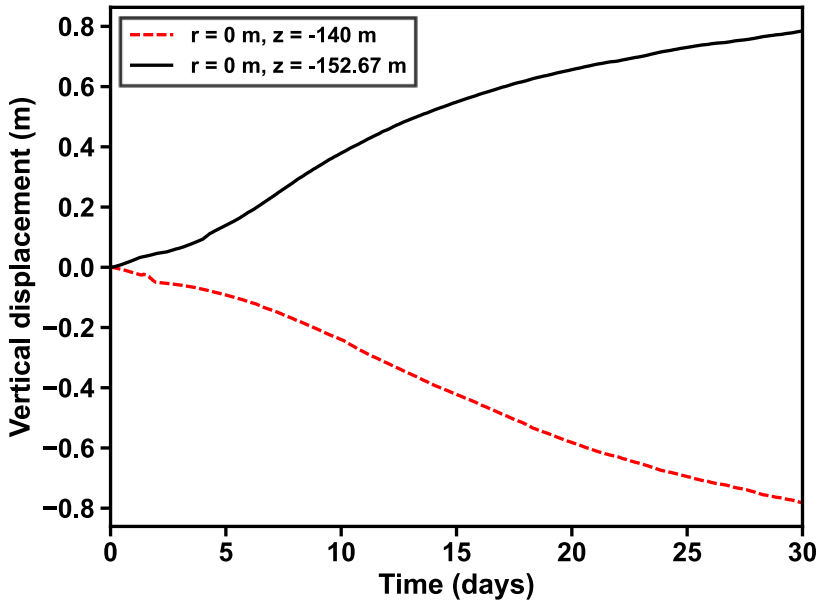

Figure 6.19 Evolution of u_z at (r, z) = (0 m, -140 m) and (r, z) = (0 m, -152.67 m) in Case U1G.

6.1.2.4. Spatial Distributions of u, σ_1', and ε_v in Case U1G

Figures 6.20, **6.21**, and **6.22** present the spatial evolution of u, σ_1', and ε_v, respectively, in Case U1G. In **Figure 6.20**, the contour plot depicts the vertical displacements, and the arrows denote the direction of the displacement vector. The formation is so soft that the upper and lower bounds of the contour plot differ significantly, leading to large displacement changes as early as at t = 10 days. At t = 10 days, the vertical displacement at (r, z) = (5 m, -140 m) is -0.11 m and at (r, z) = (5 m, -152.67 m) is 0.01 m. Along the radial direction, the formation moves toward the wellbore, and a measurable deformation can be identified at a radius r = 7 m away from the production wellbore at t = 30 days. The maximum principal effective stress in **Figure 6.21** becomes substantially large in the vicinity of the hydrate dissociation location. The volumetric strain in **Figure 6.22** is significant because of the large deformation depicted in **Figure 6.20**. The hydrate in the HBLs makes these sandy layers much stiffer than the hydrate-free MLs, and is the reason for the smaller changes in the volumetric strain of the HBLs compared to those in the MLs, as shown in **Figure 6.22**.

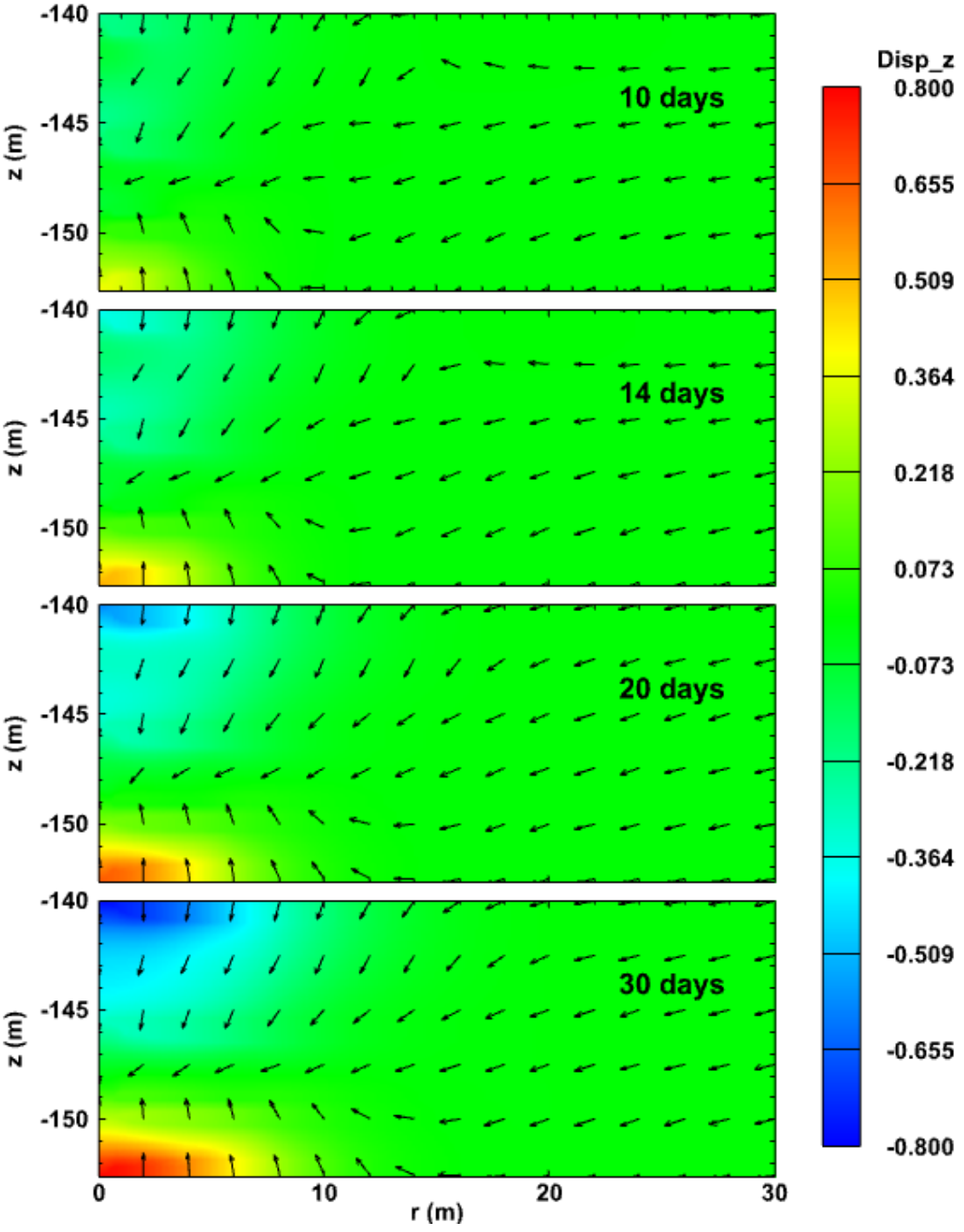

Figure 6.20 Evolution of the spatial distribution of displacements (m) in the reservoir of Case U1G.

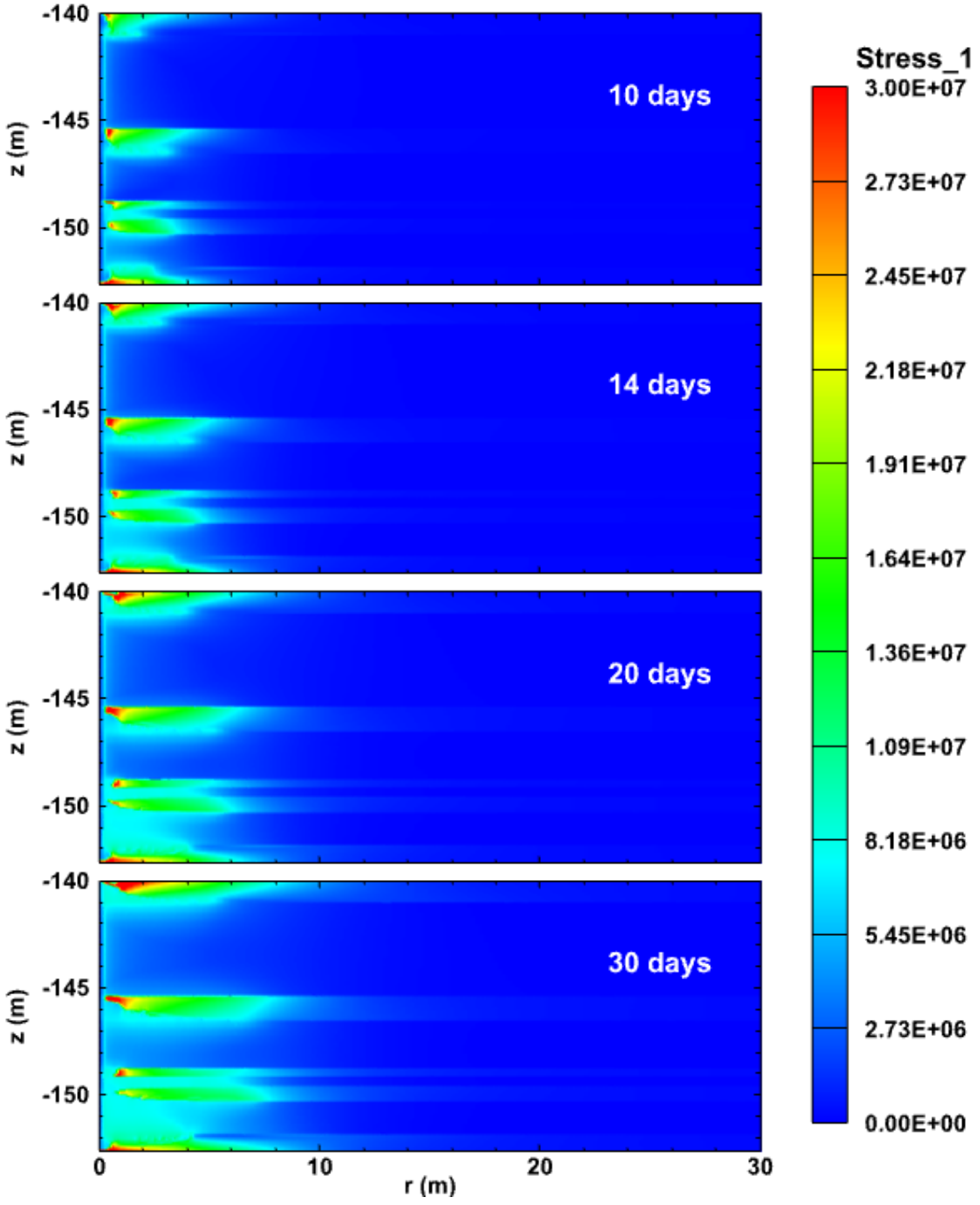

Figure 6.21 Evolution of the spatial distribution of maximum principal effective stress (Pa) in the reservoir of Case U1G.

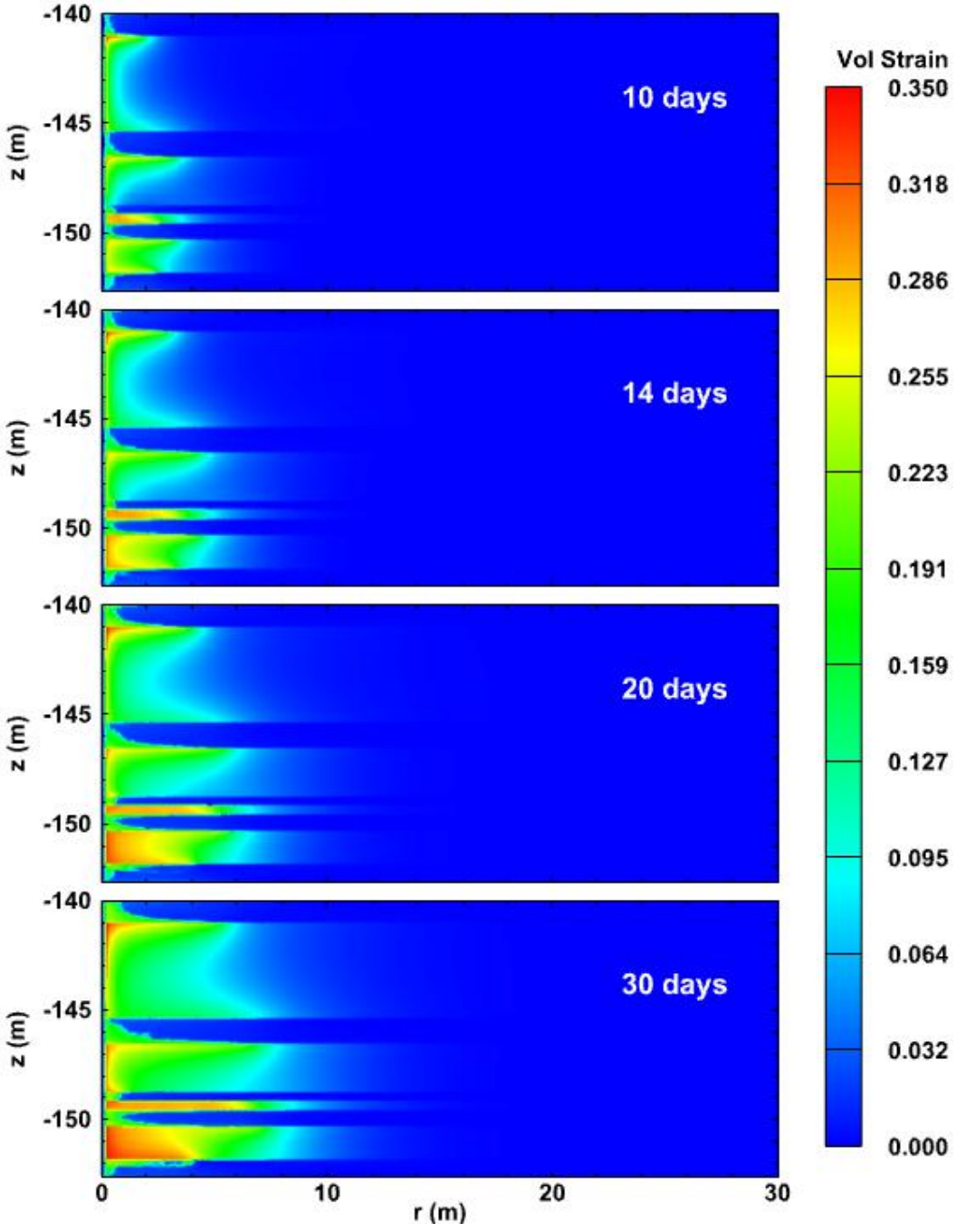

Figure 6.22 Evolution of the spatial distribution of volumetric strain in the reservoir of Case U1G.

6.2. The Two-Dimensional Cylindrical Cases U2 and U2G

These two cases were investigated in order to evaluate the influence of the mesh size on the flow and geomechanical results using the simplified and full geomechanical models.

6.2.1. Problem Description

Cases U2 and U2G are the same as Cases U1 and U1G but with a coarser discretization involving fewer gridblocks in both the *r*- and *z*-directions. The system radius r_{max} was shortened from 600 to 250 m, and the thickness of the underburden was reduced from 347.43 to 300 m. Although the corresponding domain was smaller than that of Cases U1 and U1G, the domain size was still sufficient to evaluate the geomechanics effect and the heat and water exchange with the reservoir during the 30 days of the production test.

6.2.1.1. Domain Discretization

The 2D domain discretized into 170 × 149 subdivisions in (*r*, *z*), resulting in 25,330 gridblocks. Along the radial direction, the Δr subdivisions increased in size logarithmically from an initial Δr = 0.05 m at the well to reach r_{max} = 250 m. The Δz subdivisions varied between 0.09 and 0.26 m within the hydrate accumulation and increased to larger values in the OB and the UB. The mesh used in Cases U2 and U2G is shown in **Figure 6.23**. The mesh in the hydrate accumulation near the well is shown in **Figure 6.24**. The FT problem in Case U2 involved about 101,300 equations, and the geomechanical problem in Case U2G involved another 51,300 simultaneous equations.

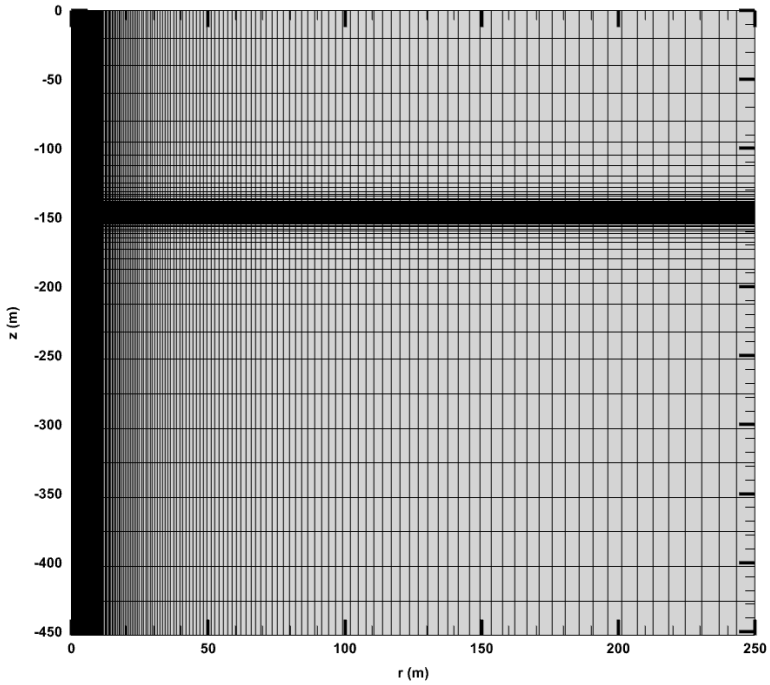

Figure 6.23 Mesh used in the problems of Cases U2 and U2G.

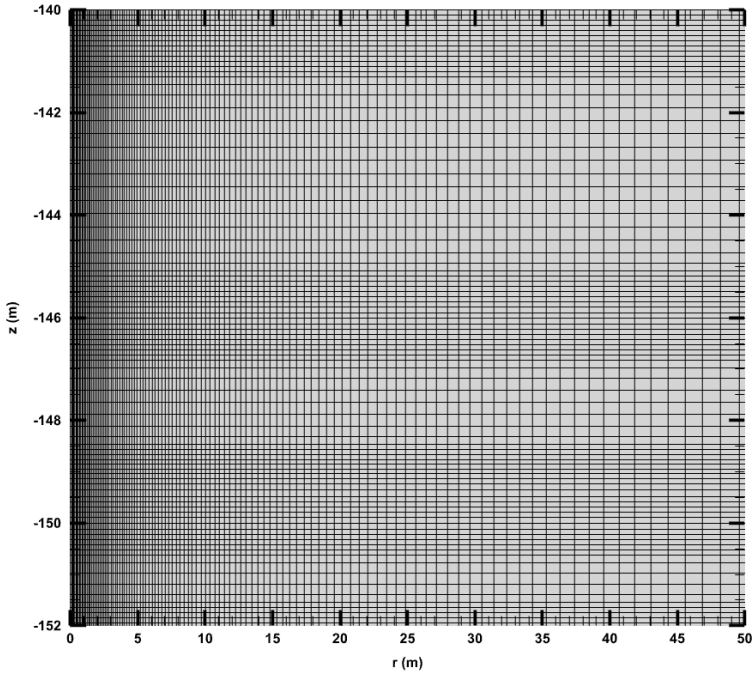

Figure 6.24 Mesh in the hydrate accumulation near the well in the problems of Cases U2 and U2G.

6.2.2. Results

The flow- and geomechanics-related conditions and parameters that were monitored in cases U2 and U2G were the same as those discussed in Cases U1 and U1G (see Section 6.1.2) and will not be listed here again.

6.2.2.1. Gas Production and Water Production in Cases U1 and U2

Figure 6.25 shows the evolution of Q_G and Q_A from the single vertical well at the center of the cylindrical reservoir in Cases U1 and U2. Compared to Case U1, the constant bottomhole pressure regime at the well yields lower Q_G and Q_A in Case U2, resulting in the lower M_G and M_A shown in **Figure 6.26**. For obvious reasons (already discussed), a lower CH_4 and H_2O production is expected in Case U2.

Figure 6.27 shows the evolution of Q_R, Q_{gG}, Q_{gA}, and Q_{gT} from the single vertical well in Cases U1 and U2. As indicated in the discussion of **Figures 6.25** and **6.26**, the Q_R, Q_{gG}, Q_{gA}, and Q_{gT} in Case U2 are all lower than those in case U1. Furthermore, the relative magnitudes of Q_R and Q_{gT} are switched in Case U2 from those in Case U1, indicating that, unlike Case U1, the majority of the produced gas originated from hydrate dissociation rather than from exsolution of gas dissolved in the water. As expected from the enhanced dissociation in this case, the amount of free gas V_F is larger in Case U2 (see **Figure 6.28**). It is obvious that the different meshes in Cases U1 and U2 result in pronounced differences in production and the overall system response during production.

The evolution of Q_W and M_W in **Figures 6.29** and **6.30** are nearly identical to the evolution of Q_A in and M_A in **Figures 6.25** and **6.26**, respectively, because H_2O is the overwhelmingly dominant species in the aqueous phase.

Figure 6.31 compares the evolution of R_{WG} and R_{WGT} in Cases U1 and U2. Both R_{WG} and R_{WGT} are higher in Case U2, indicating that the reduction in gas production is larger than that in water production. The higher X_{sA} in Case U2 after the initial drop in **Figure 6.32**, and the subsequent steeper increase, indicate either relatively larger water inflows from the boundaries (as confirmed by the results in **Figure 6.33**) or less active hydrate dissociation or both than the corresponding response in Case U1.

Figure 6.33 shows the evolution of water inflows across key boundaries in Case U2. The zero water inflows from the ocean floor and through the base of the domain prove that the domain is sufficiently large for the boundaries to behave as infinite-acting.

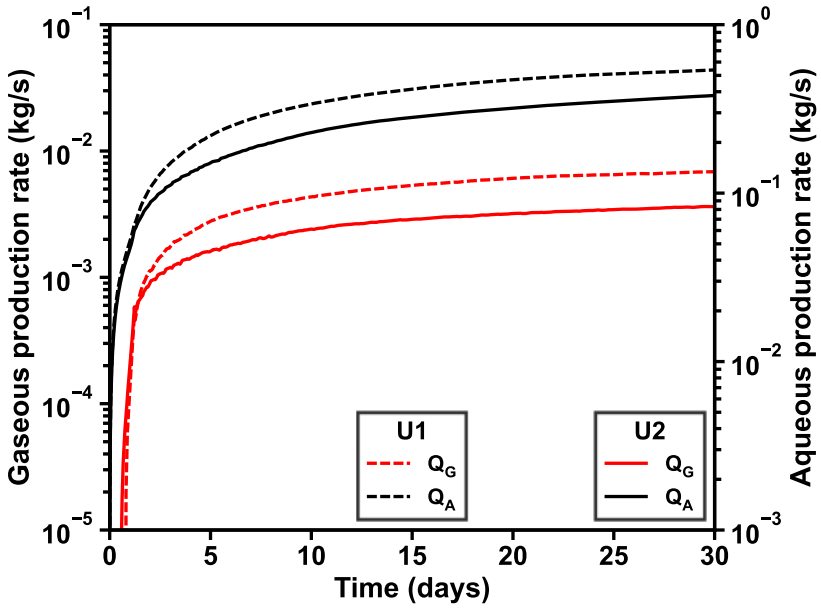

Figure 6.25 Evolution of Q_G and Q_A in Cases U1 and U2.

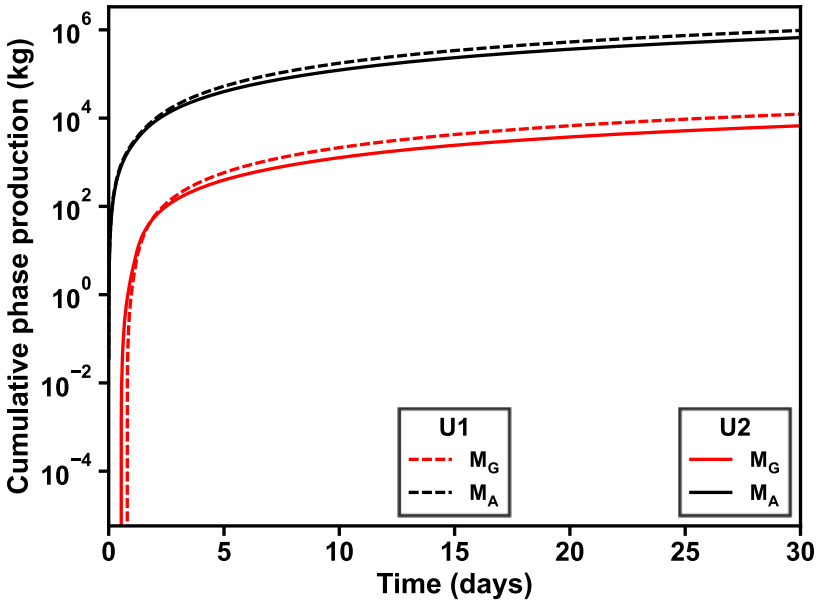

Figure 6.26 Evolution of M_G and M_A in Cases U1 and U2.

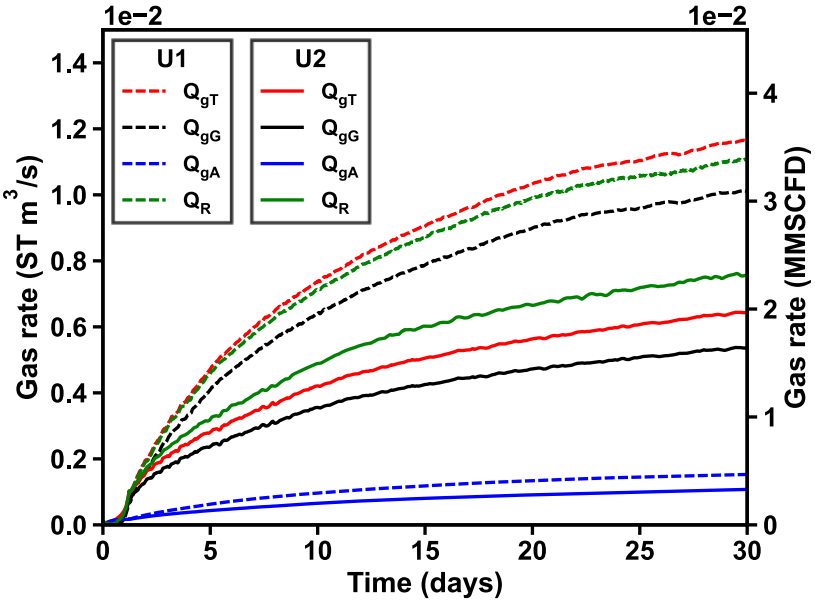

Figure 6.27 Evolution of Q_R, Q_{gG}, Q_{gA}, and Q_{gT} in Cases U1 and U2.

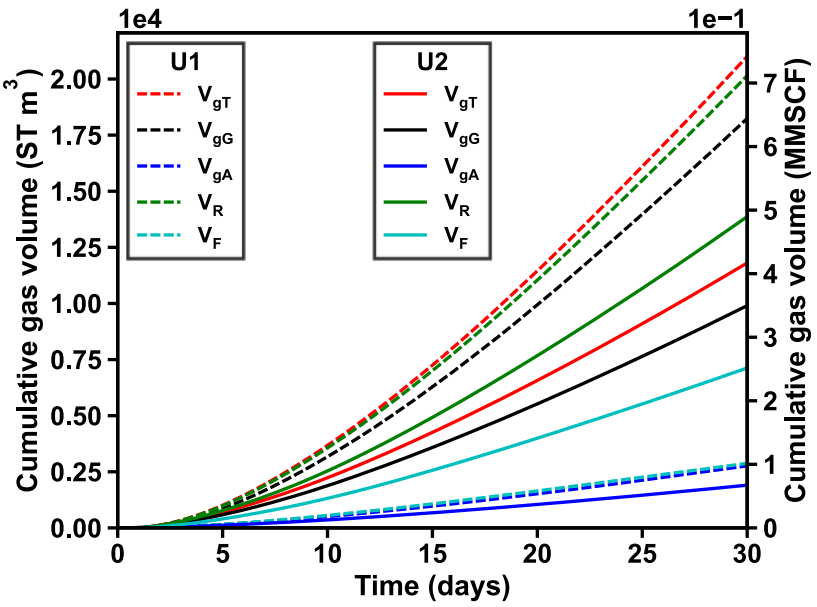

Figure 6.28 Evolution of V_R, V_{gG}, V_{gA}, V_{gT}, and V_F in Cases U1 and U2.

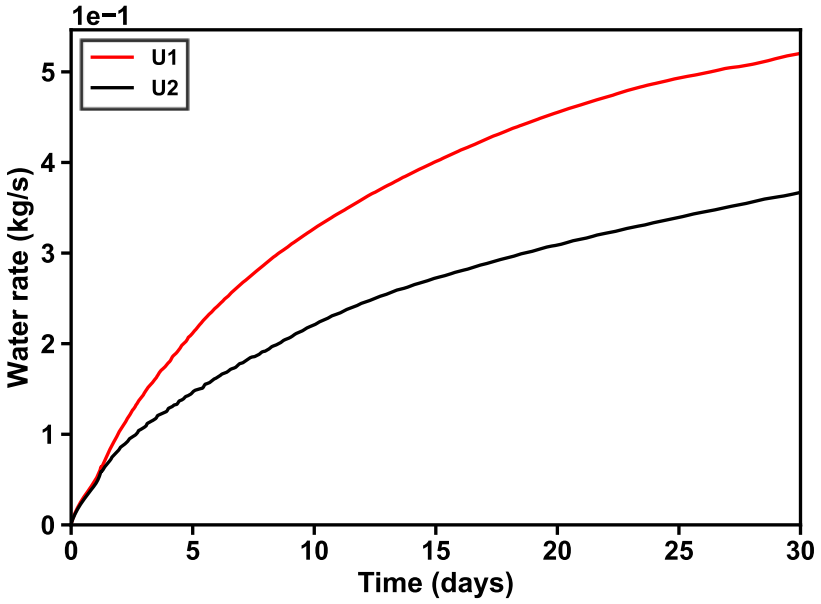

Figure 6.29 Evolution of Q_W in Cases U1 and U2.

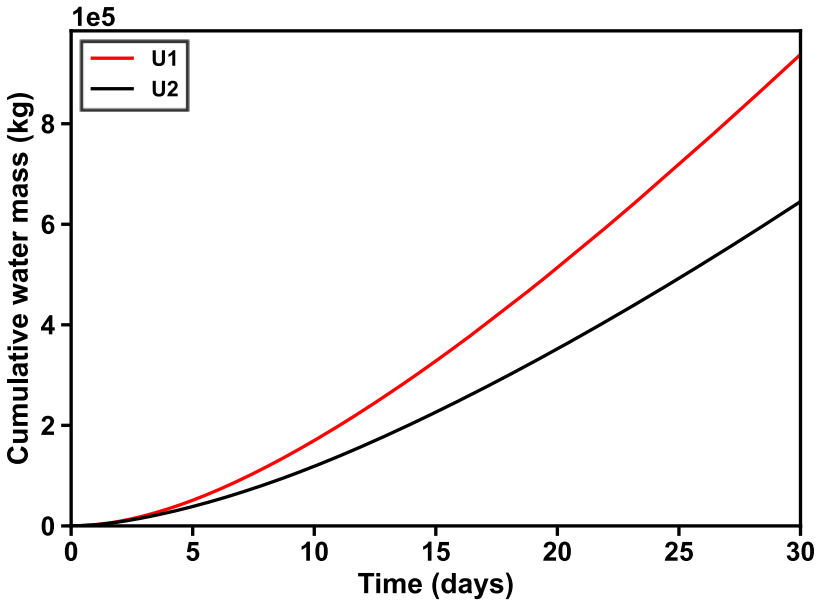

Figure 6.30 Evolution of M_W in Cases U1 and U2.

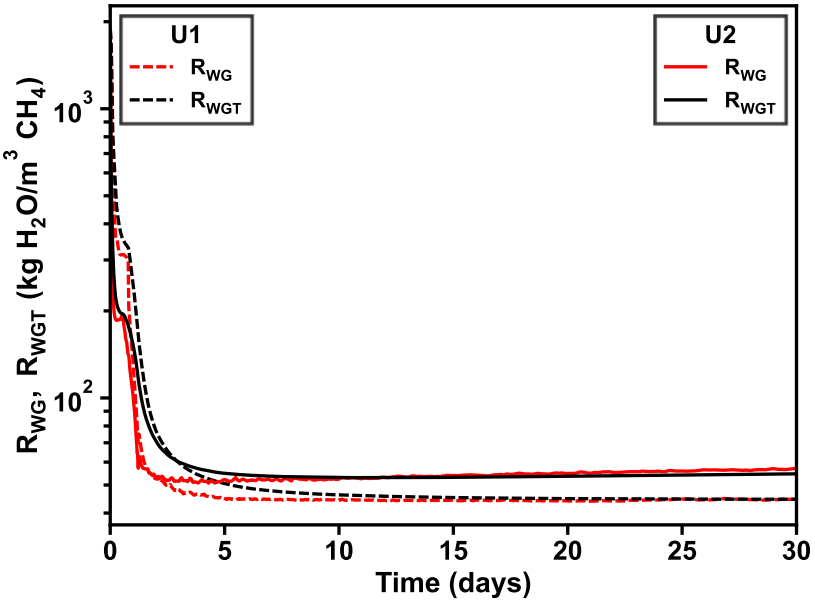

Figure 6.31 Evolution of R_{WG} and R_{WGT} in Cases U1 and U2.

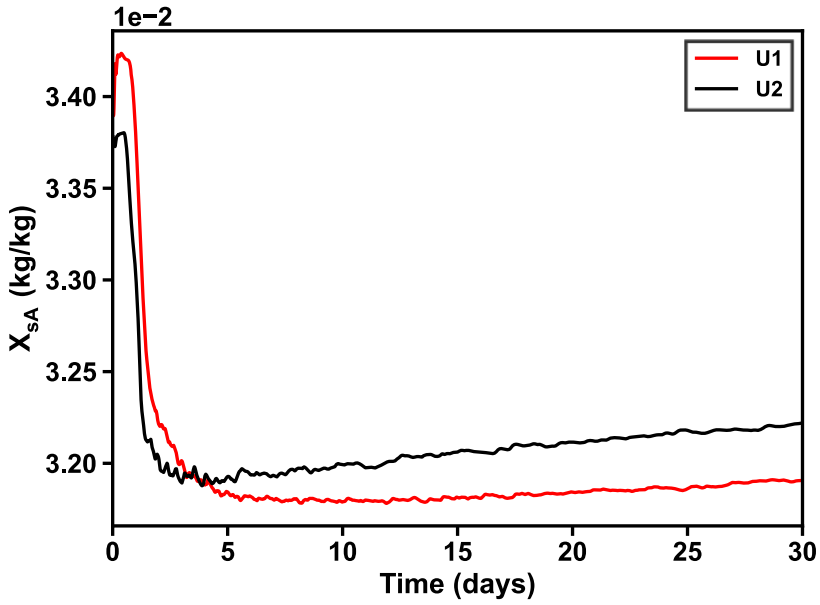

Figure 6.32 Evolution of X_{sA} in Cases U1 and U2.

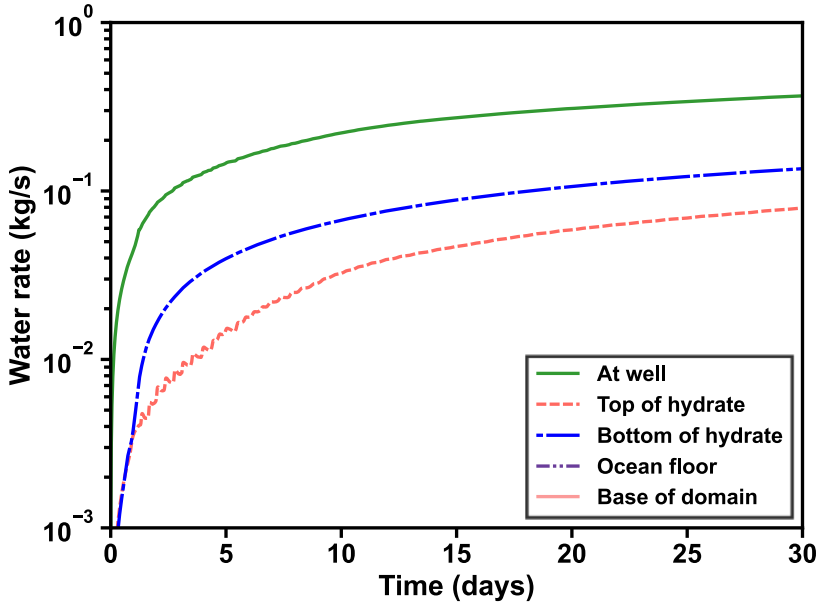

Figure 6.33 Evolution of water flows across key boundaries and interfaces, compared to Q_W in Case U2.

6.2.2.2. Spatial Distributions of P, T, S_H, and S_G in Case U2

The spatial evolution of P, T, S_H, and S_G in Case U2 (with the simplified geomechanical model) are shown in **Figures 6.34**, **6.35**, **6.36**, and **6.37**, respectively. **Figure 6.34** shows that the pressure drop near the wellbore is larger than that in Case U1 and extends over a smaller distance from the well, thus affecting a smaller reservoir volume. In addition, the pressure difference between the M4 and H5 layers is minimal compared to that in Case U1. In **Figure 6.35**, active dissociation causes lower temperatures in the HBLs and even affects the M1 layer. The wormhole initiated in the H5 layer in Case U1 is missing from the S_H distribution in Case U2 that is shown in **Figure 6.36**. Unlike the observations in Case U1, gas released from the hydrate dissociation in the HBLs in Case U2 is not trapped within these layers but migrates to the MLs, as shown in **Figure 6.37**.

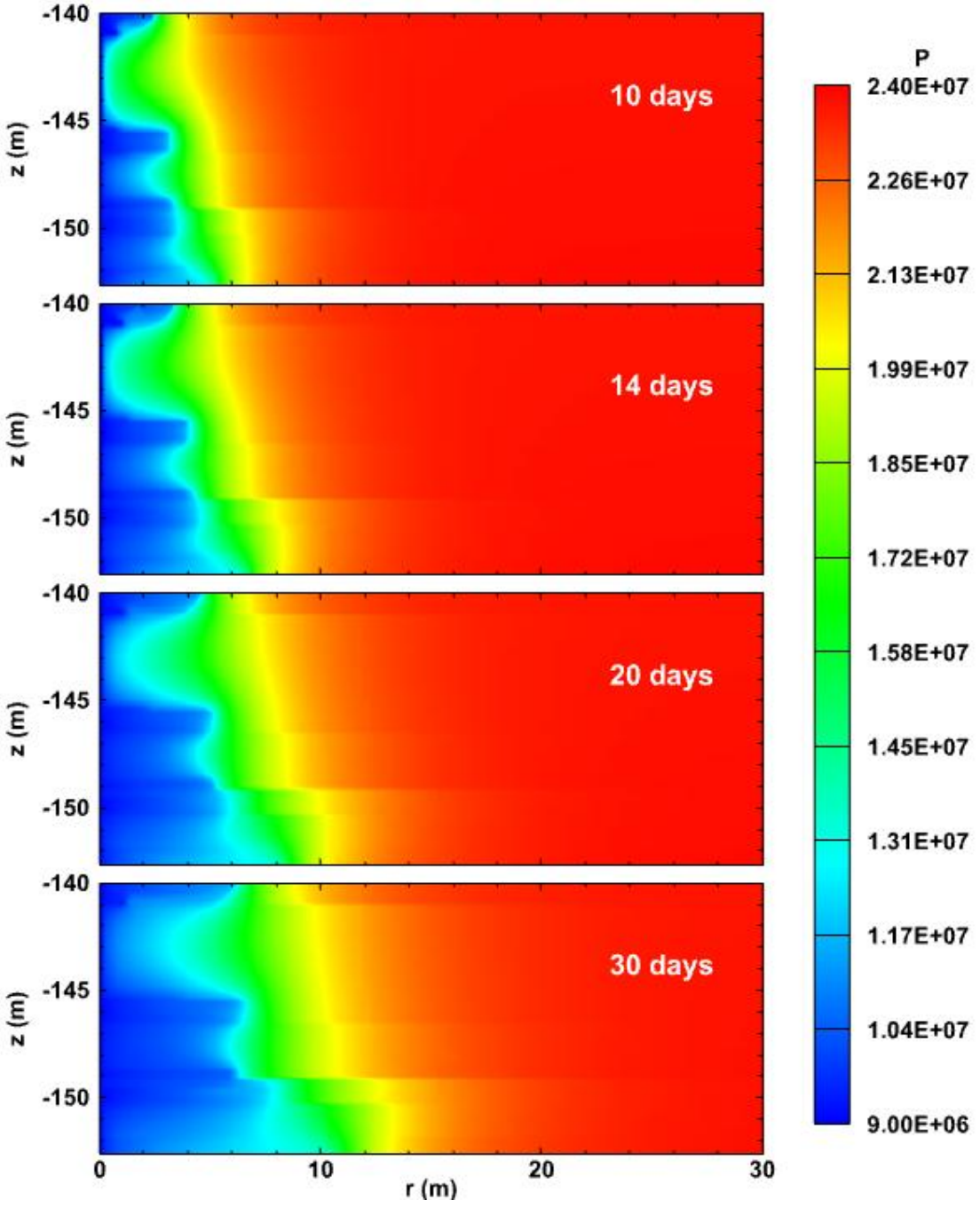

Figure 6.34 Evolution of the spatial distribution of pressure (Pa) in the reservoir of Case U2.

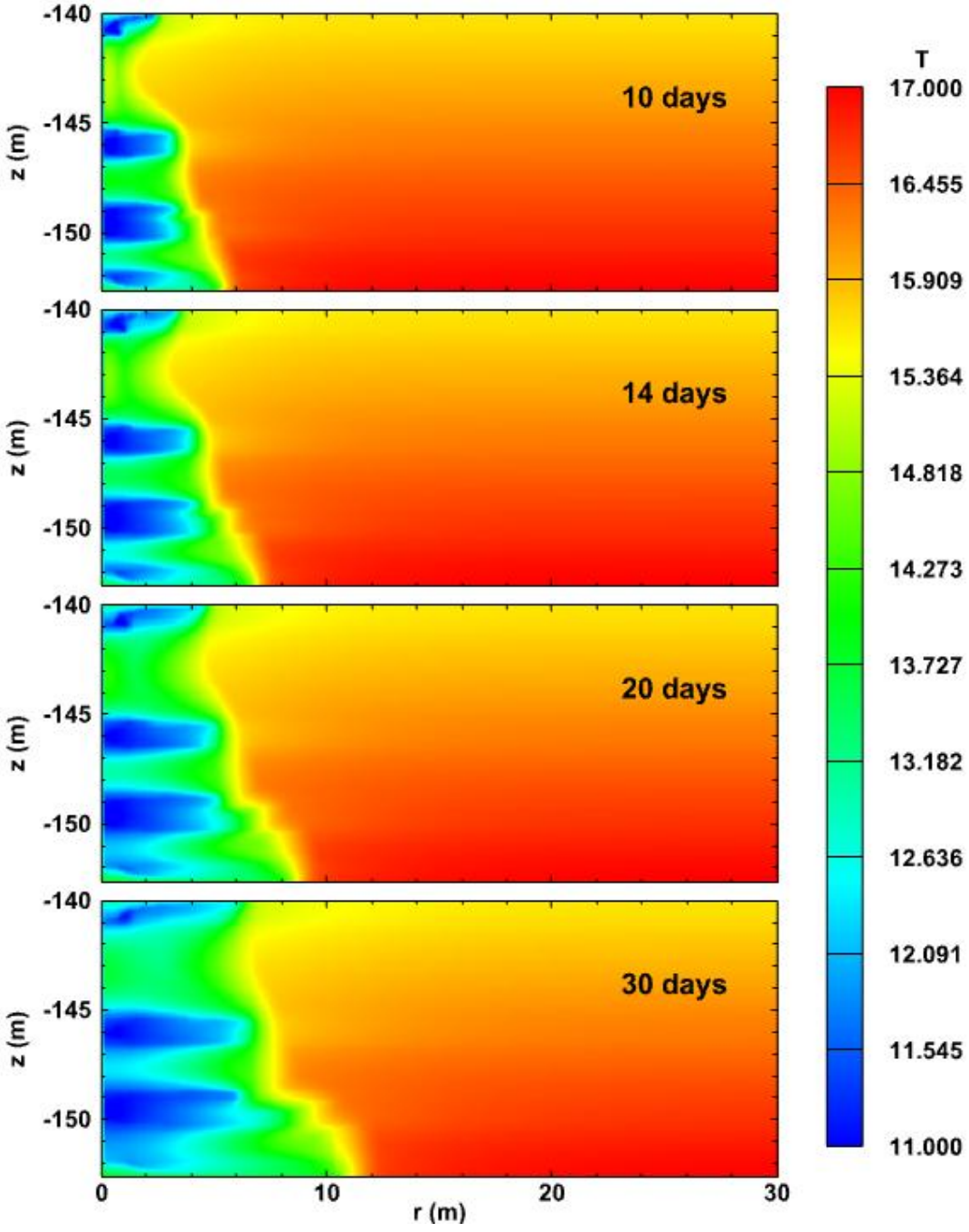

Figure 6.35 Evolution of the spatial distribution of temperature (°C) in the reservoir of Case U2.

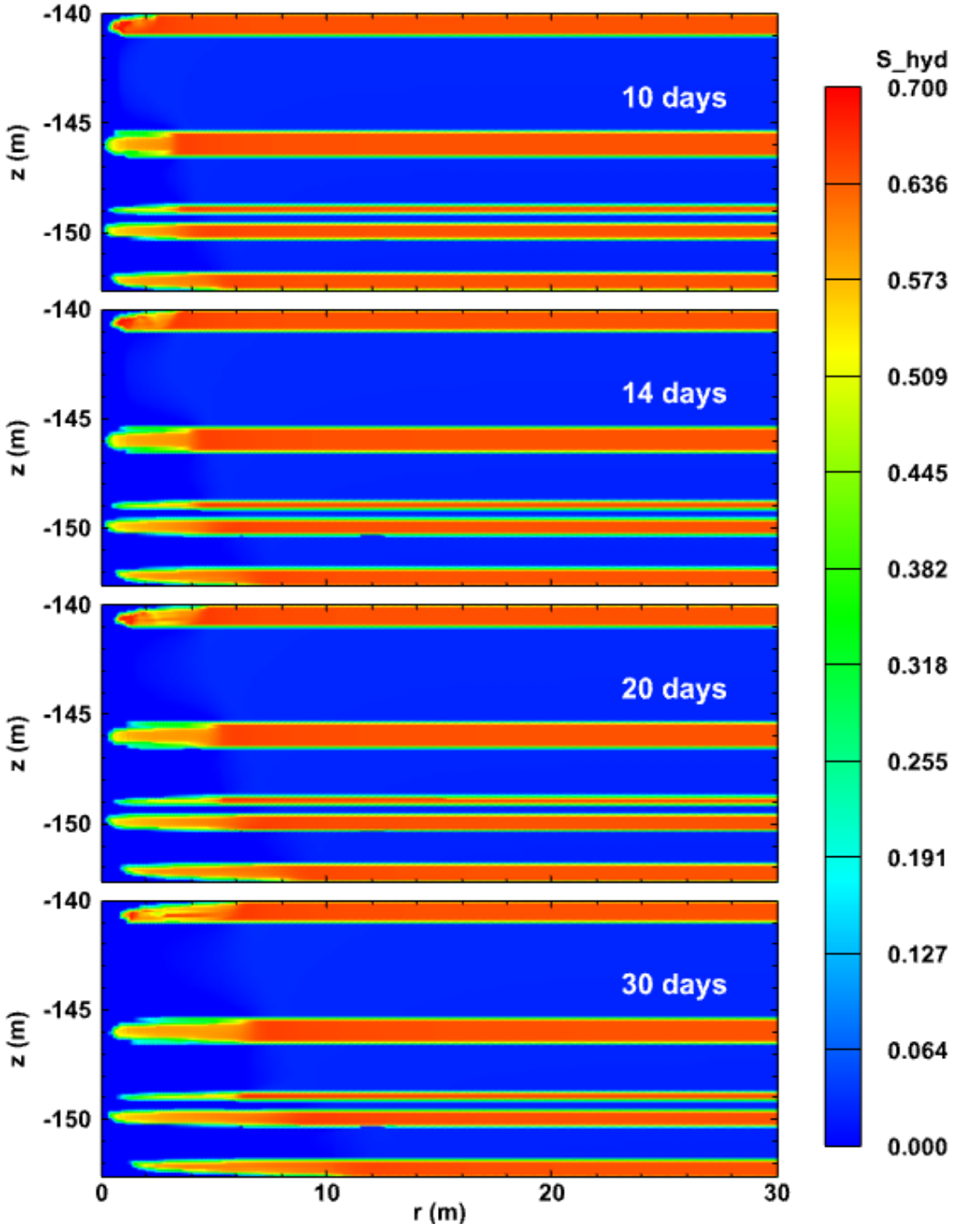

Figure 6.36 Evolution of the spatial distribution of hydrate saturation in the reservoir of Case U2.

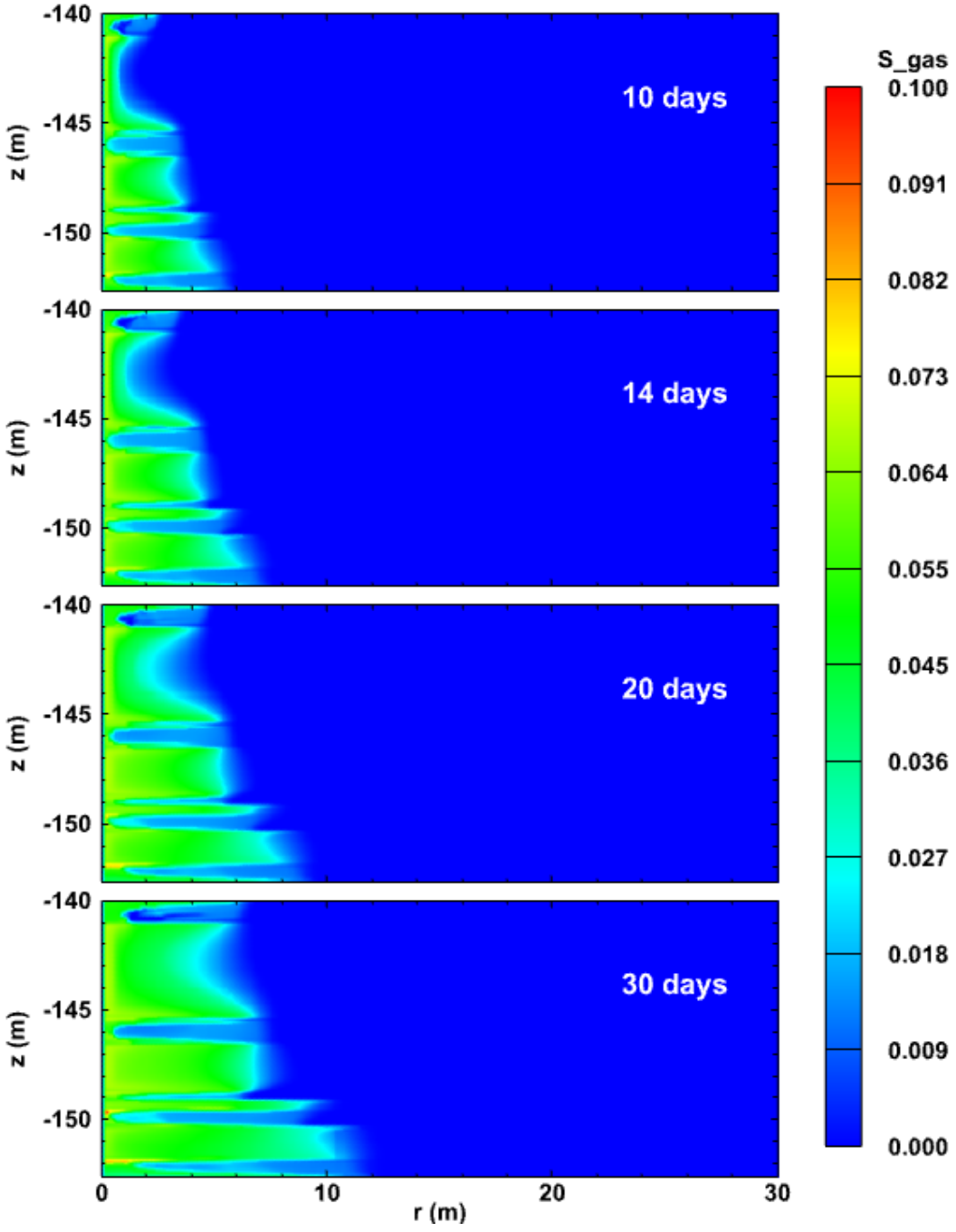

Figure 6.37 Evolution of the spatial distribution of gas saturation in the reservoir of Case U2.

6.2.2.3. Gas Production and Water Production in Cases U1G and U2G

Figure 6.38 shows the evolution of Q_G and Q_A from the single vertical well at the center of the cylindrical reservoir in Cases U1G and U2G. The Q_G and Q_A are lower in Case U2G, as was the case of the same observations in Cases U1 and U2, and lead to the correspondingly lower M_G and M_A in Case U2G that is shown in **Figure 6.39**. The coarser mesh in Case U2G could be a reason for the fluctuation in the results. **Figure 6.40** shows the evolution of Q_R, Q_{gG}, Q_{gA}, and Q_{gT} in Cases U1G and U2G. Under the same production conditions, Q_{gT} in Case U2G is less than half of Q_{gT} in Case U1G during most of the 30 days of the production test simulated in this study. It appears that the oscillations of Q_R, Q_{gG}, and Q_{gT} are related to the coarse discretization because discretization is the only difference between Cases U1G and U2G. The oscillation of Q_{gT} appears to be caused by that of Q_{gG} because Q_{gA} is stable.

Figure 6.41 shows the evolution of V_R, V_{gG}, V_{gA}, V_{gT}, and V_F in Cases U1G and U2G. With the full geomechanical model, all the results associated with Case U1G are larger than those in Case U2G. Thus, V_{gT} in Case U2G is only about 28.6 % of that in Case U1G at t = 30 days.

Figures 6.42 and **6.43** compare the evolution of Q_W and M_W in Cases U1G and U2G, which are consistent with those of Q_A and M_A for reasons already explained. **Figure 6.44** compares the evolution of R_{WG} and R_{WGT} in Cases U1G and U2G. R_{WGT} in Case U2G is higher than that in Case U1G; the R_{WG} in Case U2G exhibits significantly larger fluctuations than that in Case U1G, but they both seem to be about the same (or a sufficiently similar) mean. The evolution of X_{sA} in Case U1G in **Figure 6.45** does not allow

the identification of a clear upward trend like the one observed in Case U1G because of significant oscillations.

Figure 6.46 shows the evolution of water inflows across key boundaries in Case U2G. Compared to the inflow estimates in Case U1G that are shown in **Figure 6.10**, the water inflows across the top and bottom boundaries of the hydrate deposit (*i.e.*, from the OB and the UB) are lower.

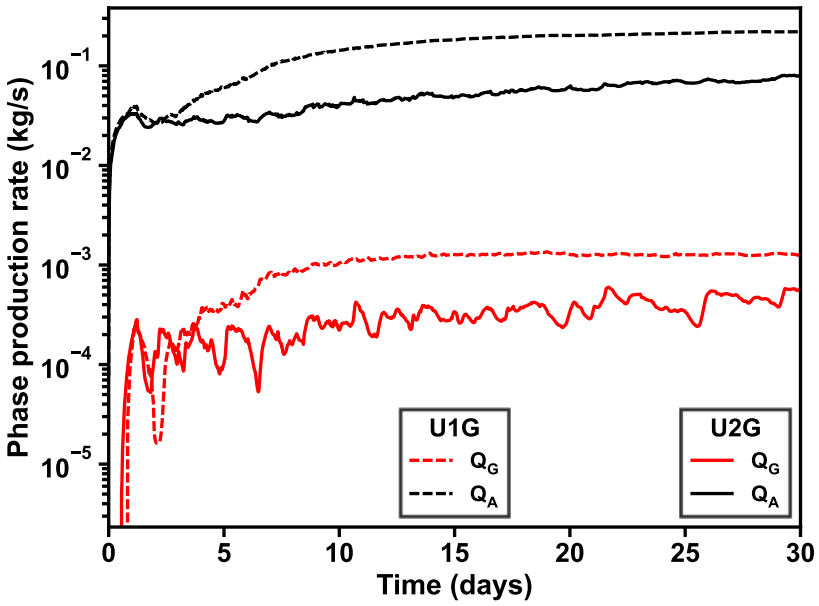

Figure 6.38 Evolution of Q_G and Q_A in Cases U1G and U2G.

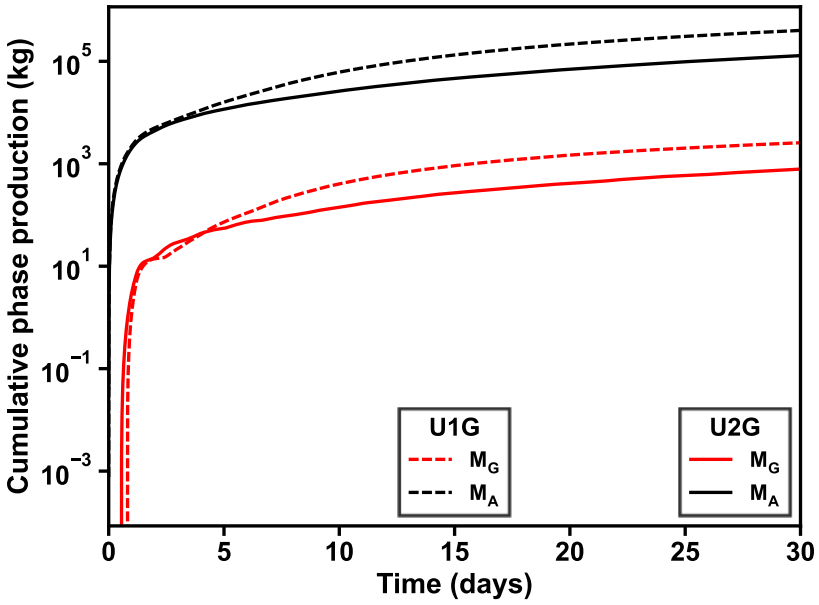

Figure 6.39 Evolution of M_G and M_A in Cases U1G and U2G.

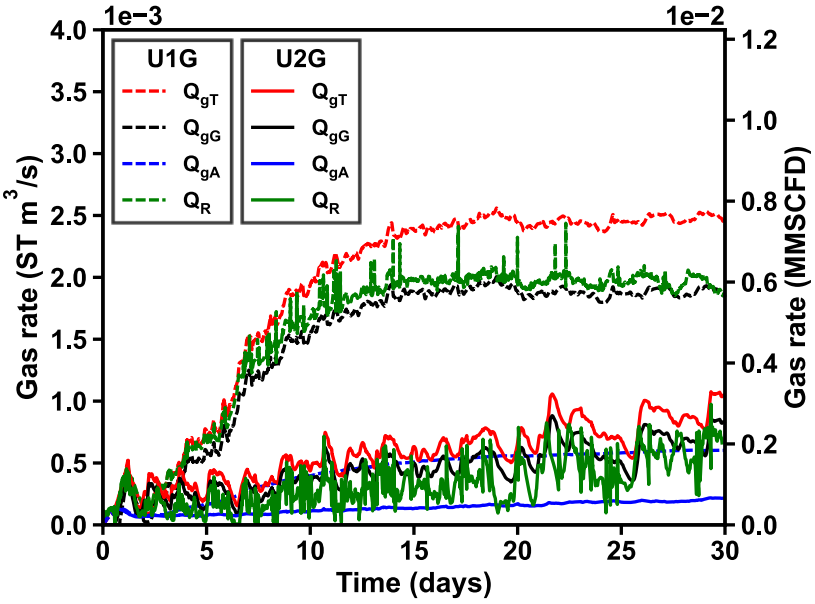

Figure 6.40 Evolution of Q_R, Q_{gG}, Q_{gA}, and Q_{gT} in Cases U1G and U2G.

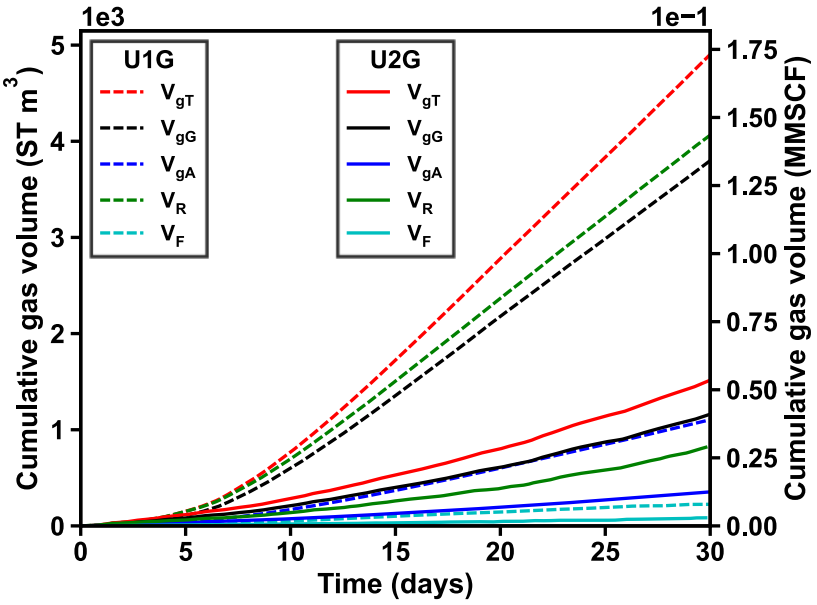

Figure 6.41 Evolution of V_R, V_{gG}, V_{gA}, V_{gT}, and V_F in Cases U1G and U2G.

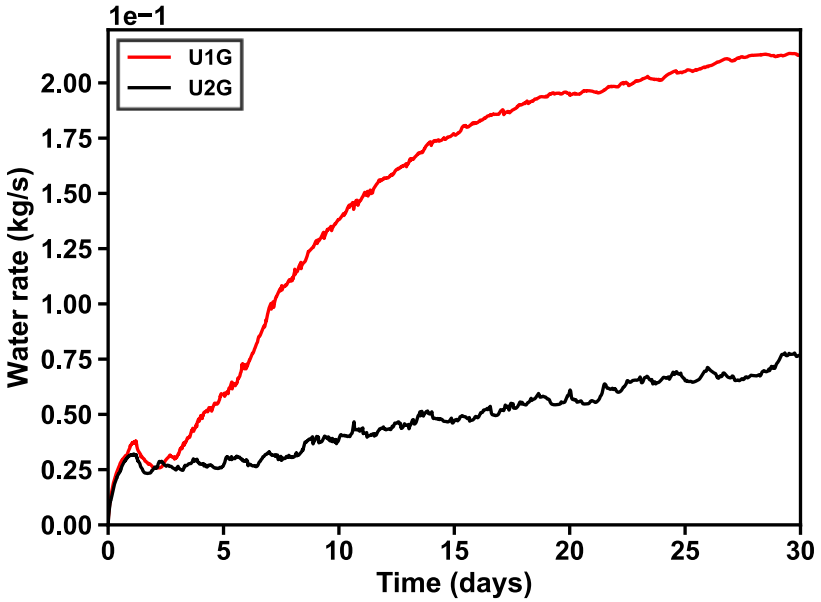

Figure 6.42 Evolution of Q_W in Cases U1G and U2G.

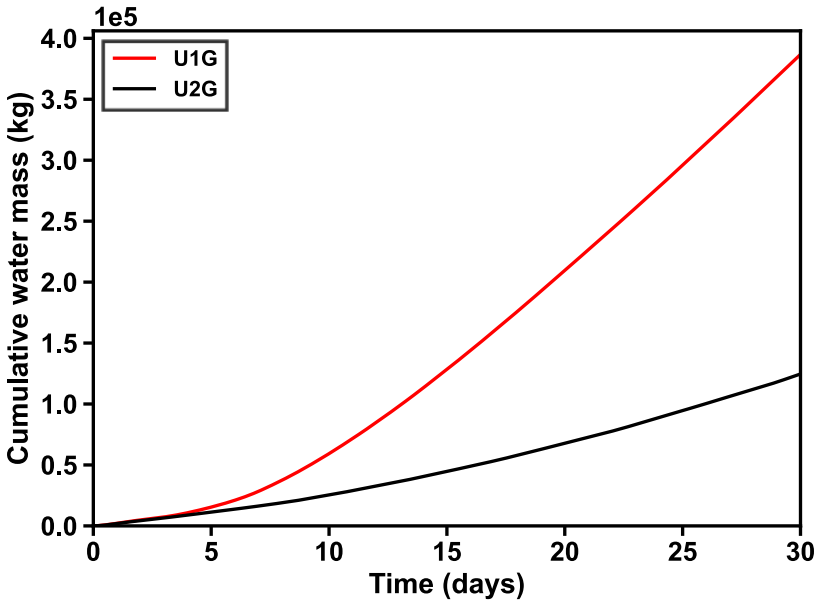

Figure 6.43 Evolution of M_W in Cases U1G and U2G.

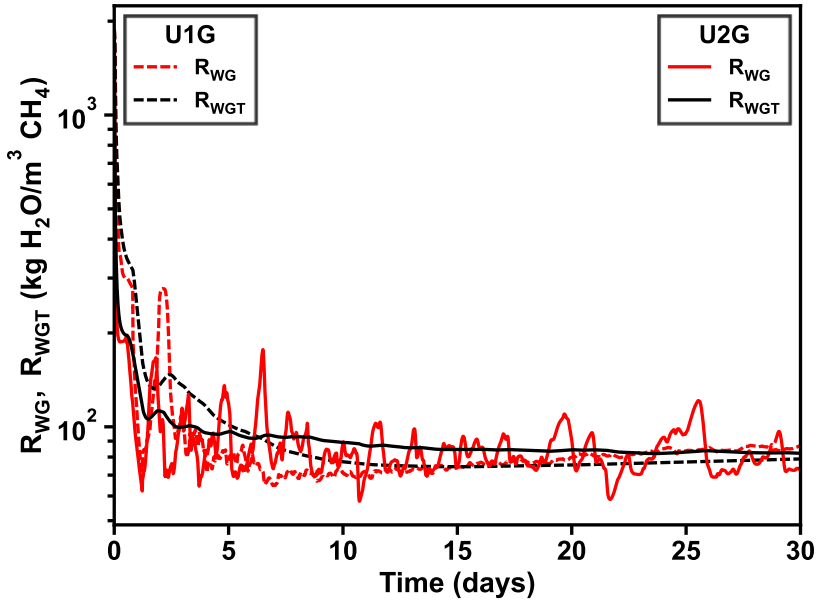

Figure 6.44 Evolution of R_{WG} and R_{WGT} in Cases U1G and U2G.

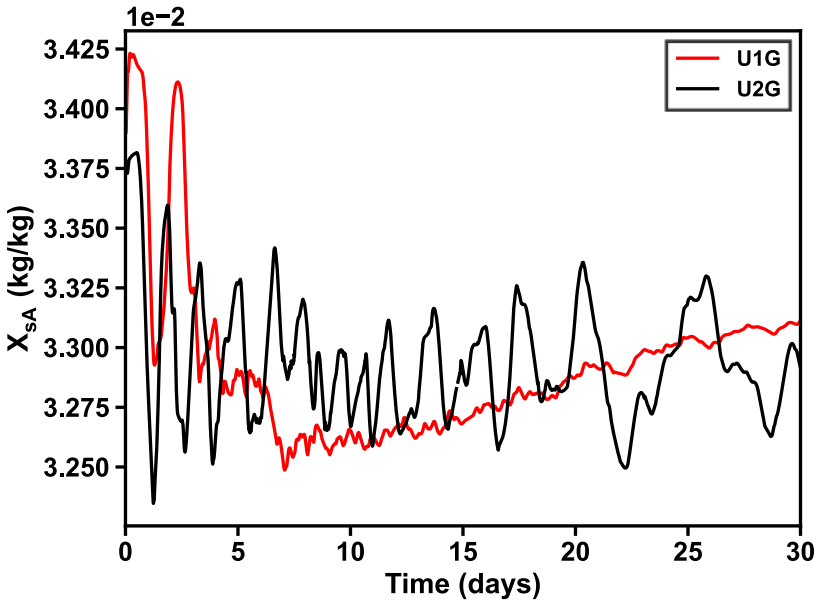

Figure 6.45 Evolution of X_{sA} in Cases U1G and U2G.

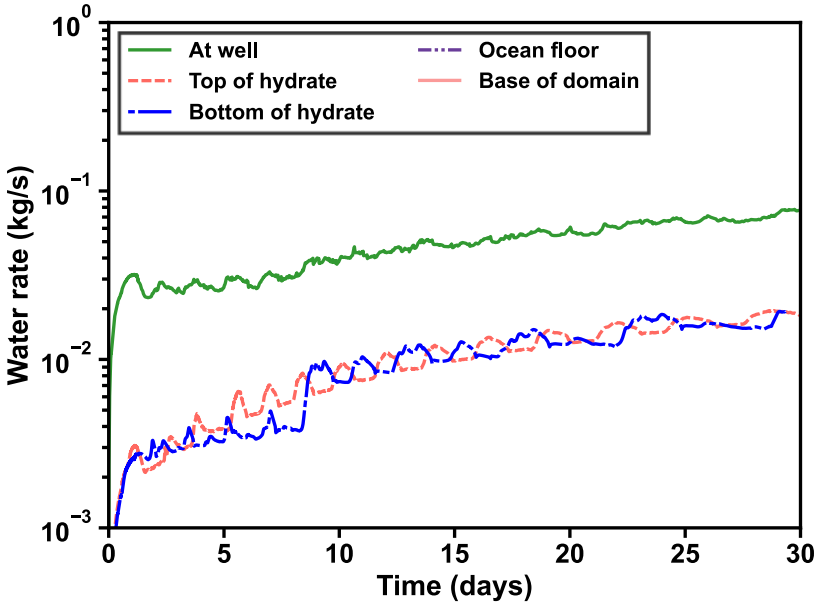

Figure 6.46 Evolution of water flows across key boundaries and interfaces, compared to Q_W in Case U2G.

6.2.2.4. Spatial Distributions of P, T, S_H, and S_G in Case U2G

The spatial evolution of P, T, S_H, and S_G in Case U2G (involving the full geomechanical model) are shown in **Figures 6.47**, **6.48**, **6.49**, and **6.50**, respectively. In **Figures 6.47** and **6.48**, the coarse mesh in Case U2G results in pressure and temperature distributions that are not as smooth as those in Case U1G (**Figures 6.15** and **6.16**). Additionally, these changes only occur within a short distance from the production wellbore in the HBLs and advance deeper into the formation only in the upper section of the H1 layer and the lower section of the H5 layer where significant hydrate dissociation is observed, as shown in **Figure 6.49**. **Figure 6.50** shows more gas in the reservoir migrating upward in Case U2G than in Case U1G.

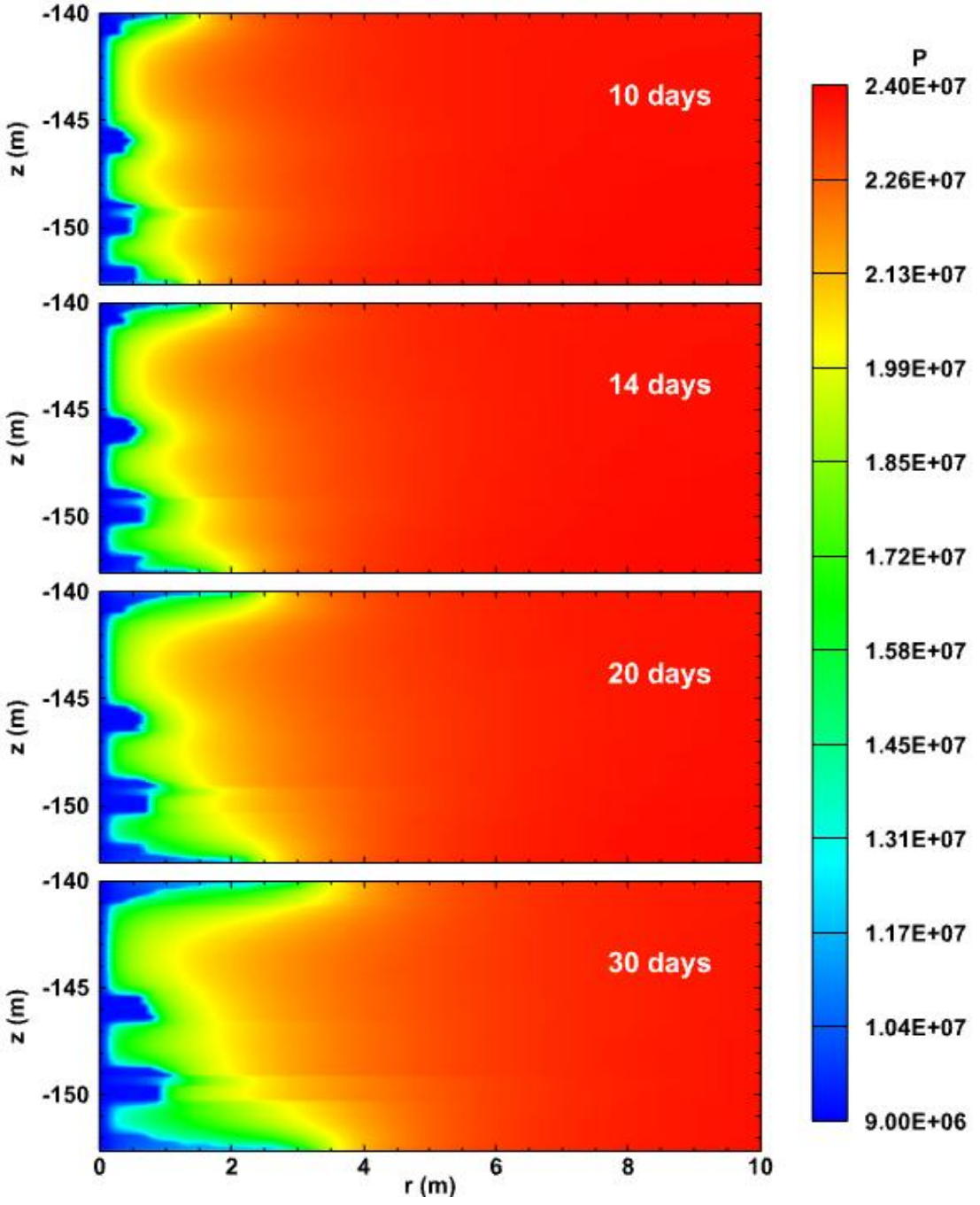

Figure 6.47 Evolution of the spatial distribution of pressure (Pa) in the reservoir of Case U2G.

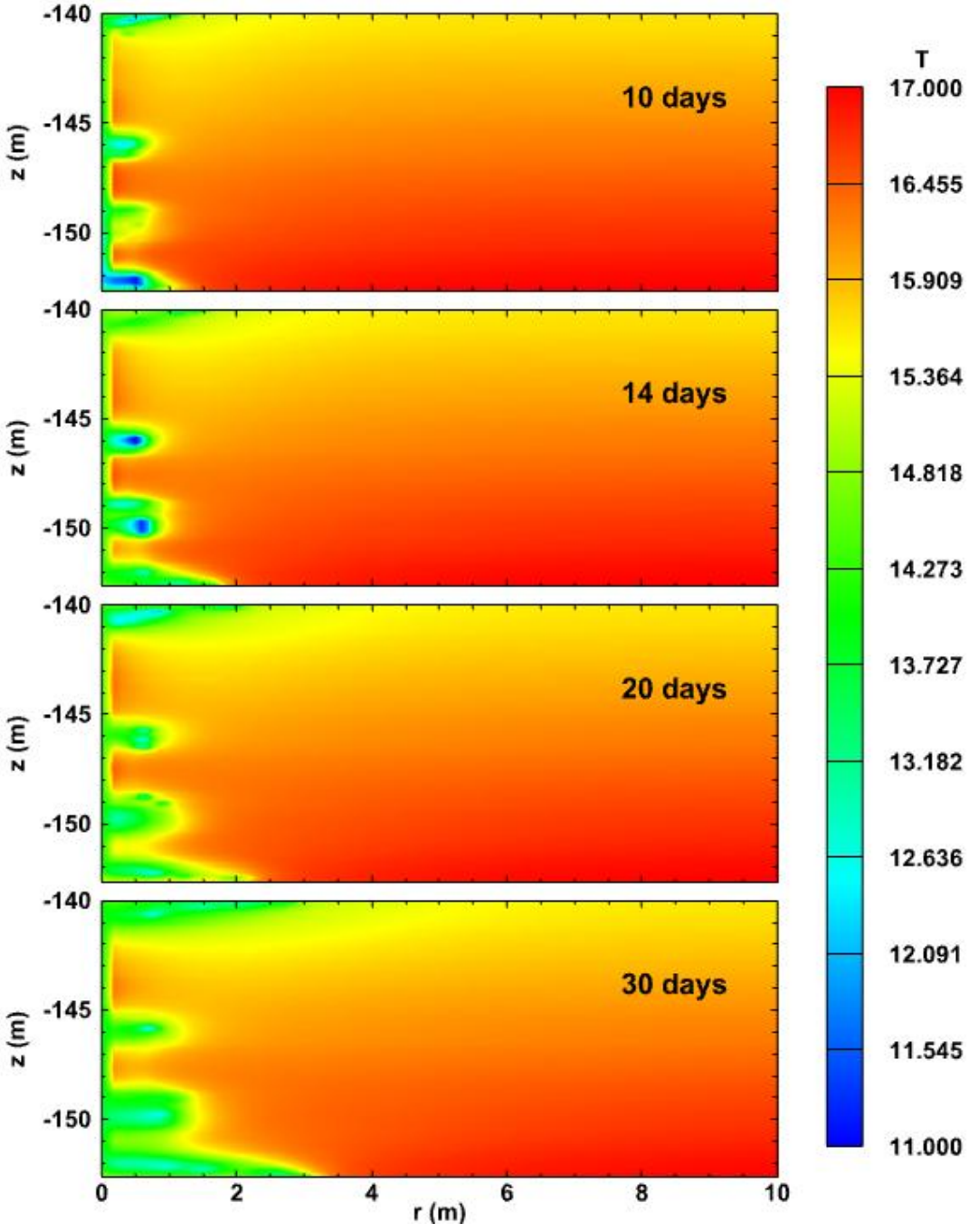

Figure 6.48 Evolution of the spatial distribution of temperature (°C) in the reservoir of Case U2G.

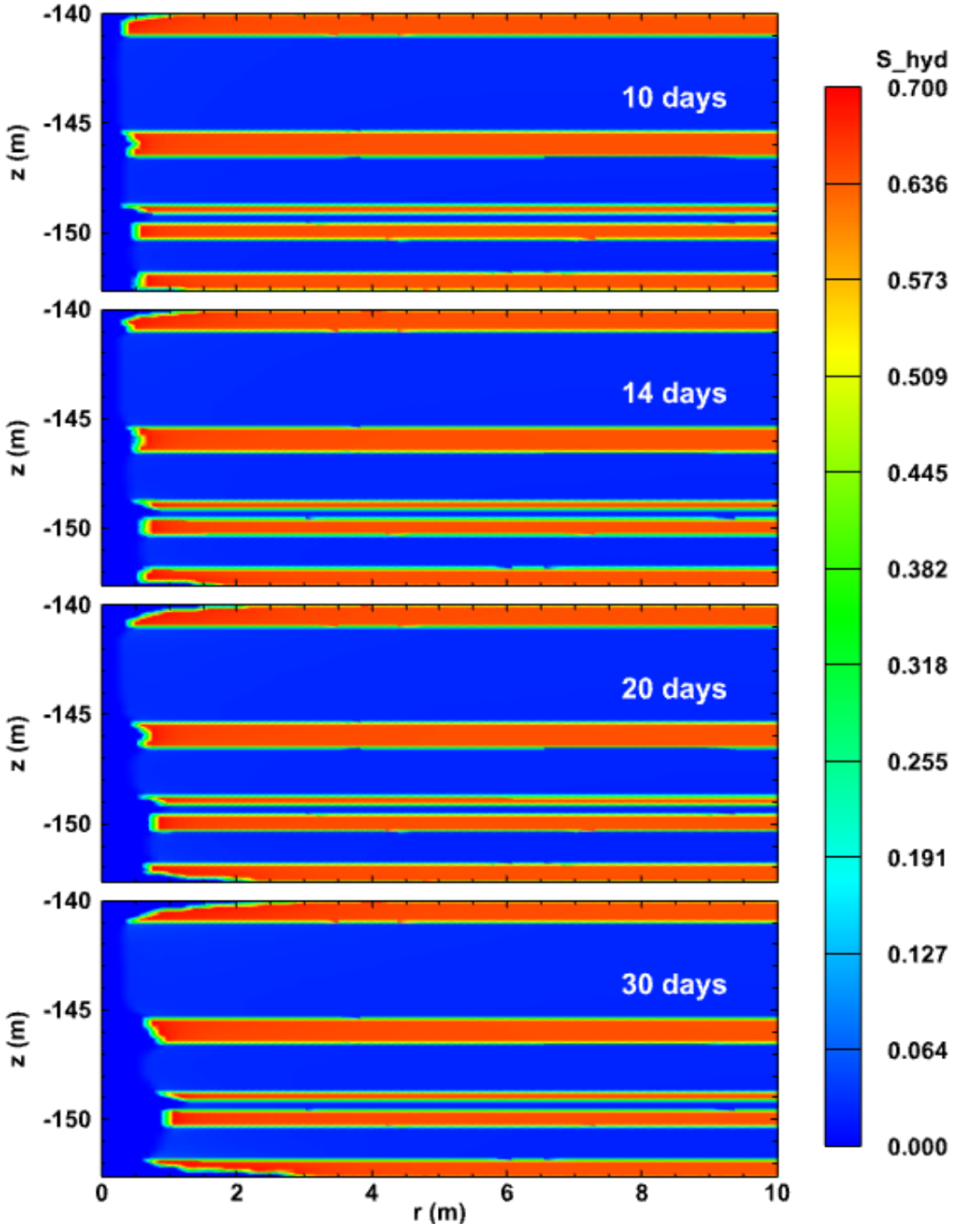

Figure 6.49 Evolution of the spatial distribution of hydrate saturation in the reservoir of Case U2G.

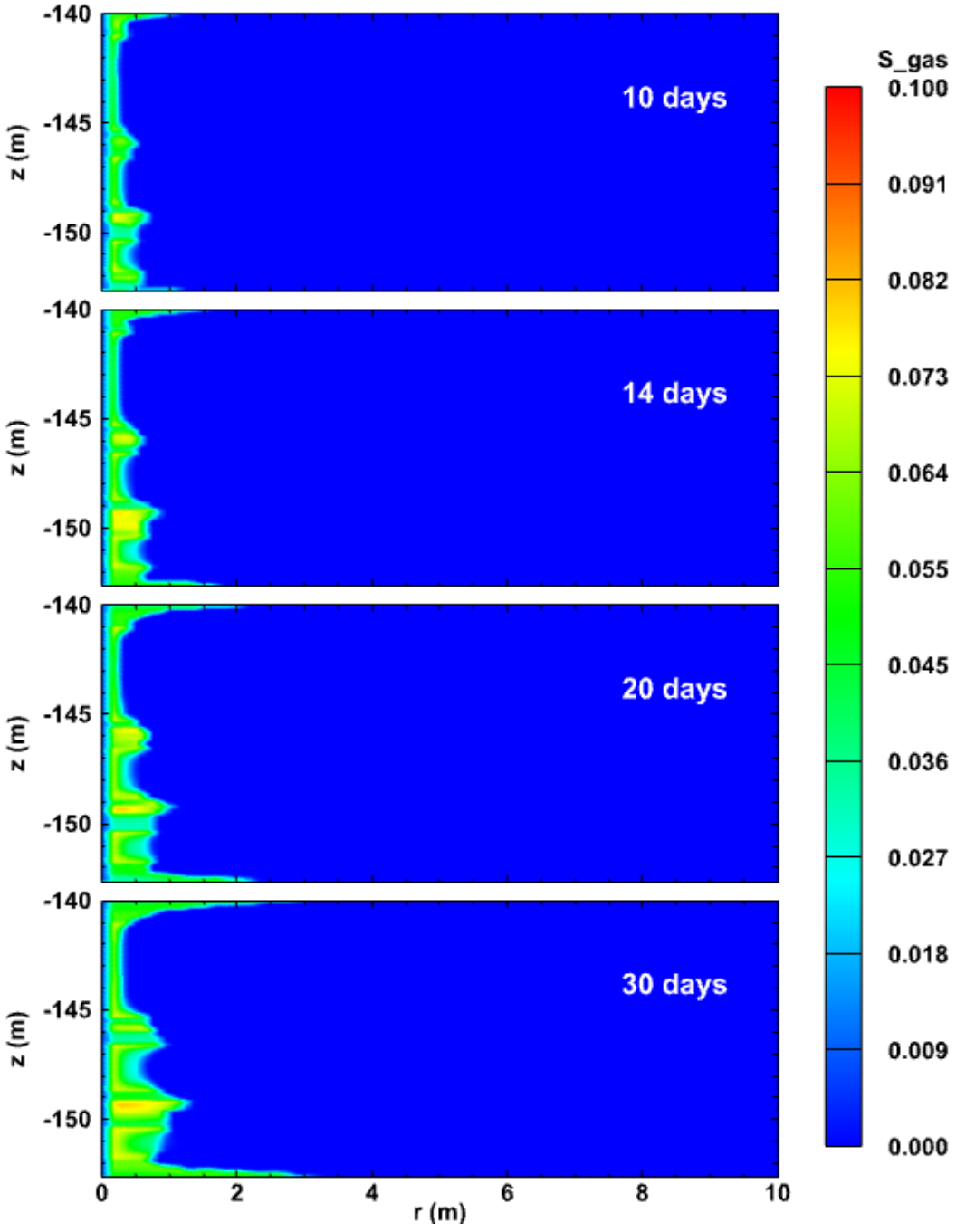

Figure 6.50 Evolution of the spatial distribution of gas saturation in the reservoir of Case U2G.

6.2.2.5. Evolution of Displacement in Cases U1G and U2G

Figure 6.51 compares the evolution of u_z in Cases U1G and U2G at the wellbore (r = 0 m) and at (a) the top of the reservoir (z = -140 m) and (b) the bottom of the reservoir (z = -152.67 m). Compared to Case U1G, Case U2G predicts similar deformations for uplift and subsidence until t = 4 and 5 days, respectively, but then the predictions diverge with the U2G-associated displacements being substantially smaller. At t = 30 days, in Case U2G the vertical displacements at (r, z) = (0 m, -140 m) and (r, z) = (0 m, -152.67 m) are -0.33 and 0.34 m, respectively, *i.e.*, slightly less than half those observed in Case U1G.

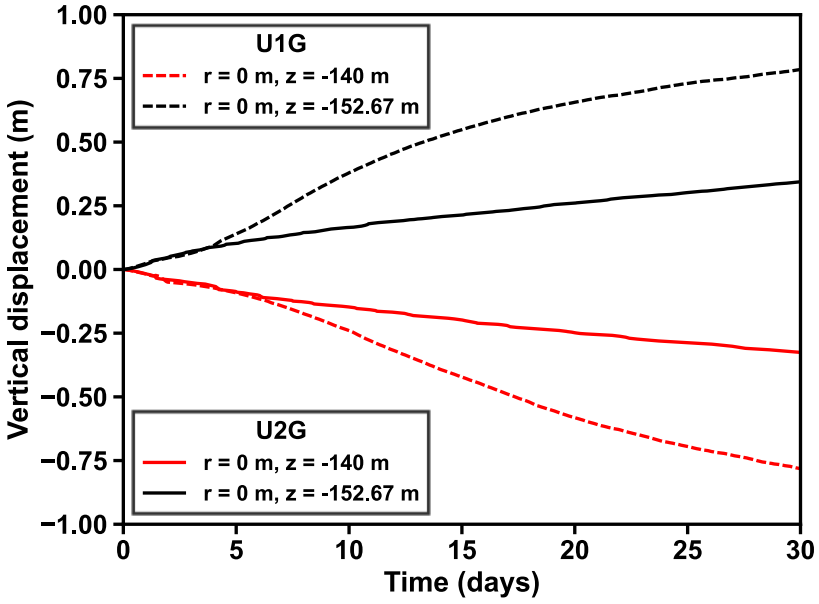

Figure 6.51 Evolution of u_z at (r, z) = (0 m, -140 m) and (r, z) = (0 m, -152.67 m) in Cases U1G and U2G.

6.2.2.6. Spatial Distributions of u, σ_1', and ε_v in Case U2G

Figures 6.52, **6.53**, and **6.54** present the spatial evolution of u, σ_1', and ε_v, respectively, in Case U2G. Note that the extent of the radial dimension in all the three figures are reduced to 10 m in order to better capture the evolution of the associated changes. Unlike the image in **Figure 6.20**, the upper and lower bound values in the contour plot of **Figure 6.52** range from 0.35 and -0.35 m, respectively. In Case U2G, significant vertical displacements only occur in the H1 and H5 layers, but they are still lower in magnitude than those in Case U1G. Note that the coarse discretization in Case U2G cannot adequately resolve the details near the wellbore, where the high compression area in the H1 and H5 layers (shown in **Figure 6.53**) and the high volumetric strain in the M3 and M4 layers (shown in **Figure 6.54**) are encountered.

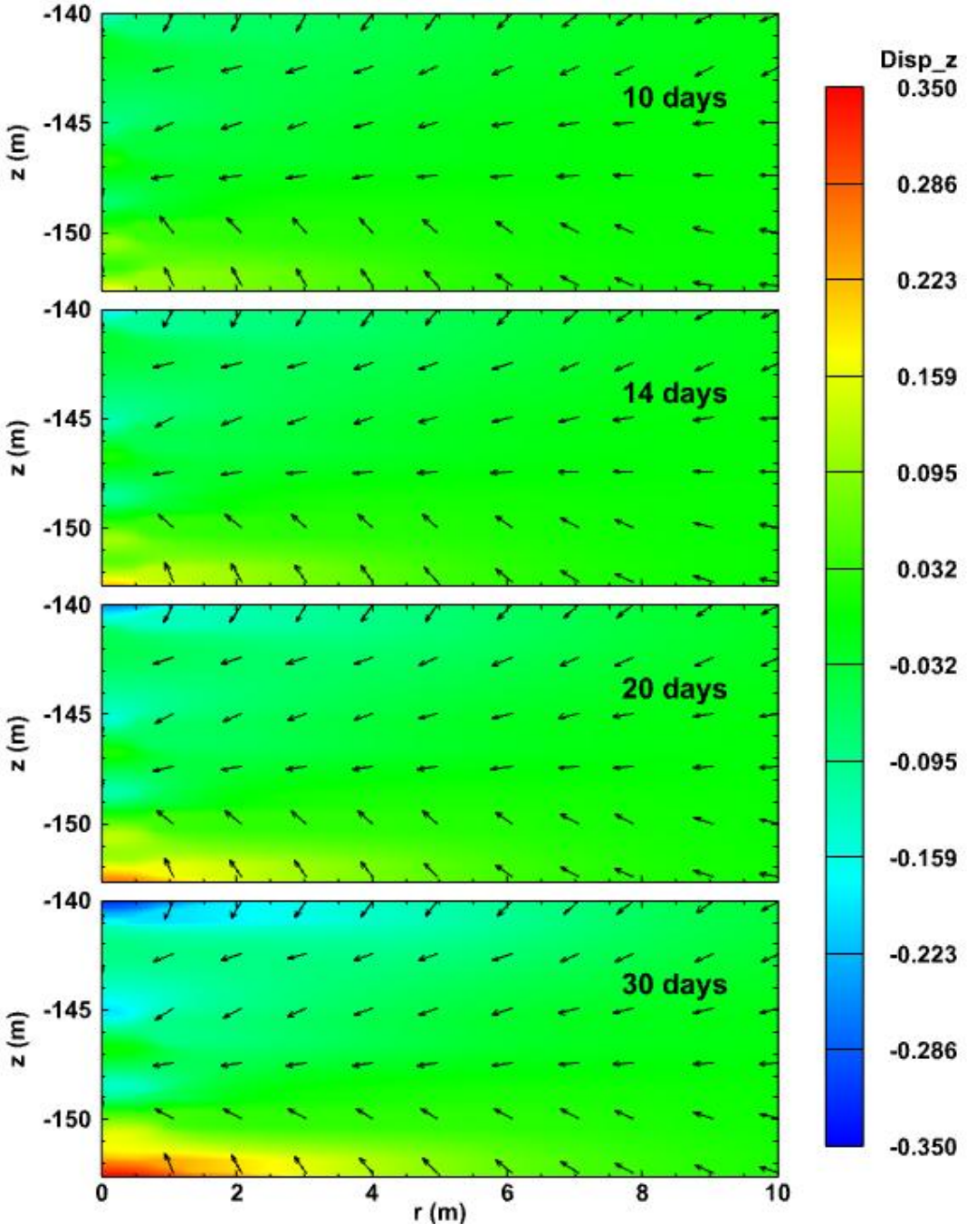

Figure 6.52 Evolution of the spatial distribution of displacements (m) in the reservoir of Case U2G.

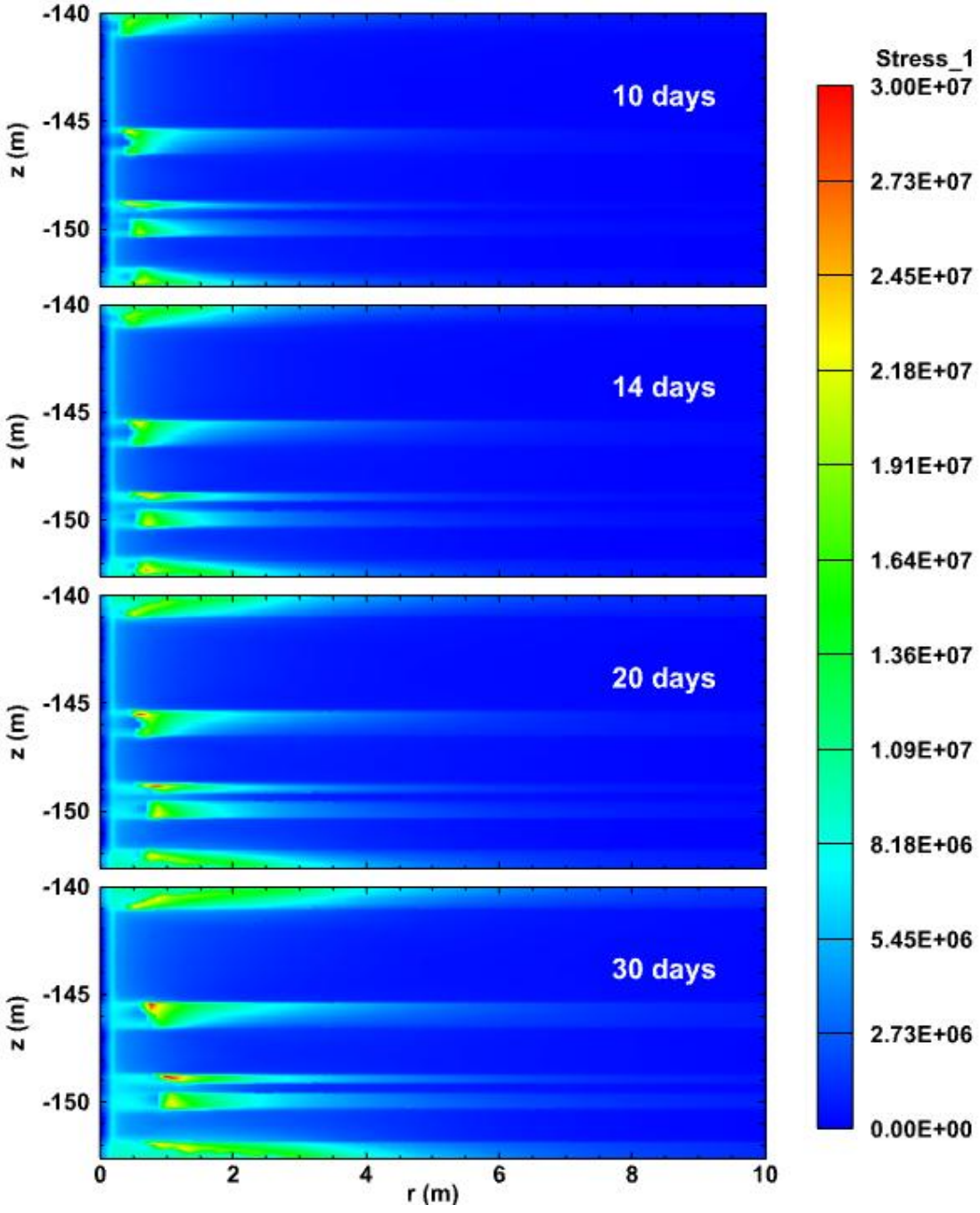

Figure 6.53 Evolution of the spatial distribution of maximum principal effective stress (Pa) in the reservoir of Case U2G.

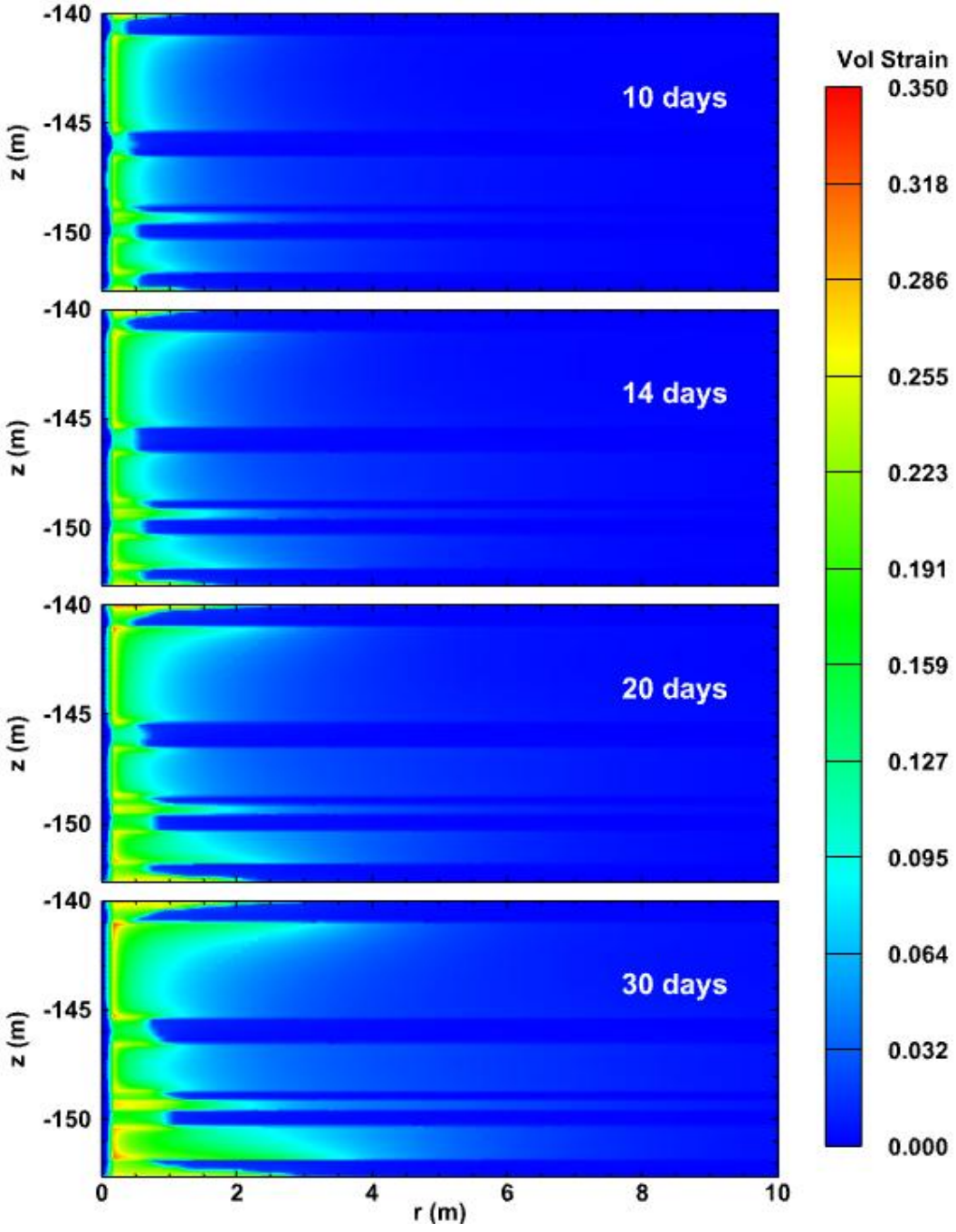

Figure 6.54 Evolution of the spatial distribution of volumetric strain in the reservoir of Case U2G.

6.3. The Three-Dimensional Cartesian Cases T1 and T1G

These two cases were investigated in order to evaluate the effect of considering a full geomechanical model in the analysis of production from this 3D oceanic hydrate deposit.

6.3.1. Problem Description

The problem descriptions of Cases T1 and T1G are provided in Sections 5.2.3 and 5.3.3, respectively.

6.3.2. Results

The flow- and geomechanics-related conditions and parameters that were monitored in Cases T1 and T1G were the same as those discussed in Cases U1, U1G, U2, and U2G (see Sections 6.1.2 and 6.2.2), excluding (a) the water flows across key boundaries and interfaces and (b) the vertical displacements at key locations. Additionally, the spatial distribution of the mass fraction of salt in the produced aqueous phase (X_{sA}) was monitored.

6.3.2.1. Gas Production and Water Production in Cases T1 and T1G

Figures 6.55 and **6.56** show the evolution of Q_G and Q_A from the vertical production well located at (x, y) = (200 m, 0.025 m) in Cases T1 and T1G. Q_G in Cases T1 and T1G fluctuates during production. Four different stages are evident: (a) an initial stage in which Q_G reaches a high level within the first 2-3 days of production because of

the significant initial pressure drop at the production well, (b) a rapidly decline until t = 8 – 10 days when the near-well hydrate has dissociated and the initial maximum pressure drop at the well has been attenuated, (c) an increase in the next 20 days of production as the depressurization-affected volume of the deposit expands and hydrate dissociation increases, and (d) a final stage of general downward trend because of the weakening of depressurization as more water moves toward the well from the boundaries and the aquifer interlayers. Q_G in Case T1G reaches zero at t = 73 days, but appears to increase after t = 89 days from the onset of production. Q_A in Cases T1 and T1G increase monotonically with time, and appear to approach a steady state near the end of the t = 90 day production period. Q_A in Case T1G is consistently higher than that in Case T1. **Figures 6.57** and **6.58** show the corresponding M_G and M_A. M_G in Case T1 is larger than that in Case T1G because of the larger Q_G in Case T1. M_G in Case T1G is consistently lower than M_G in Case T1 and reaches a plateau later in the production test as the result of the zero Q_G at that time.

Figure 6.59 shows the evolution of Q_R, Q_{gG}, Q_{gA}, and Q_{gT} in Cases T1 and T1G. Two important conclusions can be drawn from **Figure 6.59**: (a) Q_{gA} is the major contributor to Q_{gT} in Cases T1 and T1G because of a substantially large amount of Q_A, and (b) Q_{gT} is smaller than Q_R in the first 30 days of production, after which time it becomes larger in Cases T1 and T1G as exsolution of dissolved gas from the water becomes a significant contributor to production. **Figure 6.60** compares the cumulative volumes V_R, V_{gG}, V_{gA}, V_{gT}, and V_F over the testing period in Cases T1 and T1G. V_R, V_{gA}, and V_{gT} are all larger in Case T1G than in Case T1, which involves a larger V_{gG}. In Cases

T1 and T1G, V_F is nearly zero, indicating the high overall effective permeability of the system.

The evolution of Q_W and M_W from the production well in Cases T1 and T1G are shown in **Figures 6.61** and **6.62**, respectively, and are very similar to those of the aqueous phase in **Figures 6.56** and **6.58**.

Figure 6.63 presents the evolution of R_{WG} and R_{WGT} in Cases T1 and T1G. Both R_{WG} and R_{WGT} are larger in Case T1G than in Case T1. Hydrate dissociation near the production well increases gas production, leading to the fast decline of R_{WG} and R_{WGT} after the onset of production. The downward trends are altered to upward ones which last for several days by the water inflow.

Figure 6.64 shows the evolution of X_{sA} in Cases T1 and T1G. The pure water released from the hydrate dissociation dilutes the X_{sA} of the produced water, causing X_{sA} to reach its minimum value of 0.03478 kg/kg in Case T1, and of 0.03479 kg/kg in Case T1G. However, the very mild initial drop in salinity and the subsequent upward trend after the minimum values are reached are indicators of limited hydrate dissociation and of early (and substantial) water inflows through the boundaries and the water-bearing interlayers.

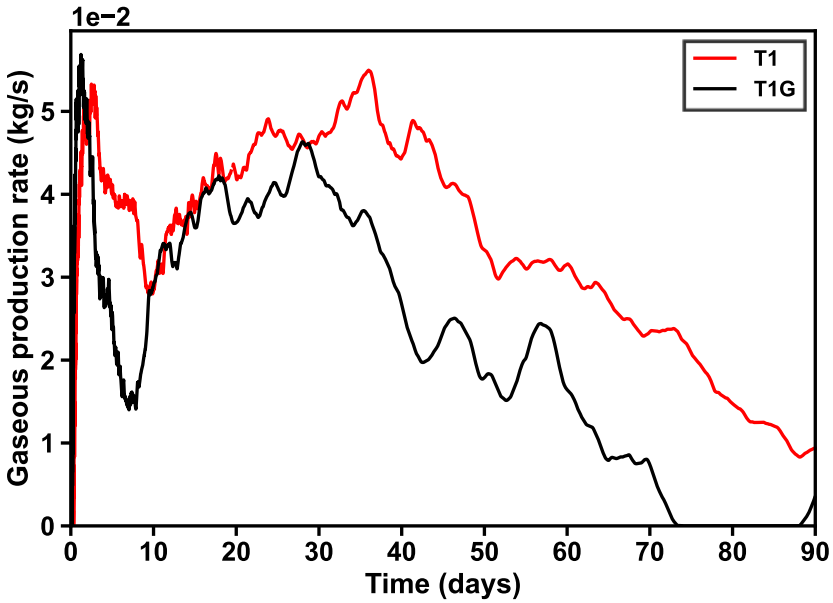

Figure 6.55 Evolution of Q_G in Cases T1 and T1G.

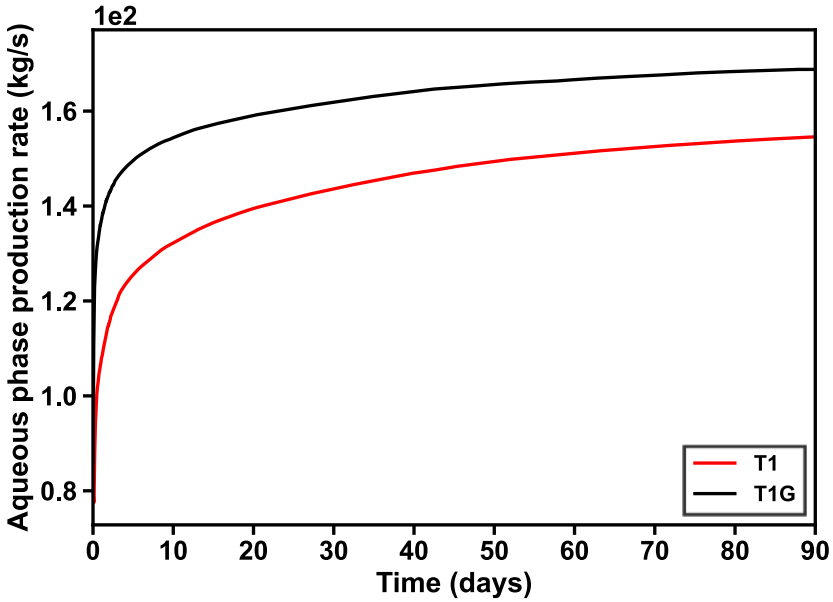

Figure 6.56 Evolution of Q_A in Cases T1 and T1G.

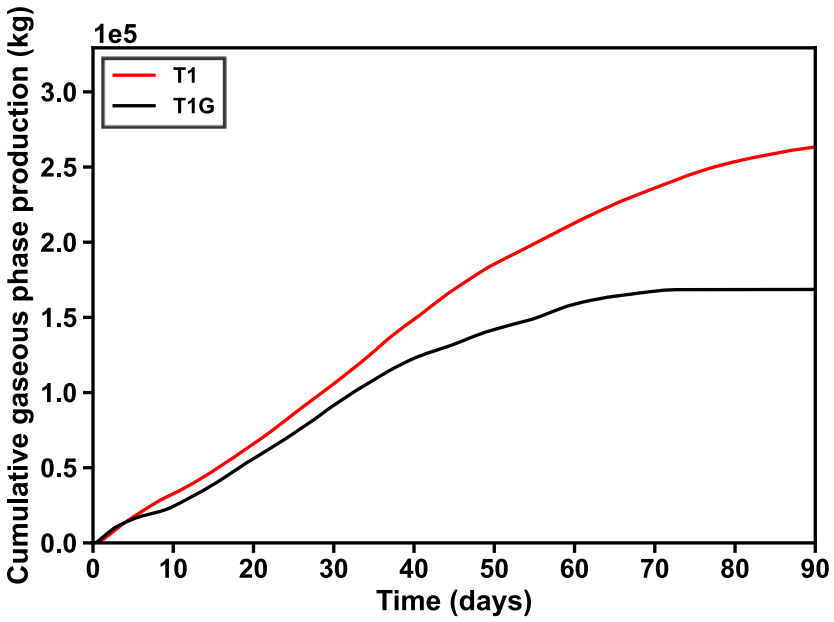

Figure 6.57 Evolution of M_G in Cases T1 and T1G.

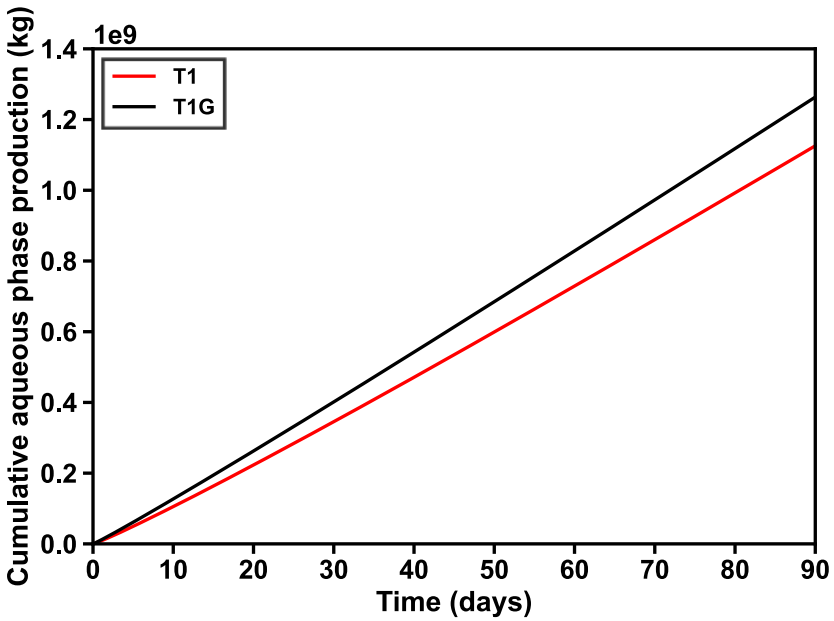

Figure 6.58 Evolution of M_A in Cases T1 and T1G.

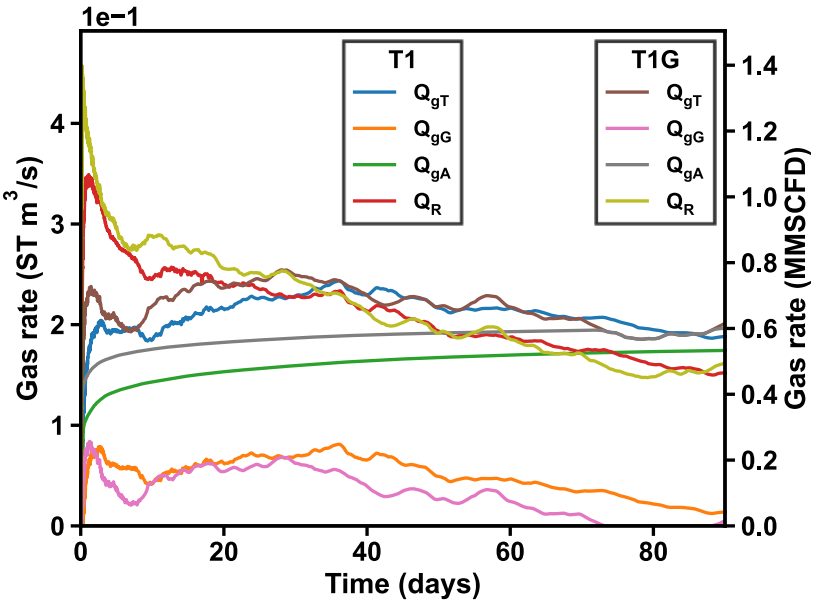

Figure 6.59 Evolution of Q_R, Q_{gG}, Q_{gA}, and Q_{gT} in Cases T1 and T1G.

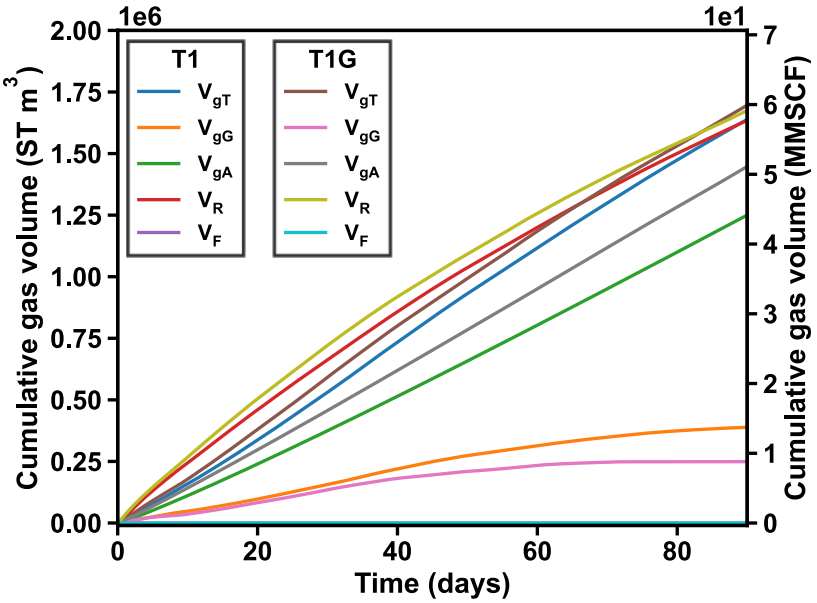

Figure 6.60 Evolution of V_R, V_{gG}, V_{gA}, V_{gT}, and V_F in Cases T1 and T1G.

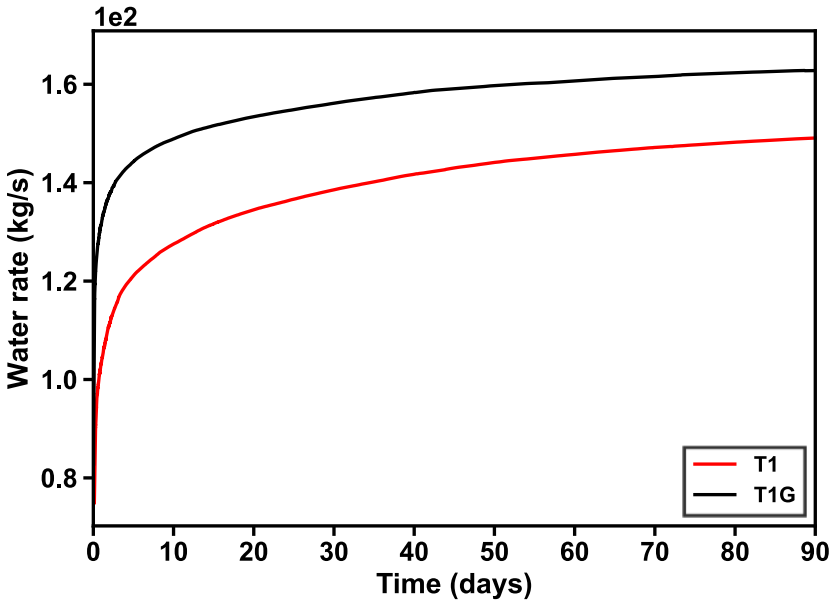

Figure 6.61 Evolution of Q_W in Cases T1 and T1G.

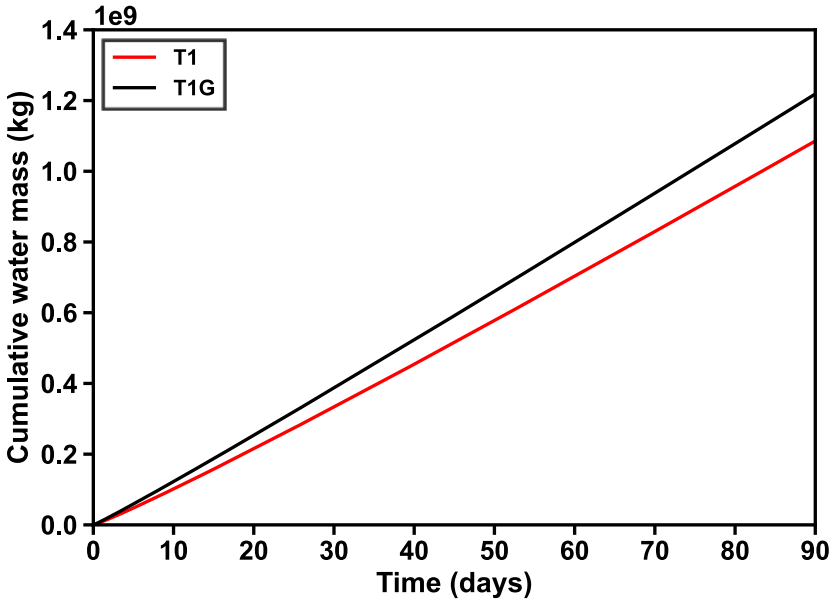

Figure 6.62 Evolution of M_W in Cases T1 and T1G.

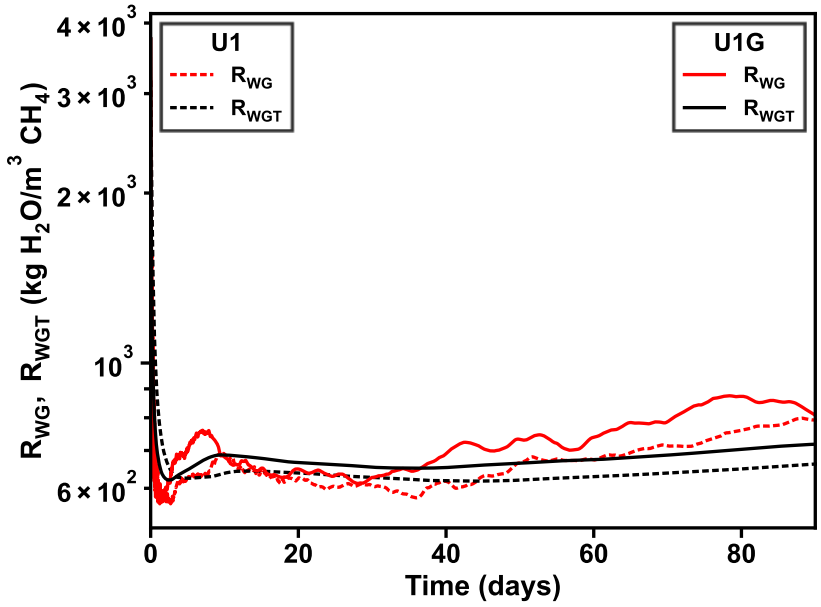

Figure 6.63 Evolution of R_{WG} and R_{WGT} in Cases T1 and T1G.

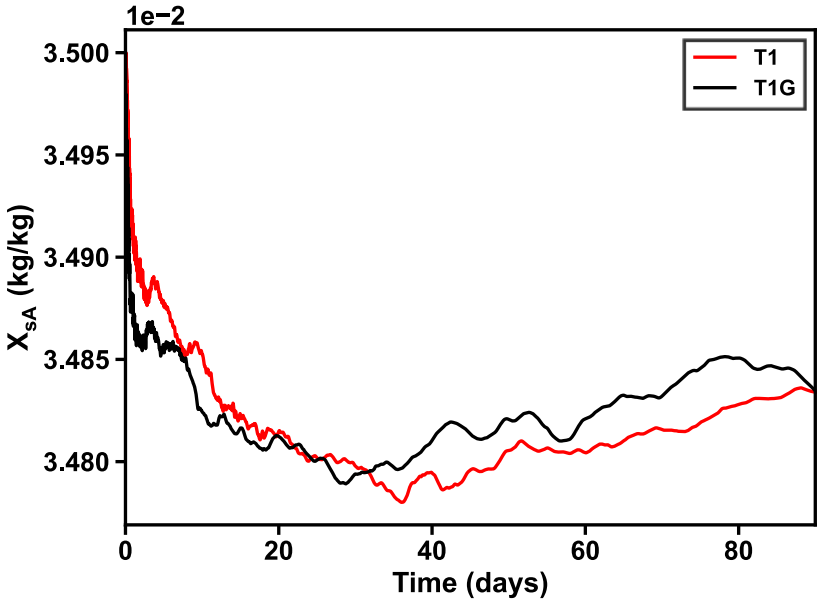

Figure 6.64 Evolution of X_{sA} in Cases T1 and T1G.

6.3.2.2. Spatial Distributions of P, T, S_H, and S_G in Cases T1 and T1G

The evolutions of the spatial distributions of P, T, S_H, and S_G on three planes are presented in this section: (a) Plane P1 that is the (x, z) vertical plane at y = 0.025 m (*i.e.*, the vertical plane that passes by the center axes of the production and injection wells); (b) Plane P2 that is the (y, z) vertical plane at x = 200 m (*i.e.*, the vertical plane that passes by the production well); and (c) Plane P3 that is the (y, z) vertical plane at x = 225 m (*i.e.*, the vertical plane that passes by the injection wells). For reference, the initial pressure and temperature at the top boundary of the reservoir are 2.77 MPa and 16.15 °C, respectively.

6.3.2.2.1. Results on Plane P1

Figures 6.65 to **6.70** present the spatial evolution of P, T, S_H, S_G, and X_{sA} on Plane P1 in Case T1 (involving the simplified geomechanical model). The pressure distribution in **Figure 6.65** indicates (a) a significant pressure drop caused by the producing well in the upper part of the hydrate deposit (from layer H1 to H5) that (b) advances laterally over a significant distance from the production well within a short time (as early as a day) but (c) does not penetrate deeper into the lower parts of the deposit because of the presence of a very-low permeability mud layer below the H5 HBL (see **Figure 5.24**) and the very high permeability of aquifers in the deposit profile (especially the thick A10 aquifer) that short-circuit the depressurization process by making large amounts of water available to the well. This results in the very stratified pressure distribution observed in **Figure 6.65**, which indicates that depressurization is prevented in the lower parts of the hydrate deposit, with the consequent adverse effects on hydrate dissociation and gas production. The

operation of the injection well increases the pressure locally (especially at later times) but does not seem to significantly counter the pressure drop because of the low injection rate.

The temperature distribution in **Figures 6.66** and **6.67** shows the expected higher temperature in the vicinity of the injection well, but also the limited penetration of the injected warm water into the main body of the hydrate deposit. The temperature scale in **Figure 6.66** has to accommodate the 60 ^{o}C of the injected water. A pathway from the injection to the production well is established very early, and most of the injected water follows it, bypassing the bulk of the hydrate. This is further facilitated by the thermal dissociation of the hydrate along this pathway, which increases its effective permeability of an ever expanding, hydrate-free "corridor" between the 2 wells (clearly shown in **Figure 6.66**), where most of the warm water flow is concentrated, thus minimizing its impact. **Figure 6.67** (differing from **Figure 6.66** in that it involves a low upper bound of the temperature scale to allow demonstration of thermal effects at lower temperatures) shows limited mixing of native and injected warm water near the injection well, and depressurization-induced cooling in the vicinity of the production well. A very important contribution of **Figure 6.66** is that the demonstration (denoted by the lower temperatures) occurs over a much larger scale than that indicated by **Figure 6.65**. Additional discussion on the subject is provided in the analysis of the S_H and X_{sA} results on this plane and on Plane P2.

Figure 6.68 shows both the heterogeneous hydrate saturation and the effect of dissociation on its spatial distribution near the wells. Two areas of hydrate destruction are evident. The first is associated with the production well, where hydrate dissociation is

induced mainly by depressurization and, to a lesser extent, by the thermal effects of injected warm water arriving at the production well (see **Figure 6.66**); the second is associated with the injection well, and is caused by the thermal dissociation of the hydrates in response to the injected warm water. The footprint of the two (hydrate-free) dissociated regions in the vicinity of the wells continues to expand as time advances. After 90 days of production, a large fraction of the hydrates around and between the two wellbores above the A10 aquifer layer (identified in **Figure 6.68** by the thick band of hydrate-free layer, below which no sign of dissociation is evident) have been dissociated. Of particular interest is the relatively good correlation of the S_H-distribution with the T-distribution in **Figure 6.66**.

The spatial distribution of free gas saturation S_G in **Figure 6.69** shows reasonably high S_G (the maximum value is around 0.1) only in the top few HBLs between two wells and on the first day of operation, *i.e.*, immediately after the application of the low bottomhole pressure at the well. Very little free gas is evident for $t > 1$ day, which, combined with the Q_{gG} results of **Figure 6.59**, indicates very low S_G levels as time advances. This is an indication of ineffective depressurization—which is by far the most effective of the two dissociation mechanisms involved in this study, as indicated by Moridis and Reagan (2007a)—because of (a) the presence of highly permeable aquifer layers within the hydrate deposit and of (b) the warm water injection. These results indicate that, while dissociation occurs over a relatively large volume of the deposit, the released gas does not survive as a substantial free phase, and appears to either exist at levels near the irreducible gas saturation (and thus unable to migrate toward the well) or

to dissolve again in the water because of increased solubility caused by the lower temperature (the result of dissociation).

The spatial distribution of X_{sA} in **Figure 6.70** shows lower X_{sA} in the pathway observed in **Figure 6.66** in the top few HBLs at t = 1 day where the pure water release from the hydrate dissociation dilutes the initial X_{sA}. The upward movement of the saline ocean water from the aquifer layers toward the production well is evident (and more so at later times). Although water at its normal ocean salinity is injected at the injection well, the salinity in its vicinity declines because of the dissociation caused by the higher temperature (60 °C) of the injected water. What is notable is that the reservoir volume in which X_{sA} declines (indicative of hydrate dissociation) is even larger than those indicated by the T-distribution of **Figure 6.67** and the S_H-distribution of **Figure 6.68**. This indicates that dissociation does occur over a large volume of the hydrate deposit but it does not reach a sufficiently high level to allow accumulation of gas and large production because of the limited effectiveness of depressurization in the presence of highly-permeable aquifer layers that short-circuit the process.

Figures 6.71 to **6.76** present the spatial evolution of P, T, S_H, S_G, and X_{sA} on Plane P1 in Case T1G (involving the full geomechanical model). Compared to the pressure distribution in Case T1, the inclusion of full geomechanical effects leads to (a) an expanded volume of more intense pressure disturbance caused by the production well in the early stages of production, (b) a larger reservoir volume affected by lower pressure during the entire 90-day period of production, (c) a progressively smaller zone of intense depressurization in the immediate vicinity of the well as time advances and the initially-

applied maximum pressure drop (when the pressure at the well is instantaneously lowered to the P_{bh} level) is attenuated, and (d) a reduced pressure impact of the injection well (**Figure 6.71**). The thermal behavior of the system is not significantly affected by geomechanics, because (a) the temperature field with the high upper bound of the color scale in **Figure 6.72** appears to be very similar to that in **Figure 6.66**, and (b) the temperature fields with the low upper bound in **Figures 6.67** and **6.73** show only a slight difference. Although the differences from **Figure 6.68** for Case T1 are subtle, careful inspection of **Figure 6.74** indicates a larger volume of hydrate-free regions around the wells, pointing to enhanced hydrate dissociation when full geomechanics are considered in Case T1G. This is *not* accompanied by evidence of more extensive occurrences of larger S_G in the domain, because differences between the S_G distributions in **Figures 6.69** and **6.75** are very limited. In **Figure 6.76**, the salinity of water flows in the high-*k* ALs is not affected by geomechanics, but X_{sA} in the low-*k* M5 mud layer is affected, leading to a larger X_{sA} (than that in **Figure 6.70** of Case T1) in the vicinity of the production well at t = 90 days that is attributed to a lower permeability in the geomechanically active Case T1G because of compaction.

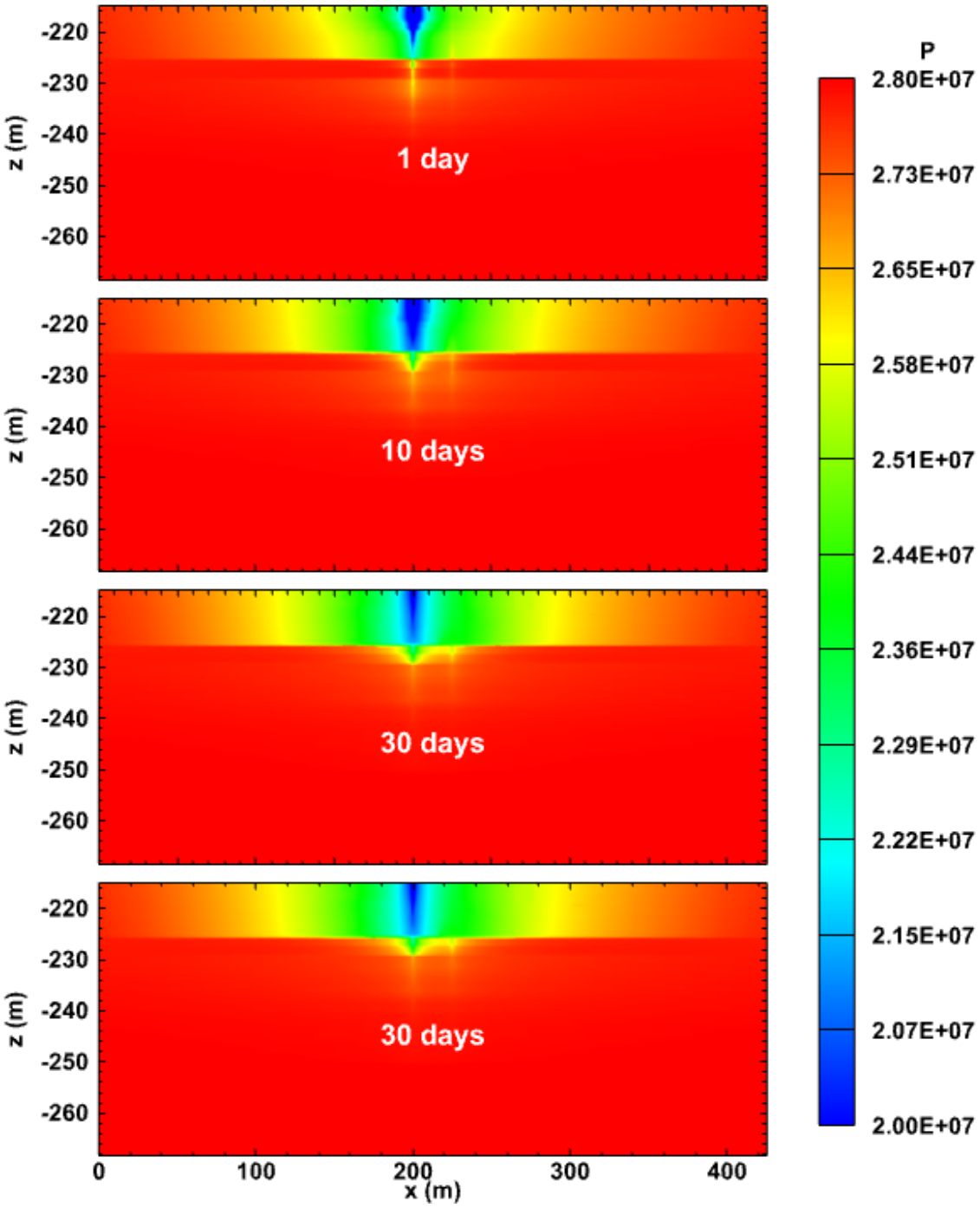

Figure 6.65 Evolution of the spatial distribution of pressure (Pa) on Plane P1 in the reservoir of Case T1.

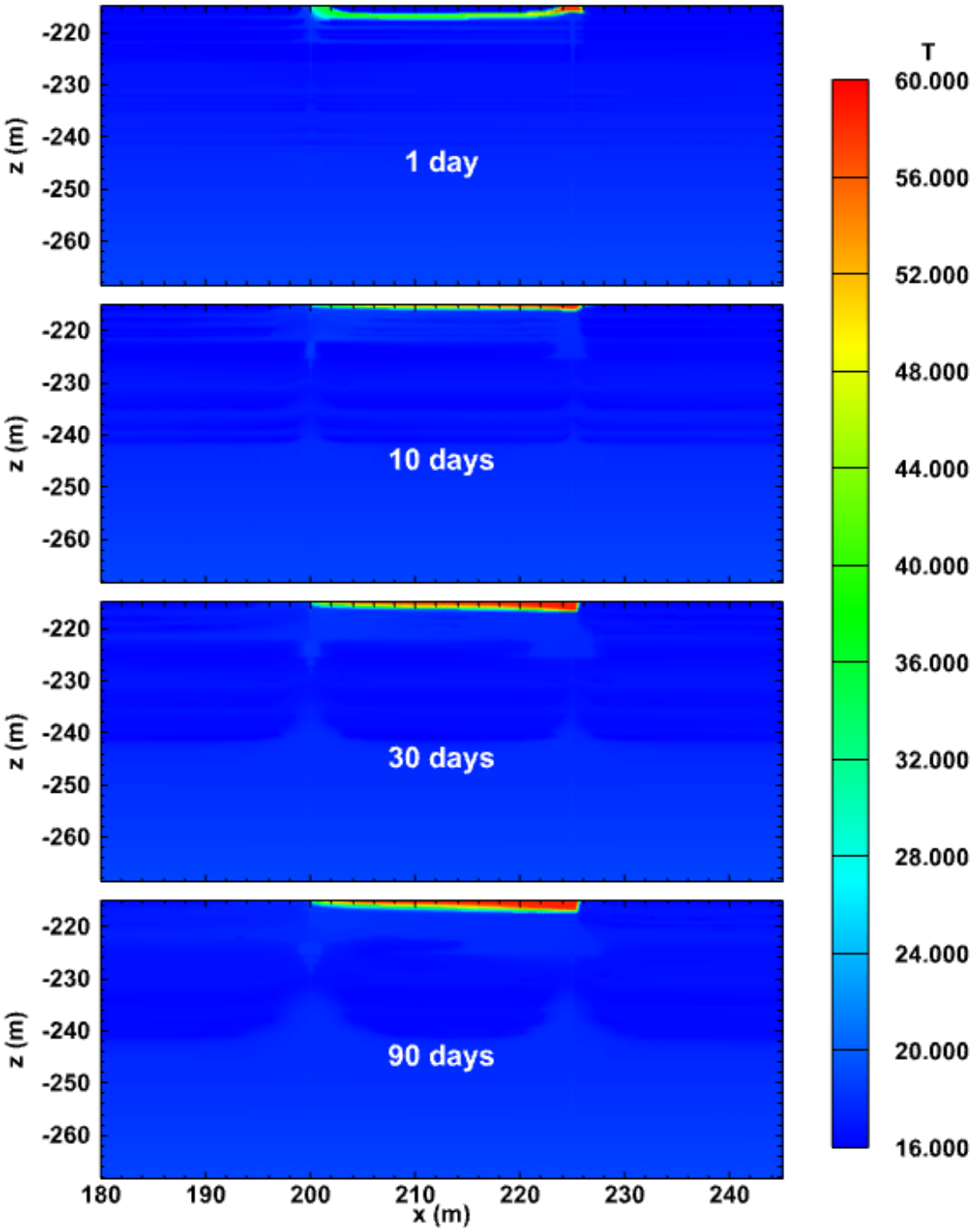

Figure 6.66 Evolution of the spatial distribution of temperature (°C) with a high upper bound of color scale on Plane P1 in the reservoir of Case T1.

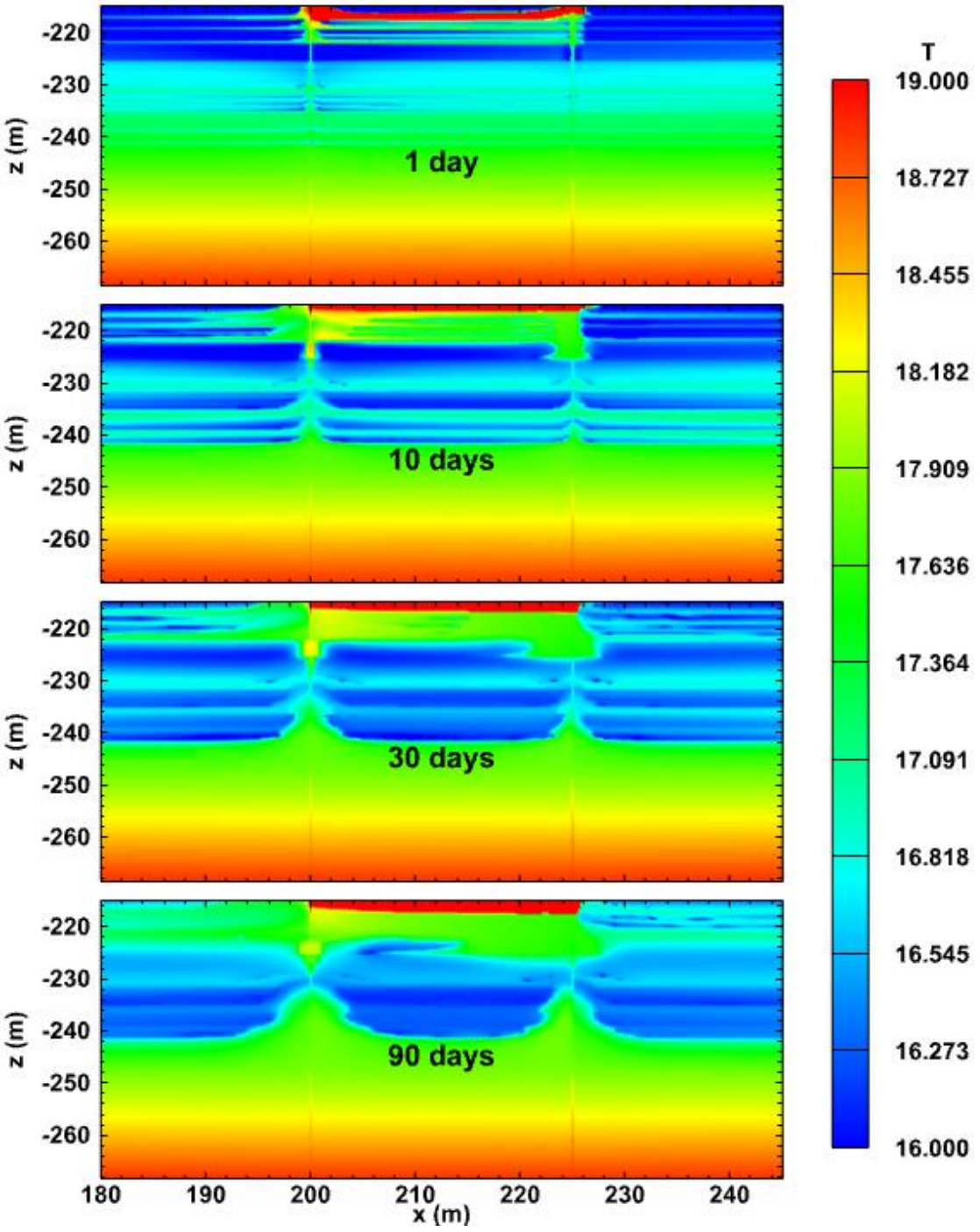

Figure 6.67 Evolution of the spatial distribution of temperature (°C) with a low upper bound of color scale on Plane P1 in the reservoir of Case T1.

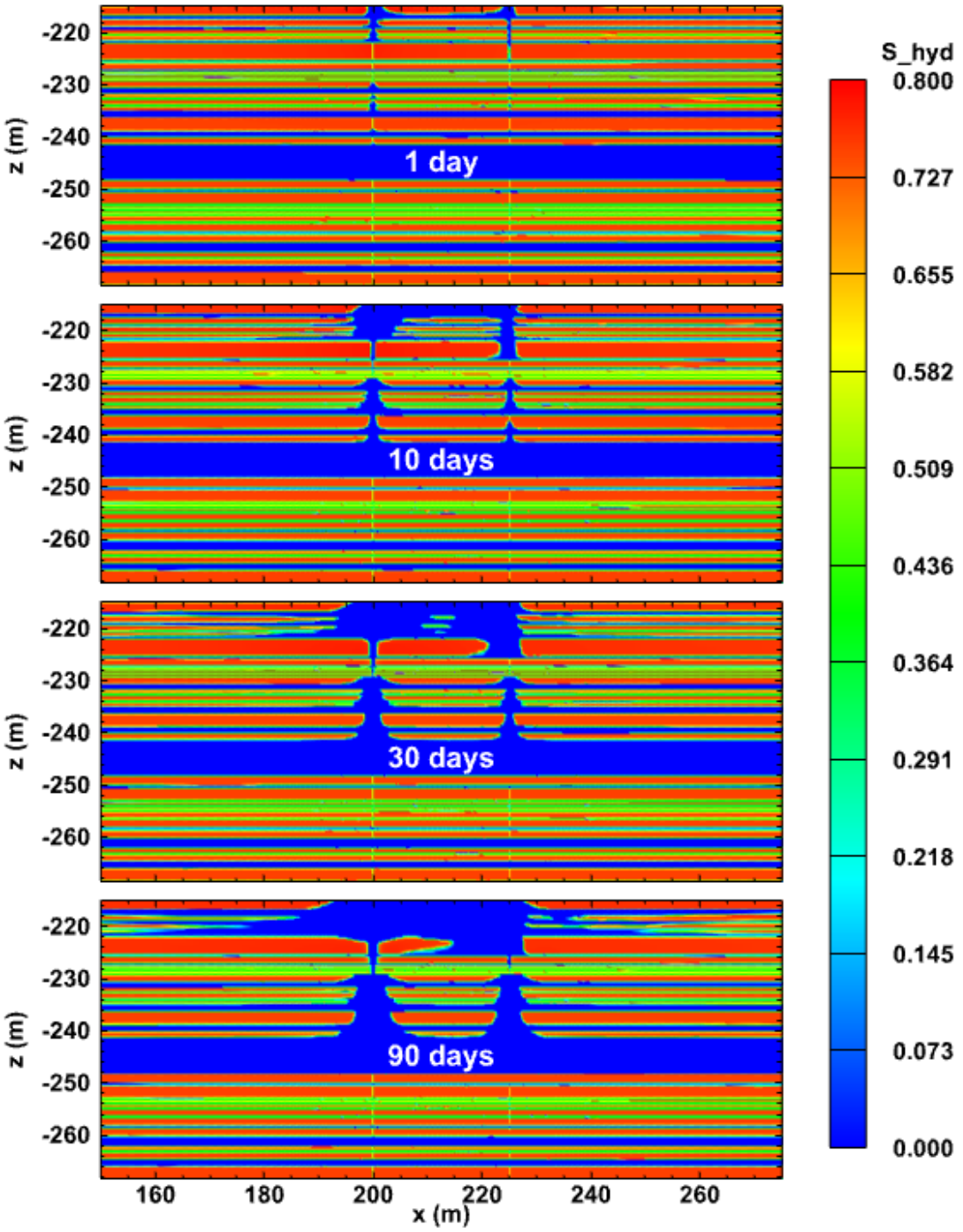

Figure 6.68 Evolution of the spatial distribution of hydrate saturation on Plane P1 in the reservoir of Case T1.

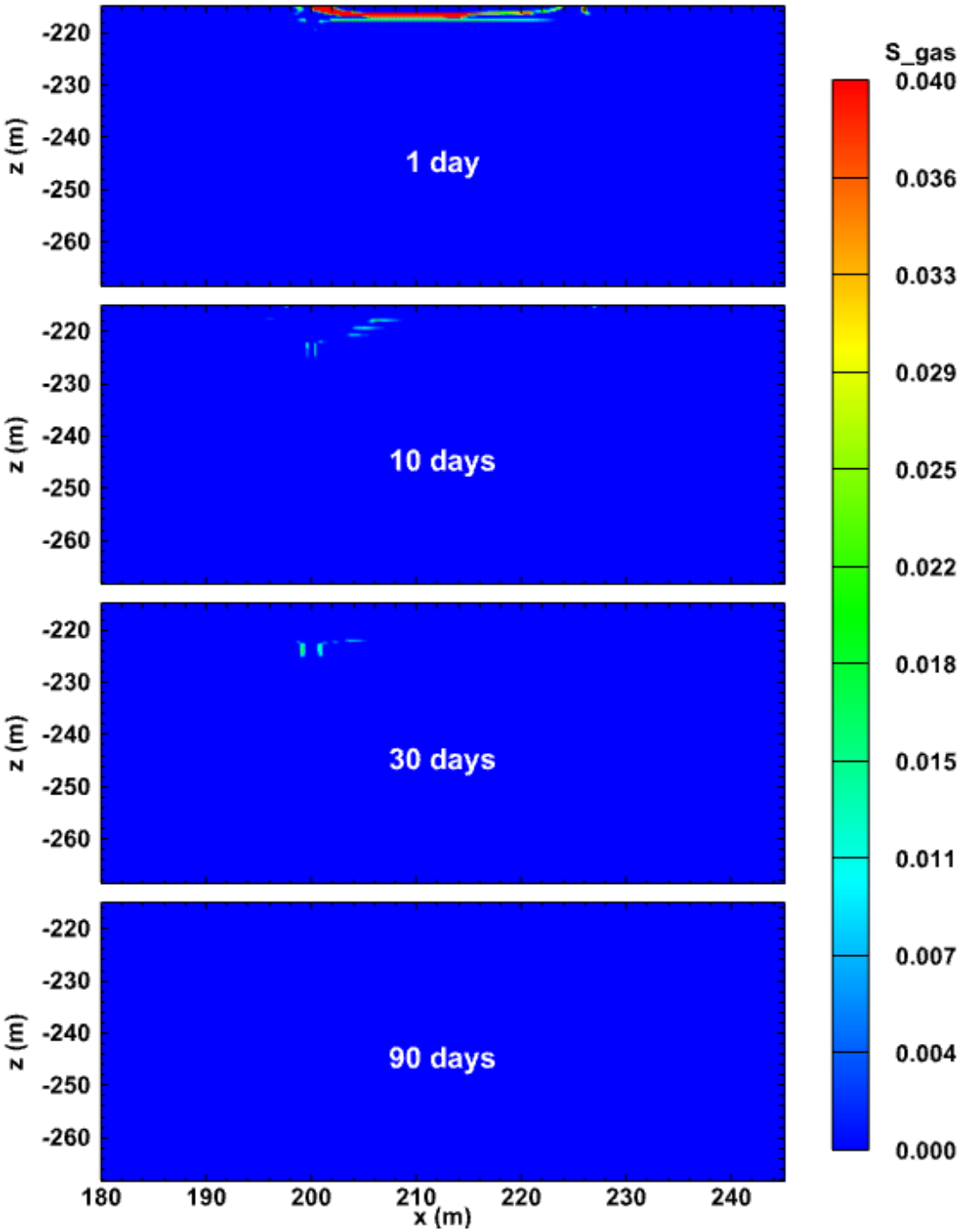

Figure 6.69 Evolution of the spatial distribution of gas saturation on Plane P1 in the reservoir of Case T1.

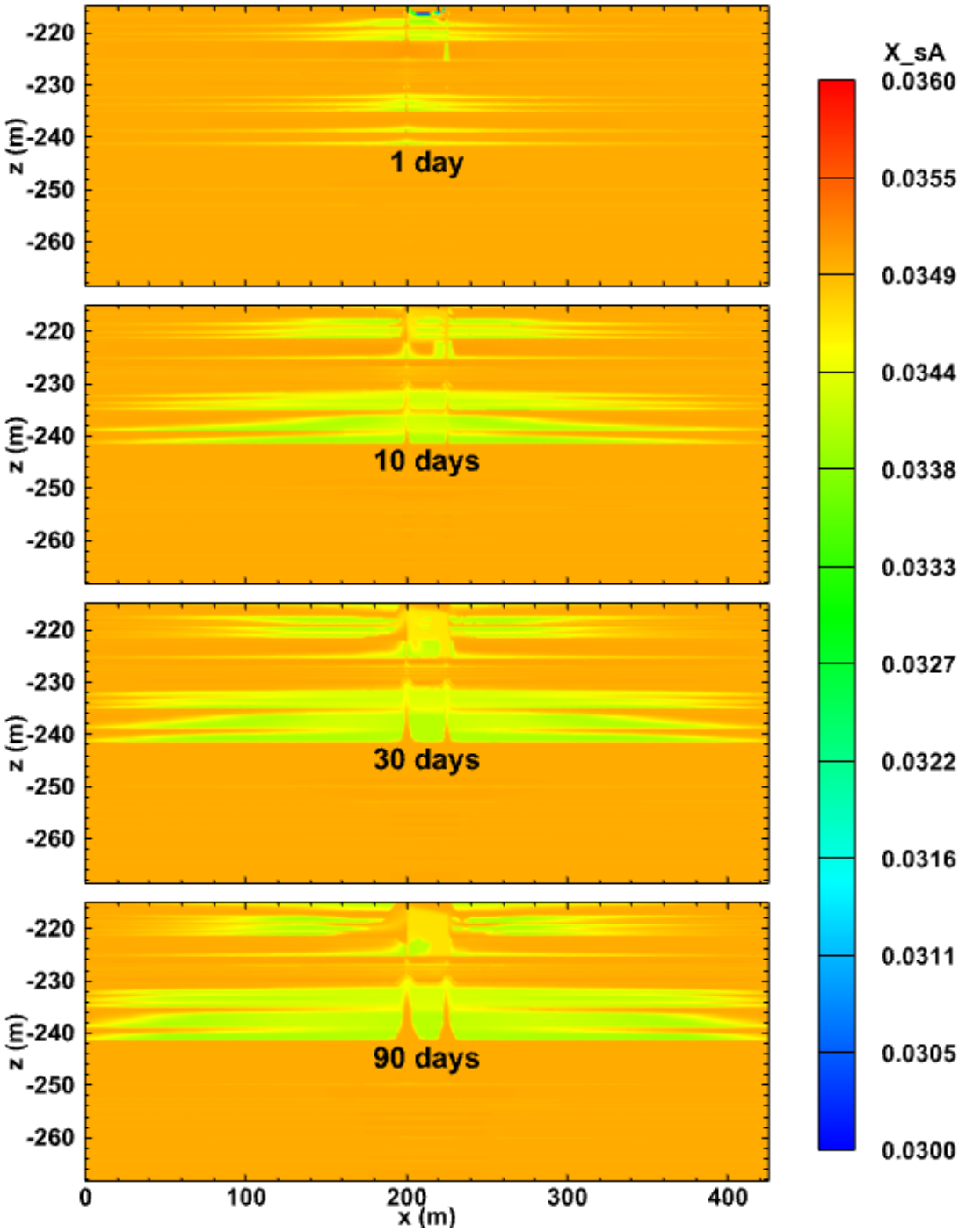

Figure 6.70 Evolution of the spatial distribution of salt mass fraction on Plane P1 in the reservoir of Case T1.

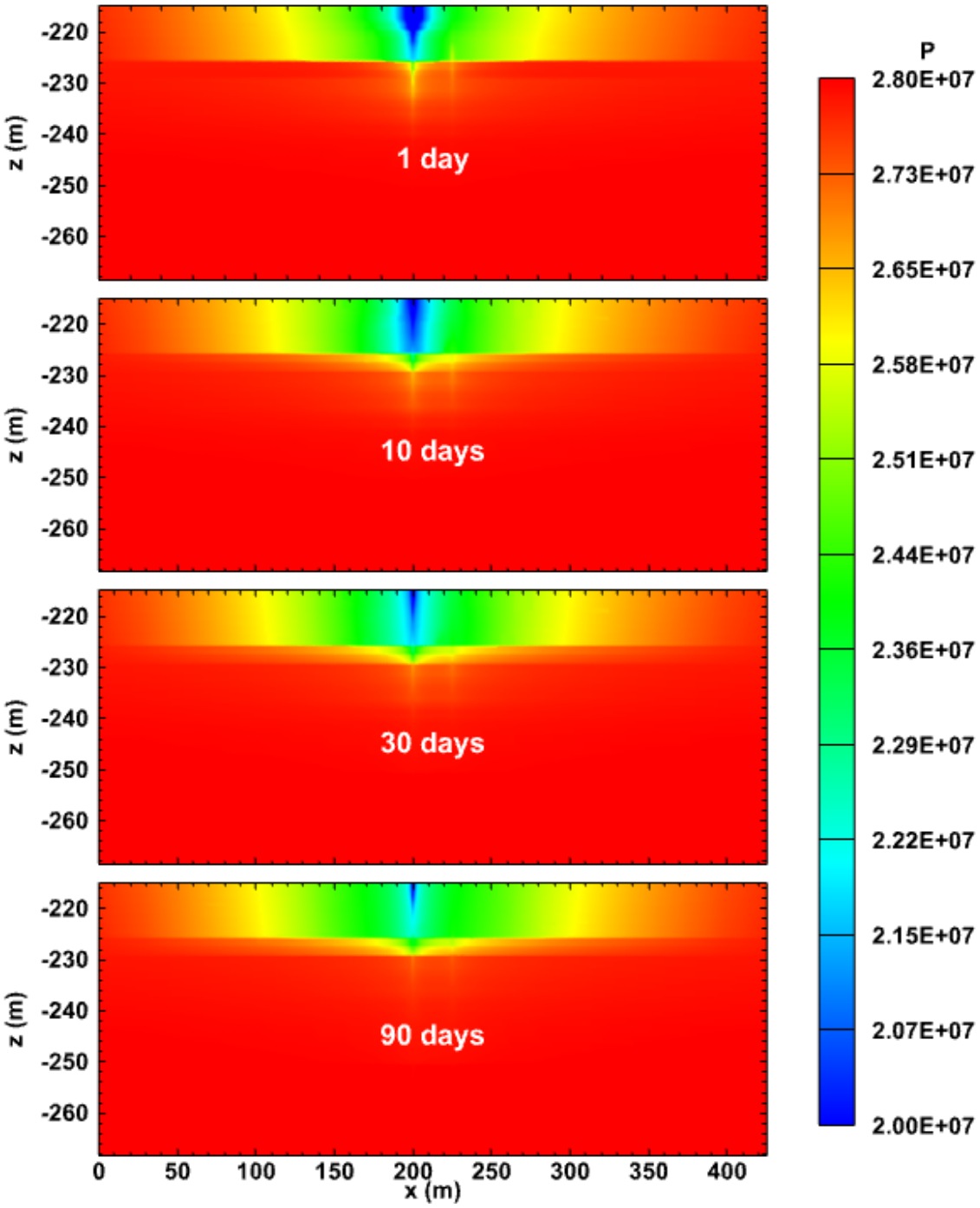

Figure 6.71 Evolution of the spatial distribution of pressure (Pa) on Plane P1 in the reservoir of Case T1G.

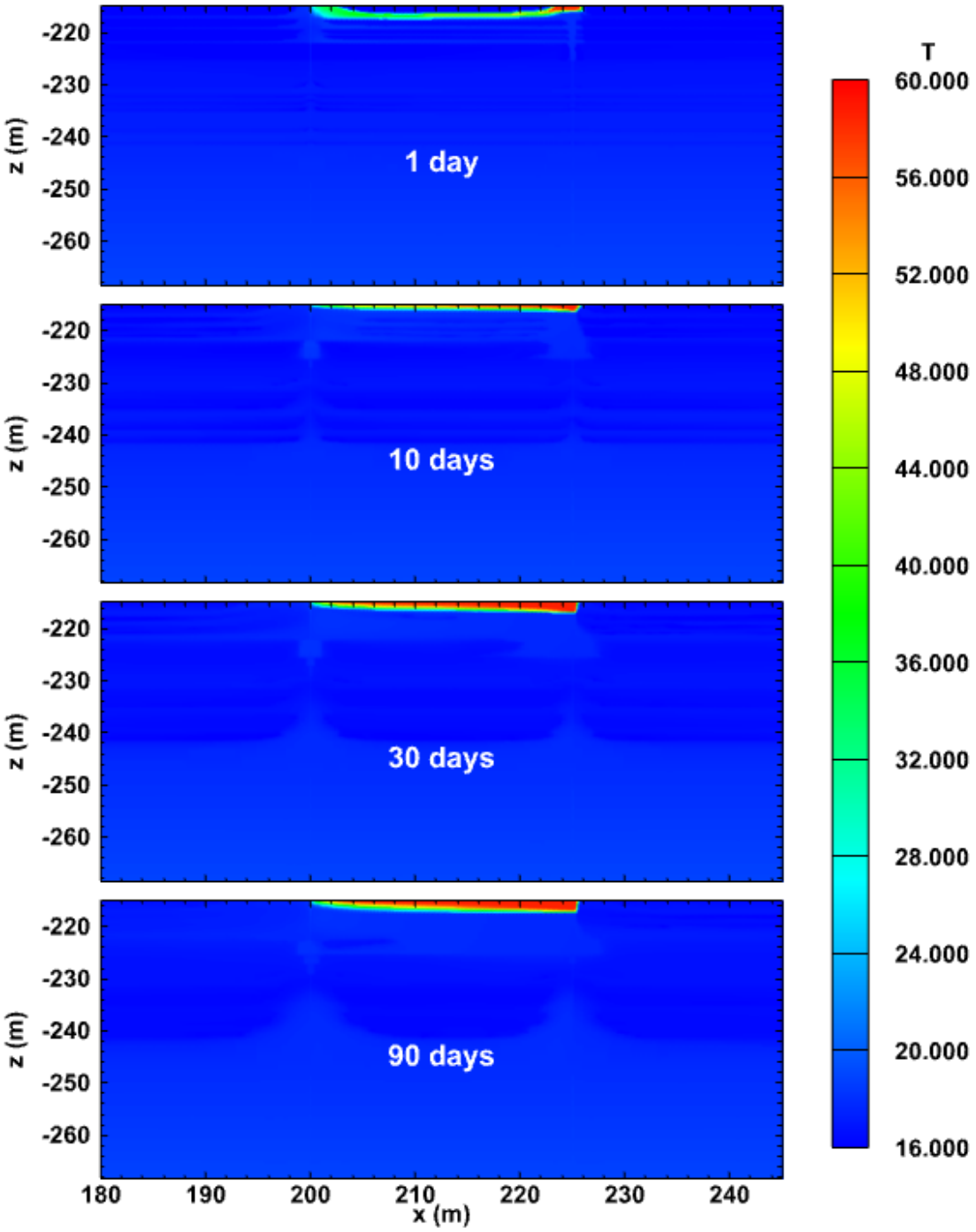

Figure 6.72 Evolution of the spatial distribution of temperature (°C) with a high upper bound of color scale on Plane P1 in the reservoir of Case T1G.

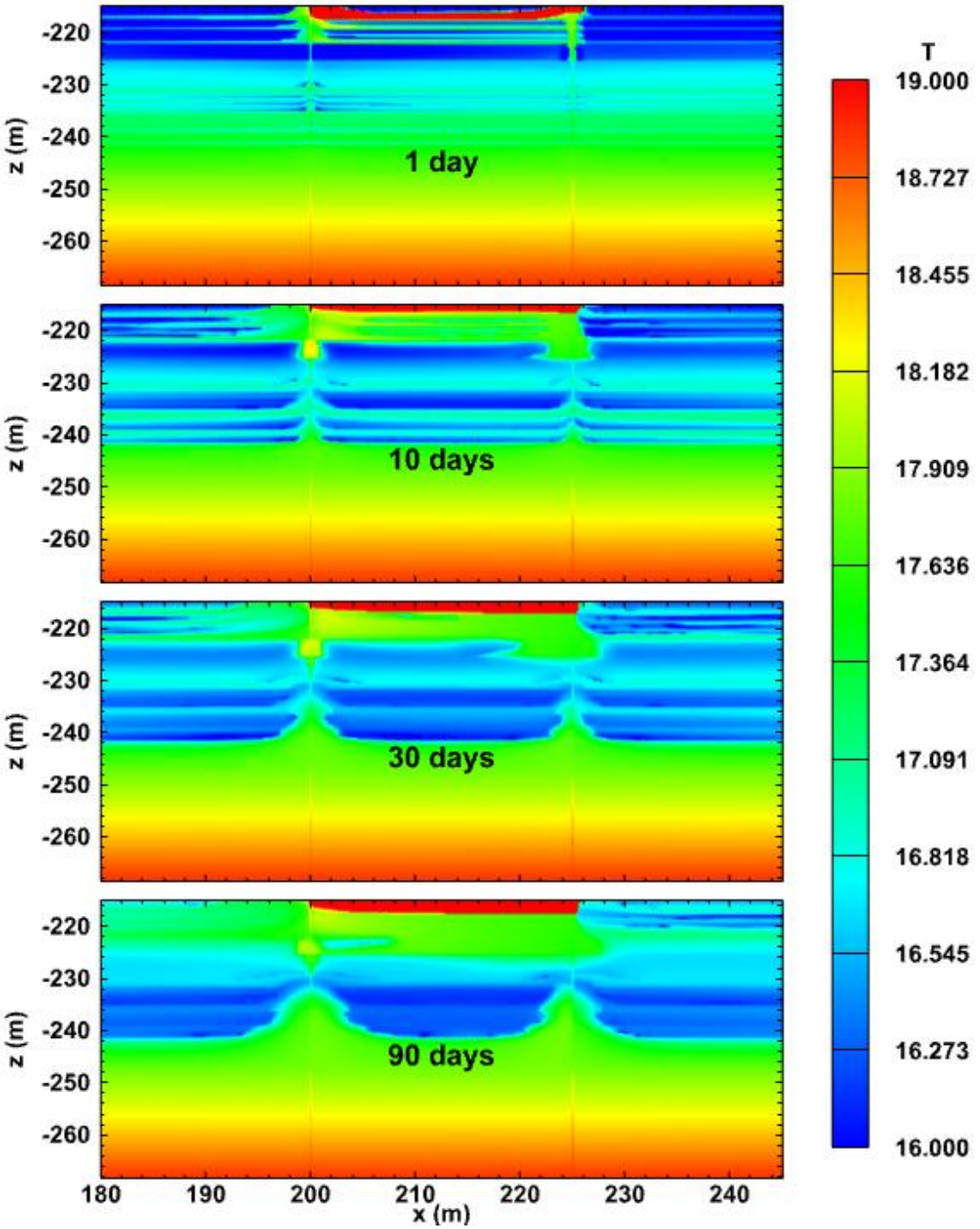

Figure 6.73 Evolution of the spatial distribution of temperature (°C) with a low upper bound of color scale on Plane P1 in the reservoir of Case T1G.

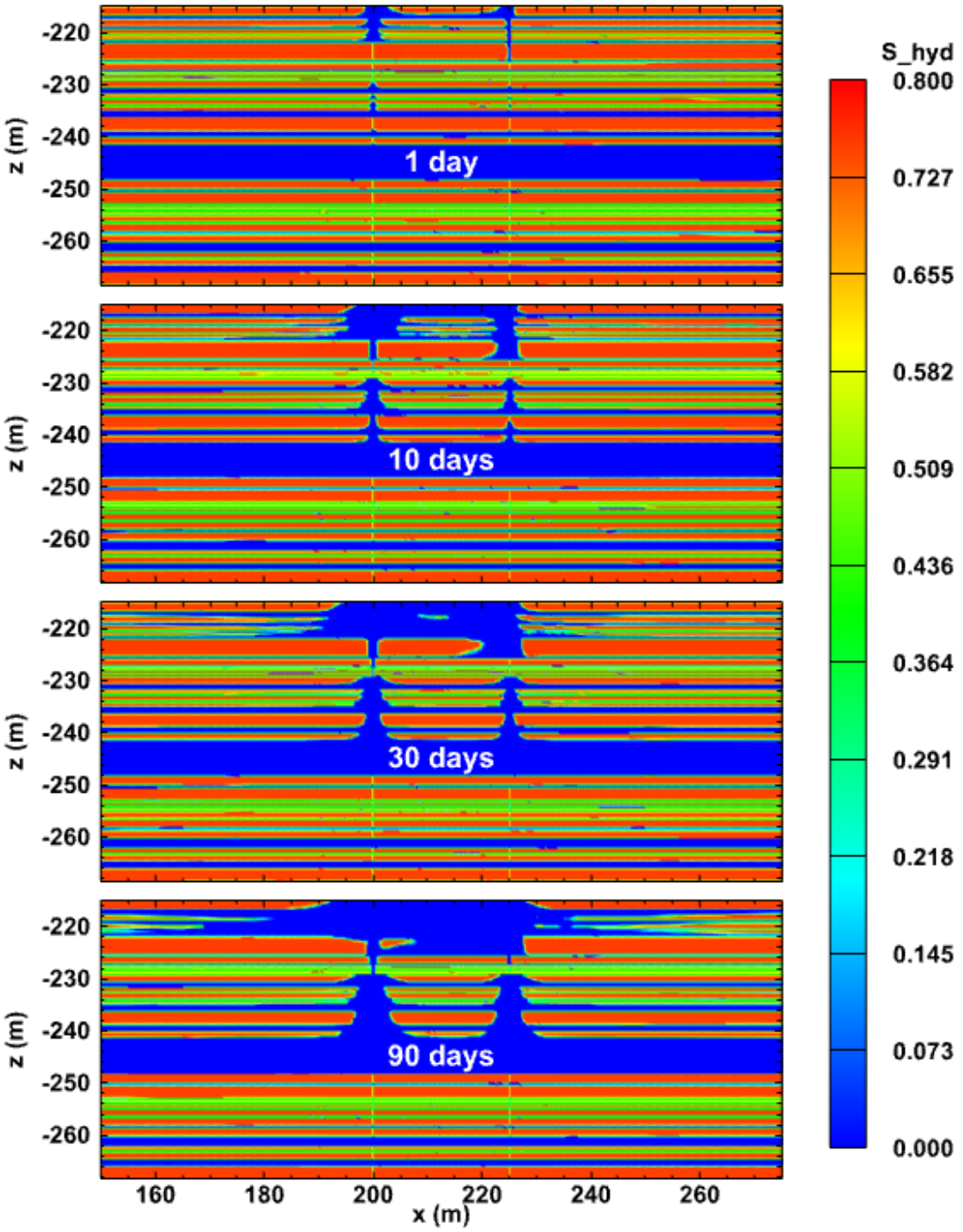

Figure 6.74 Evolution of the spatial distribution of hydrate saturation on Plane P1 in the reservoir of Case T1G.

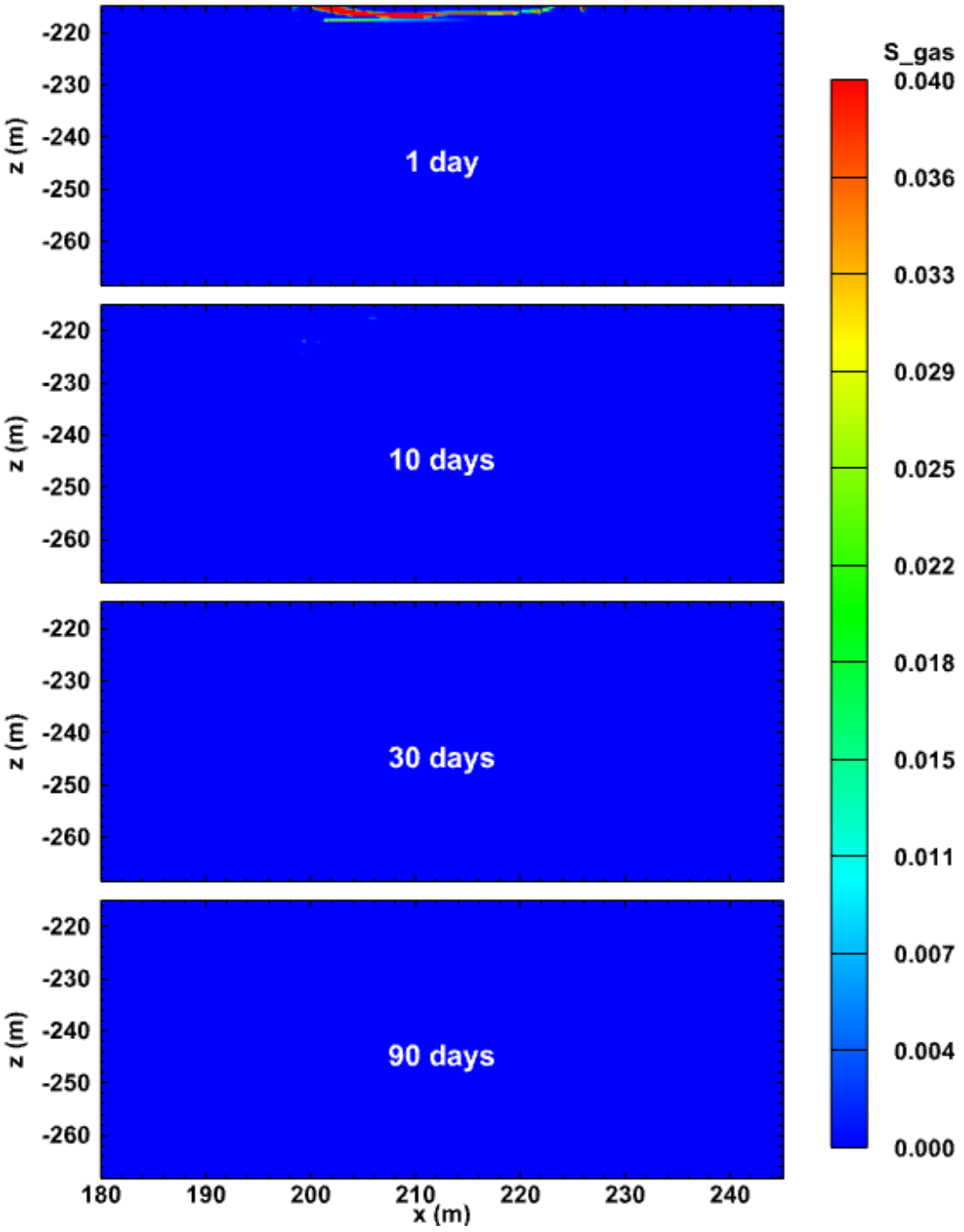

Figure 6.75 Evolution of the spatial distribution of gas saturation on Plane P1 in the reservoir of Case T1G.

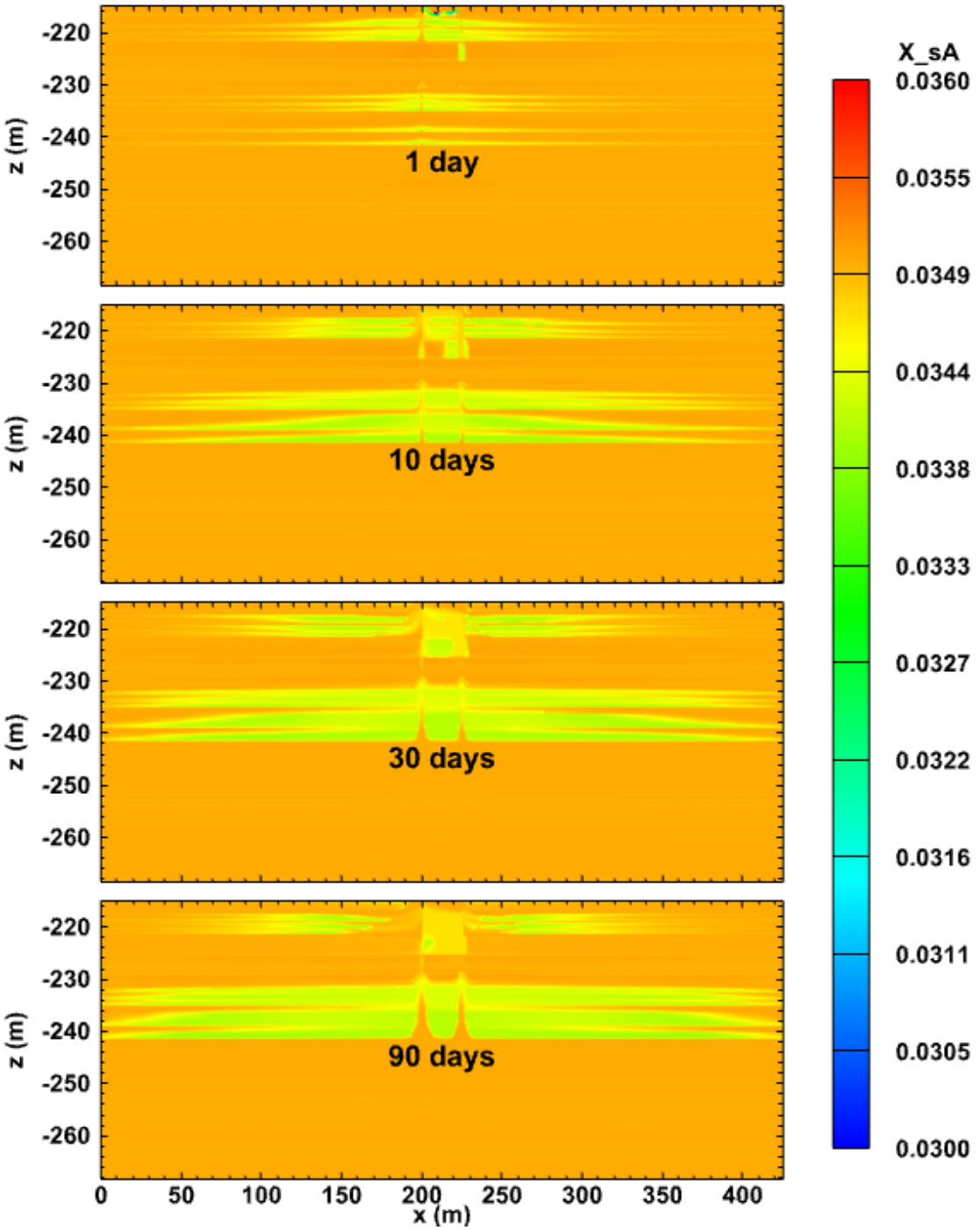

Figure 6.76 Evolution of the spatial distribution of salt mass fraction on Plane P1 in the reservoir of Case T1.

6.3.2.2.2. Results on Plane P2

Figures 6.77, **6.78**, **6.79**, **6.80**, and **6.81** present the spatial evolution of P, T, S_H, S_G, and X_{sA}, respectively, on Plane P2 in Case T1. These results were obtained using the simplified geomechanical model. The evolution of the P-distribution close to the production wellbore in **Figure 6.77** is consistent with that on Plane P1 shown in **Figure 6.65**. The zone of maximum depressurization (caused by the pressure drop that is applied instantaneously to the well by the P_{bh}) initially expands, but later shrinks as the near-well effective permeability increases in response to the hydrate dissociation. **Figure 6.78** describes the T-distribution in the y-direction near the production well. The low-T areas are indicative of active hydrate dissociation (a result of the endothermic nature of the reaction) and expand radially and downward over time as dissociation continues. Note

(a) the increasing temperatures over time at the top of the hydrate deposit as (i) the hydrate is exhausted and the cooling dissociation reactions there cease and (ii) the injected warm water reaches the production well even at early times,

(b) the very large extent of lower temperatures in the hydrate, indicating active dissociation even at low levels (as will be shown in the S_H- and S_G-distribution of the ensuing **Figures 6.79** and **6.80**), and

(c) the inability of the hydrate dissociation front to reach below the A10 aquifer layer.

The spatial evolution of S_H shown in **Figure 6.79** is not complementary of the T-distribution in **Figure 6.78** because it does not show significant hydrate degradation where lower temperatures are observed, probably because dissociation occurs at very low rates there that are too low to lead to measurable reductions in S_H. However, **Figure 6.79** does

show significant hydrate dissociation (signified by the S_H reduction) near the well, which was expected because this is the location of maximum depressurization. Note the coincidence of the "warming" regions in the vicinity of the well in **Figure 6.78** with the corresponding absence of hydrate at these locations in **Figure 6.79**. The S_G-distribution in **Figure 6.80** shows very little evidence of gas presence on Plane P2 and is an insufficient base for conclusions on this matter.

The spatial distribution of X_{sA} close to the production wellbore in **Figure 6.81** is in accordance with that on Plane P1 in **Figure 6.70** and shows active hydrate dissociation over large distances from the well (even at y = 200 m) even from the earliest times of production. The footprint of dissociation is much larger than that suggested by the S_H distribution in **Figure 6.79** but in agreement with the T-distribution of **Figure 6.78**, indicating the importance of monitoring these two properties in the analysis of the system behavior.

Figures 6.82, **6.83**, **6.84**, and **6.85** present the spatial evolution of P, T, S_H, and X_{sA}, respectively, on Plane P2 in Case T1G, which involves a full geomechanical model. The conclusions drawn from the P-distribution shown in **Figure 6.82** are in agreement with those drawn from the P-distribution on Plane P1 (**Figure 6.71**) and will not be repeated here. Compared to **Figure 6.78**, **Figure 6.83** shows a more extensive higher-T region around the well in the upper part of the formation (above the A10 layer) and at later times, which is indicative of more intense dissociation activity and exhaustion of hydrate at these locations. This is confirmed by the evolution of S_H distribution in **Figure 6.84**, which indicates more intense dissociation associated with the complex geomechanics in

Case T1G. The S_G-distributions over time in Case T1G are not provided because they are practically indiscernible from those in Case T1 (see **Figure 6.80**).

Figure 6.85 shows that the X_{sA} along the *y*-direction in the M5 layer is barely reduced below its original level as hydrate, indicating a less active hydrate dissociation at this location, in agreement with the X_{sA} observations on Plane P1 in **Figure 6.76** and attributable to the reduced ϕ and k because of compaction in the geomechanically active Case T1G.

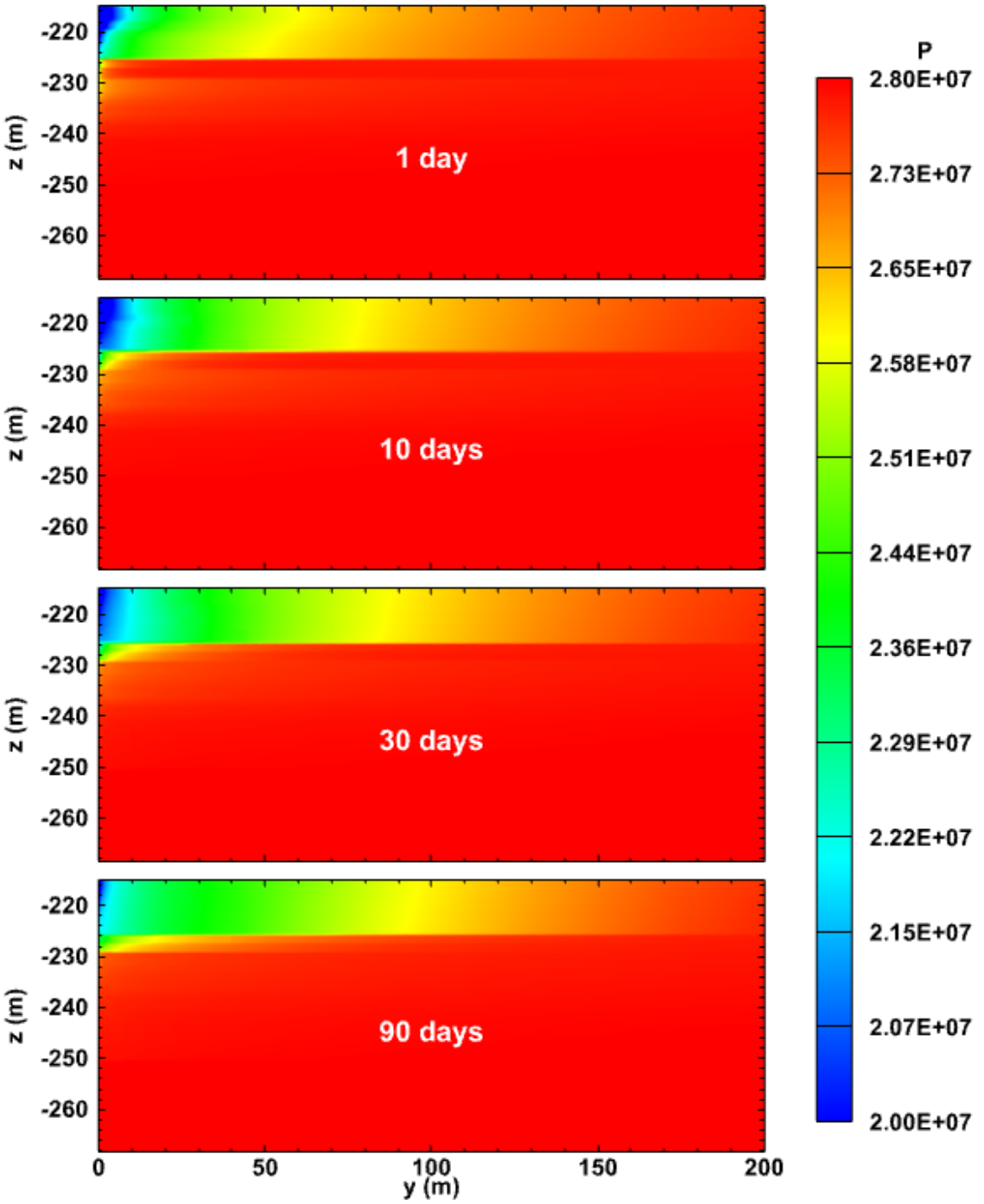

Figure 6.77 Evolution of the spatial distribution of pressure (Pa) at on Plane P2 in the reservoir of Case T1.

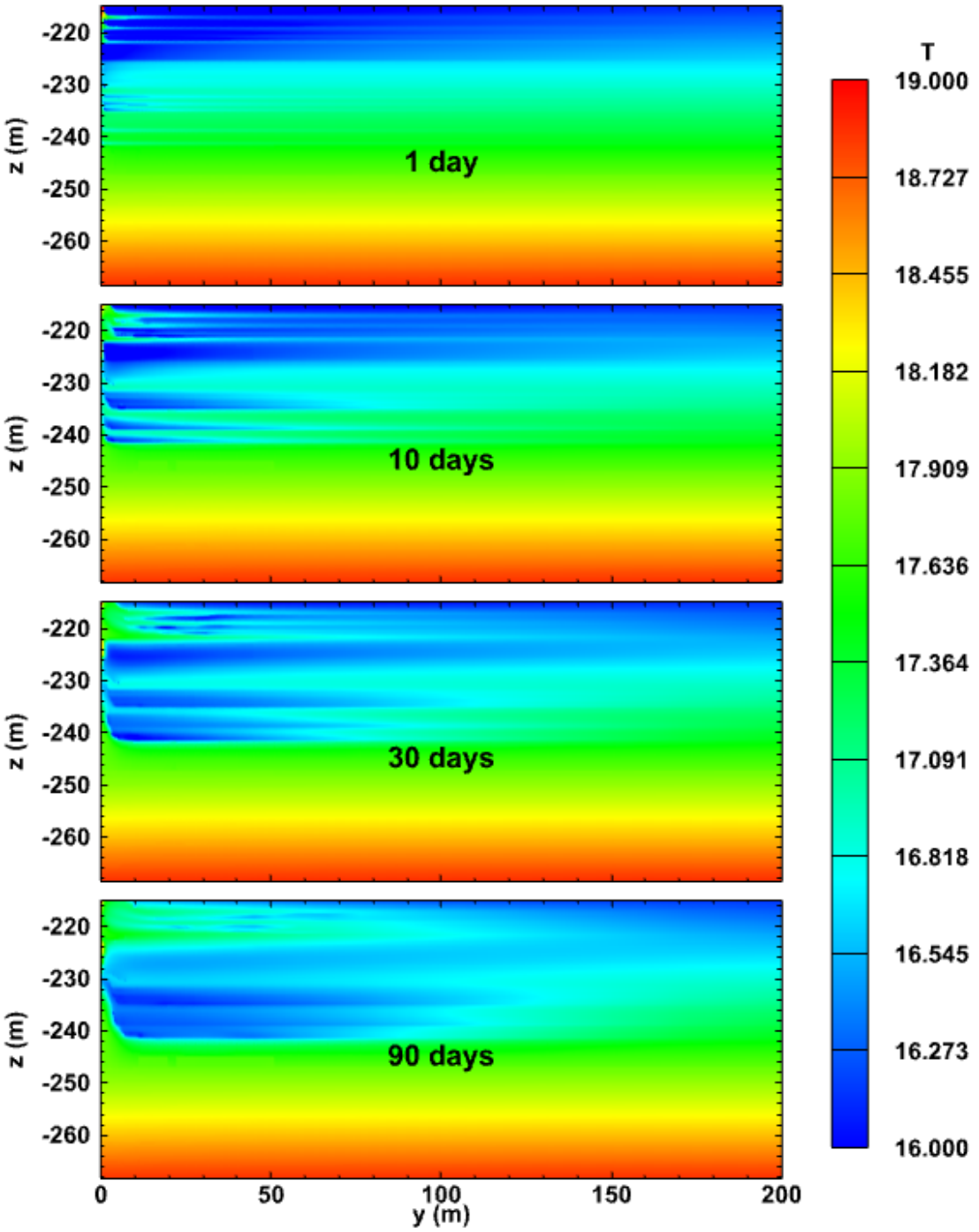

Figure 6.78 Evolution of the spatial distribution of temperature (°C) on Plane P2 in the reservoir of Case T1.

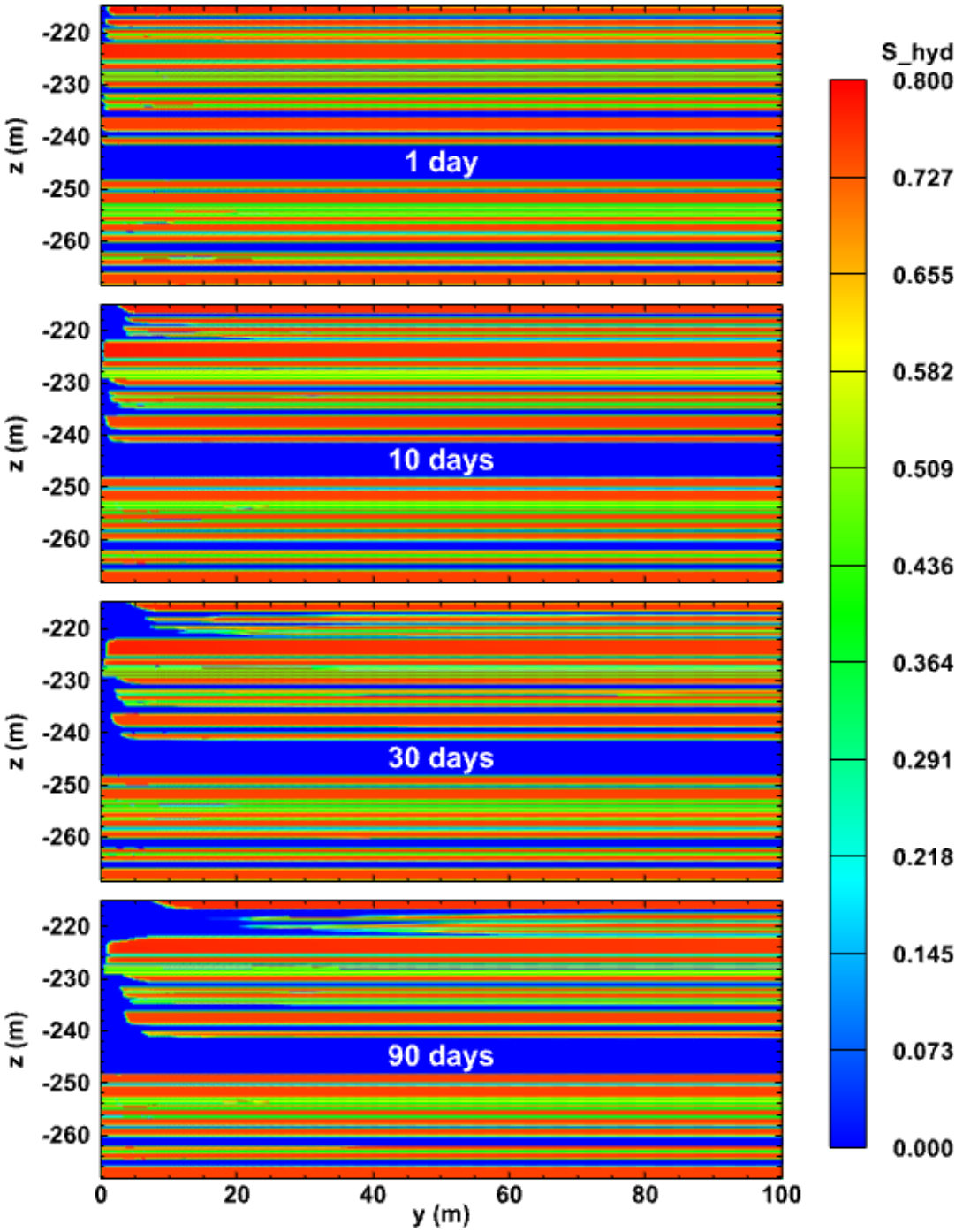

Figure 6.79 Evolution of the spatial distribution of hydrate saturation on Plane P2 in the reservoir of Case T1.

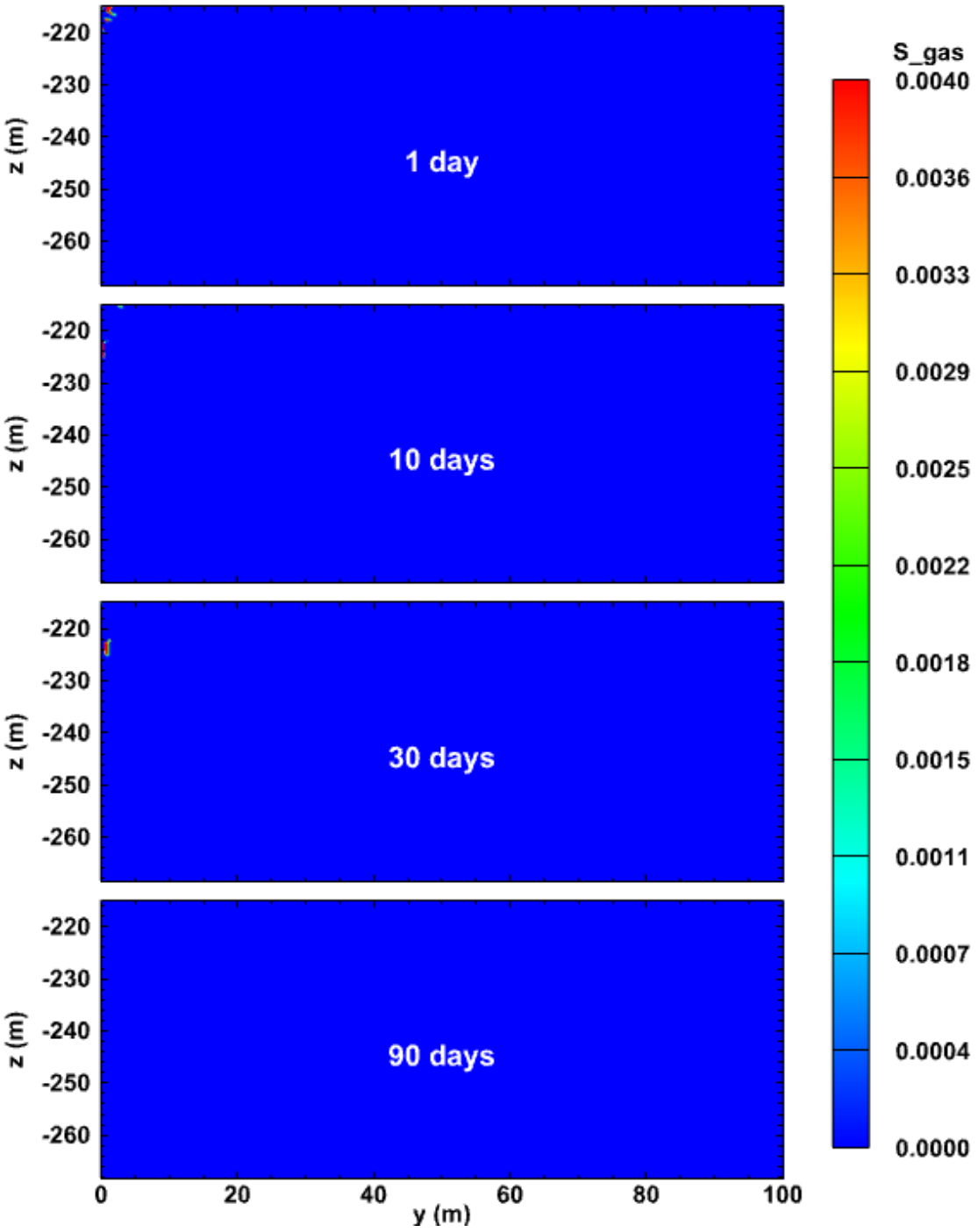

Figure 6.80 Evolution of the spatial distribution of gas saturation on Plane P2 in the reservoir of Case T1.

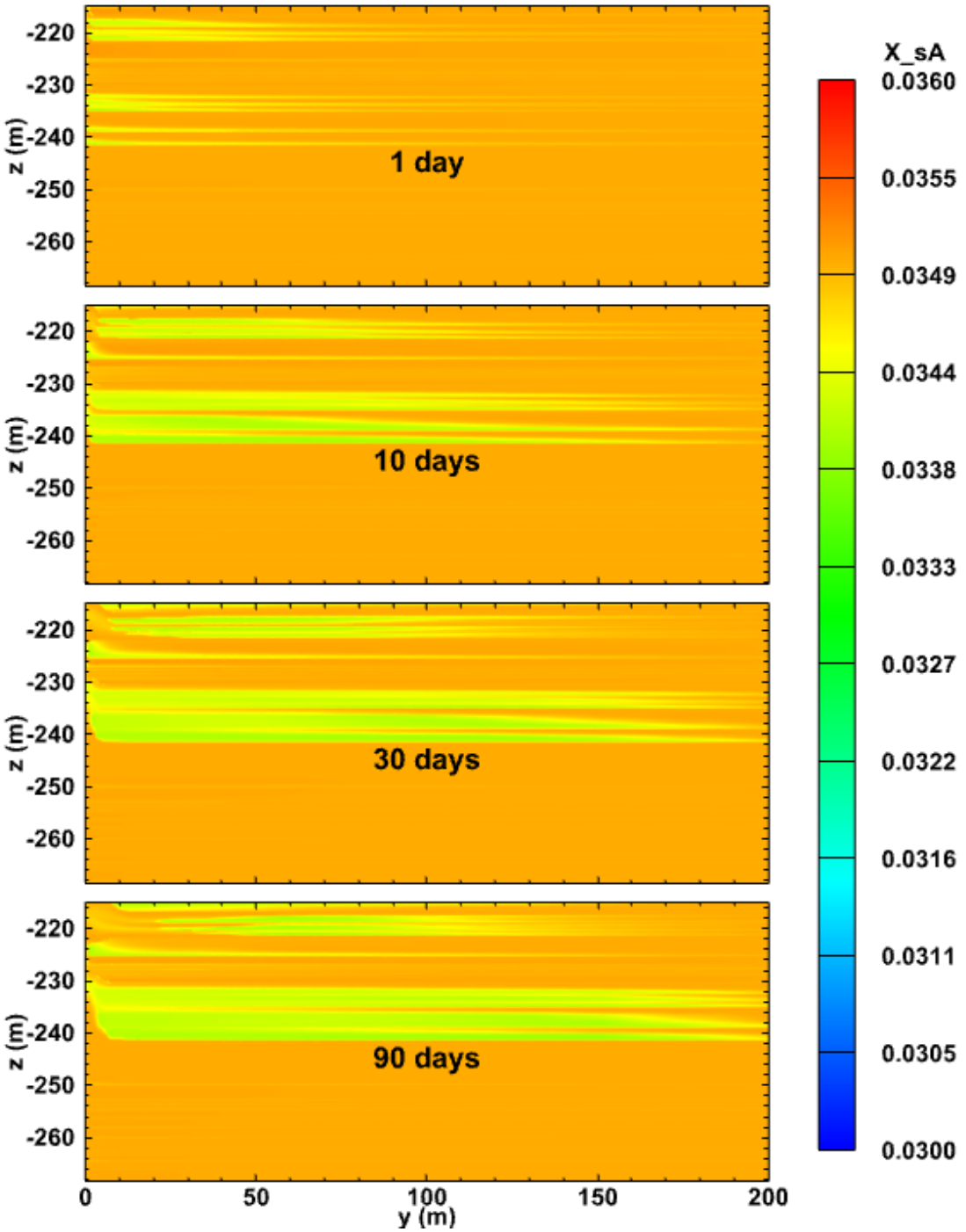

Figure 6.81 Evolution of the spatial distribution of salt mass fraction on Plane P2 in the reservoir of Case T1.

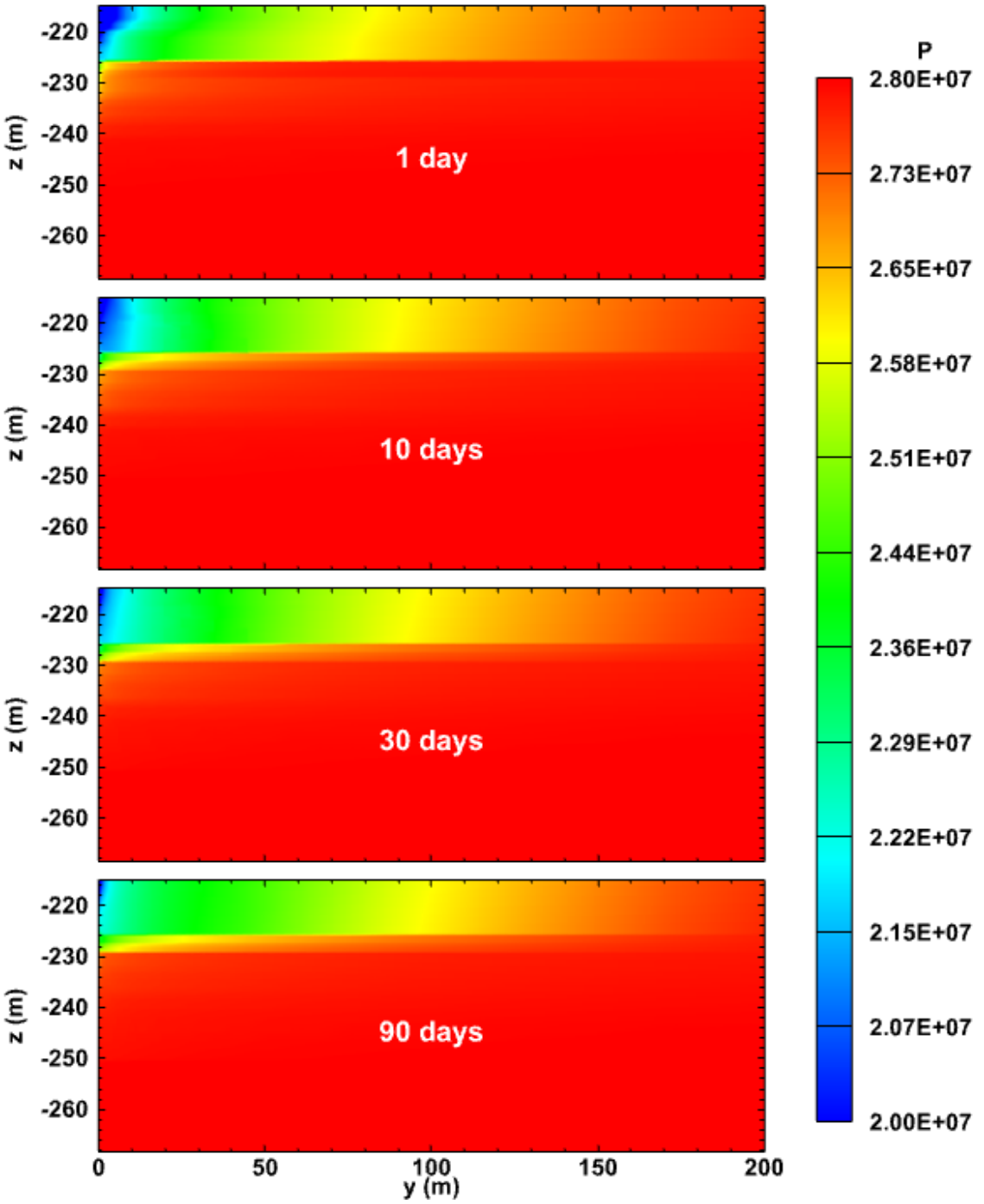

Figure 6.82 Evolution of the spatial distribution of pressure (Pa) on Plane P2 in the reservoir of Case T1G.

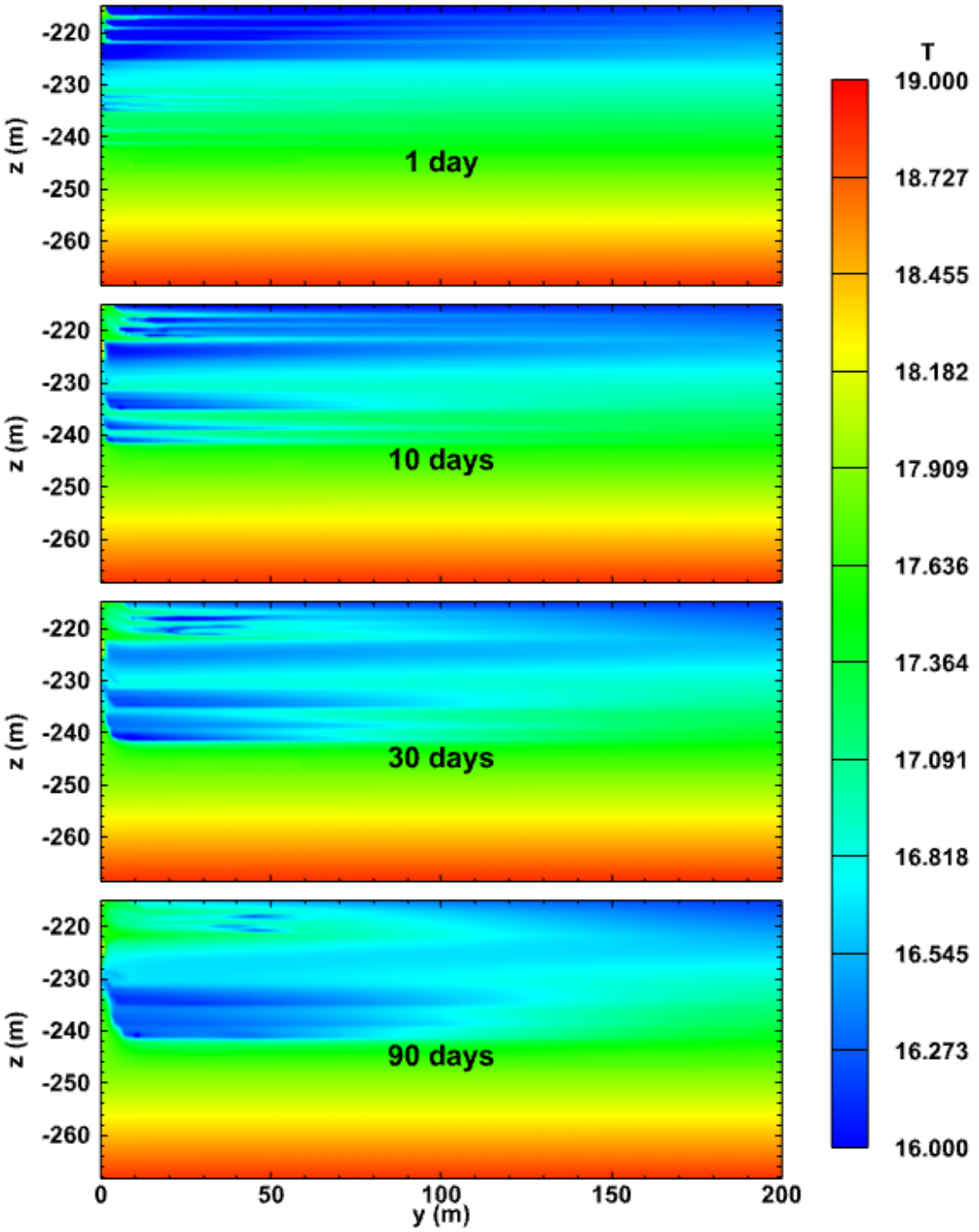

Figure 6.83 Evolution of the spatial distribution of temperature (°C) on Plane P2 in the reservoir of Case T1G.

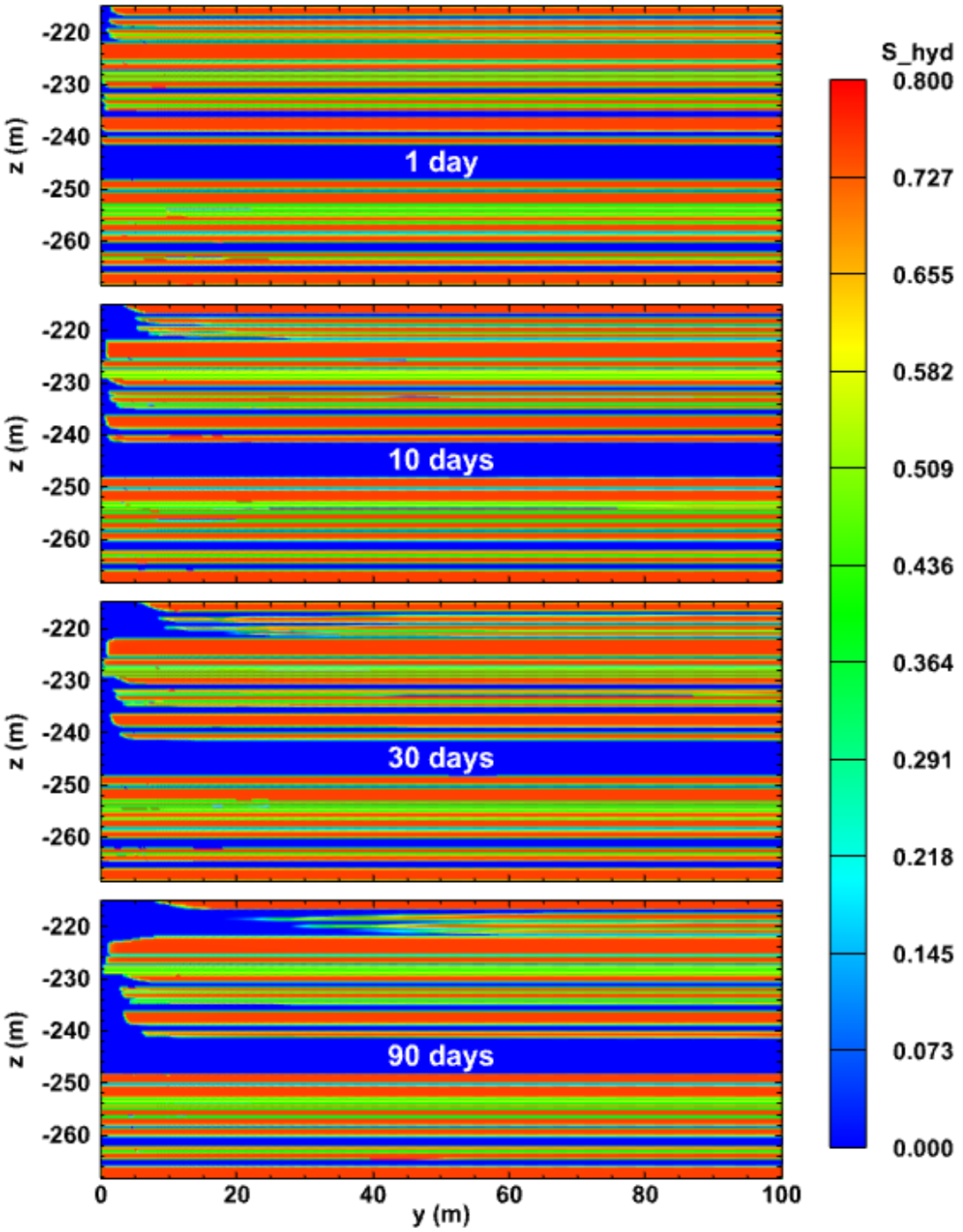

Figure 6.84 Evolution of the spatial distribution of hydrate saturation on Plane P2 in the reservoir of Case T1G.

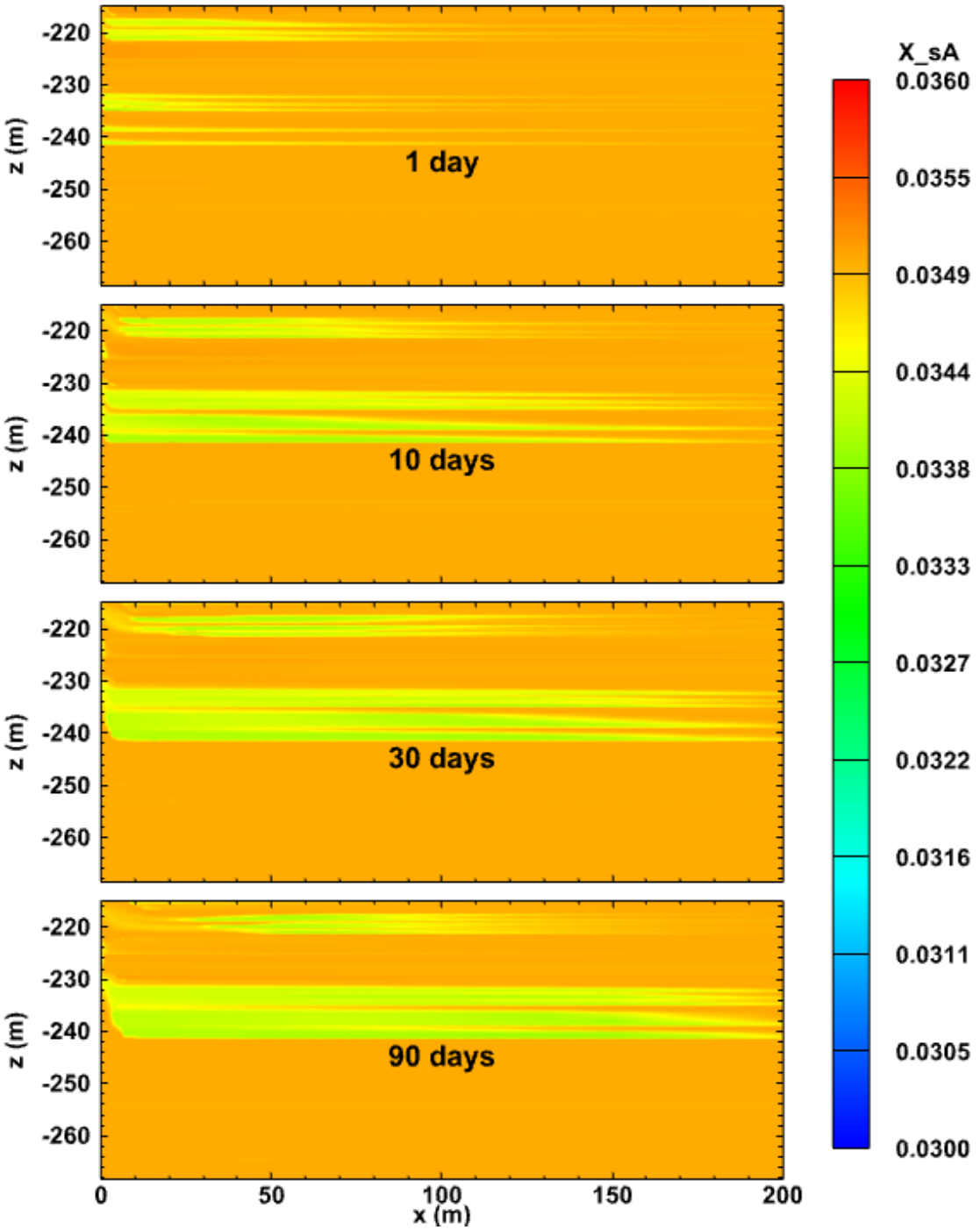

Figure 6.85 Evolution of the spatial distribution of salt mass fraction on Plane P2 in the reservoir of Case T1G.

6.3.2.2.3. Results on Plane P3

Figures 6.86 to **6.91** present the spatial evolution of P, T, S_H, S_G, and X_{sA} on Plane P3 in Case T1. Despite the continuous injection of warm water, evolution of the spatial discretization of P in **Figure 6.86** shows a pressure drop, as the injection rate is insufficient to counter the effects of the more substantial fluid withdrawal from the production well. As in all other previous related figures, the limit of depressurized zone is clearly marked by a sharp interface at the base of the H5 layer, and the pressure disturbance barely advances beyond that level even at later times for reasons already discussed: the low permeability of the underlying mud layer, and the high permeability of the aquifer interlayers in the hydrate deposit that supply large amounts of replenishable water to the production well, thus preventing effective depressurization.

Figure 6.87 (obtained with a high upper limit in the temperature color scale) shows that the injected warm water *substantially* raises the temperature only in a limited volume of the reservoir around the injection wellbore even after 90 days of injection. Additionally, the high-T region is confined to the uppermost part of the hydrate deposit and does not affect the bulk of the reservoir volume, thus severely limiting the effectiveness of the intended (and hoped for) thermal- and salt-induced hydrate dissociation of the injected saline ocean water. Of interest is the observation that the extent/reach of the high-T zone is at a maximum at t = 1 day, after which it shrinks (t = 10 days) before stabilizing for $t \geq$ 30 days—a behavior attributed to continuous mixing with the native reservoir waters.

The temperature field in **Figure 6.88** (obtained with a low upper limit in the temperature color scale) shows a very different distribution than that in **Figure 6.87**, with

the volume of the reservoir affected by the higher temperature of the injected water expanding consequently but with lower temperatures because of mixing with the colder native water, in addition to the heat consumed to support dissociation. In this figure, the presence of the lower-*k* layers (*i.e.*, HBLs with high S_H, or low-*k* muds) is identified by the limited penetration of higher temperature in the bulk of their bodies.

Early hydrate dissociation (denoted by the S_H distribution) in **Figure 6.89** appears minor because of (a) the low effectiveness of thermal dissociation compared to the one induced by depressurization (Moridis and Reagan 2007a), combined with (b) the higher pressure associated with the water injection that only partly counters the effect of depressurization at the production well. This being the case, it is possible that, in addition to the thermal dissociation, a significant part of hydrate dissociation at this location is attributable to the depressurization shown in **Figure 6.89**. What is very interesting is that some substantial hydrate destruction is evident at t = 90 days, but that does not correspond to the high-T region shown in **Figure 6.87**, thus further reinforcing the thesis that this is caused by the unavoidable depressurization. Note that here, as in all other similar cases, dissociation never advances past the A10 aquifer layer. **Figure 6.90** reveals a limited occurrence of free gas only at t = 1 day in the vicinity of the injection well on this plane. **Figure 6.91** shows that (a) the injected warm water causes some thermal dissociation in the H5 layer as X_{sA} decreases near the injection wellbore, and (b) as in all other cases of X_{sA}-distribution, the reservoir volume exhibiting some degree of hydrate dissociation (even minor) is much larger than that suggested by the distribution of any other property of the system, with the possible exception of that of the temperature (**Figure 6.88**).

Figures 6.92 to **6.96** present the spatial evolution of P, T, S_H, and X_{sA}, on Plane P3 in Case T1G, with the results obtained using a full geomechanical model. The difference of S_G-distributions over time between Cases T1 and T1G is visually imperceptible so the distribution in Case T1G is not provided. Compared to the results in Case T1, the only (minor) differences are the slightly larger extent of the zone of reduced pressure (**Figure 6.92**), a reduced extent of the high-T zone (**Figure 6.93**), attributable to the lower ϕ and k of the geomechanically-induced compaction of the depressurized region, lower T observed in some HBLs (**Figure 6.94**), a somewhat larger (dissociation-caused) hydrate-free zone at t = 90 days (**Figure 6.95**), and a smaller low-X_{sA} zone (**Figure 6.96**) because of lower hydrate dissociation for reasons already discussed.

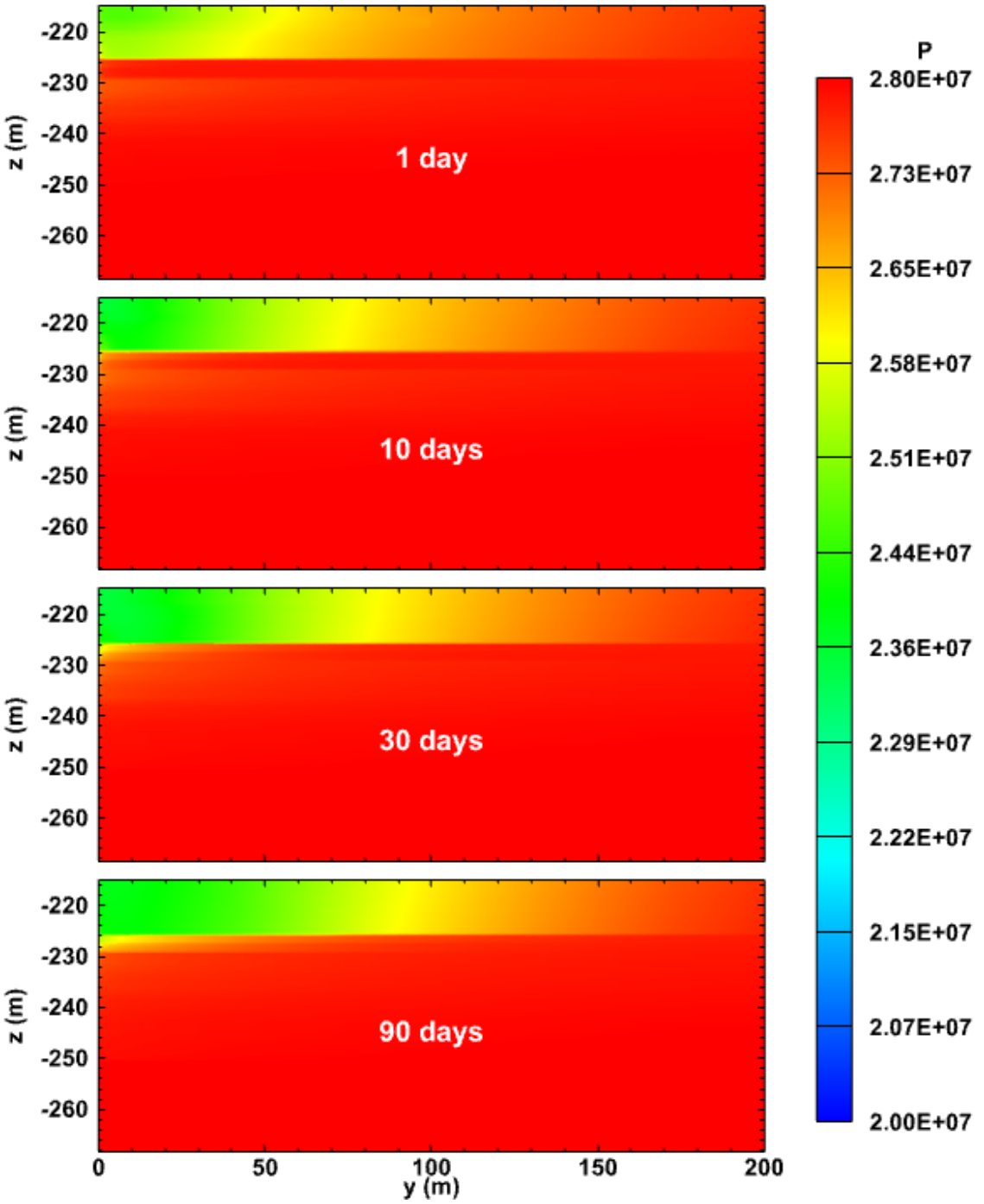

Figure 6.86 Evolution of the spatial distribution of pressure (Pa) on Plane P3 in the reservoir of Case T1.

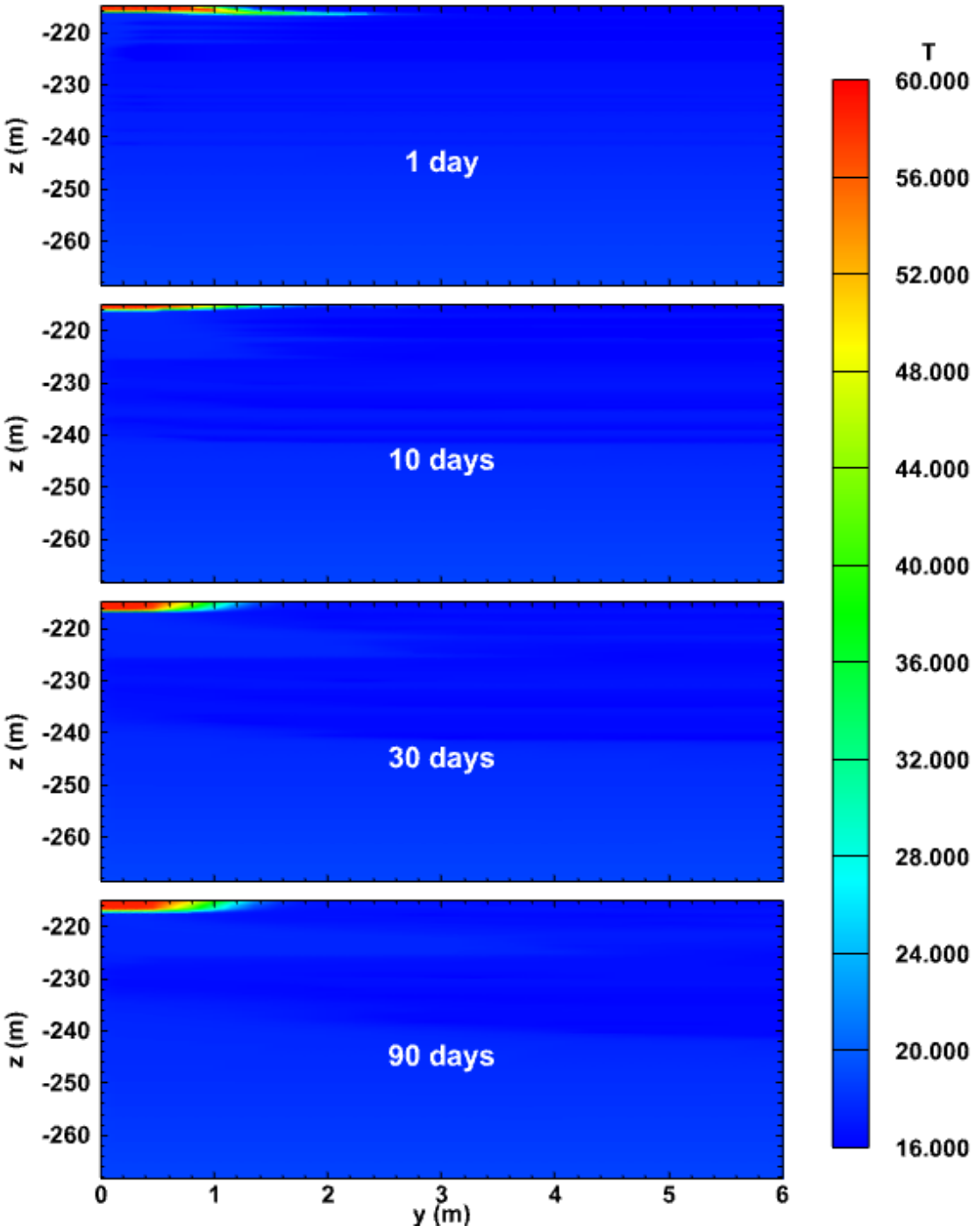

Figure 6.87 Evolution of the spatial distribution of temperature (°C) with a high upper bound of color scale on Plane P3 in the reservoir of Case T1.

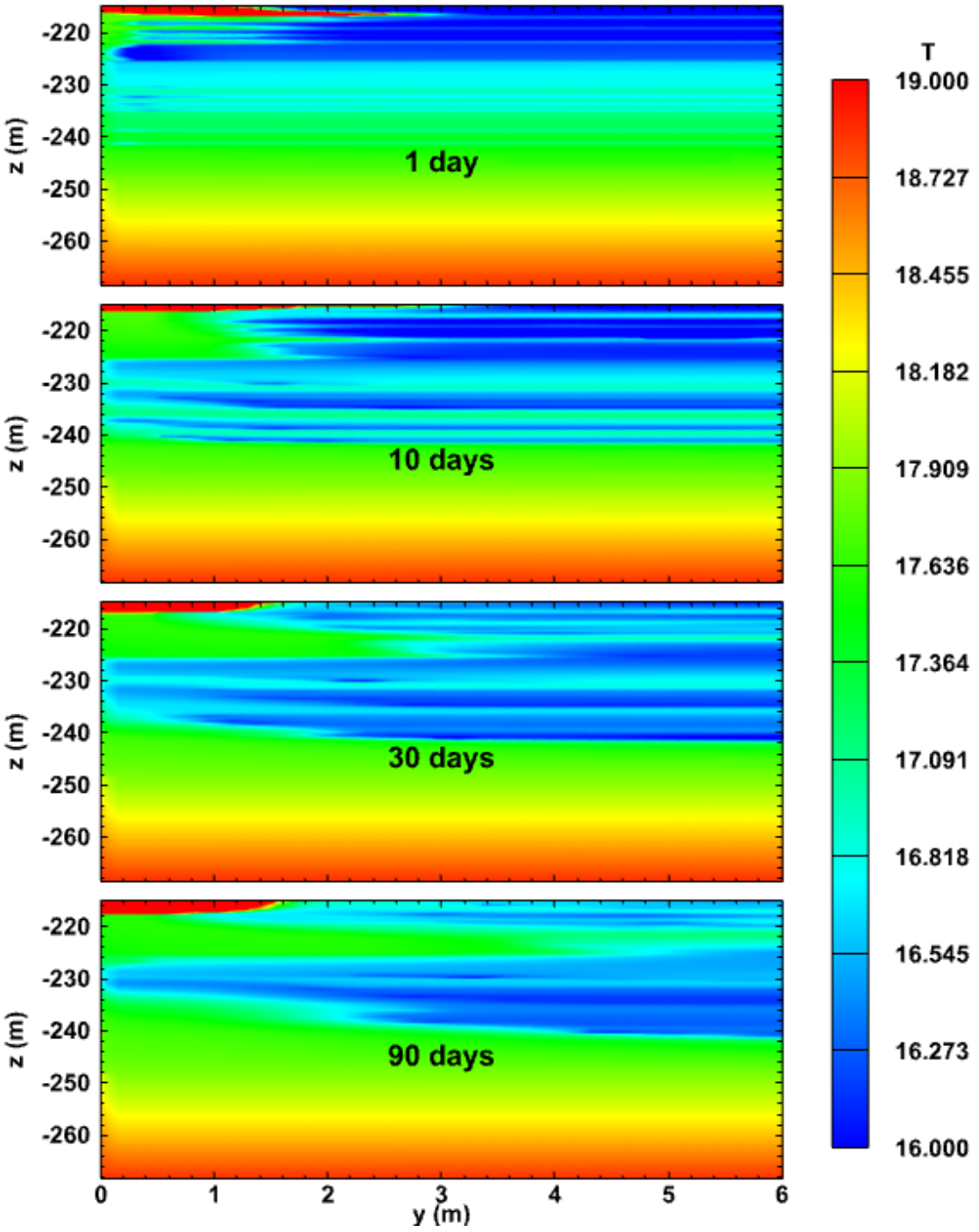

Figure 6.88 Evolution of the spatial distribution of temperature (°C) with a low upper bound of color scale on Plane P3 in the reservoir of Case T1.

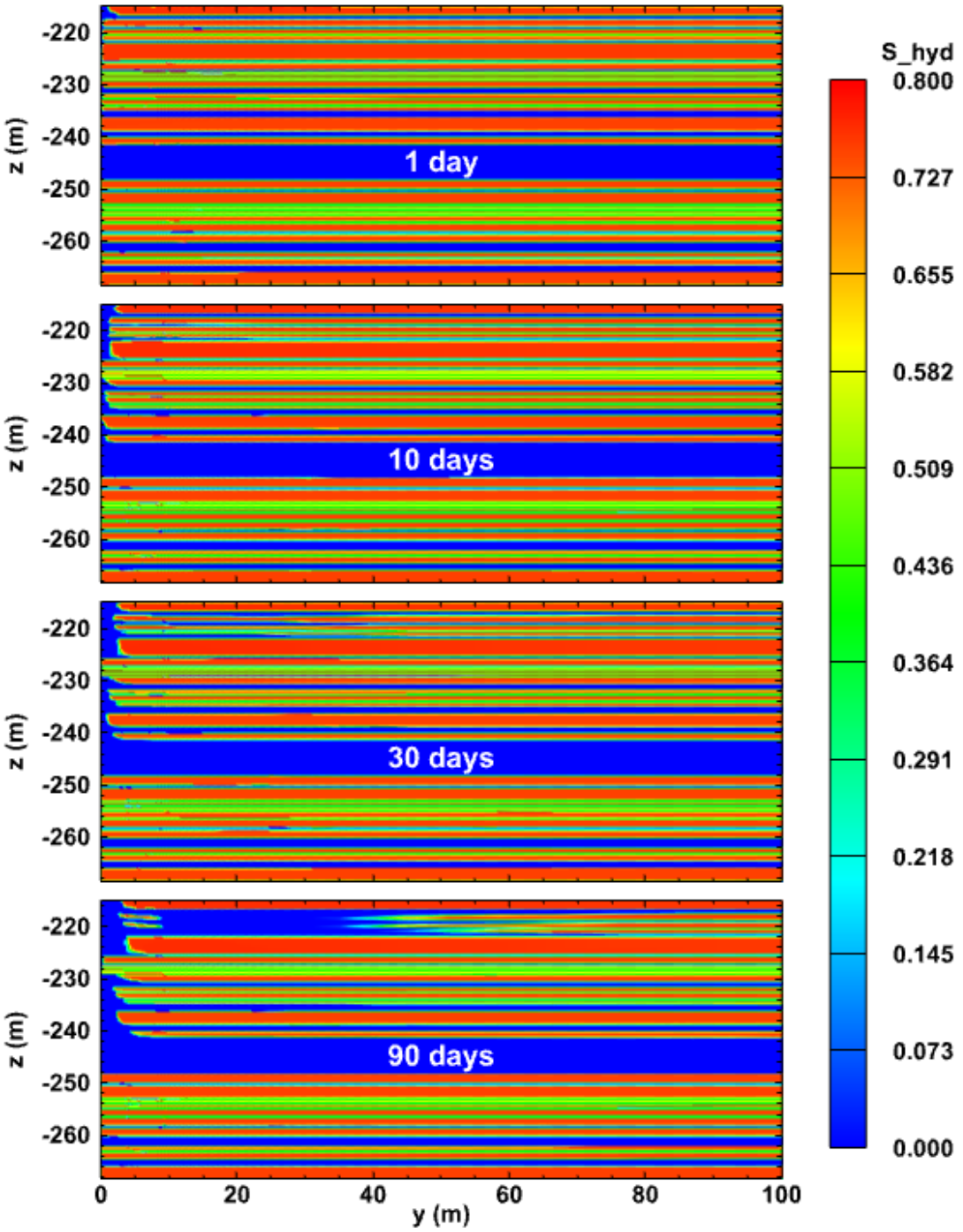

Figure 6.89 Evolution of the spatial distribution of hydrate saturation on Plane P3 in the reservoir of Case T1.

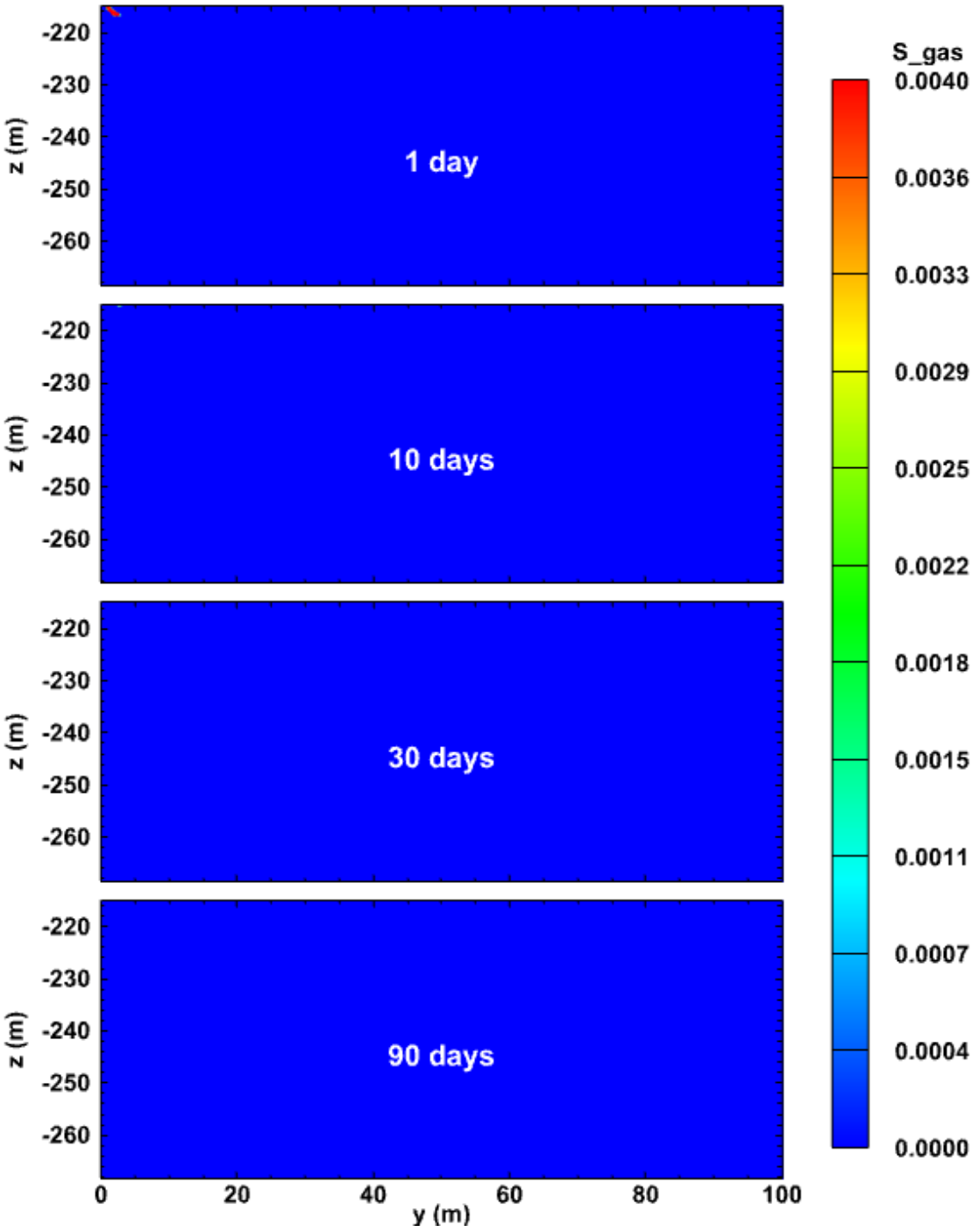

Figure 6.90 Evolution of the spatial distribution of gas saturation on Plane P3 in the reservoir of Case T1.

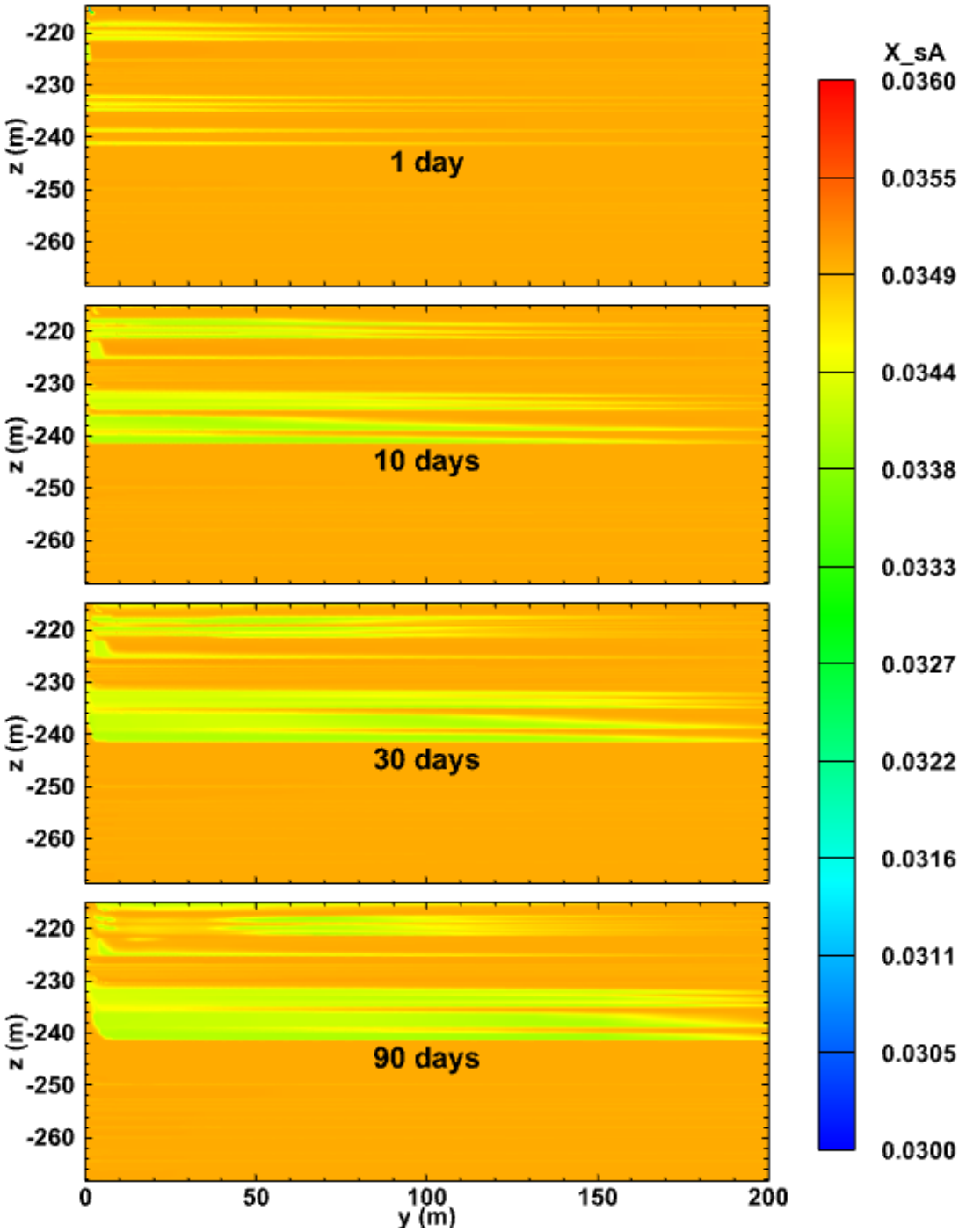

Figure 6.91 Evolution of the spatial distribution of salt mass fraction with a high upper bound of color scale on Plane P3 in the reservoir of Case T1.

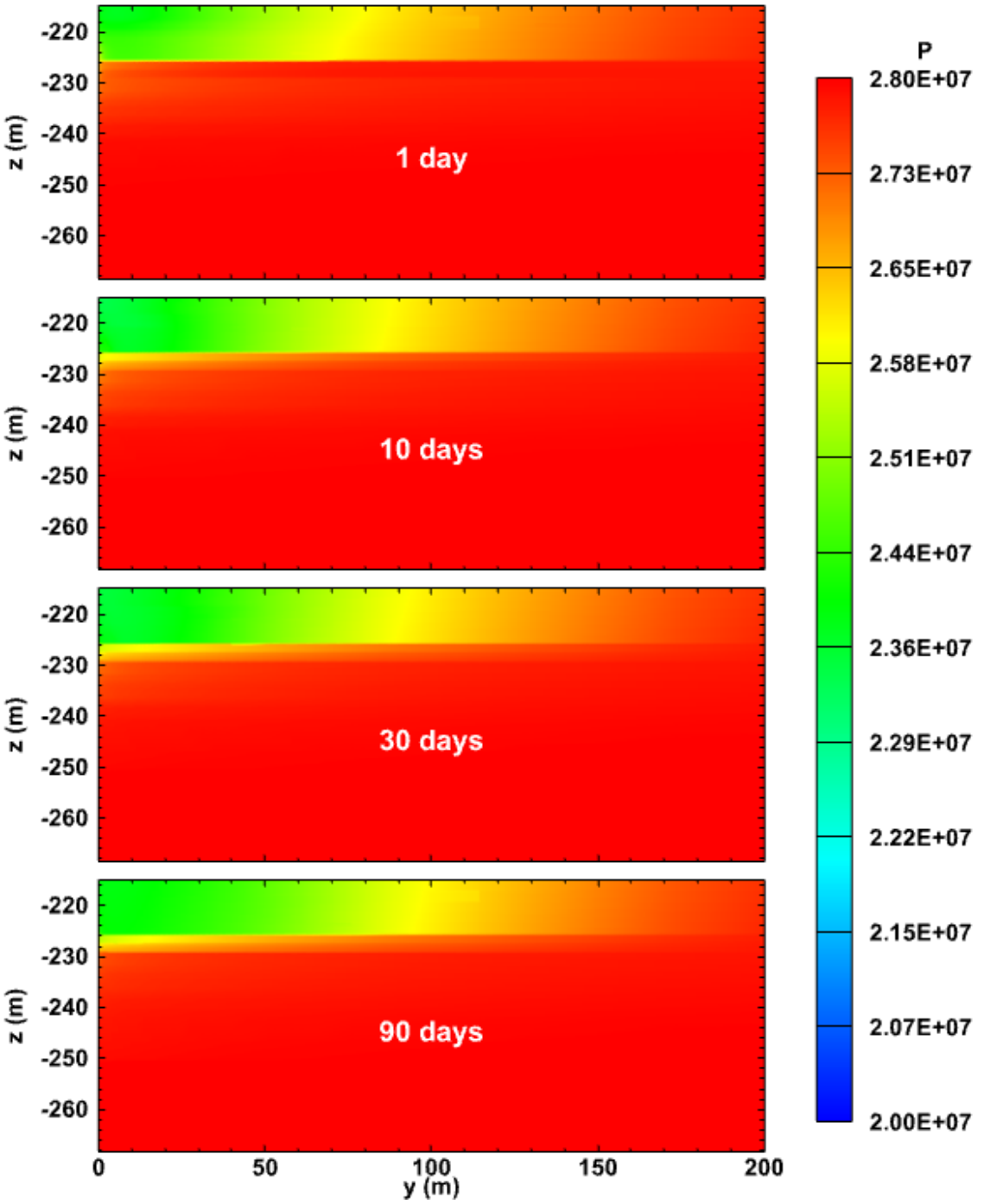

Figure 6.92 Evolution of the spatial distribution of pressure (Pa) on Plane P3 in the reservoir of Case T1G.

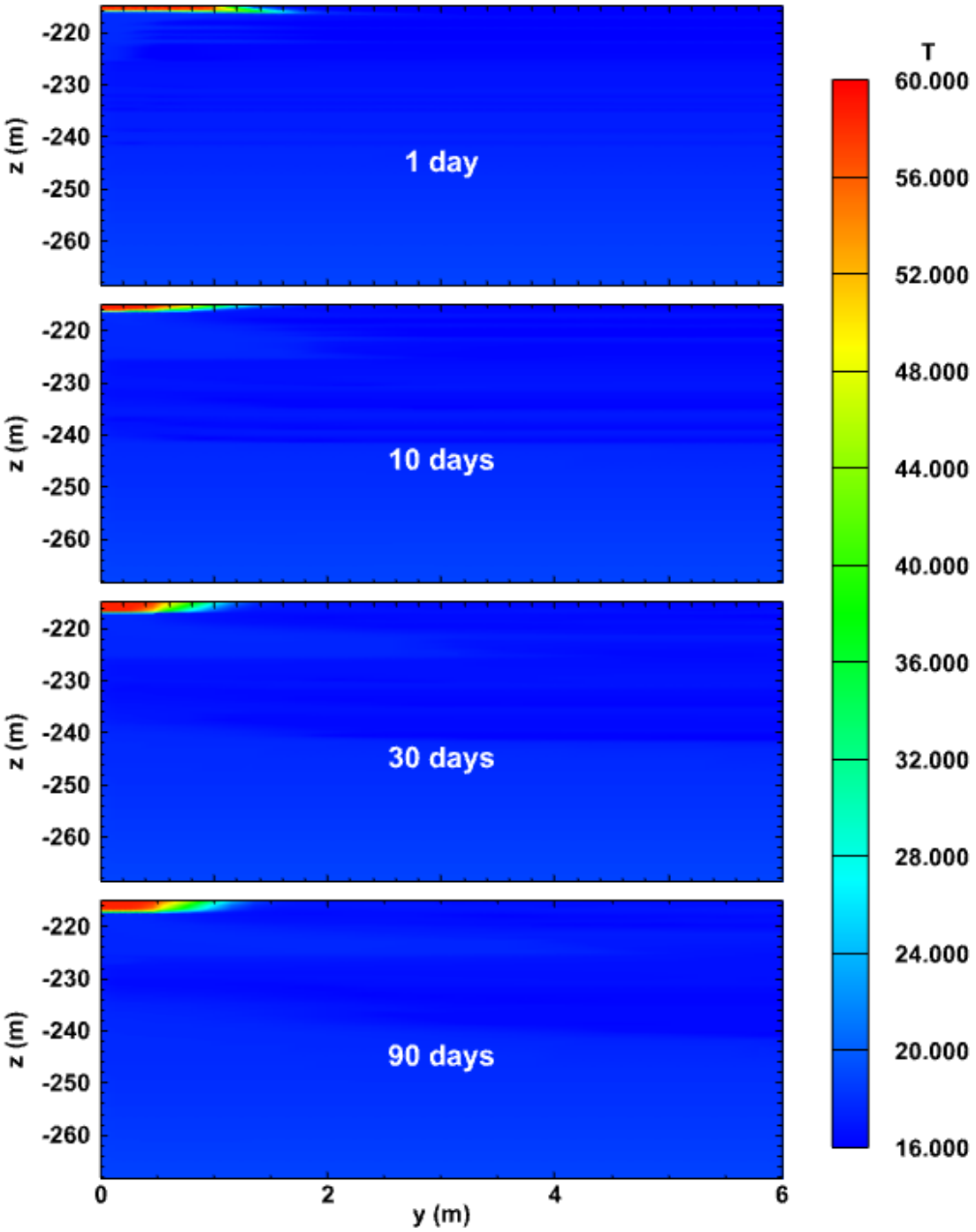

Figure 6.93 Evolution of the spatial distribution of temperature (°C) with a high upper bound of color scale on Plane P3 in the reservoir of Case T1G.

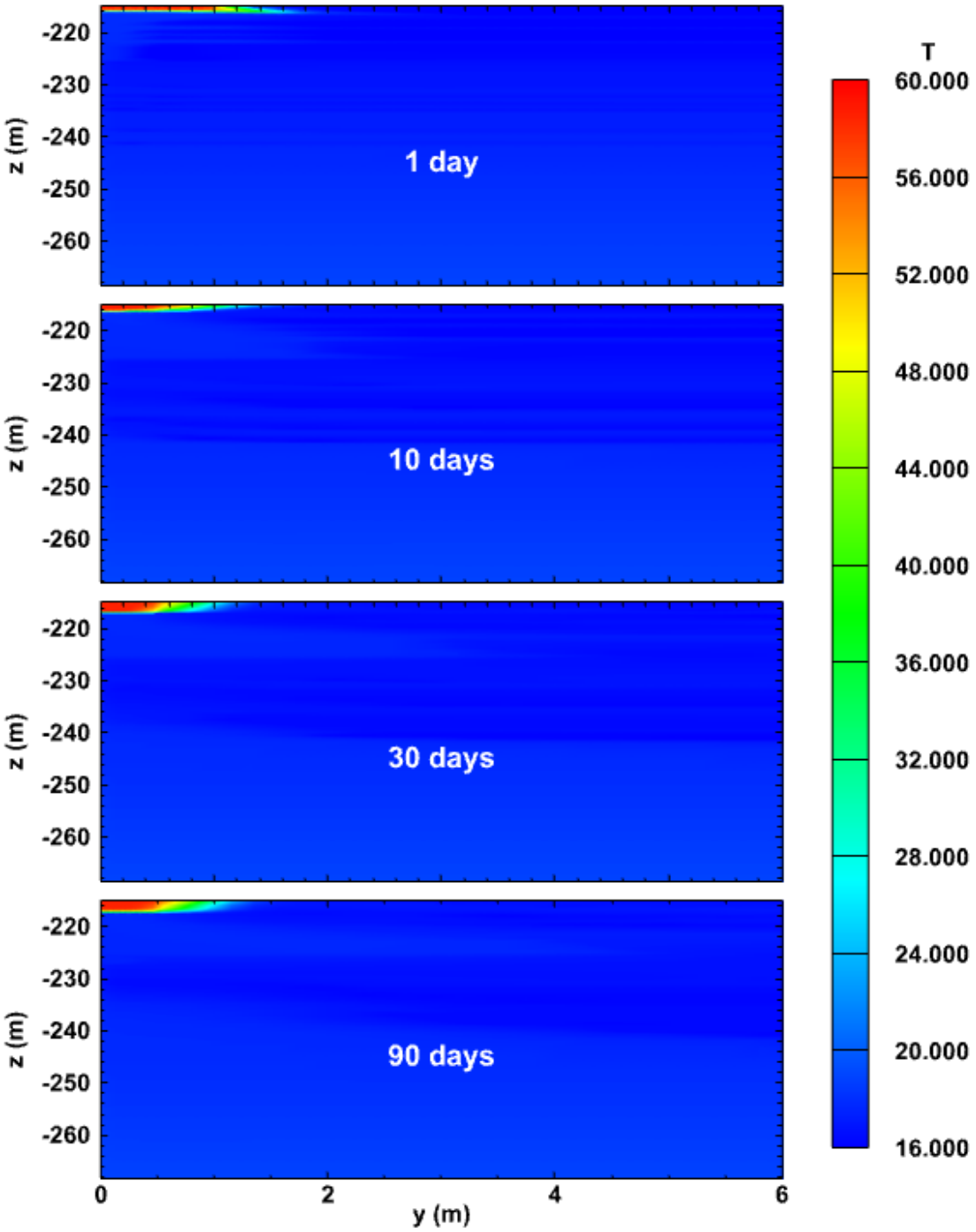

Figure 6.94 Evolution of the spatial distribution of temperature (°C) with a low upper bound of color scale on Plane P3 in the reservoir of Case T1G.

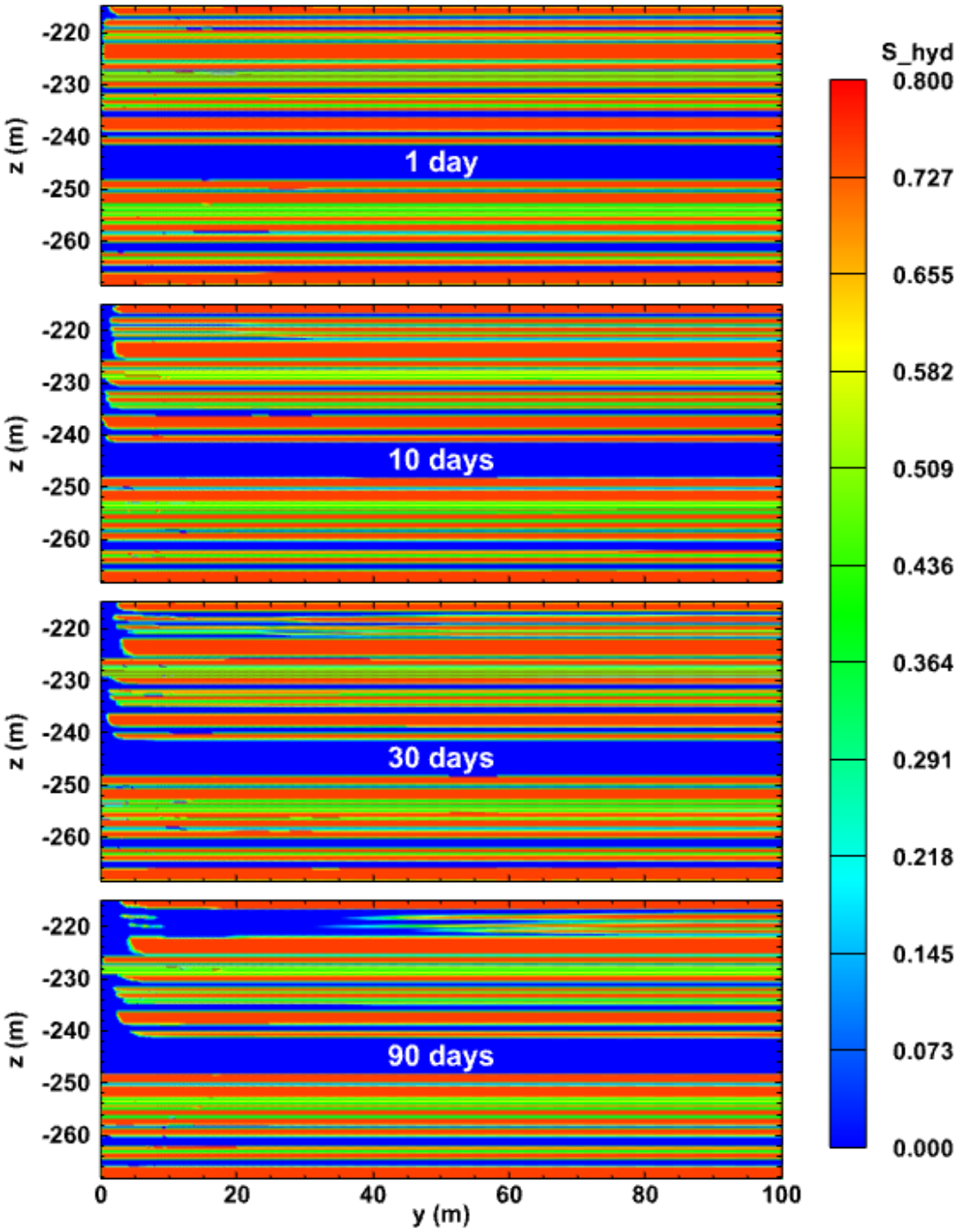

Figure 6.95 Evolution of the spatial distribution of hydrate saturation on Plane P3 in the reservoir of Case T1G.

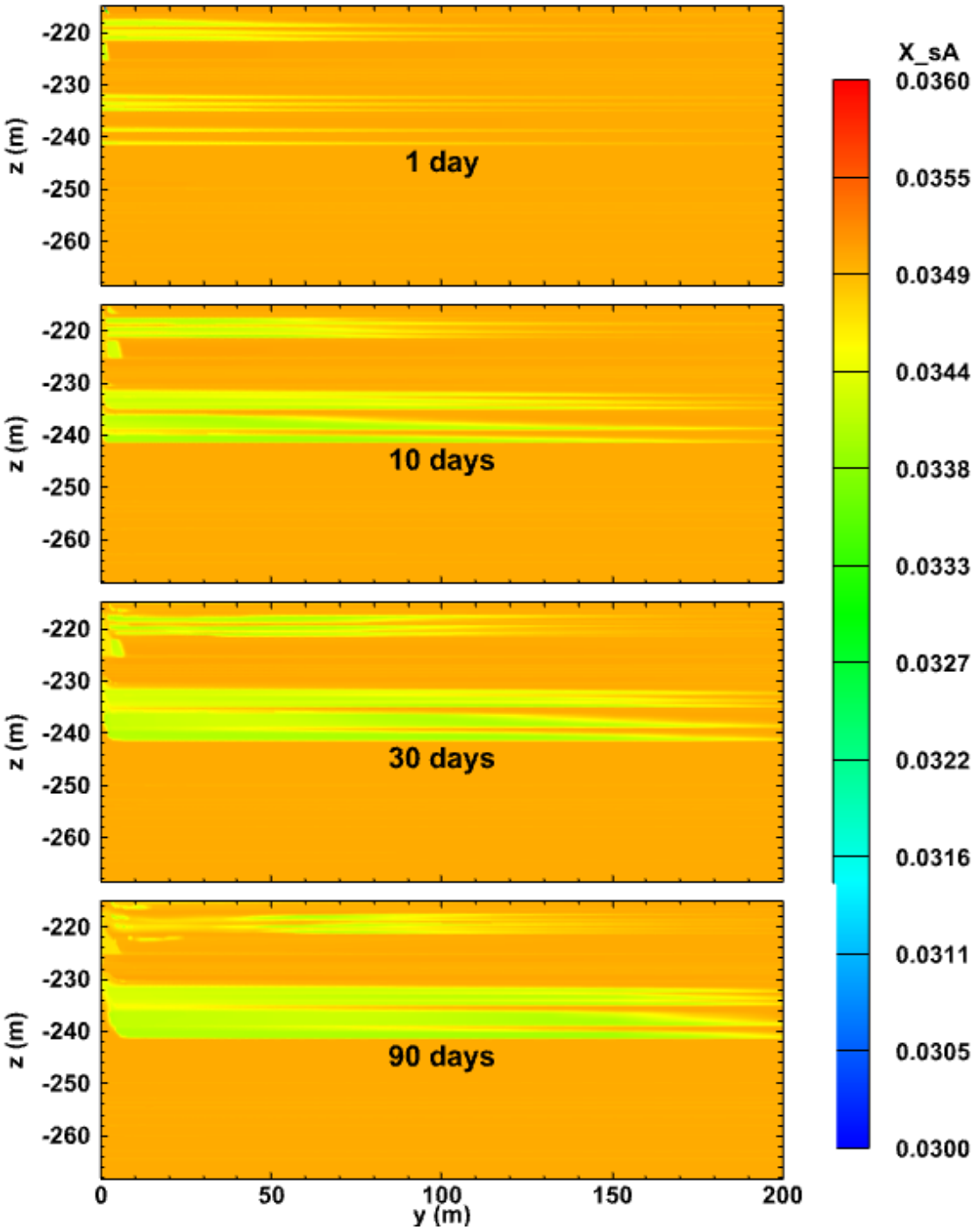

Figure 6.96 Evolution of the spatial distribution of salt mass fraction with a high upper bound of color scale on Plane P3 in the reservoir of Case T1G.

6.3.2.3. Spatial Distributions of u, σ_1', and ε_v in Case T1G

This section analyzes the spatial evolution of u_z, σ_1', and ε_v on the three planes (P1, P2, and P3) defined previously. In the visualization of the spatial evolution of u, the contour plot indicates u_z (vertical displacement), and the arrow denotes the displacement vector on this plane.

6.3.2.3.1. Results on Plane P1

Figures 6.97, **6.98**, and **6.99** present the spatial evolution of u, σ_1', and ε_v, respectively, on Plane P1 in Case T1G. As shown in **Figure 6.97**, the lower section of the OB layer and the upper section of the hydrate deposit subside, while the lower section of the hydrate deposit experiences an uplift. This is caused by the effects of the producing well, which lowers the fluid pressure in the pores and transfers stresses to the skeleton of the hydrate deposit: the constant weight of the OB causes subsidence, and the higher pressure in the UB (unaffected by production, the pressure disturbance of which barely reaches the UB) displaces that boundary upward. The combined result is the continuous compaction ("squeeze") of the hydrate deposit that advances with time and is at a maximum at any time in the vicinity of the production well. Furthermore, the reservoir in the *y* plane moves toward the production wellbore.

In **Figure 6.98**, σ_1' is at its maximum value at any time at the upper parts of the production well (*i.e.*, in the H1 layer) because this where the constant bottomhole pressure P_{bh} is applied, thus being the location of the lowest pressure in the hydrate deposit. Note that the maximum attained value of σ_1' is observed only at the beginning of production

when the bottomhole pressure (and the maximum pressure drop ΔP) is first applied at the well, and then it continuously decreases because of the influence of the injected warm water and the decline in the ΔP. The warm water injection counters only partially the effective stresses, and this clearly identifiable in **Figure 6.98** as a thin vertical zone at the location of the injection well. The elevated stresses squeeze the formation and lead to the continuously expanding volumetric strain distribution in **Figure 6.99**, the footprint of which corresponds to a subdomain of decreasing porosity and permeability. The affected area includes the top few layers of the hydrate deposit and coincides roughly with the footprint of the hydrate dissociation in the HBLs. Note that, as expected, the stress and strain changes are confined to the characteristic limited upper zone of the hydrate deposit that has been clearly evident in all the *P*-distributions discussed up to now.

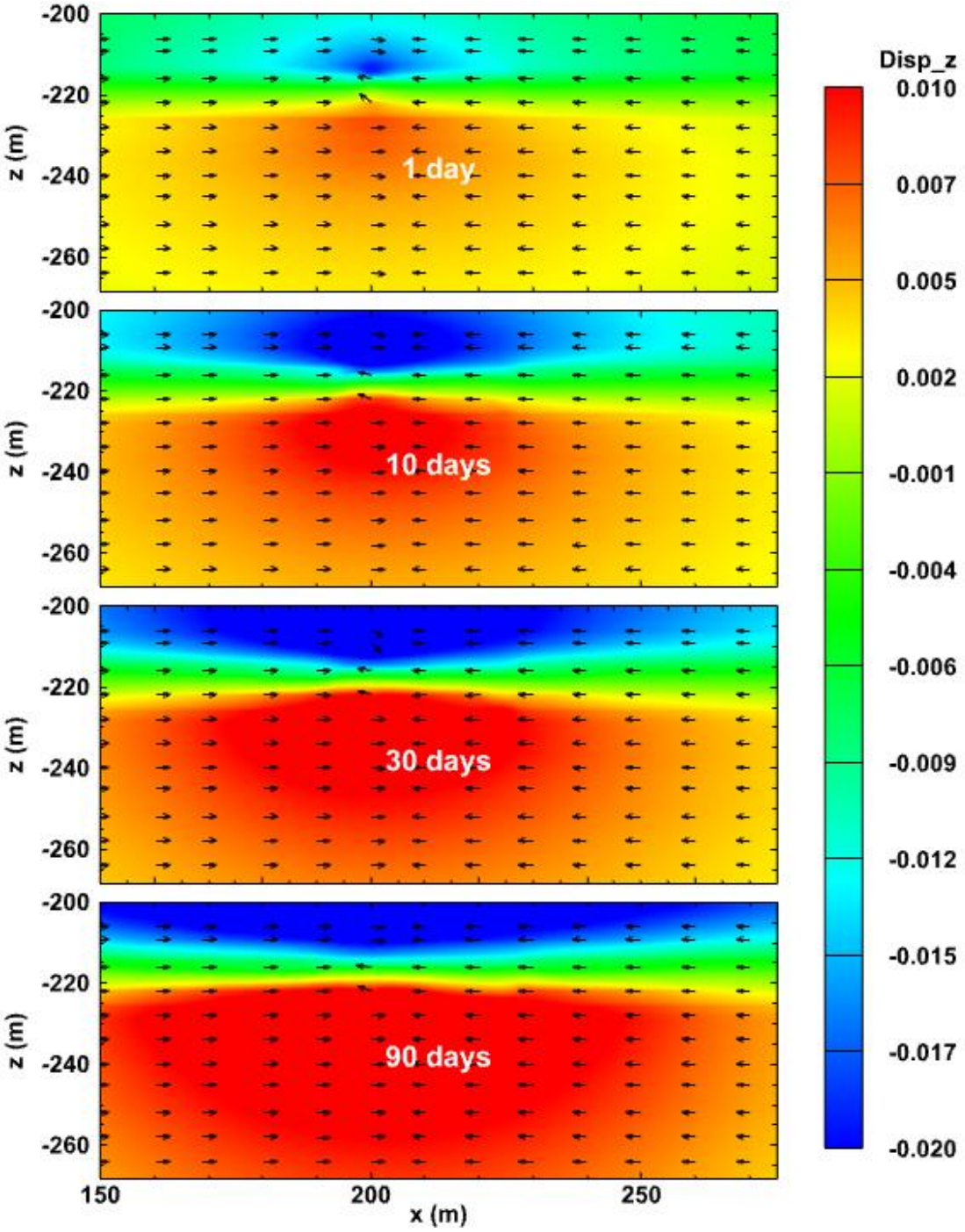

Figure 6.97 Evolution of the spatial distribution of displacements (m) on Plane P1 in the reservoir of Case T1G.

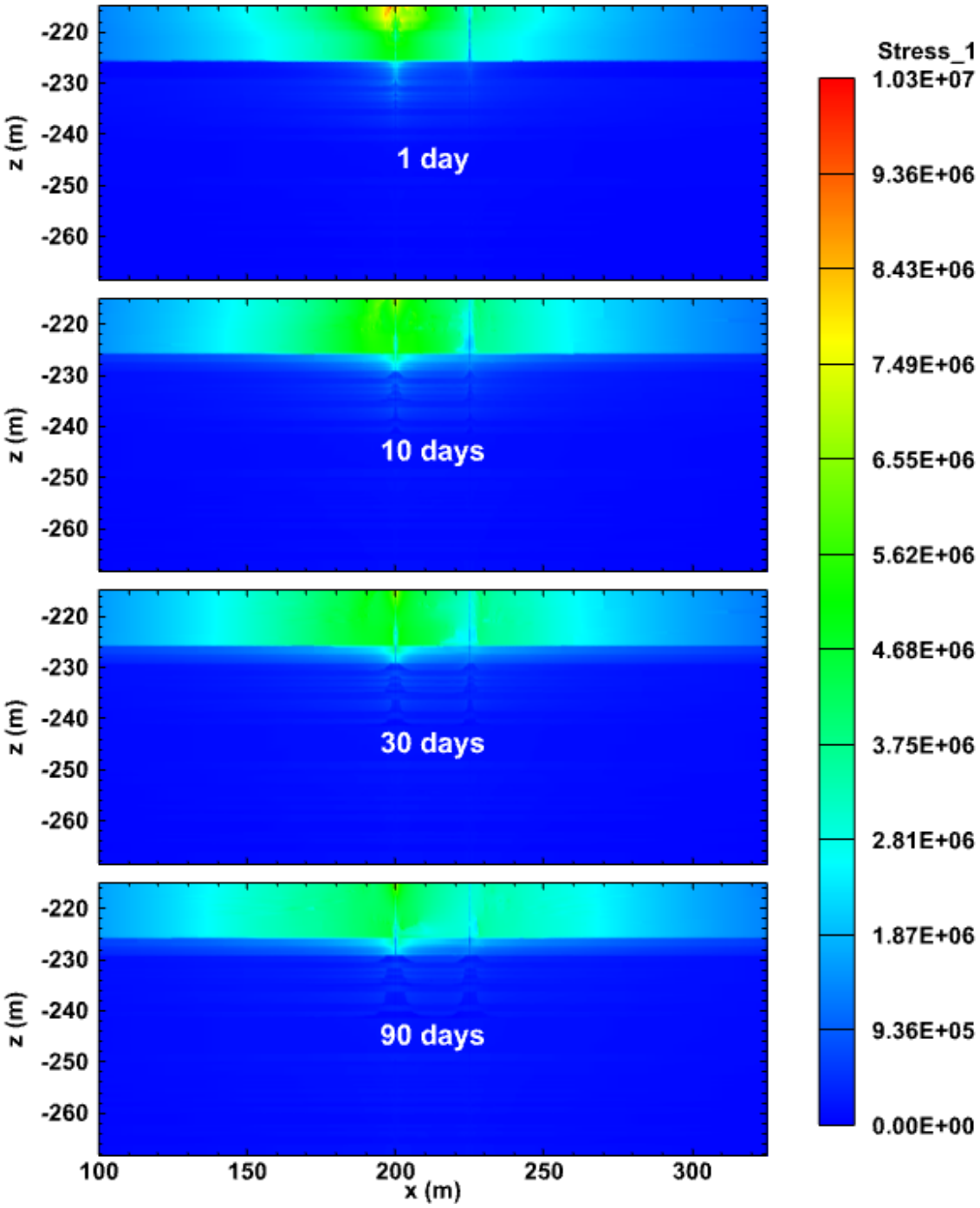

Figure 6.98 Evolution of the spatial distribution of maximum principal effective stress (Pa) on Plane P1 in the reservoir of Case T1G.

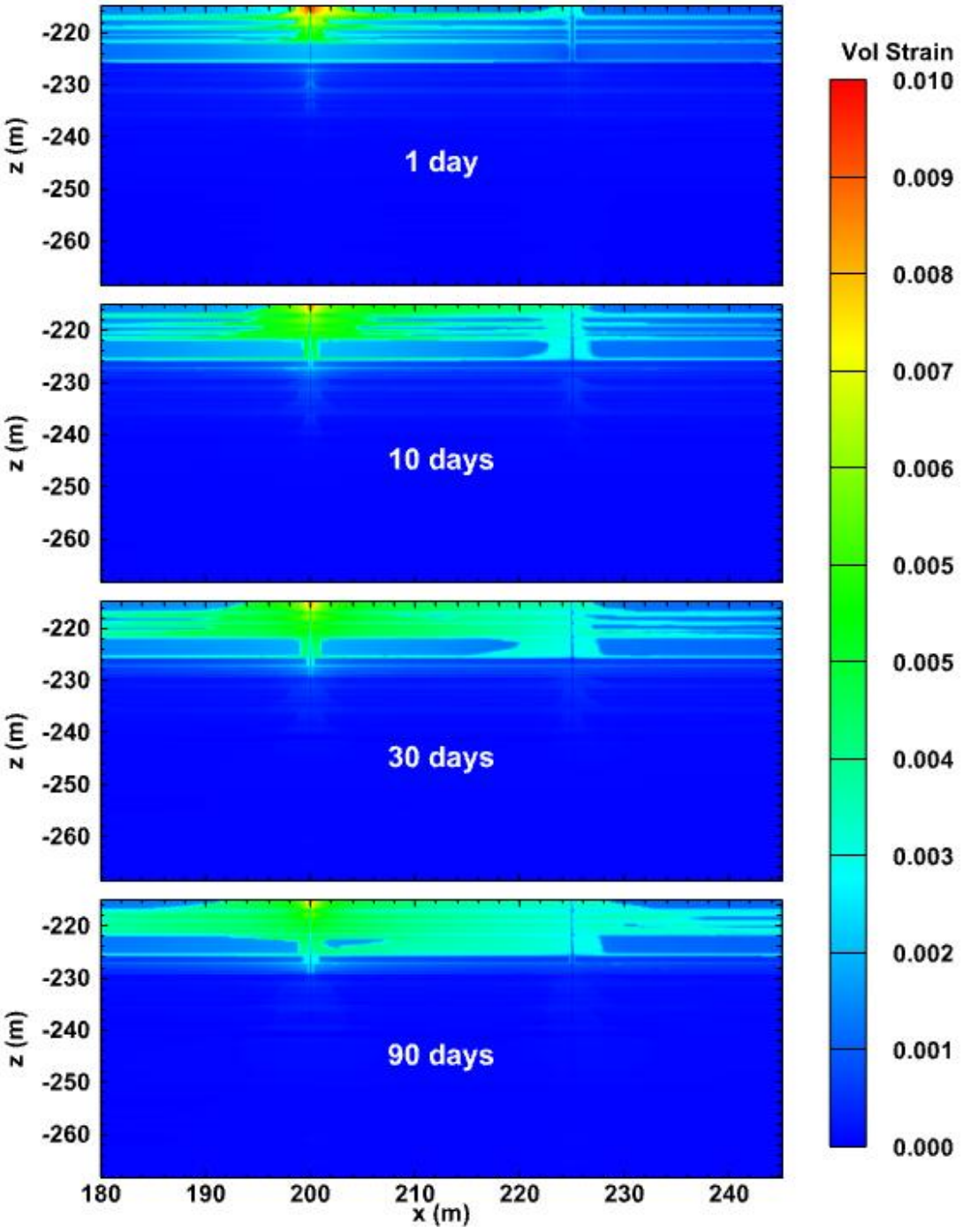

Figure 6.99 Evolution of the spatial distribution of volumetric strain on Plane P1 in the reservoir of Case T1G.

6.3.2.3.2. Results on Plane P2

Figures 6.100, **6.101**, and **6.102** present the spatial evolution of u, σ_1', and ε_v, respectively, on the P2 plane in Case T1G. **Figure 6.100** shows that (a) the subsidence and uplift (and the resulting squeeze of the hydrate deposit) progress continuously with time and (b) that they extend to significant distances from the wellbore along the *y*-direction. Of interest is the observation that the maximum displacements are observed at t = 30 days and appear slightly reduced at t = 90 days, possibly because of the enhanced late-time effect of the warm water injection (when the ΔP and the related production rate at the constant P_{bh} well are reduced). From **Figure 6.101**, the warm water injection appears (a) to continuously reduce σ_1' from its maximum level at t = 1 day (when ΔP and the production rate are at their maximum) in the vicinity of the well in the upper part of the hydrate deposit, but also (b) to expand the extent of its impact over an increasing volume of the hydrate deposit. This is evident in the distribution of the volumetric strain shown in **Figure 6.102** which, although exhibiting a continuous decline of its maximum value for the reasons already discussed, continuously increases the size of the volume it affects (and causes a corresponding reduction in its ϕ and k), reaching (and extending past) y = 50 m after 90 days of production.

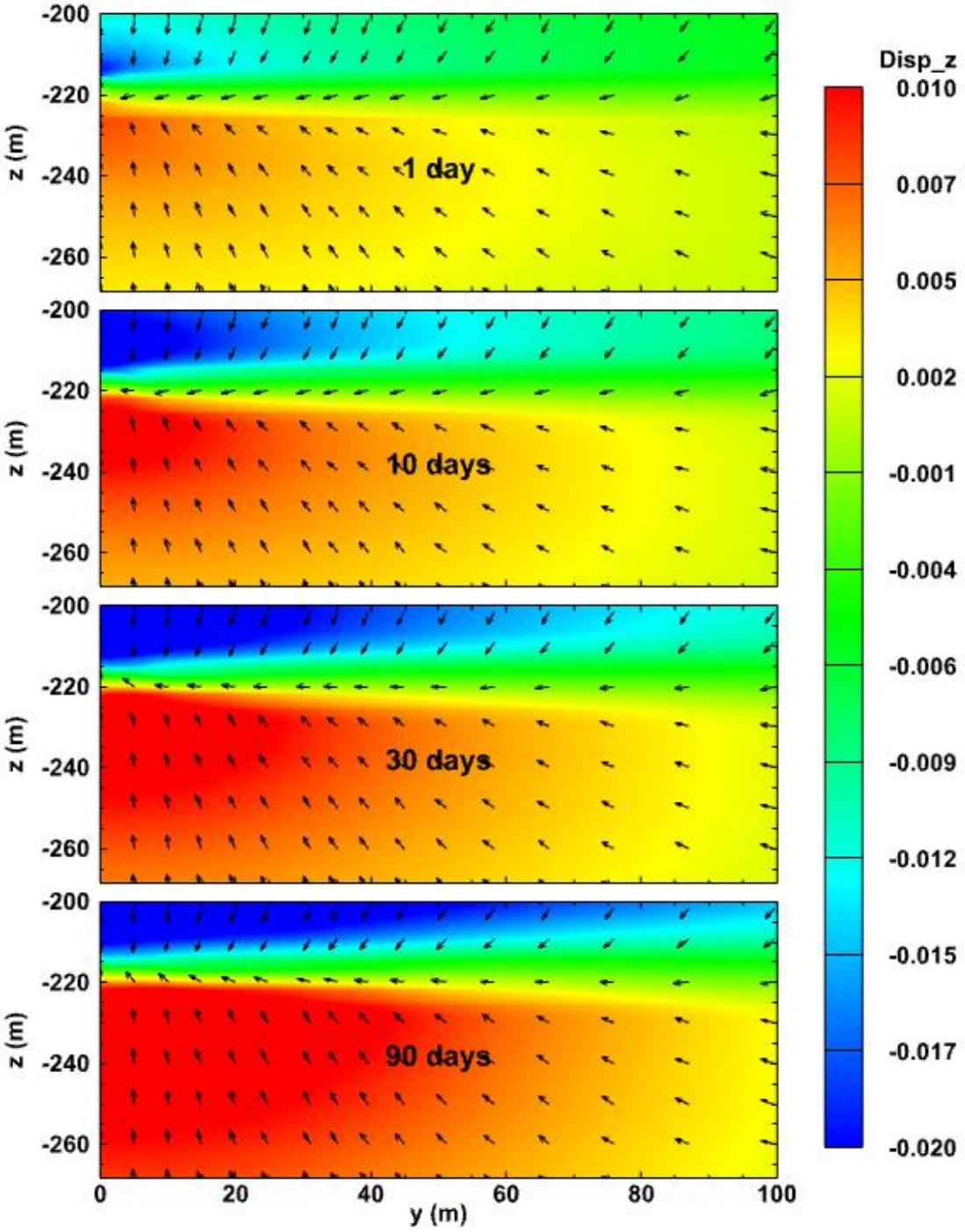

Figure 6.100 Evolution of the spatial distribution of displacements (m) on Plane P2 in the reservoir of Case T1G.

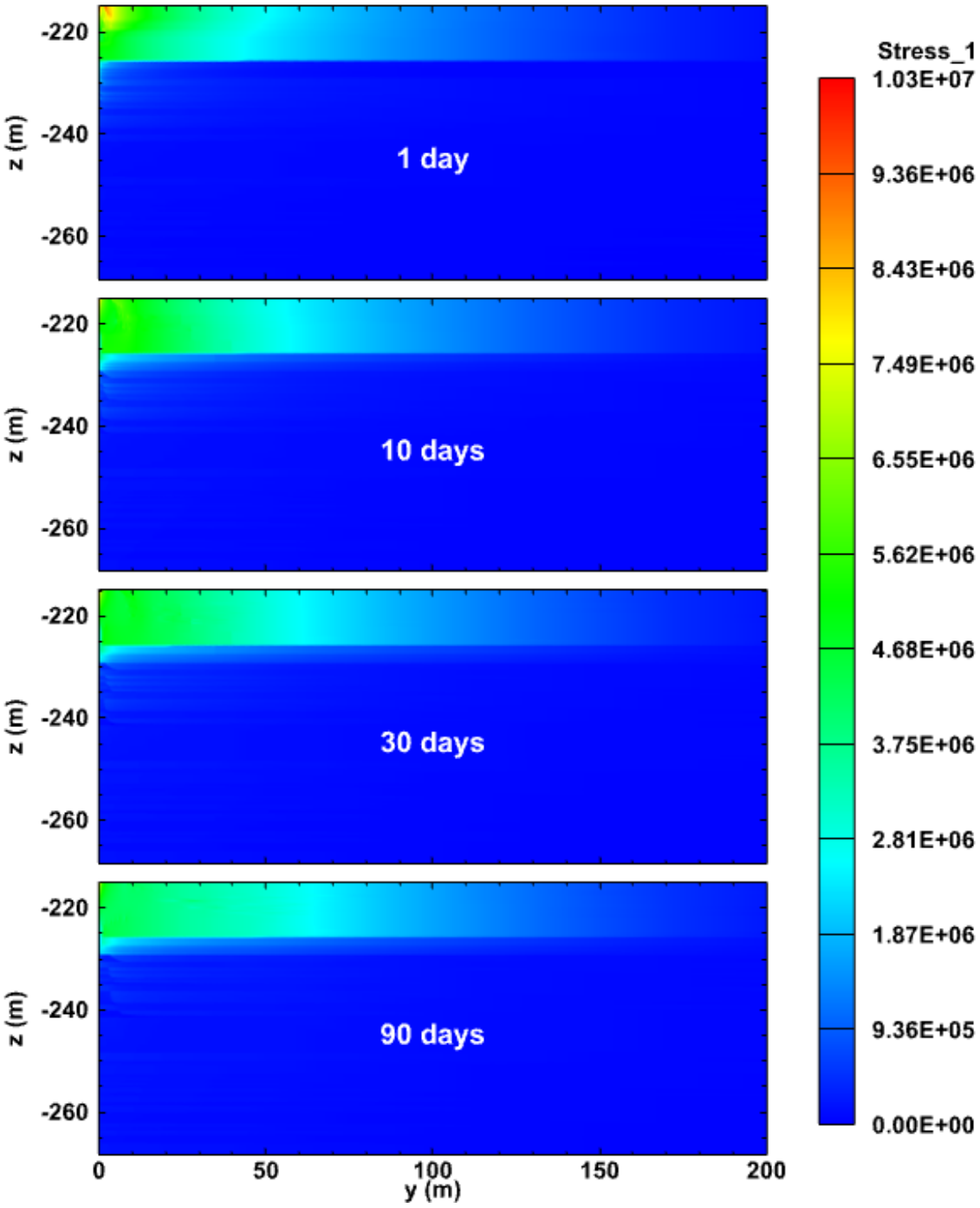

Figure 6.101 Evolution of the spatial distribution of maximum principal effective stress (Pa) on Plane P2 in the reservoir of Case T1G.

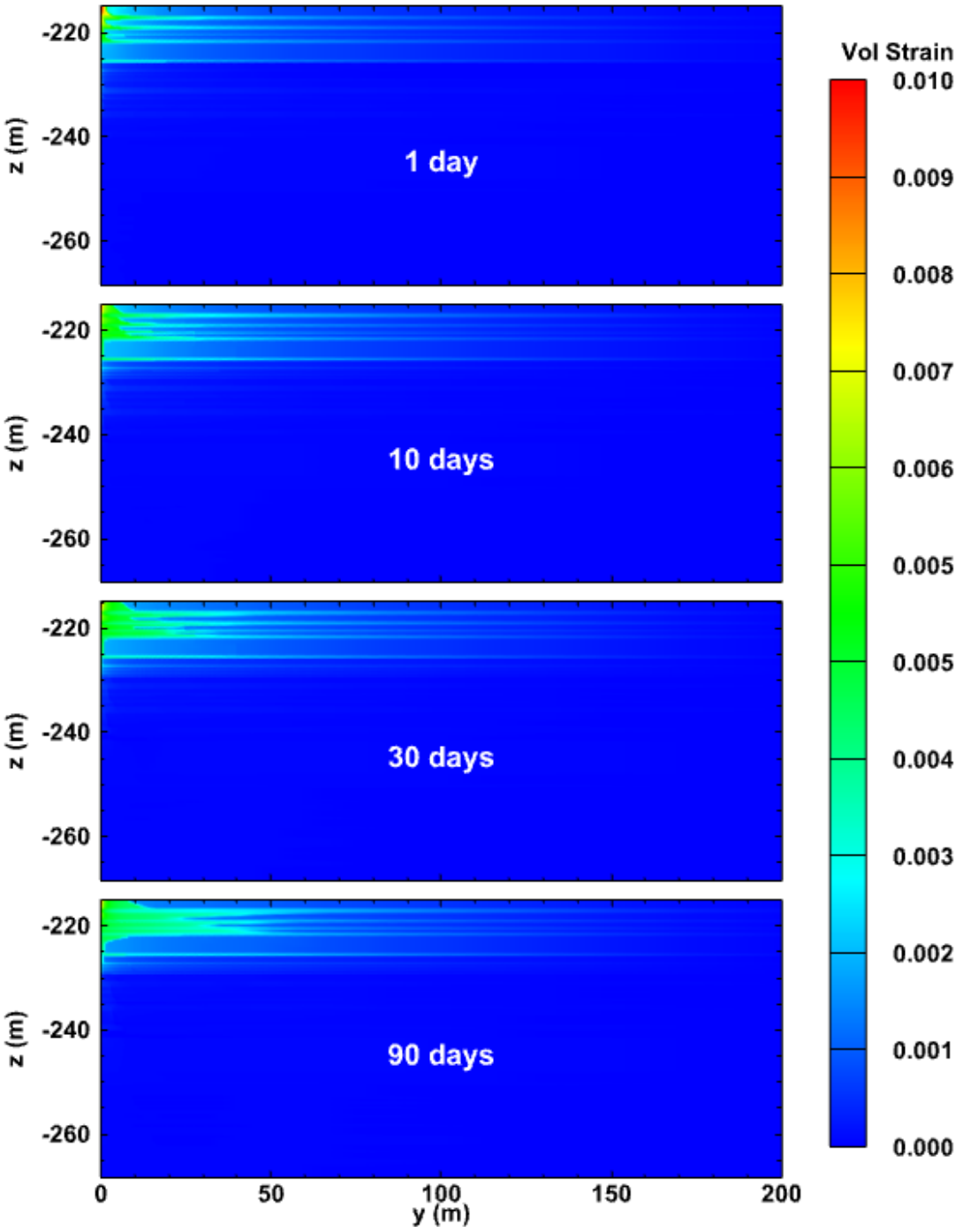

Figure 6.102 Evolution of the spatial distribution of volumetric strain on Plane P2 in the reservoir of Case T1G.

6.3.2.3.3. Results on Plane P3

Figures 6.103, **6.104**, and **6.105** present the spatial evolution of u, σ_1', and ε_v, respectively, on Plane P3 in Case T1G. As shown in **Figure 6.103**, (a) the subsidence and uplift (and the resulting squeeze of the hydrate deposit) progress continuously with time because of the continuing depressurization even in the face of continuous (low-rate) warm water injection, (b) they extend to significant distances from the wellbore along the *y*-direction, but (c) their magnitude (and the resulting squeeze of the deposit) are lower than those observed on Planes P1 and P2 because of the alleviating effect of injection. Because of the higher pressures and their continuous decline in the vicinity of the injection well on this plane, unlike the observations on Planes P1 and P2, the principal effective stress continues to increase in magnitude and expand its footprint over time (**Figure 6.104**).

This is reflected in the distribution of the volumetric strain shown in **Figure 6.105** which exhibits a continuous increase of both its maximum value (for the reasons already discussed) and of the size of the volume it affects, reaching (and comfortably extending past) y = 50 m after 90 days of production. The subdomain affected by these changes in the volumetric strain is characterized by a corresponding reduction in its ϕ and k.

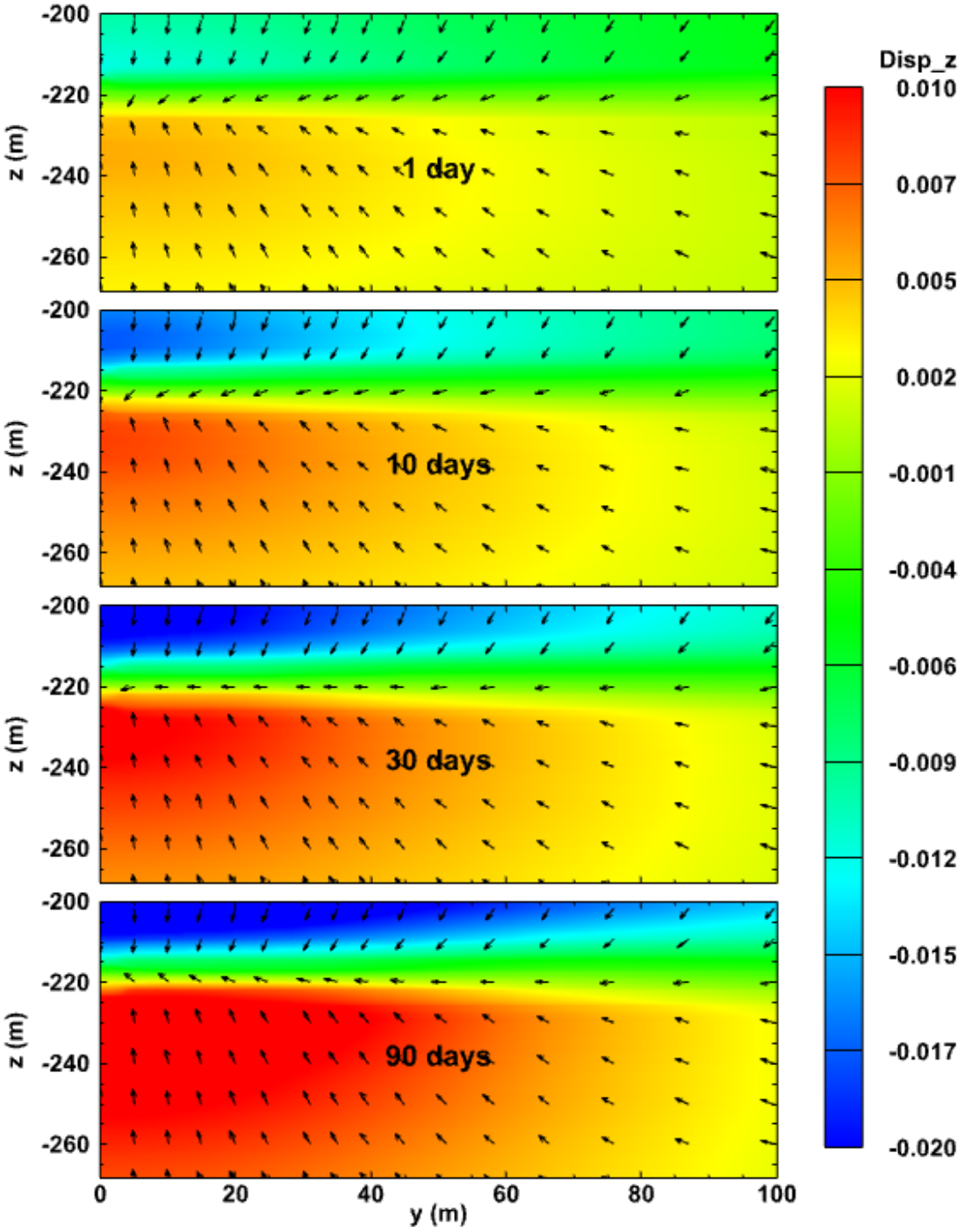

Figure 6.103 Evolution of the spatial distribution of displacements (m) on Plane P3 in the reservoir of Case T1G.

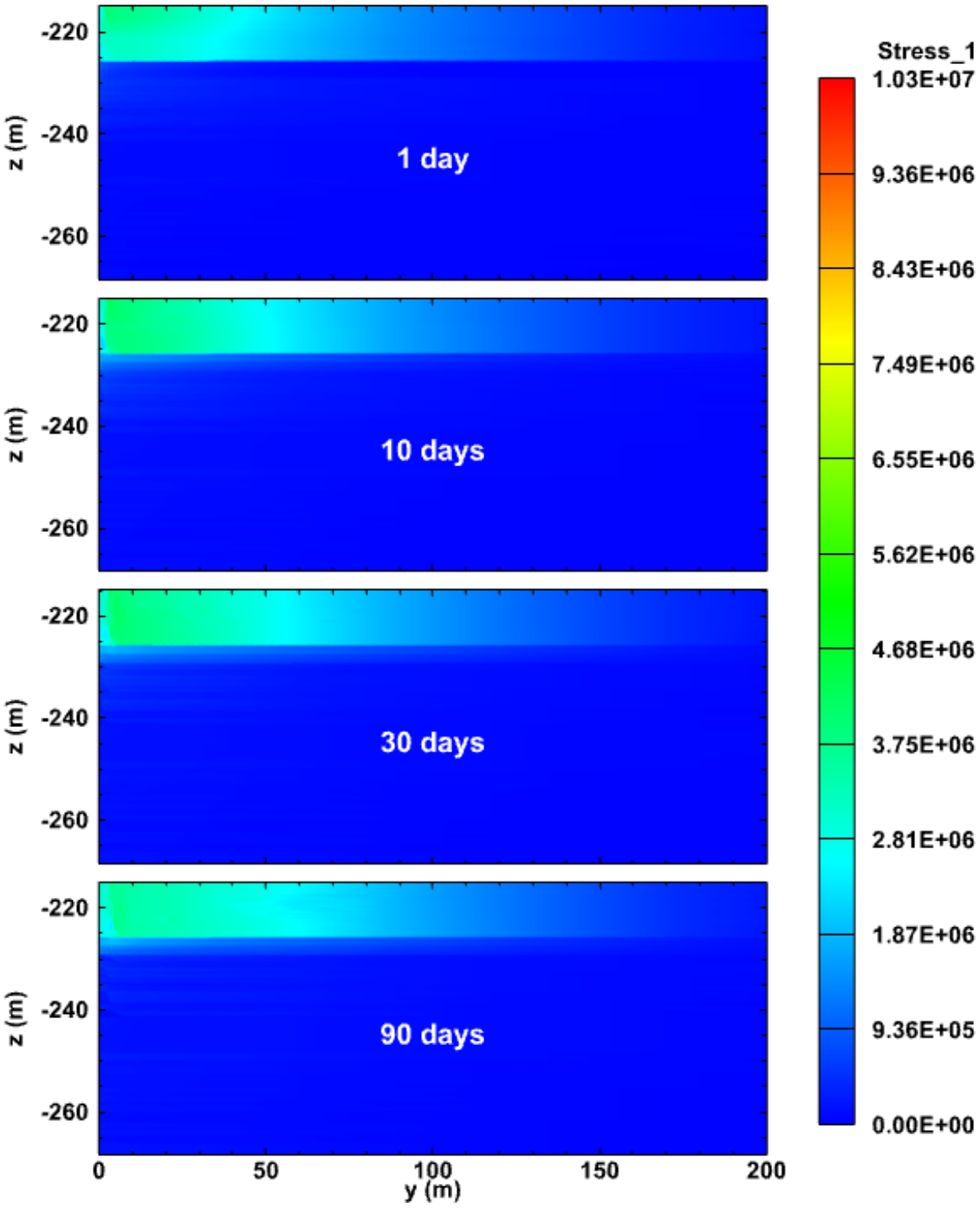

Figure 6.104 Evolution of the spatial distribution of maximum principal effective stress (Pa) on Plane P3 in the reservoir of Case T1G.

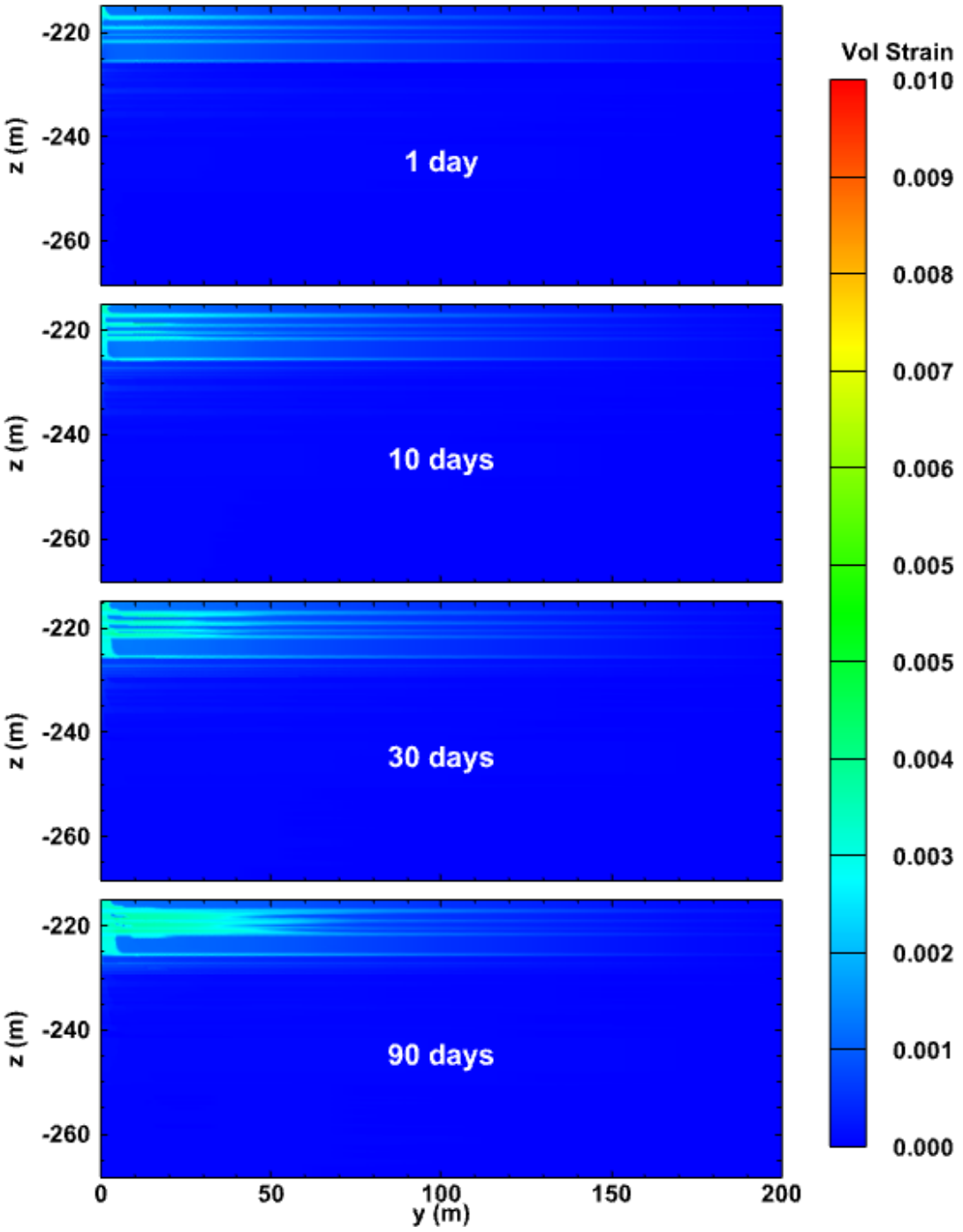

Figure 6.105 Evolution of the spatial distribution of volumetric strain on Plane P3 in the reservoir of Case T1G.

7. SUMMARY, CONCLUSIONS, AND RECOMMENDATIONS

7.1. Summary

Chapter 2 provides a detailed discussion on the Reservoir GeoMechanics Simulator (RGMS or RGM simulator) developed in this study for the investigation and analysis of the geomechanical behavior of subsurface systems to external stimuli, including the governing equations, the numerical method, the parallelization strategy, a flow chart, and validations of the numerical method and of the parallelization process. The governing equations describe the underlying physics and their mathematical representation in the modeling of the geomechanics problem. The finite element method (FEM) is the numerical method used in the solution of the geomechanical problem in RGMS, and is chosen because of its power and flexibility in the spatial discretization of complex multi-dimensional domains. To improve performance, a parallelization strategy designed for the FEM is introduced into RGMS, based on the Message-Passing-Interface (MPI) approach and involving a domain decomposition method. The domain is partitioned using the overlapped method with the box-type stencil illustrated in **Figure 2.1** to account for the influence of displacement at neighboring nodes, served by different processors. All these processes are summarized in the flow chart shown in **Figure 2.3**.

Two 2D problems (in Cartesian and radial-cylindrical coordinates) and a 3D Cartesian coordinate problem are created to validate the FEM and the parallelization method in RGMS. The total displacements and the maximum principal effective stresses

obtained from the RGMS solution of these three problems are compared to those from the commercial software Ansys Mechanical, and are shown to practically coincide.

Chapter 3 provides all the details on the development of the pTOUGH+ HYDRATE V1.5 (pT+H V1.5) simulator that is based on the MPI-based parallelization of the pre-existing serial TOUGH+HYDRATE V1.5 (Moridis 2014) code. pT+H V1.5 is used for the study of the system behavior in hydrate-bearing geologic media, and the discussion (a) covers the governing equations, the porosity-permeability relationships, a simplified geomechanical model, the underlying numerical method, and the MPI-based parallelization method, and (b) includes a flow chart and validation of the parallelization through comparisons of the serial and parallel versions of the code. The numerical method used for the space discretization in pT+H V1.5 is the integral finite difference method (IFDM), which necessitates the star-type stencil of the overlapped method in the domain partitioning process presented in **Figure 2.1** for the parallel simulations of the code. The Jacobian-based Newton-Raphson method that is used for the solution of the non-linear problems of mass and heat balances in pT+H requires MPI communications for the necessary convergence checks. **Figure 3.2** presents the flow chart of pT+H V1.5. The parallelization of pT+H V1.5 is validated by comparing its results to those from the serial T+H V1.5 code in a study that involves (a) fluid production from a large-scale 2D cylindrical system describing a real-life oceanic hydrate deposit, (b) different production scenarios and porosity-permeability relationships, and (c) a simplified geomechanical model based on hydrate-dependent pore compressibility.

Chapter 4 provides all the details in the coupled pT+H V1.5 and RGM simulator for the study of the system behavior in hydrate-bearing geologic media in response to external stimuli (such as fluid and/or heat withdrawal and/or injection), fully accounting for the relationship and interdependence of flow, thermal, thermodynamic, chemical and geomechanical processes. The discussion (a) covers the coupling method and the parallelization process, and (b) includes a flow chart and validations of the code coupling and of the parallelization. As shown in **Figure 4.1**, the coupling method is based on the fixed-stress split iterative scheme that provides significant flexibility in the coupling of the two constituent simulators, solves their respective equations separately, and ensures accuracy of the solutions through an iterative process.

A new domain decomposition method is introduced to account for the different numerical methods involved in the RGMS and the pT+H V1.5 codes. The flow chart of the coupled pT+H V1.5 and RGM simulator is shown in **Figure 4.2**. The coupling method is validated by comparing the numerical results to the analytical solutions of the Terzaghi and the McNamee-Gibson problems. The parallelization validation of the coupled simulator is achieved by comparing the results obtained for different numbers of processors in the solution of the problems used for the pT+H V1.5 parallelization validation with the full geomechanical model.

Chapter 5 presents the results from the parallel performance (a) of the individual RGMS code, (b) of the individual pT+H V 1.5 simulator, and (c) of the coupled pT+H V1.5 and RGM codes. The RGMS test problems for the parallelization validation involve domains with different discretizations. They include 2D Cartesian, 2D cylindrical, and 3D

Cartesian coordinate problems (Cases G1, G2, and G3, respectively) discretized into 4×10^6, 4×10^6, and 3.365×10^6 elements, respectively.

The problems used for testing the pT+H V1.5 code involve a simplified geomechanical model based on S_H-dependent pore compressibility, and include a 2D cylindrical problem (Case U1) involving 2.4×10^5 elements and a 3D Cartesian problem (Case T1) involving 3.6×10^6 elements. Both problems describe actual (real-life) oceanic hydrate deposits. The test problems for the coupled pT+H V1.5 and RGM simulator are Cases U1G and T1G, in which the addition of the "G" to the names of Cases U1 and T1 denotes the application of the full geomechanical model. All the cases mentioned above are tested on the Ada Linux cluster using up to 512 processors and on a Mac Pro desktop computer using up to 12 processors. The two options available in the METIS partitioning software that were tested in the Ada Linux cluster runs are based on objectives that seek to (a) minimize the number of edge-cuts or (b) minimize the communication volume. Only the former option is used in the Mac Pro simulations.

On the Ada Linux cluster, the maximum simulation cycling speedups in Cases G1, G2, and G3 are 218.89, 188.13, and 284.70, respectively; the maximum total speedups in Cases U1 and T1 are 174.25 and 341.67, respectively; and the maximum total speedups in Cases U1G and T1G are 134.97 and 331.80, respectively. Note that all the maximum speedups were achieved when running 512 processors.

On the Mac Pro, the maximum simulation cycling speedups in Cases G1, G2, and G3 are 6.19 (with 12 processors), 6.09 (with 12 processors), and 7.19 (with 12 processors), respectively; the maximum total speedups in Cases U1 and T1 are 4.44 (with 8 processors)

and 4.21 (with 12 processors), respectively; and the maximum total speedups in Cases U1G and T1G are 4.10 (with 12 processors) and 3.93 (with 6 processors), respectively.

The partitioning options in METIS should be selected to minimize the number of edge-cuts in Cases G1, G2, and G3 with 128 or more processors in pure RGMS studies. Despite occasional deviations in simulations involving relatively few processors, the communication volume option appears to have a clear advantage in large simulations.

Chapter 6 (a) compares the simulation results with the simplified and full geomechanical models in Cases U1, U1G, T1, and T1G, (b) investigates the effects of discretization on solutions with simplified geomechanical and full geomechanical models in Cases U1, U2, U1G, and U2G, and (c) discusses in detail observations from the study of 3D problem involving combined depressurization and thermal stimulation for gas production from a real-life oceanic hydrate deposit. The following flow-related results are monitored: spatial distributions of pressure, temperature, gas saturation, hydrate saturation, and salinity (mass fraction) of salt; water and gas production, and the corresponding cumulative productions; instantaneous and cumulative water-to-gas ratio; and salinity of salt in the production stream at the well. The following geomechanics-related results are monitored: spatial distributions of displacements, maximum principal effective stress, and volumetric strain.

7.2. Conclusions

The following conclusions are reached from this study:

- Work in this project included (a) the development of the RGMS parallel geomechanics simulator, (b) the development of pT+H V1.5 code by parallelizing the pre-existing T+H V1.5 serial code for the description of system behavior during hydrate dissociation or formation in porous/fractured media, and (c) the coupling of the RGMS and pT+H V1.5 code. The validity and reliability of the parallel codes (a) RGMS, (b) pT+H V1.5, and the (c) coupled pT+H V1.5 and RGM simulators—in terms of their ability to solve the physics of complex problems—are proved by the excellent agreement of their results to existing (known) analytical and numerical solutions.
- As indicated by the execution times and the associated speedups, the parallel performances of the RGMS, the pT+H V1.5, and the coupled pT+H V1.5 and RGM simulators on both the Ada Linux cluster and the Mac Pro are very satisfactory.
- On the Ada Linux cluster, the simulation cycling speedups of RGMS are 218.89, 188.13, and 284.70 in Cases G1 (2D Cartesian problem), G2 (2D cylindrical problem), and G3 (3D Cartesian problem), respectively, when the number of processors N_p = 512. For the same N_p,
    - — The total speedups of pT+H V1.5 are 174.25 and 341.67 in Cases U1 (2D cylindrical problem) and T1 (3D Cartesian problem), respectively, and
    - — The total speedups of the coupled pT+H V1.5 and RGM simulators are 134.97 and 331.80 in Cases U1G (2D cylindrical problem) and T1G (3D Cartesian problem), respectively.
- On the Mac Pro, the maximum speedups are not always achieved using 12 processors because of different architecture and memory management. Actually, it is possible that

the parallel performance with multiple processors could be worse than that for a single processor. The maximum simulation cycling speedups of RGMS are achieved with N_p = 12 processors and are 6.19, 6.09, and 7.19 in Cases G1, G2, and G3, respectively. This is attributed to the fact that RGMS solves the numerically less demanding quasi-static geomechanics problem that does not require significant processor communications, thus enabling continuously improving performance with an increasing N_p in the limited number of processors available in the Mac Pro. The maximum total speedups of pT+H V1.5 in Cases U1 and T1 are 4.44 and 4.21, and are obtained with N_p = 8 and 12, respectively. The maximum total speedups of the coupled pT+H V1.5 and RGM simulator in Cases U1G and T1G are 4.10 and 3.93, and are obtained N_p = 12 and 6, respectively. In all parallel simulations, and especially on desktop systems such as a Mac Pro, it is highly advisable to conduct preliminary tests of the problem under investigation (involving different N_p and a limited number of time steps) in order to determine whether the maximum available number of processors will provide the highest performance.

- The partitioning options in the domain decomposition package METIS are crucial in the speedup of parallelization, especially when running with hundreds of processors. In Cases G1, G2, and G3 (geomechanics-only problems with uniform discretization), the option of minimizing the number of edge-cuts provides the best performance when used with 512 processors. Despite occasional deviations in pT+H V1.5 and coupled RGMS-pT+HV1.5 simulations involving relatively few processors, the option that

minimizes the communication volume appears to have a clear advantage in the solution of large-scale problems.

- In Cases U1 and U1G, the inclusion of the full geomechanical model leads to localized decreases in porosity and permeability because of compaction that confines the pressure drops in a smaller volume of the hydrate deposit, inhibits wormhole formation and growth, changes the locations of active hydrate dissociation, and results in lowers gas and water production.
- In Case U1G, the geomechanical analysis shows large deformations in the reservoir, including (a) subsidence of the top of the hydrate deposit (because of the continuing unchanged vertical stresses caused by the weight of the overburden, the pressure of which is practically unaffected by the producing well), (b) uplift of the base of the deposit because of the higher pressure in the very-low permeability underburden, and (c) the resulting "squeeze" of the reservoir thickness in the vicinity of the well. These changes cannot be captured without a full geomechanical model and indicate the importance of coupling pT+H V1.5 with RGMS for realistic predictions of the behavior of the entire system.
- Comparison of the results from Cases U1 and U2 to those from Cases U1G and U2G indicates that discretization influences the solutions with either the simplified or full geomechanical model, and coarse grids are unable to capture some critical processes. The reasons are that (a) coarse discretization averages the system thermal behavior over larger volumes, thus attenuating the expected sharp pressure and temperature changes associated with hydrate dissociation, and (b) hydrate dissociation is not a

process that becomes more diffusive with time, but is characterized by sharp fronts that persist for very long time. This means that not only fine discretizations are needed, but also that these cannot be confined to the vicinity of the well and need to be applied to the entire domain if reliably representative solutions are to be obtained. The resulting computational effort is substantial and exceeds the capabilities of most single-processor systems if realistic problems are to be investigated, making the use of efficient and powerful parallel simulators (such as pT+H V1.5 and the coupled pT+H V1.5 and RGMS codes) a necessity.

- The comparison of the results in Cases T1 and T1G shows that the full geomechanical model shows complex effects on the spatial distributions and predicts less gas production and more water production.
- In all cases, a large volumetric strain is observed in the hydrate-bearing layers (usually unconsolidated sandy units, in which most of the mechanical strength is provided by the hydrate, and which respond rapidly to its dissociation by deforming), and mud layers (soft, easily deformable units, in which the presence of hydrates is minimal, and which respond rapidly to depressurization by deforming).
- The study of coupled depressurization and thermal stimulation for gas production from hydrate deposits in Cases T1 and T1G using a combination of two vertical wells (production and injection) does not appear very promising at a particular site in the Krishna-Godawari basin, as gas production and free gas saturation in the reservoir appear to decline rapidly with time, while water production increases and tends toward a constant level. Of particular interest is that the volumetric extend of dissociation, as

denoted by changes in temperature and the salinity in the reservoir, is much larger than that described by the reduction in the hydrate saturation, indicating a low-level dissociation that is insufficient to lead to significant gas releases. These observations apply to both Cases T1 and T1G.

7.3. Recommendations

The following recommendations are made:

- The study of partitioning objectives in the application of METIS needs more problems of various complexity and size in order to generate some general rules.
- Different solvers with various preconditioners need to be tested in order to obtain a more thorough understanding of the performance of RGMS, pT+H V1.5, and the coupled pT+H V1.5 and RGM simulator and to identify optimal options in their application.
- In the production of methane from hydrates in situations such as those in Cases U1 and U1G, the effect of varying bottomhole pressures needs to be investigated in an effort to determine the highest permissible pressure that can affect economically viable gas production without causing unacceptable deformation of the reservoir and well stability problems.
- In the study of coupled depressurization and thermal stimulation in Cases T1 and T1G, a thorough sensitivity analysis (involving different well configurations, injection and production schedules and rates, and temperature and salinity of the injected water) is

needed to determine the technical feasibility and economic viability of gas production from the hydrate reservoir at this site.

- More studies of problems with varying discretizations in each case are necessary to better understand the mesh influence on the production prediction and the overall system response. This is an issue that has barely been addressed in the study of hydrates.

REFERENCES

Balay, S., Abhyankar, S., Adams, M. F., Brown, J., Brune, P., Buschelman, K., and Kaushik, D. 2014. PETSc Users Manual. Argonne National Laboratory, Lemont, Illinois, USA.

Boswell, R., Myshakin, E., Moridis, G. J., Konno, Y., Collett, T. S., Reagan, M. T., Ajayi, T., and Seol, Y. 2019. India National Gas Hydrate Program Expedition 02 Summary of Scientific Results: Numerical Simulation of Reservoir Response to Depressurization. *Journal of Marine and Petroleum Geology* **108**: 154–166. https://doi.org/10.1016/j.marpetgeo.2018.09.026.

Commer, M., Kowalsky, M. B., Doetsch, J., Newman, G. A., and Finsterle, S. 2014. MPiTOUGH2: A Parallel Parameter Estimation Framework for Hydrological and Hydrogeophysical Applications. *Computers & Geosciences* **65**: 127–135. https://doi.org/10.1016/j.cageo.2013.06.011.

Coussy, O. (2004). *Poromechanics*. John Wiley & Sons.

Dana, S., Ganis, B., and Wheeler, M. F. (2018). A Multiscale Fixed Stress Split Iterative Scheme for Coupled Flow and Poromechanics in Deep Subsurface Reservoirs. *Journal of Computational Physics* **352**: 1–22. https://doi.org/10.1016/j.jcp.2017.09.049.

De La Fuente M., Vaunat J., Marín-Moreno H. 2019. Thermo-Hydro-Mechanical Coupled Modeling of Methane Hydrate-Bearing Sediments: Formulation and Application. *Energies* **12** (11): 2178. https://doi.org/10.3390/en12112178.

Edwards, A. L. 1972. TRUMP: A Computer Program for Transient and Steady State Temperature Distributions in Multidimensional Systems. Technical Report, National Technical Information Service, National Bureau of Standards, Springfield, VA (September 1972).

Falgout R. D. and Yang U. M. 2002. *hypre*: A Library of High Performance Preconditioners. International Conference on Computational Science, Amsterdam, The Netherlands, 21–24 April.

Geertsma, J. 1957. The Effect of Fluid Pressure Decline on Volumetric Changes of Porous Rocks. *Transactions of the American Institute of Mining and Metallurgical Engineers* **210** (12): 331–340. SPE-728-G-MS. https://doi.org/10.2118/728-G-MS.

Guo, X., Kim, J., and Killough, J. 2017. Hybrid MPI-OpenMP Scalable Parallelization for Coupled Non-Isothermal Fluid-Heat Flow and Elastoplastic Geomechanics. Paper presented at the SPE Reservoir Simulation Conference, Montgomery, Texas, USA, February 2017. SPE-182665-MS. https://doi.org/10.2118/182665-MS.

Guo, X., Wang, Y., and Killough, J. 2016. The Application of Static Load Balancers in Parallel Compositional Reservoir Simulation on Distributed Memory System. *Journal of Natural Gas Science and Engineering* **28**: 447–460. https://doi.org/10.1016/j.jngse.2015.12.030.

Heppner I., Lampe M., A. Nägel, Reiter S., Rupp M., Vogel A., and Wittum G. 2013. Software framework UG4: Parallel multigrid on the hermit supercomputer. ed. W. E. Nägel, D. H. Kr¨oner, and M. M. Resch, *High Performance Computing in Science and Engineering '12*, 435–449. Springer Berlin Heidelberg.

Hughes, T. J. R. 1987. *The Finite Element Method: Linear Static And Dynamic Finite Element Analysis*. Englewood Cliffs: Prentice-Hall.

Jin, G., Lei, H., Xu, T., Xin, X., Yuan, Y., Xia, Y., and Juo, J. 2018. Multiscale Fixed Stress Split Iterative Scheme for Coupled Flow and Poromechanics in Deep Subsurface Reservoirs. *Marine and Petroleum Geology* **92**: 424–436. https://doi.org/10.1016/j.marpetgeo.2017.11.007.

Karypis, G. and Kumar, V. 1998. Multilevelk-way Partitioning Scheme for Irregular Graphs. *Journal of Parallel and Distributed Computing* **48** (1): 96–129. https://doi.org/10.1006/jpdc.1997.1404.

Karypis, G. and Kumar, V. 1999. Parallel Multilevel Series k-way Partitioning Scheme for Irregular Graphs. *SIAM Review* **41** (2): 278–300. https://doi.org/10.1137/S0036144598334138.

Kim, J. and Moridis, G. J. 2012. Modeling And Numerical Simulation For Coupled Flow And Geomechanics In Composite Gas Hydrate Deposits. Paper presented at the 46th US Rock Mechanics/Geomechanics Symposium, Chicago, Illinois, USA. ARMA-2012–297.

Kim, J. and Moridis, G. J. 2013. Development of the T+M coupled flow-geomechanical simulator to describe fracture propagation and coupled flow-thermal-geomechanical processes in tight/shale gas systems. *Computers & Geosciences* **60**: 184–198. https://doi.org/10.1016/j.cageo.2013.04.023.

Kim, J. and Moridis, G. J. 2013. Gas Flow Tightly Coupled to Elastoplastic Geomechanics for Tight and Shale Gas Reservoirs: Material Failure and Enhanced Permeability. Paper presented at the SPE Americas Unconventional Resources Conference, Pittsburgh, Pennsylvania, USA. SPE-155640-MS. https://doi.org/10.2118/155640-MS.

Kim, J., Tchelepi, H. A., and Juanes, R. 2011a. Stability, Accuracy, and Efficiency of Sequential Methods for Coupled Flow and Geomechanics. *SPE Journal* **16** (02): 249–262. SPE-119084-PA. https://doi.org/10.2118/119084-PA.

Kim, J., Tchelepi, H. A., and Juanes, R. 2011b. Stability and Convergence of Sequential Methods for Coupled Flow and Geomechanics: Fixed-Stress and Fixed-

Strain Splits. *Computer Methods in Applied Mechanics and Engineering* **200** (13–16): 1591–1606. https://doi.org/10.1016/j.cma.2010.12.022.

Kowalsky, M. B. and Moridis, G. J. 2007. Comparison of Kinetic and Equilibrium Reaction Models in Simulating the Behavior of Gas Hydrates in Porous Media, *Journal of Energy Conversion and Management* **48** (6): 1850–1863. https://doi.org/10.1016/j.enconman.2007.01.017.

Lei, H., Xu, T., and Jin, G. 2015. TOUGH2Biot – A Simulator for Coupled Thermal-Hydrodynamic-Mechanical Processes in Subsurface Flow Systems: Application to CO_2 Geological Storage and Geothermal Development. *Computers & Geosciences* **77**: 8–19. https://doi.org/10.1016/j.cageo.2015.01.003.

Li, G., Moridis, G. J., Zhang, K., and Li, X.-S. 2010. Evaluation of Gas Production Potential from Marine Gas Hydrate Deposits in Shenhu Area of the South China Sea. *Energy & Fuels* **24**: 6018–6033. https://doi.org/10.1021/ef100930m.

Liu, Y. Z., Liu, L. J., Leung, J. Y., and Moridis, G. J. 2020. Sequentially Coupled Flow and Geomechanical Simulation With a Discrete Fracture Model for Analyzing Fracturing Fluid Recovery and Distribution in Fractured Ultra-Low Permeability Gas Reservoirs. *Journal of Petroleum Science and Engineering* **189**: 107042. https://doi.org/10.1016/j.petrol.2020.107042.

Makogon, Y. 1997. *Hydrates of Hydrocarbons*. PennWell Publishing Company.

McNamee, J. and Gibson, R. E. 1960a. Displacement Functions and Linear Transforms Applied to Diffusion through Porous Elastic Media. *The Quarterly Journal of Mechanics and Applied Mathematics* **13** (1): 98–111. https://doi.org/10.1093/qjmam/13.1.98.

McNamee, J. and Gibson, R. E. 1960b. Plane Strain and Axially Symmetric Problems of the Consolidation of a Semi-Infinite Clay Stratum. *The Quarterly Journal of Mechanics and Applied Mathematics* **13** (2): 210–227. https://doi.org/10.1093/qjmam/13.2.210.

McPhee, C., Reed, J., and Zubizarreta, I. 2015. Chapter 12 – Geomechanics Tests. In *Developments in Petroleum Science*, Vol. 64, 671–779. Elsevier. https://doi.org/10.1016/B978-0-444-63533-4.00012-3.

Message Passing Interface Forum 2008. MPI: A Message-Passing Interface Standard, Version 2.2. *International Journal of Supercomputer Applications* **8**.

Moridis, G. J. 2003. Numerical Studies of Gas Production From Methane Hydrates. *SPE Journal* **8** (4): 359–370. SPE-87330-PA. https://doi.org/10.2118/87330-PA.

Moridis, G. J. 2014. User's Manual for the Hydrate v1.5 Option of TOUGH+ v1.5: A Code for the Simulation of System Behavior in Hydrate-Bearing Geologic Media. Lawrence Berkeley National Laboratory, Berkeley, California, USA.

Moridis, G. J. 2016. User's Manual of the Meshmaker v1.5 Code: A Mesh Generator for Domain Discretization in Simulations of the TOUGH+ and TOUGH2 Families of Codes. Lawrence Berkeley National Laboratory, Berkeley, California, USA.

Moridis, G. J. and Pruess K. 2014. User's Manual for the TOUGH+ Core Code v1.5: A General-Purpose Simulator of Non-Isothermal Flow and Transport Through Porous and Fractured Media. Lawrence Berkeley National Laboratory, Berkeley, California, USA.

Moridis, G. J. and Reagan, M. T. 2007a. Strategies for Gas Production From Oceanic Class 3 Hydrate Accumulations. Paper presented at the Offshore Technology Conference, Houston, Texas, USA, 30 April–3 May. OTC-18865-MS. https://doi.org/10.4043/18865-MS.

Moridis, G. J. and Reagan, M. T. 2007b. Gas Production From Oceanic Class 2 Hydrate Accumulations. Paper presented at the Offshore Technology Conference, Houston, Texas, USA, 30 April–3 May. OTC-18866-MS. https://doi.org/10.4043/18866-MS.

Moridis, G. J. and Reagan, M. T. 2011a. Estimating the Upper Limit of Gas Production From Class 2 Hydrate Accumulations in the Permafrost, 1: Concepts, System Description and the Production Base Case, *Journal of Petroleum Science and Engineering* **76**: 194–201. https://doi.org/10.1016/j.petrol.2010.11.023.

Moridis, G. J. and Reagan, M. T. 2011b. Estimating the Upper Limit of Gas Production From Class 2 Hydrate Accumulations in the Permafrost, 2: Alternative Well Designs and Sensitivity Analysis, *Journal of Petroleum Science and Engineering* **76**: 124–137. https://doi.org/10.1016/j.petrol.2010.12.001.

Moridis, G. J. and Sloan, E. D. 2007a. Gas Production Potential of Disperse Low-Saturation Hydrate Accumulations in Oceanic Sediments. *Energy Conversion and Management* **48** (6): 1834–1849. https://doi.org/10.1016/j.enconman.2007.01.023.

Moridis, G. J., Collett, T. S., Boswell R., Kurihara M., Reagan M. T., Koh C., and Sloan E. D. 2009. Toward Production From Gas Hydrates: Current Status, Assessment of Resources, and Simulation-Based Evaluation of Technology and Potential, *SPE Reservoir Evaluation & Engineering* **12** (5): 745–771. SPE-114163-PA. https://doi.org/10.2118/114163-PA.

Moridis, G. J., Kim, J., Reagan, M. T., and Kim, S. J. 2013. Feasibility of gas production from a gas hydrate accumulation at the UBGH2-6 site of the Ulleung basin in the Korean East Sea. *Journal of Petroleum Science and Engineering* **108**: 180–210. https://doi.org/10.1016/j.petrol.2013.03.002.

Moridis, G. J., Kowalsky, M. B., and Pruess, K. 2007b. Depressurization-Induced Gas Production From Class 1 Hydrate Deposits. *SPE Reservoir Evaluation and Engineering* **10** (5): 458–481. SPE-97266-PA. https://doi.org/10.2118/97266-PA.

Moridis, G. J., Queiruga, A. F., and Reagan, M. T. 2019. Simulation of Gas Production from Multilayered Hydrate-Bearing Media with Fully Coupled Flow, Thermal,

Chemical and Geomechanical Processes Using TOUGH plus Millstone. Part 1: Numerical Modeling of Hydrates. *Transport in Porous Media* **128** (2): 405–430. https://doi.org/10.1007/s11242-019-01254-6.

Moridis, G. J., Reagan M. T., Boyle, K. L., and Zhang, K. 2011a. Evaluation of the Gas Production Potential of Challenging Hydrate Deposits. *Transport in Porous Media* **90**: 269–299. https://doi.org/10.1007/s11242-011-9762-5.

Moridis, G. J., Reagan, M. T., Queiruga, A.F., and Boswell, R. 2019. Evaluation of the Performance of the Oceanic Hydrate Accumulation at Site NGHP-02-09 in the Krishna-Godavari Basin During a Production Test and During Single and Multi-Well Production Scenarios. *Journal of Marine and Petroleum Geology* **108**: 660–696. https://doi.org/10.1016/j.marpetgeo.2018.12.001.

Moridis, G. J., Silpngarmlert, S., Reagan, M. T., Collett, T., and Zhang, K. 2011b. Gas Production From a Cold, Stratigraphically-Bounded Gas Hydrate Deposit at the Mount Elbert Gas Hydrate Stratigraphic Test Well, Alaska North Slope: Implications of Uncertainties. *Marine and Petroleum Geology* **28**: 517–534. https://doi.org/10.1016/j.marpetgeo.2010.01.005.

Narasimhan, T. N. and Witherspoon, P. A. 1976. An Integrated Finite Difference Method for Analyzing Fluid Flow in Porous Media. *Water Resources Research* **12** (1): 57–64. https://doi.org/10.1029/WR012i001p00057.

Narasimhan, T. N., Witherspoon, P. A., and Edwards, A. L. 1978. Numerical Model for Saturated-Unsaturated Flow in Deformable Porous Media, part 2: The Algorithm. *Water Resources Research* **14** (2): 255–261. https://doi.org/10.1029/WR014i002p00255.

Pan, F. 2009. Development and Application of a Coupled Geomechanics Model for a Parallel Compositional Reservoir Simulator. PhD dissertation, The University of Texas at Austin, Austin, Texas (Decemeber 2009).

Peaceman, D.W. 1977. *Fundamentals of Numerical Reservoir Simulation*, Elsevier, Amsterdam, The Netherlands.

Queiruga, A. F., Moridis, G. J., and Reagan, M. T. 2019. Simulation of Gas Production from Multilayered Hydrate-Bearing Media with Fully Coupled Flow, Thermal, Chemical and Geomechanical Processes Using TOUGH plus Millstone. Part 2: Geomechanical Formulation and Numerical Coupling. *Transport in Porous Media* **128** (1): 221–241. https://doi.org/10.1007/s11242-019-01242-w.

Reagan, M. T., Moridis, G. J., Freeman, C. M., Boyle, K. L, and Keen, N. D. 2013. Massively Parallel Simulation of Production from Oceanic Gas Hydrate Deposits. Paper presented at the International Petroleum Technology Conference, 26–28 March, Beijing, China. IPTC-17026-MS. https://doi.org/10.2523/IPTC-17026-MS.

Reagan, M. T., Queiruga, A. F., and Moridis, G. J. 2019. Simulation of Gas Production from Multilayered Hydrate-Bearing Media with Fully Coupled Flow, Thermal,

Chemical and Geomechanical Processes Using TOUGH plus Millstone. Part 3: Production Simulation Results. *Transport in Porous Media* **129** (1): 179–202. https://doi.org/10.1007/s11242-019-01283-1.

Rutqvist, J. 2017. An Overview of TOUGH-based Geomechanics Models. *Computers & Geosciences* **108**: 56–63. https://doi.org/10.1016/j.cageo.2016.09.007.

Rutqvist, J. and Moridis, G. J. 2009. Numerical Studies on the Geomechanical Stability of Hydrate-Bearing Sediments. *SPE Journal* **14** (2): 267–282. SPE-126129-PA. https://doi.org/10.2118/126129-PA.

Rutqvist, J. and Tsang, C.-F. 2002. A Study of Caprock Hydromechanical Changes Associated with CO_2 Injection into a Brine Aquifer. *Environmental Geology* **42**: 296–305. https://doi.org/10.1007/s00254-001-0499-2.

Rutqvist, J., Wu, Y.-S., Tsang, C.-F., and Bodvarsson G. 2002. A Modeling Approach for Analysis of Coupled Multiphase Fluid Flow, Heat Transfer, and Deformation in Fractured Porous Rock. *International Journal of Rock Mechanics and Mining Sciences* **39** (4): 429–442. https://doi.org/10.1016/S1365-1609(02)00022-9.

Terzaghi, K. and Peck R. B. 1948. *Soil Mechanics in Engineering Practice*, second edition. New York: John Wiley and Sons.

Tuminaro, R. S., Heroux, M., Hutchinson, S. A., and Shadid J. N. 1999. Official Aztec User's Guide, Ver 2.1, Massively Parallel Computing Research Laboratory, Sandia National Laboratories, Albuquerque, New Mexico, USA.

Wang, B. 2014. Parallel Simulation of Coupled Flow and Geomechanics in Porous Media. PhD dissertation, The University of Texas at Austin, Austin, Texas (Decemeber 2014).

Zhang, K., Wu, Y.-S., and Pruess, K. 2008. User's Guide for TOUGH2-MP – A Massively Parallel Version of the TOUGH2 Code. Lawrence Berkeley National Laboratory, Berkeley, California, USA.

Zhao, N. 2012. Integration of Reservoir Simulation and Geomechanics. PhD dissertation, The University of Utah, Salt Lake City, Utah, (May 2008).

Zienkiewicz O. C., Taylor R. L., and Zhu J. Z. 2005. The Finite Element Method: Its Basis and Fundamentals, sixth edition. Elsevier Butterworth-Heinemann.